Strong-field Quantum Electrodynamics in the extremely intense light of relativistic plasma mirrors

Antonin Sainte-Marie

To cite this version:

Antonin Sainte-Marie. Strong-field Quantum Electrodynamics in the extremely intense light of relativistic plasma mirrors. High Energy Physics - Phenomenology [hep-ph]. Université Paris-Saclay, 2023. English. NNT : 2023UPASP021 . tel-04057676

HAL Id: tel-04057676
https://theses.hal.science/tel-04057676

Submitted on 4 Apr 2023

Strong-field Quantum Electrodynamics in the extremely intense light of relativistic plasma mirrors

Électrodynamique quantique en champs forts dans la lumière extrêmement intense de miroirs plasma relativistes

Thèse de doctorat de l'université Paris-Saclay

École doctorale n° 572, Ondes et matière (EDOM)
Spécialité de doctorat : Physique
Graduate School : Physique. Référent : Faculté des sciences d'Orsay

Thèse préparée dans l'unité de recherche **LIDYL (Université Paris-Saclay, CEA, CNRS)**, sous la direction d'**Henri VINCENTI**, directeur de recherche, et le co-encadrement de **François GELIS**, directeur de recherche

Thèse soutenue à Paris-Saclay, le 14 février 2023, par

Antonin SAINTE-MARIE

Composition du jury

Membres du jury avec voix délibérative

Thomas GRISMAYER Directeur de recherche, Instituto de Plasmas e Fusão Nuclear, *Lisbonne, Portugal*	Rapporteur & Président
Antonino DI PIAZZA Professeur, Max Planck Institut für Kernphysik, *Heidelberg, Allemagne*	Rapporteur & Examinateur
Arkady GONOSKOV Professeur, University of Gothenburg, *Göteborg, Suède*	Examinateur
Jean-Marcel RAX Professeur, Laboratoire de physique des deux infinis Irène Joliot-Curie, *Orsay, France*	Examinateur

THESE DE DOCTORAT

NNT : 2023UPASP021

ÉCOLE DOCTORALE
Ondes et matière
(EDOM)

Titre : Électrodynamique quantique en champs forts dans la lumière extrêmement intense de miroirs plasma relativistes

Mots clés : Électrodynamique quantique en champs forts, calcul parallèle exascale, simulation PIC, plasma, laser de ultra-haute intensité, plasma quantique relativiste

Résumé :

La thèse présentée vise à spécifier les phénomènes physiques appelés à se produire dans la lumière extrêmement intense issue de miroirs plasma relativistes, d'intensités comprises entre 10^{24} et $10^{29}\ \mathrm{W.cm^{-2}}$, dans différentes configurations. Ces travaux s'inscrivent dans la continuité des progrès continus de l'intensité lumineuse accessible par lasers ultra-brefs de haute puissance, motivant la recherche de phénomènes relevant de l'électrodynamique quantique en champs forts, quasiment inobservés à présent. Si réaliser de telles expériences permettrait le test de théories fondamentales, établies ou spéculatives, ainsi que la génération de sources secondaires de particules remarquables, nombre d'entre elles requièrent des intensités supérieures à $10^{25}\ \mathrm{W.cm^{-2}}$, hors de portée même des infrastructures de classe Pétawatt. Les miroirs plasma relativistes (MPR) offrent une alternative séduisante, permettant de réaliser les champs forts requis avec les technologies actuelles.

L'interaction de la lumière MPR avec le vide quantique du champ électron-positron a été étudiée via la diffusion photon-photon, dont nous calculons les signatures expérimentalement observables. De même, un seuil d'intensité est défini pour la conversion du champ électromagnétique MPR dans le vide en paires électron-positron par le processus de Schwinger. L'interaction avec de la matière préexistante a été envisagée sous deux formes : la focalisation du faisceau MPR sur une cible solide, ou la collision avec un faisceau d'électrons de 10 GeV. Dans le premier cas, une production exponentielle de particules a lieu par l'effet de « cascade QED », aboutissant à des faisceaux d'électron-positron relativistes de densité extrême ($> 10^{28}\ \mathrm{cm^{-3}}$) et de durée attoseconde. Dans le second cas, le champ électrique dans le référentiel du faisceau d'électrons atteint des valeurs telles que, selon la conjecture de Ritus-Narozhny, les notions usuelles d'électrons, positrons et photons perdraient leur validité théorique, ouvrant une possible fenêtre empirique sur un régime d'interactions lumière-matière actuellement inconnu.

universite PARIS-SACLAY
ÉCOLE DOCTORALE
Ondes et matière
(EDOM)

Title : Strong-Field Quantum Electrodynamics in the Extremely Intense Light of Relativistic Plasma Mirrors

Keywords : Strong-Field Quantum Electrodynamics, Exascale Computing, PIC Simulation, Plasma, Ultra-Intense Laser, Relativistic Quantum Plasma

Abstract :

The present thesis aims at specifying the physical processes to occur in the extremely intense light of relativistic plasma mirrors, with intensities ranging from 10^{24} to 10^{29} $\mathrm{W.cm^{-2}}$, in different configurations. These works take ground in the continuous progress of achievable light intensity offered by ultra-short high power lasers, motivating the search for strong-field Quantum Electrodynamics phenomena, yet essentially unobserved to this day. While achieving such experiments would allow for the test of fundamental theories, either established or speculative, together with the generation of remarkable secondary sources of particles, many would require intensities beyond 10^{25} $\mathrm{W.cm^{-2}}$ that even Petawatt-class infrastructures can not reach. Relativistic Plasma Mirrors (RPM) offer one promising alternative for producing the required field strengths with present day technology.

RPM light interaction with the quantum vacuum of the electron-positron field was studied through the process of light-by-light scattering, whose experimentally observable signatures were computed. We also specified an intensity threshold for the conversion of RPM light into electron-positron pairs *via* the Schwinger process. Interaction with pre-existing matter was considered in two forms : the focusing of the RPM beam on a solid target, or the collision with a 10 GeV electron beam. In the first scenario, an exponential rise of particle number takes place by the effect of "QED cascade", resulting in extreme density ($> 10^{28}$ $\mathrm{cm^{-3}}$) relativistic electron-positron beam of attosecond duration. In the second scenario, the electric field in the reference frame of the incident electron beam reaches values so high that, according to the Ritus-Narozhny conjecture, the usual notions of electrons, positrons and photons break down, possibly opening an empirical window on a currently little known regime of light-matter interaction.

Acknowledgements

Any work of human character certainly is by definition the work of many, however this thesis is such in a much plainer way. I am therefore pleased to thank all the people who concurred to shape it, all in different manners.

First of all, I would like to thank my thesis supervisor Henri Vincenti for his support during these three years from both a human and a scientific point of view. Thank you for your unwavering trust, the accompanying freedom I could enjoy and for your communicative drive that certainly is core to the engaging atmosphere in the PHI group. I thank my co-supervisor François Gelis as well, for a most illuminating teaching without which I would surely not have enjoyed the same sight on this matter.

I would also like to express my vivid gratitude towards Fabien Quéré, for convincing me twice to work in the PHI group, and for your accurate advice more generally. I also owe a lot to Guy Bonnaud in the same manner, but in addition as a teacher, thank you for your benevolent support this whole time.

I would then naturally like to sincerely thank Felix Karbstein, for a most agreeable and, for my part, elucidating scientific collaboration. Thank you for your patience and all our lively exchanges, I am convinced that this thesis would not have looked remotely the same without them.

Ces trois années ont été de nombreux de jours, dont de nombreuses heures dans une pièce généralement chaude ou froide avec mes collègues du groupe PHI, que je tiens bien sûr à remercier. Merci Luca Fedeli, pour beaucoup de choses, et certainement pour une forme quasi-boudhique de solicitude, notamment au début quand nous étions deux dans la pièce et que j'avais beaucoup de questions d'ordinateur – cela dit merci de même pour les recommandations alimentaires «bizarres». Merci également Neïl Zaim, pour un soutien non moins déterminant et d'autres fois. Merci Thomas Clark pour l'esprit en général et les histoires en particulier, et merci Ilian Kara-Mostefa pour la fraîcheur.

Ces jours ont également été ceux de mes amis, de ma famille et de mes proches, merci. La gravité progressant en raison inverse de l'intervalle, merci Juliette, témoin des scènes énigmatiques avec une clarté dont je te rends grâce.

Merci enfin pour leurs empreintes à la lisière de tout ceci à Fuzzi, Ossiane, Rocco, Altaï, Djinni, Koba, Ulisse, Galaad, Styx, Tikita, Nanouk et Shibuya.

Introduction

Electromagnetic interactions permeate virtually all tangible phenomena, and this reality was elucidated more than a century ago. Yet, this knowledge could never materialize as a practical force fully until the laser was invented, offering unprecedented degrees of control on the electromagnetic field, and thus on its interactions with matter. Laser-based systems have since then blossomed towards all spheres of production, including fundamental science.

In particular, in the last two decades a consistent research field has emerged around "ultra-high intensity" physics, studying the interactions of the most intense achievable laser pulses with matter, thereby converted into particles and plasmas. These efforts could uncover many rich phenomena and gave birth to several applications. Though benefiting from steady progress in laser technology, leading to a continuous rise in laser intensity, these methods could rely on a qualitatively well-defined set of elementary physical processes, all described by the classical mechanics of fields and particles at relativistic energies [1].

The strong-field frontier of ultra-high intensity physics

The current situation is however likely to be a turning point, for last-generation infrastructures, lasers of more than a Petawatt (10^{15} W) peak power, hold the potential for revealing radically new processes. All would stem from the quantum aspect of particles and fields, and collectively delineate the physical realm of "strong-field Quantum Electrodynamics" (sf-QED) [2]. Accessing such phenomena would prove of both fundamental and practical value, allowing for empirical test of established or speculative theories [3], and for the generation of exotic sources of radiation and particles [4]. This strong-field frontier of laser physics has consequently received a growing attention, and now drives the regular activity of many scientists as well as the commissioning of ambitious experimental facilities.

Nonetheless, if first signatures of these effects can be detected in a near future [3, 4], the path towards deeper regimes of sf-QED unfortunately appears much steeper than its shores. Consider for definiteness the central sf-QED process of the conversion of a photon into an electron-positron pair. If forecast facilities can expect to detect some created positrons, the strong depletion of the field into an electron-positron plasma and their emitted photon radiation, producing a qualitatively new physical dynamics, would only occur at ten to a hundred times higher intensities still. However, multi Petawatt-class infrastructures are now approaching industrial scales, implying ever more complex laser engineering, so that a technological wall can not be excluded in the short term[1] [5]. As a consequence, alternative schemes towards stronger fields already are actively being investigated [4].

---

[1] The issue of scaling is of course not intrinsic to laser physics, as one may find analogous situations in high-energy accelerators, thermonuclear fusion facilities, and certainly other mature fields reaching the material scale and cost of competing collective endeavours.

Strong-field Quantum Electrodynamics in the extremely intense light of relativistic plasma mirrors

Relativistic plasma mirrors appear as one very promising way to achieve the highest possible fields with present day lasers [6–11]. As an intense pulse reaches a sharp solid interface, it turns it into a dense plasma which oscillates at speeds close to that of light, thus reflecting the pulse while compressing it by Doppler effect. Properly tuning this interaction, the reflected pulse can also be naturally focused to spot sizes only limited by its now shortened wavelength, concentrating light in much tighter volumes than allowed by the initial laser source, which results in intensity increases between two and five orders of magnitude [12, 13]. The corresponding fields would come near the critical value at which a field spontaneously decays into electron-positron pairs, known as the Schwinger field, which may allow studying critical sf-QED effects such as light self-interaction, and certainly would facilitate entering deep into the quantum-dominated regime of sf-QED.

The core of my work has consisted in specifying the main physical phenomena to be expected at the interaction point of these relativistic plasma mirror sources. In this thesis, I will be presenting the predictions derived from a closer study of different interaction scenarios. Light couplings to the electron-positron field in a vacuum will be studied first, deriving observable signatures in different experimental setups, including scattered photon spectra and Schwinger pair creation threshold. These subtle effects when no matter is there leave room to to prolific pair creation as soon as one charged particle comes in. This process of field-matter interaction occurs for different types of initial seed, a Schwinger pair, a dense target, high-energy electron beams, affecting the involved elementary processes and the macroscopic system state. In particular, solid targets could allow the formation of relativistic quantum and extremely dense electron-positron plasma jets, while high-energy particle beams collisions with the light pulses could allow testing the Ritus-Narozhny conjecture, pertaining to the behavior of strong-field Quantum Electrodynamics in a regime where even the notion of photon, electron and positron particles breaks down.

Table of contents

Abstract of Part I

The material and intellectual context in which the present thesis takes ground is exposed, introducing our aims and methods.

Chapter 1 presents the state-of-the-art of ultra-high intensity field sources and the current horizon of accessing qualitatively new strong-field phenomena. Relativistic plasma mirrors are introduced as a bridge towards much stronger fields still, motivating our study of expected processes in their light.

Chapter 2 reviews a reference theoretical framework encompassing this physics, and its numerical realization in the form of *ab initio* PIC-QED simulations. A more specialized formalism we used for computing vacuum quantum electrodynamical processes is introduced as well.

PART I

State-of-the-art and aims

Chapter 1

Plasma mirrors as a path towards strong electromagnetic fields

In the wake of steady progress in laser technology opening up to an ever wider range of physical configurations, a consistent research community has developed around so-called "ultra-high intensity" physics. Although the quantitative meaning of such name has been shifting by many orders of magnitude already, during the last two decades it has been referring to a fairly stable set of applications and physical regimes, essentially described by the classical mechanics of fields and particles at relativistic energies. The current situation is however likely to be a turning point, for radically different physical phenomena are expected in last-generation facilities, either planned or under construction, revealing the quantum aspect of particles and fields.

Relying on a scheme explicitly designed to foster the ongoing transition, the present thesis fully takes ground in such context. By generating pulses exceeding forecast laser intensities by two to five orders of magnitude, relativistic plasma mirrors could allow entering the quantum-dominated regime of strong-field Quantum Electrodynamics, with fundamental and instrumental implications. Our research was devoted to try and predict some of them explicitly.

In this chapter, we wish to provide an understanding of how this work articulates with its overall material context. An overview of ultra-high intensity lasers physics and technology will be given first, detailing the performances expected from last generation infrastructures. The novelty encountered at higher intensity will then be exposed, with an emphasis on the physical consequences of strong-fields, essentially leaving aside the rich technicalities of their (actively developing) theoretical depiction. After a review of other means envisaged to reach strong enough fields, relativistic plasma mirrors are introduced as a promising way to magnify laser intensities, in principle up to near the Schwinger field, at which the electromagnetic and electron-positron fields significantly interact even in a the absence of particles. Last section will finally expose the directions pursued in this work.

1.1 Physics of ultra-high intensity lasers today

Since the first laser systems were built in the 1960s their derivatives have fanned out to virtually all spheres of production, with individual, industrial and scientific uses. Within the corresponding variety of designs, some were dedicated to achieving the highest possible light *intensity*. This number quantifies the transformation that a laser pulse can induce in another system, locally in space in some period of time, and thereby determines the range of underlying physical processes, or *regime*. For the last two decades at least, these instruments have grown into an autonomous branch of fundamental research, generating a specific set of phenomena, opening to exclusive features in applications, thus motivating ever higher intensity systems.

In this section we briefly trace back this evolution, grounding the view of an homogeneity of the physical regimes accessed in the last two decades, all characterized by classical electrodynamics with relativistic particles. For definiteness, typical applications will be reviewed, better illustrating our stance. Finally we will make contact with the state-of-the-art, operational or forecast systems, so as to introduce the new *strong-field regime* they open to, and give a sense of the scales relevant for the corresponding phenomena and infrastructures.

1.1.1 Decades of progress in attainable light intensity

Electromagnetic intensity The physical notion of "light intensity" refers to local properties of the electromagnetic field. The formulation of electromagnetic phenomena in terms of a *field* distinct from other known physical systems[1] certainly is among the most incidental achievement of XIXth century Physics [14]. When gravitational phenomena can be neglected, a field is fruitfully conceived as variables attached to each point of space, physical as they can interact with other physical systems. In particular, field variables exchange energy among themselves and their environment, which classically translates into a continuity equation [15],

$$\frac{d}{dt}\int_{\Omega} d\mathbf{x} u_{\mathrm{em}}(\mathbf{x},t) + \oint_{\partial\Omega} d\sigma \cdot \mathbf{\Pi}(\mathbf{x},t) = -\int_{\Omega} d\mathbf{x} w_{\mathrm{m}}(\mathbf{x},t) \tag{1.1}$$

with t the time variable, Ω a space domain of boundary $\partial\Omega$, u_{em} the local electromagnetic energy density, w_{m} the net energy exchange rate with any non-electromagnetic system[2] and $\mathbf{\Pi}$ the Poynting vector. It therefore appears that energy is transported by the electromagnetic field from one space region to the next, at a rate given by the flux of the Poynting vector through the considered interface. Then, for any oriented surface Σ,

$$\textbf{Electromagnetic power } [\mathrm{W}]\textbf{:}\ \boxed{P_\Sigma = \oint_\Sigma d\sigma \cdot \mathbf{\Pi}} \tag{1.2}$$

is the instantaneous *power* transmitted by the electromagnetic field through Σ, expressed in Watts [W], and we define,

$$\textbf{Electromagnetic intensity } [\mathrm{W.cm}^{-2}]\textbf{:}\ \boxed{I \triangleq \|\mathbf{\Pi}\|} \tag{1.3}$$

the local instantaneous electromagnetic *intensity*, conventionally expressed in Watts per centimetre squared [W.cm^{-2}] in laser physics. This quantity relates to the local values of the electric and magnetic vectors as,

$$I = \frac{c^2\varepsilon_0}{2}\|\mathbf{E}\times\mathbf{B}\| \tag{1.4}$$

with ε_0 the vacuum dielectric permittivity and c the speed of light. On the other hand, the local instantaneous electromagnetic energy density is given by,

$$u_{\mathrm{em}} = \frac{\varepsilon_0}{2}\left(\mathbf{E}^2 + (c\mathbf{B})^2\right) \tag{1.5}$$

In the absence of interaction with matter, the field equations of motion entail the propagation of any local disturbance in the field at a speed c, resulting in travelling

---

[1] See App. A for "physical system", a "field" is a physical system with an infinite number of variables.

[2] This essentially coincides with the notion of "matter" in classical physics.

configurations known as electromagnetic waves. Moreover, such propagation generically leads to a symmetry between the local values of $\mathbf{E}$ and $\mathbf{B}$, resulting in a direct relation between u_{em} and I. In the limiting case of a plane wave (always indicated by a p.w. superscript in the following) we find,

$$I \overset{\text{p.w.}}{=} c u_{\mathrm{em}} \overset{\text{p.w.}}{=} c\varepsilon_0 \mathbf{E}^2 \tag{1.6}$$

Finally, in the presence of charged matter particles,

$$w_{\mathrm{m}} = \mathbf{j} \cdot \mathbf{E} = \sum_i q_i \bar{\mathbf{v}}_i \cdot \mathbf{E} \tag{1.7}$$

with q_i the charge of the i-th kind of present charged particle $\bar{\mathbf{v}}_i$ their local mean speed, adopting a macroscopic description as relevant in plasma physics (*cf.* Sec. 2.1.1). Now as charged particles are affected by the Lorentz force,

$$\mathbf{f} = q\left(\mathbf{E} + \mathbf{v} \times \mathbf{B}\right) \tag{1.8}$$

it clearly appears that *high intensity* fields will induce fast and significant energy transfers.

In concrete terms, immersed in a wave of intensity $I = 10^{18}$ W.cm^{-2}, already attainable 20 years ago [5], a carbon atom becomes fully ionized simply by potential barrier suppression [16], and an electron initially at rest becomes relativistic in about 4×10^{-16} s, that is a fraction of an optical laser period. At the currently highest intensity achieved, of $I = 1 \times 10^{23}$ W.cm^{-2} [17], this time would decrease to around 3×10^{-18} s and even protons would near the speed of light in an optical cycle. All considered "ultra high-intensity" laser-matter physics therefore consist in the interaction of electromagnetic fields either with charged particles or plasma states, typically of relativistic kinetic energies.

High-intensity laser systems Lasers Physics forms a vast field of study [18]. From an instrumental perspective, lasers can simply be conceived as a way to produce electromagnetic waves with a unique degree of coherency and control, notably on energy, duration, direction and wavelength in the broadly near-optical range. These properties allow in particular for an efficient focusing of the generated pulses, down to near an optical wavelength, and thereby very high electromagnetic intensities.

In practice, lasers designed to reach the highest intensities typically emit visible to near-infrared light with a wavelength centred around $\lambda = 800$ nm, corresponding to a laser period $\delta t \simeq 2.67 \times 10^{-15}$ s $\equiv 2.67$ fs ("femtoseconds") and a total duration of about ten cycles $\tau \simeq 25$ fs, defining the class of "ultra-short lasers". The most commonly used lasing medium consists of sapphire crystals doped with titanium ions (Ti:Sa) [16]. In a first approximation, one may consider that the temporal properties of the pulse are mostly shaped already at its emission from the primary laser cavity, or "oscillator", however its energy is then very low, of the order of a few μJ. The pulse therefore is furthermore "amplified" passing through additional lasing media, leveraging on "chirped pulse ampmification" (CPA)[3] [1, 19], resulting in final energies of up to hundreds of Joules.

Historical trends for general high-power lasers in the last two decades can be read in Fig. 1.1. Three distinct data groups can be discerned. Two facilities stand apart on the far end of the energy spectrum, they are aimed at thermonuclear fusion and therefore not

---

[3] This technique consists in spatially separating the laser frequencies so as to decrease the local intensity in amplifier crystals, thus allowing for higher gains without exceeding the material damage threshold.

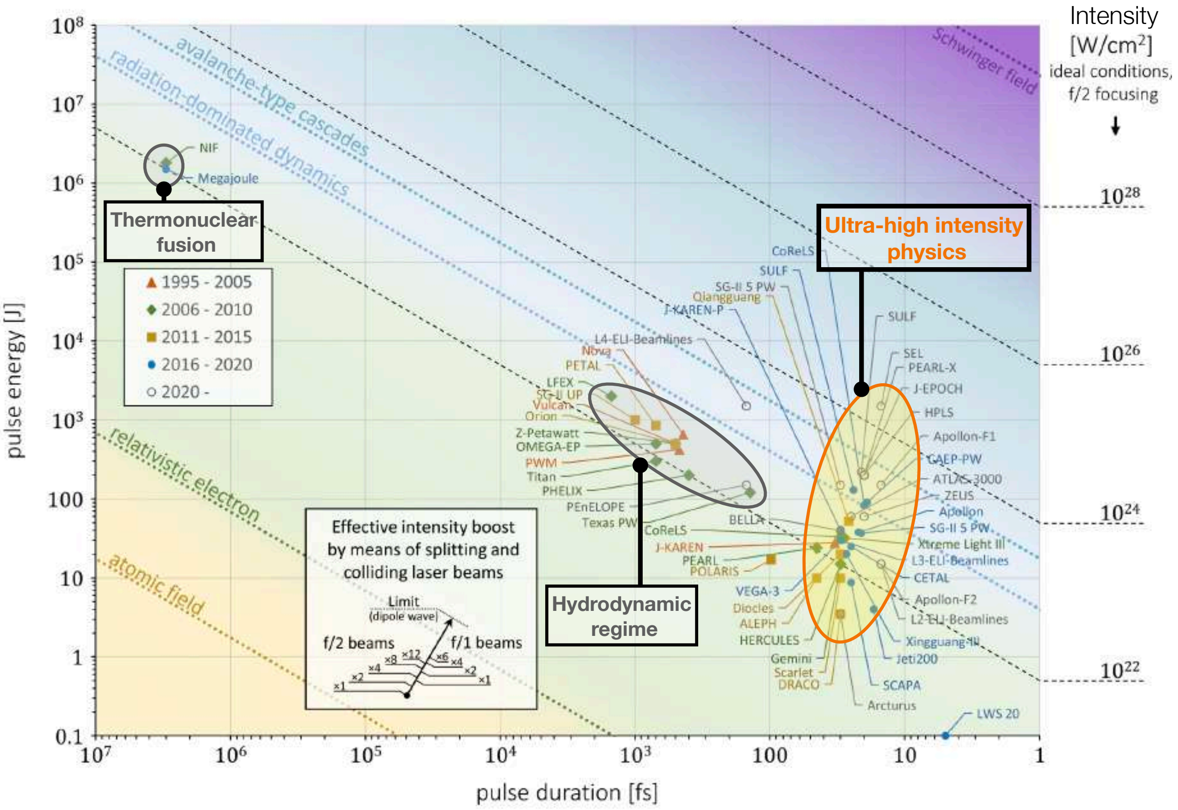

Figure 1.1: **Operational and forecast laser facilities worldwide (from [4]).** The intensity projections are calculated from energy and duration assuming $\lambda = 1\ \mu$m and a 2λ sized focal spot. The splitting and recombination method for intensity increase shown in the inset is detailed in [20]. Coloured areas correspond to distinct physical regimes; atomic field ($I = 3.5 \times 10^{16}$ W.cm^{-2}) corresponds to a one atomic unit field strength; relativistic electron ($I = 1.37 \times 10^{18}$ W.cm^{-2}) to $\xi = 1$ (*cf.* Sec. 1.1.2); radiation-dominated dynamics ($I = 8 \times 10^{22}$ W.cm^{-2}) and avalanche-type cascades ($I = 3.5 \times 10^{23}$ W.cm^{-2}) give indications as to when quantum effects of high-energy photons emission and decay into electron-positron pairs become significant in the dynamics; the Schwinger field is reached at $I = 4.65 \times 10^{29}$ W.cm^{-2} for a plane wave (*cf.* Sec. 1.2.1).

conceived for achieving high intensities[4]. There is another group centred around a maximal intensity of 10^{22} W.cm^{-2}, with durations of the order of a picosecond (10^{-12} s). Those are called "long pulses" and interact with matter on hydrodynamical scales. However, their intensity is strongly bounded by their comparatively narrow spectral content which hinders application of the CPA technique to them.

On the opposite, we see that the most recent lasers responsible for the peak intensity increase beyond 10^{22} W.cm^{-2} belong to the last category of "ultra-short" lasers, with a duration of about $20 - 30$ fs. Last built facilities typically have a total energy of 20 J to 100 J for focused intensities of about 10^{22-23} W.cm^{-2}, with a current record set at 1×10^{23} W.cm^{-2} [17]. Most forecast facilities envision energies above 100 J but would not exceed 10^{24} W.cm^{-2}, though one notable exception displays the ambition of 1.5 kJ energy in 15 fs (SEL), which would result in intensities of around 2×10^{24} W.cm^{-2}.

---

[4] The extrapolated 10^{22} W.cm^{-2} intensity displayed on the figure is not relevant, as it assumes the coherent combination of all (about 200) pulses focused near diffraction limit ($w_0 = 2\lambda$). In actual operations the intensity at experimental chamber focus is set around 10^{15} W.cm^{-2}, while at diffraction limit each individual beam would only reach $I_{\text{beam}} \approx 5 \times 10^{20}$ W.cm^{-2}.

1.1.2 Ultra-high intensity physics in the classical regime

As made clear in Fig. 1.1, all the more realistically assuming pulse focusing looser than the diffraction limit, all high-intensity lasers of the last two decades have been fully grounded in the "relativistic electron" regime. In order to better delineate the corresponding physical phenomena, we will now provide an elementary formalization of their shared particle dynamics and briefly review their most actively studied applications.

Classical relativistic particle dynamics in a field Let us simply define the relativistic regime reasoning on a the dynamics of a single electron in an external field[5]. Introducing the three spatial coordinates of the electron $\mathbf{q} = (q_1, q_2, q_3)$ as our variables the Lagrangian writes [22],

$$L(\mathbf{q}, \dot{\mathbf{q}}) = -mc^2\sqrt{1 - \frac{\dot{\mathbf{q}}^2}{c^2}} - e\dot{\mathbf{q}} \cdot \mathbf{A}(\mathbf{q}) + e\phi(\mathbf{q}) \tag{1.9}$$

with ϕ and $\mathbf{A}$ the electromagnetic potential components. The canonical momentum is,

$$\mathbf{P} \equiv \frac{\partial L}{\partial \dot{\mathbf{q}}} = \mathbf{p} - e\mathbf{A} \tag{1.10}$$

where we have introduced the "kinetic momentum" $\mathbf{p} = m\gamma\dot{\mathbf{q}}$ with $\gamma = 1/\sqrt{1 - \dot{\mathbf{q}}^2/c^2}$, and the Hamiltonian writes,

$$H = mc^2\gamma - e\phi \tag{1.11}$$

Now the equations of motion simply give,

$$\begin{cases} \dot{\mathbf{q}} = \dfrac{\partial H}{\partial \mathbf{P}} = \dfrac{\mathbf{p}}{m\gamma} & (1.12) \\ \dot{\mathbf{P}} = -\dfrac{\partial H}{\partial \mathbf{q}} = -mc^2\nabla\gamma + e\nabla\phi & (1.13) \end{cases}$$

with $\nabla = \partial/\partial\mathbf{q}$, or focusing on the momentum equation[6],

$$\boxed{\frac{d}{dt}\left(\tilde{\mathbf{p}} - \mathbf{a}\right) + \frac{c}{\gamma}\nabla\mathbf{a} \cdot \left(\tilde{\mathbf{p}} - \mathbf{a}\right) = -\frac{c}{2\gamma}\nabla\mathbf{a}^2 + \nabla\varphi} \tag{1.14}$$

where we have introduced the normalized kinetic momentum $\tilde{\mathbf{p}} = \mathbf{p}/mc$ and potentials $\mathbf{a} = e\mathbf{A}/mc$, $\varphi = e\phi/mc$. The first term on the RHS is quadratic and interestingly does not depend on the sign of charge, it corresponds to a ponderomotive force, driving all charges away from strong field regions.

Then, as can be seen *e.g.* perturbatively expanding $\tilde{\mathbf{p}} - \mathbf{a}$ for small $\nabla\mathbf{a}/\gamma$ in a gauge $\varphi \equiv 0$ in Eq. 1.14, an electron initially at rest will generically evolve in the field with a normalized momentum amplitude $\mathbf{a}$. For instance, in a plane wave, invariance along the transverse and wavefronts directions directly yields [23],

$$\begin{cases} \mathbf{p}_\perp \overset{\text{p.w.}}{=} \mathbf{a} & (1.15) \\ \mathrm{p}_\parallel \overset{\text{p.w.}}{=} \dfrac{\mathbf{a}^2}{2} & (1.16) \end{cases}$$

for an electron initially at rest in a 0 of $\mathbf{a}$, where $\mathbf{p}_\perp(\mathrm{p}_\parallel)$ refer respectively to the transverse (longitudinal) components with respect to the wavevector.

---

[5] Working in the canonical formalism (*cf.* App. A), the self-consistent description of N particles and the field would require at least the "contrained" formalism and will therefore not be pursued here [21]. A theoretical framework adequate for plasma physics is introduced in sec. 2.1.1.

[6] With the dyadic convention $\nabla\mathbf{a} \cdot \mathbf{P} \equiv \partial_i(a_j)P_j$ for $a_ib_i \equiv \sum_i a_ib_i$.

Considering a field of maximal amplitude A_0[7], we therefore define,

Classical field strength parameter

$$\boxed{\xi \triangleq \frac{eA_0}{mc} \overset{\text{p.w.}}{\equiv} \frac{eE_0}{mc\omega_0}} \tag{1.17}$$

where the second equality holds for a monochromatic plane wave of frequency ω_0. If $\xi \geq 1$, we have $\|\mathbf{p}\| \geq mc$ and the electron motion is relativistic. The parameter ξ hence controls dynamics and is called the *classical field strength parameter*.

In terms of intensity, modelling a focused beam at lowest order in a paraxial approximation we find the practical relation [4],

$$\xi = 0.86\lambda_0[\mu\text{m}]\sqrt{I_0[10^{18}\ \text{W.cm}^{-2}]} \tag{1.18}$$

where λ_0 is the central beam wavelength and I_0 the peak intensity at focus. Therefore, dynamics needs indeed be described by relativistic mechanics as soon as $I_0 \geq I_{\text{rel}} = 2 \times 10^{18}$ W.cm^{-2} for the typical laser wavelength $\lambda_0 = 800$ nm.

When relativistic intensities are reached, interactions with matter, *i.e.* particles and plasmas, become strongly non-linear, leaving room for physical phenomena such as high-energy particles acceleration or field harmonics generation. For more definiteness we now briefly review some of the most salient.

Applications in a vacuum: direct particle acceleration and scattering One straightforward application of ultra-high intensities is to accelerate electrons directly by interaction with a light pulse. This configuration is referred to as “Vacuum Laser Acceleration” (VLA) [26–30]. In practice, this method must overcome the difficulty that in order to perform a net energy gain, electrons must exit the strong field region at the right time, without entering decelerating field gradients. This implies tuning the spacetime field profile, or the electron injection conditions on sub-wavelength scales, which indeed proves highly non-trivial, though plasma mirrors have been suggested to this end (*cf. infra*).

Another possibility is to proceed in the reverse direction, using the laser pulse to strongly decelerate high-energy electron, and thereby produce high-energy photon beams of high brightness. This process is called “Inverse Compton scattering” [4, 31–33]. Using electron beams of a hundred MeV to a few GeV, multi-MeV photons can be generated [4], opening to nuclear phenomena. Electron beams in this energy range can be produced in radio-frequency accelerators, or directly by another laser pulse *via* as explained below.

Application in an underdense plasma: laser wakefield electron acceleration One promising use of ultra-short and intense pulses is the acceleration of electrons up to GeV energies on mm to cm scales [1, 34]. The basic process consists in sending an intense laser pulse in a gas of density below the critical plasma density at the laser wavelength, or underdense, allowing the pulse propagation and resonant generation of plasma waves in its wake by the ponderomotive force. Such plasma structure results in strong electrostatic fields configurations (around ~ 100 GV.m^{-1}) travelling with a phase velocity close to c, and thus able to efficiently accelerate copropagating electrons. The present energy record is around 8 GeV for in 20 cm, and high quality 100 MeV beams achieved on cm scales are routinely operated [35].

---

[7] In a more formal framework it can be given a Lorentz and gauge-invariant meaning [24, 25]. In the case of a plane wave in the absence of sources, one can simply take $a_0 \equiv e\sqrt{-A_\mu A^\mu}/mc$.

Applications with overdense targets: ions acceleration and plasma mirror high harmonics generation As the target density is increased, its plasma frequency eventually exceeds that of the pulse. At this point, the laser does no longer propagate inside the plasma giving rise to qualitatively new phenomena. For instance, ion beams can be expelled from initially solid target with up to MeV energies by the "Target normal sheath acceleration" mechanism [36–38]. The resulting ion beams have in particular comparatively high densities, which is of interest *e.g.* to study fast nuclear processes [39]. Ion beams have other interesting properties, relevant notably for medical applications, justifying active research in several laser-based ion acceleration schemes [37, 38].

Solid targets can also be used to act on laser light. In particular, high-harmonics generation of the fundamental laser frequency can be performed on overdense plasmas from the non-linear surface electrons oscillatory motion [40]. Besides, relativistic field-electrons interactions lead to kinetic processes such as electron injection in the reflected field. These electrons essentially travel in-between the reflected field fronts, driven by its Lorentz force until they are expelled from the beam as a result of its finite transverse size, typically after its focal point [41]. When the intensity is increased beyond $\sim 10^{18}$ W.cm^{-2}, laser-solid interaction can enter the so-called "relativistic plasma mirror" regime which, by coherent time-compression of incident light into attosecond (10^{-18} s) pulses, has been numerically demonstrated to provide a source for extremely high-intensity fields. This physical process provides the ground for the present work, and will be detailed in Sec. 1.3.5.

1.1.3 High-intensity physics at the strong-field frontier

All the reviewed applications have been demonstrated experimentally in the last two decades, at least in their principle, for they simply require reaching $\xi \sim 1$ or even less, *e.g.* for laser wakefield acceleration. Though the development of high power lasers [5] has naturally benefited these fields and significant progresses were made, the underlying elementary physical processes have remained qualitatively the same. This relatively well-defined set of methods and physical phenomena allowed for a stabilized notion of "relativistic regime" of laser-matter interactions [1].

This situation is however shifting with the recent commissioning of multi-petawatt (1 PW = 10^{15} W) laser facilities, possibly coupled to conventional accelerators [33, 42–44] (*cf.* also Fig. 1.1). These infrastructures open the perspective of detecting signatures of "strong-field" phenomena for the fist time, such as electrons recoils by radiation emission, electron-positron pairs creation, or optical nonlinearities in a vacuum, defining a new physical regime of "strong-field electrodynamics" [2]. All those effects are controlled by a field scale called the *Schwinger field*,

Schwinger field strengths

$$\boxed{\begin{cases} E_S \simeq 1.32 \times 10^{18} \text{ V.m}^{-1} \\ B_S = \dfrac{E_S}{c} \simeq 4.40 \times 10^{9} \text{ T} \end{cases}} \tag{1.19}$$

which translates in a plane-wave intensity,

Schwinger intensity

$$\boxed{I_S = c\varepsilon_0 E_S^2 = \simeq 4.62 \times 10^{29} \text{ W.cm}^{-2}} \tag{1.20}$$

More specifically, considering processes involving a massive charged particle the relevant interaction parameter is the field in the rest frame of the particle[8], namely [4],

Quantum interaction parameter

$$\boxed{\chi = \frac{\sqrt{-(F_{\mu\nu}p^{\nu})^2}}{mcE_S} = \gamma\frac{\sqrt{(\mathbf{E}+\mathbf{v}\times\mathbf{B})^2-(\mathbf{v}\cdot\mathbf{E}/c)^2}}{E_S}} \tag{1.21}$$

If $\chi \gtrsim 1$, strong-field effects become sizeable. When electrons are accelerated directly by the laser field (*e.g.* laser-target configurations) one finds the scaling law [4],

$$\chi \simeq 0.09\lambda[\mu\text{m}]I_0[10^{23}\ \text{W.cm}^{-2}] \tag{1.22}$$

If, alternatively, their incoming energy is large compared to that provided by the laser (*e.g.* laser-accelerator configurations) one finds [4],

$$\chi \simeq 0.18\mathcal{E}_0[\ \text{GeV}]\sqrt{I_0[10^{21}\ \text{W.cm}^{-2}]} \tag{1.23}$$

Either way, we understand why only at the highest possible intensity to date strong-field effects start to manifest, and hardly still. In the following, we are going to review some schemes specifically designed to reach the strong-field regime, using lasers or not, ending with relativistic plasma mirrors, that we show could allow entering much deeper into the strong-field dominated regime.

Before proceeding, we now provide a physical understanding of the Schwinger field value, so as to reach a bird's eye view of the motivations for achieving strong fields.

1.2 The realm of strong electromagnetic fields

Relating the above given figures for the electromagnetic intensity to distinct physical processes requires a definite theoretical framework. All qualitatively new processes at strong fields are naturally depicted by quantum mechanics in its special relativistic formulation, that is quantum field theory. As the quantum description of fields has long been remote from any practical use in a macroscopic context such as laser-plasma interactions, it would be desirable to properly introduce, if not adapt, concepts from both physical domains and their connection. Some general elements are provided to this purpose in App. B, and a more specific focus on some operational methods of strong-field QED in Chapter 2. In this first section, we take a preliminary step by giving a qualitative justification of the link between strong and quantum fields, which may appear contradictory at first glance.

On the other hand, the physical configurations in which these quantum processes are expected to take place, *e.g.* in the bulk of a dense macroscopic plasma immersed in a strong coherent electromagnetic field, are very estranged also from those to which Quantum Field Theory is routinely applied[9], and thus tested. In particular, if Quantum Electrodynamics is rightfully celebrated as the most accurate theory in the history of science, its records were established in a near vacuum state while, experimentally, the realm of strong fields mostly remains *terra incognita* to the present days. We will therefore review the motivations for actually achieving such exotic configurations in the laboratory, and show that they pertain both to fundamental and applied physics.

---

[8] For a photon last expression still holds with $\gamma \equiv \|\mathbf{p}\|/mc$ and $v = c$, and the intuitive understanding of χ virtually coincides with the case of an ultra-relativistic massive particle of equivalent momentum.

[9] Notable exceptions are condensed matter systems and heavy ions collisions, both featuring dense media and ambient fields. They still differ from the laser-plasma context though, the former due to usually non-relativistic energy/spacetime scales, the latter due to very different scales also but in the high energy end and to the predominance of chromodynamical effects.

1.2.1 Why do quantum phenomena occur in strong fields?

In the absence of a dimensional constant in the theory of vacuum electromagnetism[10], there is in particular no field scale past which the dynamics should be expected to qualitatively change. Furthermore, in the event of such change it can first seem obscure why it should involve quantum mechanics, commonly associated to "small scale" phenomena[11]. As we will now show, this difficulty is lifted when the coupling to charged massive particles is considered.

Introducing a mass m and charge Q, one can build spatial scales which equivalently translate in field scales. Depending on the use of the Planck constant in this process or not, classical and quantum scales can be built and compared. For it plays a primary role as the lightest known charged particle, general expression will be numerically evaluated for the (anti-)electron parameters. Starting from the classical theory, a classical electromagnetic length can be defined as,

Classical EM radius

$$r_c = \frac{Q^2}{4\pi\varepsilon_0 mc^2} \overset{e}{\simeq} 2.82 \times 10^{-15} \text{ m} \tag{1.24}$$

the distance between two point particles at which their electrostatic interaction energy equals their rest energy. Such quantity appears in radiation phenomena, in particular the self-interaction of a particle through its own field [23]. The corresponding field scale follows as,

Classical critical field

$$E_c = \frac{mc^2}{Qr_c} = \frac{4\pi\varepsilon_0 m^2c^4}{Q^3} \tag{1.25}$$

$$\overset{e}{\simeq} 1.81 \times 10^{20} \text{ V.m}^{-1} \tag{1.26}$$

which produces a work of mc^2 on a distance r_c. The predicted physical effect consists in the modification of the particle dynamics as a result of its energy-momentum transfer to the electromagnetic field. The corresponding force is known as "radiation reaction" and is very well described by the approximate Landau-Lifschitz equation [23]. Although some intriguing mathematical questions arise when treating this self-interaction exactly [46–50], this phenomenon arguably does not lead to fundamentally new physics.

Let us now write the quantum and relativistic length scale[12],

Compton length

$$\lambda_C = \frac{\hbar}{mc} \overset{e}{=} r_c/\alpha \tag{1.27}$$

$$\overset{e}{\simeq} 2.43 \times 10^{-12} \text{ m} \tag{1.28}$$

---

[10] As read *e.g.* in the action, or Maxwell's equations.

[11] More precisely actions small compared to $\hbar$, which quantifies the non-commutativity of conjugate variables, or equivalently small quantum numbers $\langle \mathcal{O} \rangle_\rho$ compared to commutators $\langle [\mathcal{O}, \mathcal{O}'] \rangle_\rho$ (*cf.* App. A Eqs. A.36-A.37). This is true of the electromagnetic field as well, for instance when the total field energy becomes of the order of its constituent photons, or more specifically when the photons number per mode becomes small, revealing their discreteness. Following [45], the intensity below which such effect becomes sizeable can be estimated as $I_0 \sim c\frac{\hbar\omega_0}{\lambda_0^3}$, *i.e.* $I_0 \lesssim 10^4$ W.cm^{-2} for a central wavelength $\lambda_0 = 800$ nm.

[12] It is called the *Compton length* of the particle. As the scale controlling free propagators in relativistic quantum theory (*cf.* App. B.2.2, Eq. B.73), it can be interpreted as the quantum coherence length (that is, reasoning on a position observable, the wavelength of probability interference terms Eq. A.43) of processes involving energy-momentum transfers of the order of the particle rest-mass.

with $\alpha = e^2/4\pi\epsilon_0\hbar c \approx 1/137$ the fine structure constant. Accordingly, the quantum electromagnetic field scale is,

Quantum critical field (Schwinger field)

$$E_s = \frac{m^2c^3}{Q\hbar} \overset{e}{=} \alpha E_c \tag{1.29}$$

$$\overset{e}{\simeq} 1.32 \times 10^{18}\ \mathrm{V.m}^{-1} \tag{1.30}$$

The smallness of α therefore implies that in practice the dynamics of fields and particles changes according to the consequences of quantum mechanics before the classical strong-field regime is reached. Now as all fundamental systems are fields permeating all space (*cf.* Sec.B.1.1), such coupling can never be discarded, even in the absence of charged particles in the initial state[13]. Dynamics of the electromagnetic field will therefore depart from Maxwell's theory due to interaction with the electron-positron field whenever $E, B \sim E_S, B_S$[14], hence consistently defining a *strong field regime* of electrodynamics.

We can further understand this quantum threshold E_s, known as the Schwinger field, noticing that it produces a work of mc^2 on a distance λ_C. In other words, it presents an interaction potential of a rest-mass energy on a quantum coherence scale, therefore allowing sizeable transition amplitudes between states with different number of particles. An even more direct picture can be given introducing a field frequency ω, as then $e\lambda_C E_s/\hbar\omega = n_{\text{absorbed}} = mc^2/\hbar\omega$, explicitly showing that an electric field amplitude E_s allows the absorption of enough photon to gain a total mc^2 energy within a coherence length.

At this point all features of quantum mechanics naturally intervene, discreteness manifests through matter particles creation/annihilation and finite energy-momentum photon emission, randomness by the probabilistic nature of any of these processes, and indeterminacy between observations allows for particles self-interactions and notably the so-called vacuum polarization *via* transitional electron-positron states. These processes clearly affect the physics of electromagnetism much more profoundly than classical particle self-interaction, and indeed lead to phenomena as incidental as coherent emission from highly magnetized pulsars [51–53], disruption [54, 55] and radiation [56, 57] in beam-beam collisions, or substantial depletion of coherent light into electron-positron pairs [58, 59]. We devote next section to try and obtain a more systematic picture of the interest of actually observing such fields in the laboratory or in the universe.

1.2.2 The scientific value of accessing strong-field physics

Taking as an anchor point the above given description of the strong-field regime as the onset of fundamental fields interactions through the non-vanishing electromagnetic field expectation value, implications of observing such physics in controlled conditions can be drawn. As we will now expose, strong-fields then appear to open appealing perspectives for fundamental physics, phenomenology of known systems, as well as instrumental applications.

---

[13] This configuration of "interaction with the vacuum" is the subject of Chapter 8.

[14] Actually, whenever the local Lorentz-invariants of the field $\mathcal{F} = ((c\mathbf{B})^2 - \mathbf{E}^2)/2E_S^2, \mathcal{G} = -c\mathbf{B}\cdot\mathbf{E}/E_S^2$ near 1 (see Sec. 2.1.2), which usually is a reasonably close criterion for non-crossed fields.

An uncharted experimental territory The most naive argument in favor of achieving fields of unprecedented strengths in the laboratory is that, by definition, we do not yet know what follows in a strict empirical sense. As technology progresses, the primary role of scientific research can indeed be conceived as to actually cover the practically available experimental space. This line of reasoning is typically more authoritative in fundamental research, for instance particle physics [60], which directly aims at extending the frame in which observation is thought. Now as of course all that is practically possible cannot practically be done, and given that ultra-high intensity lasers are becoming of large infrastructures scales, refined criteria for what should be pursued have to be put forward based on relevant theory. It turns out that several arguments have emerged in this direction, pointing at reasonable possibilities to test speculations beyond the Standard Model with strong fields [3]. The rationale then is to scan parameter space regions either competitively compared to more expansive means, or some that could not be reached otherwise.

A first testable class of theories is those predicting new particles outside the Standard Model. There exists a large number of such theories, for some significant part motivated by the search of “dark matter” fields that would help solving the persistent gravitational anomalies observed beyond stellar scales [61]. Strong-fields would typically stimulate some processes involving such particles if charged, and thus contribute to exclude larger region in their parameter space. These could be for instance “axion-like” [62–70], “mini-charged” particles [71–76], or magnetic monopoles [77–80]. Another possibility would be to detect modifications to QED without additional fields, for instance through nonlinearities in its lagrangian, as in Born-Infeld theory [81–83], or noncommutativity of spacetime coordinates [84].

A different approach would be to use strong-fields as a source for secondary particles, *e.g.* bright high-energy photon or electron beams, so as to probe processes beyond the Standard Model in their subsequent interaction with a chosen target. This is the idea of the LUXE-NPOD experiment [85].

Windows to the Standard Model Looking at the trend in high-energy physics, besides constraining potential extensions of the Standard Model access to a new physical regime can also prove a valuable source of information on the already discovered fields. The strong-field directly couples to all electrically charged particles, which thus entails a variety of electroweak processes [86–89], as well as coupling to the muon generation[15]. More generally, one can revisit all kind of processes in the presence of a background field, which can boost interactions by providing extra-energy momentum to the involved particle, including Higgs production [90–92], kaon decay, CPT symmetry violation [93] and Z boson production [94]. As neutrino also indirectly couple to the strong-field *via* charged particle loops, an opportunity is given to access some of their properties [95–101]. Though spacetime and field scales are different, some bridges could also be made with heavy-ion collisions, which indeed generate extremely strong electromagnetic and color fields [102–108].

A forge for formal tools All the above options require very accurate predictions in order to result in any experimental evidence. Therefore, research in strong-field QED is likely to catalyse the development and validation of theoretical tools, that could be of use in other QFTs as well. One straightforward example is the application of Non-equilibrium QFT to strong-field QED, which both provides a motivation for pushing

---

[15] The tau generation being out of reach of currently realistic field values.

forward this framework, and could result in new *e.g.* numerical methods benefiting all its domains of use. Another interesting stage is the very high χ regime of sf-QED, where the Ritus-Narozhny motivates the analysis and resummation of higher-order diagrams, which again one can hope to result in some more general techniques. Particles in strong fields can also impact theory development as an analogous system, hence allowing to test our mathematical control of the mimicked theories. Along this line, the interaction of an electron with a strong plane electromagnetic wave can inform on gravitational observables through the "double copy" correspondence [109, 110], as well as on Lorentz violating theories such as "Very special Relativity" by fast and slow variables separation [111–113].

A new physical system: relativistic quantum plasmas However promising for probing elementary degrees of freedom, yet undisclosed or not, the environments created by strong fields within established physics prove extremely rich for themselves. Considering specifically the quantum dominated regime, strong-fields will distinctively give rise to configurations of photons, electrons and positrons with high density, quasi-neutral charge, relativistic energy distributions and strongly influenced by non-classical processes. These states of matter and radiation can be qualified as "relativistic quantum plasmas" [4, 114–116]. Though essentially unobserved in the laboratory yet, they are predicted at intensities to be reached in the near future and their phenomenology holds the potential to provide both new explanations for observations and instrumental applications [4, 114]. This can be illustrated in the typical scenario of initially non-relativistic charged particles, say electrons for definiteness, interacting with fields of increasing magnitude. As electrons accelerate in the field, they start to transfer momentum to electromagnetic radiation, first in the form of low-energy photons according to the Landau-Lifschitz formula [4, 23], then according to a quantum corrected one [117]. When the quantum parameter χ reaches 1, photon discreteness becomes manifest through stochasticity [118–123], possibly favoring higher energy emission (*straggling*) [44, 124, 125], or not emitting at all (*quenching*) [126, 127], and revealing a characteristic cut-off in photon spectrum associated with energy-momentum conservation in individual emission processes [128]. The consequence of quantum radiation reaction can be as dramatic as particle trapping and attraction to the highest field regions [4, 129–133] ("Anomalous Radiative Trapping"). Given realistic particle densities, these photons typically have (Compton) photon-particle scattering mean free paths much larger than the high-intensity region size, but their photon-field interaction length can become much smaller, especially from the onset of the Breit-Wheeler process of conversion into an electron-positron pair [4, 134–139]. The combination of photon emission and decay to a pair can thus give rise to exponential creation of electron-positron pairs, a phenomenon known as "QED cascade". If the cascade is efficient enough to strongly affect the background field, then a plasma of electrons and positrons is formed, relativistic and quantum by nature. In this process, extremely high density can be reached, up to a million times solid density [4, 114]. In the most extreme cases, degeneracy effects could be triggered [140].

There are many possibilities to exploit these processes as a source for specific particle beams (see *e.g.* [20] sec. VI and references therein). For instance, bright gamma beams can be generated by inverse Compton scattering [20]-VI.A.1, while high photon fluxes and conversion efficiency are expected from solid target irradiation [4]-VI.A.2. Another strongly motivated application of strong fields would be of course to manage positron production, either with greater efficiency, ease of coupling to acceleration or interaction stages, or, promisingly, with very high densities [114]-III, [4]-VI.B.

Astrophysical strong fields Creating relativistic quantum plasmas in the laboratory would certainly help understanding similar physics realized elsewhere in the universe. Though such conditions are understandably rare, they are fully met around compact magnetized objects, that is magnetized neutron stars [141] and black holes [142]. The magnetic flux compression in the collapse of stellar-sized objects indeed produces magnetic fields ranging from 10^{7-9} T ($B_S = 4.41 \times 10^9$ T) [143], to more than 10^{11} T in the most extreme cases known as "magnetars" [144, 145]. The creation of a pair plasma screening the electric field induced by the stellar magnetic dipole rotation is believed to play a central role in the pulsar mechanism [146, 147]. This process is however highly unsteady [148], so that strong electric fields can accelerate particles to more than 10 TeV energies [143], driving prolific QED cascades [149, 150], photon splitting cascades [151, 152], and, allegedly, coherent emission [123, 147, 153]. Analogous processes are predicted around black holes [154–156]. Around magnetars, the (super-)critical regime of sf-QED could be observed, for instance *via* the distinctive process of vacuum birefrigence [157, 158].

Beam fields in collisions In configurations where quasi-neutrality is violated, which could happen as a result of dynamics in a strong-field[16] or more generally around charged beams, yet another type of strong fields can exist sourced by the particles charge. Accounting for sf-QED in such contexts could prove especially crucial to future lepton collider designs [60, 159], where search for higher brilliance and energies implies dense highly Lorentz-boosted beams, in turn enabling strong field processes at the interaction point [160, 161]. This collective field can primarily affect the on-coming particles dynamics, which is called "disruption" [162, 163], thereby generating radiation, which is called "beamstrahlung" [164, 165]. The net result can be a reduced center-of-mass energy of particle collisions as well as additional emissions due to *e.g.* Breit-Wheeler pairs creation [166], hindering particle physics observations. For this reason, mitigation strategies have been developed [167]. However, maximizing these effects instead would open a new path to sf-QED physics, including high luminosity photon-photon collision [168], a high-brightness photons and electron-positron secondary beams [161], or even, with suitable collider development, access the fully nonperturbative regime of strong-field QED [169].

1.3 State-of-the-art of strong-fields sources

Driven by the above-listed motivations along with technological progress, there is at present growing hope to achieve QED-relevant strong fields experimentally. During the last few decades, some seminal experiments have been able to graze the quantum regime of $\chi \sim 1$ using conventional accelerators, and evidence the first deviations from classical dynamics in the strong field of lasers [170, 171] or of nuclei in aligned crystals [172–175]. The quantum dominated regime of sf-QED, where quantum processes determine the global system dynamics, is however yet to be reached.

In the following we give an overview of the latest efforts to approach it, setting the landscape in which the solution presented in this work operates. In particular, we will show that purely optical laser systems face an intensity gap of several orders of magnitude before entering the quantum dominated regime, which jeopardizes a trivial scaling up solution. We therefore review how laser-accelerator schemes partly bypass this difficulty, and envisioned methods to fully enter the deep strong-field regime.

---

[16] A definite example of this process is exposed in Ch. 9.

1.3.1 The technological gap ahead of optical laser sources

In the presence of particles, the onset of strong-field processes is characterized by a quantum parameter $\chi \gtrsim 1$ (Eq. B.126). Without assuming externally provided high-energies, the typical quiver energy of charges in laser fields only allows crossing this threshold above 10^{24} W.cm^{-2} (Eq. B.127), which still lies beyond available intensities [4]. In order to observe processes in a vacuum directly, even higher intensities must be reached, as noted in the many schemes devised for observing light self-interaction [176–196], or even pair creation from the coherent field [58, 59, 197–203] (see sec. 1.4.1). These experiments are all the more challenging that they require maximizing the electromagnetic field invariants (*cf. infra* Eqs. 2.41) instead of χ, which typically implies colliding multiple laser pulses, each of about 10^{24} W.cm^{-2} peak intensity.

Relying on standard ultra-intense lasers only, the quantum-dominated regime should therefore not be attained before several tens of petawatt peak power are achieved. Though such performances are envisioned in several forecasted facilities [3], all correspond to long run projects and large scale infrastructures.

1.3.2 Accelerators as a ladder to the edge of strong-fields

One direct way to achieve $\chi > 1$ then simply appears to combine lasers with accelerators, directing ultrarelativistic massive particles into coherent field configurations, which hence need not be as strong in the laboratory frame (Eq. B.128). The seminal works evoked in the introduction to this section relied on this principle, for instance in the E144 experiment combining the 46.6 GeV electron beam of the SLAC facility with a 1.3×10^{18} W.cm^2 peak intensity laser (meaning a field $E \lesssim 10^{-6} \times E_S$) [170, 171, 204]. Some photon spectral signatures could be observed, as well as some pair creation events.

Now this technique can benefit both from an increase in beam energy or field amplitude. This motivates plans for updated versions of the same. At SLAC, the E320 experiment will consist in colliding the FACET-II 13 GeV electron beam with a 10 TW laser, achieving $\xi \sim 7$ and $\chi \sim 1$ [169]. Similarly, the LUXE experiment at the European XFEL facility comprises a 17.5 GeV beam with a 30 TW laser, allowing for $\xi \sim 2$ and $\chi \sim 0.4 - 2$ [205]. An interesting variation planned in this case is to direct the GeV electron to a high-Z target so as to convert them into gamma rays by brehmsstrahlung. This presents a number of advantages [206–209], linked to the fact that photons are classically not deflected from high fields regions. Several experiments have been proposed along this line [210, 211]. Wakefield acceleration also holds a good potential for reaching the required energy. Pushed by rising energy records [212–215] and possibly high charges [216], all-optical schemes have been devised to collide laser-accelerated high energy electrons against intense lasers [217]. Experiments with the Gemini laser at the Rutherford Appleton Laboratory have begun detecting quantum corrections to radiation spectra in such setups [174, 175]. This kind of experiment again find natural complements in the generation of high energy photons instead of electrons [218, 219]. Besides, some optimizations of the angle of collision [220] and field focusing have been shown to enhance interactions [221, 222].

In all mentioned experiments, created particles only amount for a negligible fraction of the system energy, or equivalently, sf-QED processes occur with too low probability to trigger sizeable QED cascades, and rather act as corrections to an essentially classical dynamics. As technology can only improve slowly, further progress at this point requires qualitatively new schemes.

1.3.3 Optimizing the field at a fixed power: dipole waves

Interestingly, the limiting case of the optimal coherent superposition of multiple pulses for achieving the highest intensity from a given total power can be studied analytically, and has been shown to be relevant also with regards to the maximization of several quantum processes [20, 223, 224]. Such configuration is known as a "dipole wave" [225], for it is time-reversal of a dipolar source emission[17], and is currently conceived as a plausible way to achieve significant steps towards the deep strong-field regime.

Pair creation in such fields has been studied in a vacuum through the Schwinger process [226], as well as from seed electrons [227]. In this configuration, when pair creation occurs the intensity is high enough so as to confine particles near focus *via* Anomalous Radiation Trapping (*cf.* sec 1.2.2) [20], favoring QED cascades in this region, further enhancing the effect [228]. Simulations predict resulting densities ranging from 10^{25} cm^{-3} at 8 PW power, to more than 10^{28} cm^{-3} above 20 PW [229]. These exotic conditions could prove interesting from the standpoint of astrophysics [230]. Interaction with a secondary beam and subsequent particle radiation has also been envisioned [221, 222]. As manifest from the expected phenomena, such dipole source could allow entering well into the quantum-dominated regime of sf-QED. The difficulty naturally lies in building such facility, which implies the collocation of about ten state-of-the-art multi-PW lasers. It is remarkable enough that the physics of relativistic quantum plasmas can in principle be studied with current technology though, and some implementation designs are being studied [231, 232].

1.3.4 An ideally unbounded amplifier: the relativistic mirror

If the pulse energy is ascribed by technological limits, and the dipole wave is the optimal spatial configuration for a given power, then a natural path to reach higher intensities is to increase the peak power by compressing the pulse in time. One long-standing suggestion along these lines is to use a mirror moving at relativistic velocity [233]. In the ideal counter-propagating case, the reflection of light on a moving mirror with Lorentz factor γ_M indeed entails a time compression of the field by a factor $4\gamma_M^2$ [234], upshifting amplitude and frequency. Most importantly, the upshifted frequency translates into smaller diffraction limit, so that for perfect reflection and focusing final intensity gains scale as $\sim \gamma_M^6$. The core issue then is of course to find how to physically realize this simple thought experiment.

The density cusp produced at the rear of the nonlinear wakefields of an intense laser propagating in an underdense plasma has been envisioned as a relativistic mirror candidate [235], benefiting also from a focusing parabolic shape [236]. As the same moving mirror reflects and focuses light, length of the focal spot scales as $\sim 1/\gamma_M$ so that the ideal final gain in this case is $\sim \gamma_M^4$. Accounting for the reflection coefficient of the wake corrects this value by factors of γ_M^{-3} or γ_M^{-4} depending on plasma models [237]. Tailoring the curvature of the plasma wake so as to achieve diffraction limit in the laboratory frame has been proposed [238], and proof-of-principle experiments have been conducted [237, 239–241]. Another implementation of the relativistic mirror relies on the dense electron sheets that can be ejected by thin solid targets under intense laser irradiation [242–245], so that a second counterpropagating laser can then benefit from the $\sim \gamma_M^2$ intensification [246]. In this case also, plasma instabilities in the electron sheet [247], as well as transparency induced by plasma density drop and pulse frequency upshift in the electrons frame [248], constrain the final achievable gain.

---

[17] Which correctly suggests that two types exist, associated with electric or magnetic source dipole.

1.3.5 Relativistic plasma mirrors as an open path towards the Schwinger field

Though currently the only available concept allowing for in principle unbounded intensity increase from a given electromagnetic energy, an effective materialisation of the relativistic mirror idea remains to be desired. The collective non-linear oscillations of electron populations at laser-irradiated sharp vacuum-overdense plasma interfaces may however come very close, notably in terms of amplification effect.

These so-called “relativistic plasma mirrors” (RPM) are the sources of the fields studied in this work, allegedly the strongest free fields within reach of present day technology. Using a Petawatt-class laser as the driver beam could result simultaneously in efficient harmonics generation, that is time-compression of each incoming optical cycle to tens of attoseconds duration pulses, and focusing to wavelength-limited spot sizes, resulting in intensity gains between two and five orders of magnitude [12]. The corresponding fields would come near the critical value in the laboratory frame, which may allow studying critical sf-QED effects such as light self-interaction, and certainly would facilitate entering deep into the quantum-dominated regime of sf-QED.

A more detailed discussion of the physics at RPM focus will be given in section 1.4. Here, we wish to give an overview of the generating process of this extremely intense light. The mechanism of electromagnetic pulse compression – equivalently, harmonics generation – at the plasma surface is long-studied and now relatively well understood. Nonetheless, it remains a complex, inherently non-linear phenomenon, and analytical models lack the ability to predict harmonic spectra accurately. Furthermore, the interplay of widespread spatio-temporal scales, again inherent to the spectral range to be resolved, pushes generic time-domain PIC algorithms to the limits of current computational capabilities, thus delaying, if not prohibiting, large scale numerical studies with such tools. Leveraging on the pseudo-spectral scalable PIC code WarpX[18], the PHI group has been able to accurately compute the harmonics spectra and perform extensive parameter scans. The outcome of these works on harmonics generation and optimization will be presented in section 1.3.5. A second step is to focus the generated beam. Several schemes have been put forward to this end, which implement various notions of curved RPM or separate harmonic beam focusing, but generically suffer from stringent requirements in terms of laser alignment, pulses synchronisation or X-UV optics quality. In section 1.3.5 we will concentrate on two recent proposals, the optically-curved RPM and the optically-flat RPM, that we believe decisively alleviate the physical constraints usually plaguing this stage.

A. Plasma mirror generated high harmonics beams

Since the advent of the Chirped Pulse Amplification technique [19] ultra-short pulses duration have been continuously decreasing while comprising more and more energy, so that irradiated matter could be efficiently ionized and its electrons set into relativistic motion ($I \gtrsim 10^{18}$ W.cm^{-2}) already for more than two decades [1]. In particular, studies of the interaction of ultra-intense femtosecond pulses with solid targets in these regimes have long been conducted, giving rise to the notion of “relativistic plasma mirrors” [6–11]. Starting from the physical depiction of this phenomenon, this section will briefly trace back the accumulated knowledge on these systems, theoretical and practical, with

---

[18] See <https://warpx.readthedocs.io/en/latest/> for an overview of the code, for scientific presentations see [249–255].

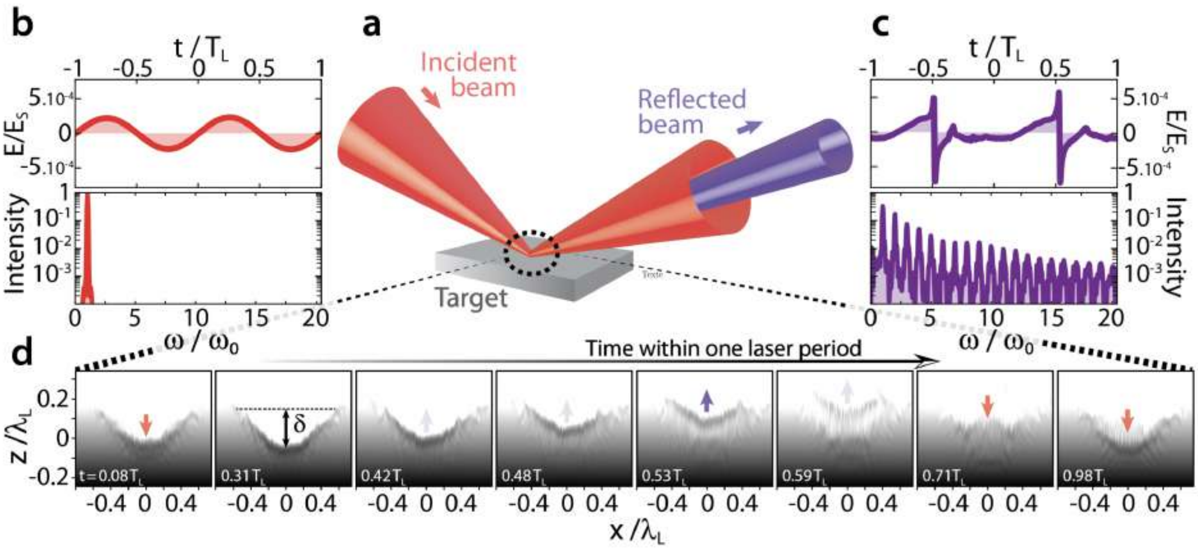

Figure 1.2: **Illustrated summary of the relativistic plasma mirror high-order harmonics generation mechanism.** **(a)** Illustration of the interaction geometry: the incident infrared beam is reflected in the specular direction, enriched with a high-order harmonics spectral content **(b,c)** Temporal and spectral profiles of the pulse respectively before and after reflection on the RPM, extracted from a PIC simulation. The time-compression and its counterpart of slowly decreasing harmonic spectrum are clearly visible. **(d)** Instantaneous spatial slices of the electron density in the incidence plane on a full RPM oscillation cycle. An electron layer is pressed by the driving laser (red arrows) below its initial plane on half a cycle, then accelerated to relativistic energies outwards the mirror before being quickly stopped, thereby radiating (violet arrows), and then push back inside the mirror. Note the timestamps are non-uniform; in particular, the strongly emitting phase (full violet) is concentrated around $t \sim 0.53T_L$, and lasts for less than a tenth of the original laser period T_L (adapted from [13])

an emphasis on early proposals to exploit them as light-amplifiers along the relativistic mirror idea.

Physical description of the phenomenon When an ultra-intense ($I \gtrsim 10^{15}$ W.cm^{-2}) laser interacts with solid matter, atoms are quasi-instantaneously ionized to form a plasma which interacts with the field and expends towards vacuum. In the case of an infrared ultra-short pulse, such as produced by the widespread titane-saphire oscillators, plasma densities $n_p \sim 10^{23}$ cm^{-3} reach hundreds of times the critical density $n_{800\ \mathrm{nm}} \simeq 1.7 \times 10^{21}$ cm^{-3}, while expansion is comparatively slow, so that the pulse interacts with an essentially static vacuum-to-overdense plasma interface characterized by a gradient length L. Finally, by compressing the laser intensity rise duration [256–258], the plasma expansion time can be made so small that L becomes a fraction of the incident wavelength [259–262], and the main pulse hits an optically-smooth surface effectively reflecting it in its specular direction [263]. Under such circumstances, an optical-quality solid target is thus referred to as a "plasma mirror", and can play diverse roles in high-intensity optics [6, 12, 264–271].

Turning to intensities of 10^{19-22} W.cm^{-2} as reached by 100 TW to PW-class lasers, the irradiated plasma electrons become relativistic, inducing a non-linear oscillating motion. More specifically, electron populations are pushed towards the target by the Lorentz force on half an optical cycle, then pulled back at the surface by the combined second half-cycle Lorentz force and charge separation fields, thereby reaching Lorentz factors of $\gamma_p \sim \xi \gtrsim 10$, until the next incoming optical front and reversed-direction charge separation field suddenly decelerate them, at which point they coherently emit an electromagnetic burst specularly directed and time-compressed by the *beaming effect* (see Fig 1.2). This mechanism of *relativistic oscillating mirror* [8–11, 272–276] is responsible for the conversion of the femtosecond incident pulse into a train of pulses of (tens of) attoseconds duration, each separated by one initial laser wavelength. In the spectral domain, this amounts to the conversion of quasi-monochromatic ω_0-centred light into a high-order harmonics beam of frequencies $\{n\omega_0\}_{1\leq n\leq n_h}$ [263, 277, 278]. As the resulting beam can be focused down to the effective wavelength $\sim \lambda_0/n_h$ associated to each individual attosecond pulse, relativistic plasma mirrors have soon been recognized to open the perspective of extreme light amplification [6, 279] in principle.

Progresses in theoretical understanding Since this general vision emerged, key progresses have been made towards a definite realization. The theoretical understanding of RPM dynamics is now well established, with several consistent analytical models available [8–11, 272–276]. However, the crucial observable of attainable peak intensity at RPM focus still eludes accurate synthetic prediction. It has long remained out of reach of *ab initio* numerical computation as well. Due to the numerical dispersion relation of time-domain Maxwell solvers used in most PIC algorithms, resolving the wide spectral content of the reflected beam required prohibitive computational resources [251, 252, 280]. Recent development of the WarpX-PICSAR pseudo-spectral Maxwell solver [249–252] lifted this obstacle, allowing for realistic computation of RPM high-order harmonics generation for the first time [251, 252, 280]. The cut time-to-solution allowed for extensive parametric studies of the generation mechanism and attainable intensity gain *via* hundreds of 2D simulations. As a result, the optimal parameters for RPM light amplification could be reliably identified [12, 281], revealing the full potential of this paradigm. Namely, above 1 PW peak power (normalized amplitude $\xi \gtrsim 10$ on plasma mirror) magnifications of the incident laser intensity of up to five orders of magnitude is possible, by coherent focusing of about a hundred harmonic orders only [281], contrasting with the thousands required in previous schemes [6, 9, 282].

Experimental achievements and prospects Decisive steps have been crossed on the experimental side as well. Though most interesting for high-intensity operations, achieving the plasma mirror effect in the relativistic regime has long remained a hurdle. This is due to time profile of concrete highly amplified laser pulses, where the main femtosecond pulse is typically preceded by a precursor light called the *pedestal*, possibly of nanosecond time extent and low slowly rising intensity, whose ratio to the global peak intensity is called the *contrast*. Though an ubiquitous parasite product of CPA technology, pedestal light can be innocuous or even beneficial depending on the situation. In the context of relativistic laser-solid interaction, it proves able to totally suppress the plasma mirror effect by early target ionization, removing any control of the vacuum-plasma interface, let alone a putative gradient scale. As nanosecond irradiation[19] can ionize matter at intensities as low as 10^{11} W.cm^{-2}, maintaining target integrity until the rising edge of a 10^{18-22} W.cm^{-2} femtosecond pulse requires laser contrasts of the order of 10^{8-11}. This

---

[19] On these timescales collisional processes and heating play a role, that is totally eclipsed by mean-field effects at the main pulse time and field scales.

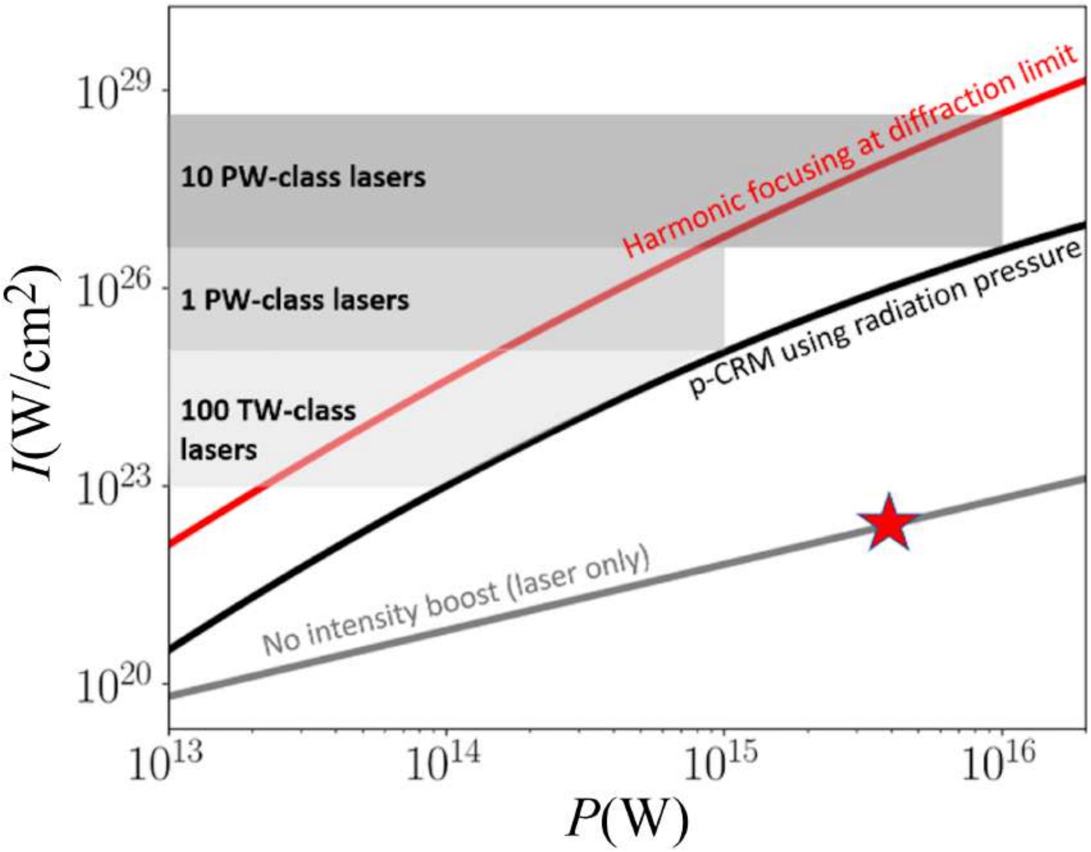

Figure 1.3: **Expected intensities using RPM harmonic beams.** The current intensity record is represented with a red star, it corresonds to $I = 1.4 \times 10^{23}$ W.cm^{-2} and was obtained on the 2.7 PW CoReLs laser [17]. The oc-RPM values correspond to the black curve (here called p-CRM for "plasma curved relativistic mirror"), while the diffraction limit is shown with a red curve; the of-RPM values would generically lie anywhere between those two. (adapted from [13])

was solved by the use of auxiliary plasma mirrors before the main RPM target, on which the laser is focused so as to to trigger the (non-relativistic) plasma mirror effect just at the rising edge of the main pulse, thus achieving separation from the pedestal [256–258, 283]. In order to then independently control the plasma length L, a critical parameter of RPM harmonics generation [259, 260, 284], a simple system was devised to extract a pre-pulse from the now high-contrast main pulse, ionizing the target in advance with known energy and adjustable delay [265, 267]. In combination, these methods applied to 100-TW class lasers have lead to many experimental demonstrations that RPMs are highly reproducible [260, 284–287] and can be finely controlled in practice [259, 264–266, 285, 286, 288, 289]. Accurate spatio-temporal characterization and shaping of the harmonic beams could also be conducted [285–287].

B. Focusing plasma mirrors as a source for extremely high intensities

Even when time-compressed pulses are generated, they need to be tightly focalized in order to reach their highest possible intensity. A coneptually most straigthforward method is to treat both stages independently, optically manipulating the RPM beam after generation using dedicated X-UV optics [290]. In a more compact design, the generating PM itself could be taken as the focusing device, simply by carving its surface into a parabolic shape [6, 11, 248, 291]. In both cases, however, the cost of decorelating generation and focalisation is an extreme sensitivity to physical imperfections — *e.g.* misalignment, carving defect, laser jitter[20] — eventually translated in a soar of experimental complexity. Several proof-of principle experiments were conducted without demonstrating sizable intensity gains [292–294].

A milestone towards higher intensities from *ab initio* simulations Further integration proving desirable, the rich optical properties of the PM dynamical system provide a promising track. It has long been noticed that RPMs produce diverging harmonic beams [284], which in the context of high-harmonics generation as a source for subsequent pump-probe studies was perceived as detrimental. However, as *e.g.* numerical simulation reveal, this far-field divergence is actually a signature of the focusing nature of the RPM, which posses a real focal point typically a few primary laser Rayleigh lengths above its surface. As was later elucidated, the inhomogeneous intensity distribution on the PM surface during the primary laser reflection tends to press electrons at the center more than on the periphery, which spontaneously induces an optical curvature of the PM. A theoretical analysis based on momentum balance on the laser-plasma interface showed this PM "denting" to precisely scale as $\sim \ln I$, hence forming a parabola for a gaussian transverse laser profile [295] whose opening depends on the peak intensity. The notion of "optically curved relativistic plasma mirror" (oc-RPM) naturally follows. Considering a 3 PW $\lambda_0 = 800$ nm ten cycles laser as the driving beam, *ab initio* WarpX-PICSAR 3D numerical simulations were able to show that intensity gains of the order of $\Gamma \approx^3$ ($I \approx 10^{25}$ W.cm^{-2}) robustly arise at RPM focus, simply by the effect of the optically induced PM curvature. Studying the theoretical dependance of Γ upon the PM denting δ_p, all else being equal, one finds that shifting from $\delta_p \simeq 0.1\lambda_0$ as in the simulation to $\delta_p \simeq \lambda_0$, the gain moves from $\Gamma \approx 10^3$ to 10^5. The full potential of the oc-RPM thereby appears along with its main limitation. Indeed, when the plasma length changes of more than a fraction of λ_0 all else is not equal, as in particular the harmonics generation efficiency drops[21].

A path towards the Schwinger field In order to reach beyond the oc-RPM, yet another method disentangling the plasma length and pulse curvature is required. In particular, as the plasma length is key to efficient harmonics generation, keeping it around its optimum value would be very beneficial, which means the RPM should be initially flat and its optical denting remain as small as possible. The necessary extra aperture then has to be provided externally again to benefit from the then very high theoretical intensity gains. In regard of the pitfalls evoked earlier when focalization follows generation, a very appealing idea would simply be to incorporate it from the start in the infrared driving pulse. If the primary beam reaches the target surface more than approximately two Rayleigh lengths before its focal plane, then its wavefronts curvature naturally encode its numerical aperture, which could be accurately transmitted to the specularly reflected beam, as occurs exactly with ideal flat mirrors. In principle, arbitrary apertures could be

---

[20] The quality of an optical element being quantified in terms of pulse wavelength, the magnitude of such defects should be controlled on a *nanometric* scale, thus far beyond the standards of ultra-intense laser engineering.

[21] Both effective harmonics number and PM reflectivity are found to significantly decrease for $L \gtrsim 0.1\lambda_0$, using 2D simulations parameter scans [12, 281].

conferred to the harmonic beam in this way, which in practice would inherit the limits of infrared laser optics — instead of that of X-UV optics. A possibly more serious constraint could reside in the intensity profile of real laser pulses out of focus which, as adaptative optics is usually applied to optimize it at focus, could turn out quite unpredictable without specific attention. Again, the major edge of this last scheme, which one may call "out-of-focus relativistic plasma mirrors" or "optically-flat relativistic plasma mirror", is to allow for nearly five orders of magnitude intensity magnification virtually only relying on conventional laser engineering.

In the event that the RPM harmonics generation and focusing schemes presented above succeed, sources of unusually strong-fields would thus be made available. For reference one can map these configurations to interaction parameters diagrams on which the different sf-QED regimes can be easily located, allowing to picture the regime shift performed by RPM conversion of standard Petawatt lasers. Assuming perfect focusing, this process indeed essentially translates into $\lambda_0 \to \lambda_0/n_h$ and $\xi \to \xi\sqrt{n_h}$. This is shown in Fig. 1.4, in terms of focused power, normalized potential ξ (there denoted a_0) and wavelength. One sees that RPM conversion of current and near-term lasers generically brings us from below to above the quantum dominated regime threshold $\chi \gtrsim 1$. Remarkably, in the most favorable case the combination of wavelength shortening and pulse amplification results into a non-vanishing probability of Schwinger pair creation over the total beam volume, a landmark for the critical regime of sf-QED. This entails that non-trivial processes can occur in these beams both in the presence or absence of matter at focus.

1.4 Objectives of the thesis

The core of our work has consisted in specifying the main physical phenomena to be expected at the interaction point of these relativistic plasma mirror sources. In this section, we will be presenting the expectations derived from a closer study of different interaction scenarios. Light couplings to the electron-positron field in a vacuum will be studied first, deriving observable signatures in different experimental setups, including scattered photon spectra and Schwinger pair creation threshold. These subtle effects when no matter is there leave room to to prolific pair creation as soon as one charged particle comes in. This process of field-matter interaction occurs for different types of initial seed, a Schwinger pair, a dense target, high-energy electron beams, affecting the involved elementary processes and the macroscopic system state. These phenomena will be presented in a second section.

1.4.1 Observing vacuum QED processes in the light of relativistic plasma mirror sources

The quasi-stability of the fermionic vacuum state in sf-QED means that, provided it is strong enough, an electromagnetic field couples to fermionic degrees of freedom even in the absence of charged particles. The most straightforward manifestation of this fact is electron-positron pair creation from coherent field decay, which persists even in the limit of infinitely low field photon frequency, which is known as the Schwinger process. Within the locally constant field approximation, its local rate can be computed as [199, 296]:

$$\Gamma_S = \frac{1}{4\pi^2}\lambda_C^{-4}\mathcal{E}\mathcal{B}\coth\left(\frac{\pi\mathcal{B}}{\mathcal{E}}\right)\exp\left(-\frac{\pi}{\mathcal{E}}\right) \tag{1.31}$$

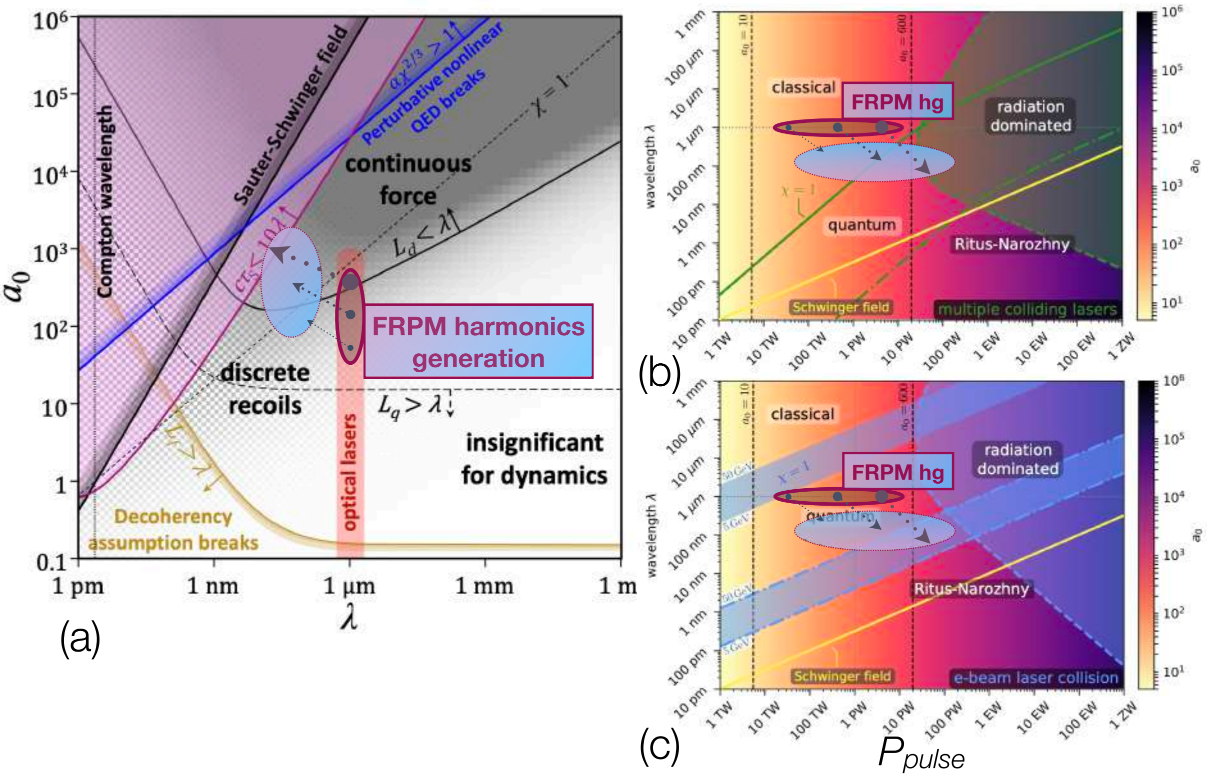

Figure 1.4: **Parameter diagrams displaying the effect of Focusing Relativistic Plasma Mirror harmonics conversion of Petawatt-class optical lasers. (a)** RPM shift in wavelength and normalized potential. The accessed regime is characterized by $\chi > 1$, fast radiation of whole electron energy ($L_d < \lambda$), and may cross the Schwinger pair creation threshold. (adapted from [4]) **(b)** RPM shift in wavelength, peak power, and normalized potential assuming 2λ focal size; in the context of interaction with a target at rest. The quantum regime is accessed, and possibly the quantum dominated regime (here referred to as "radiation dominated"). **(c)** Same as (b); in the context of collision with high-energy electron beams. Collision with a 50 GeV beam would allow enter the fully non-perturabative regime of sf-QED (dashed blue lines). (adapted from [114])

where λ_C is the reduced Compton length of the electron. The non-perturbative nature of the process mathematically translates into non-analyticity of the occurrence rate around $\mathcal{E} \sim 0$, which effectively results into exponential suppression as long as $\mathcal{E} \lesssim 1$. This implies that so-called "vacuum pair creation" is relevantly conceived as a threshold effect, forbidden below a given field value and growing very fast past it. Note that because the final probability typically scales as $P_S \equiv \mathcal{V}_{sf}\Gamma_S$, where $\mathcal{V}_{sf} \sim \lambda^4 \gg \lambda_C^4$ is the spacetime volume where a field of wavelength λ is strong, the threshold specific to a macroscopic configuration can be significantly lower than $E \sim E_S$ in the laboratory frame [197–200]. Nonetheless, the lowest required intensities lying around $I \gtrsim 10^{27}$ W.cm^{-2} for a working wavelength of 800 nm [226], observing vacuum pair creation seems precluded in any current or forecasted facility [3].

- In contrast, we could demonstrate that focused RPM harmonic beams open a tantalizing possibility to achieve this process. If the harmonics produced by a 200 PW class laser, ranging up to harmonic order $\lesssim 100$, can be efficiently focused near diffraction limit $w_0 \sim 50$ nm, then Schwinger pair creation could be observed in the laboratory.

In the conservative assumption that such threshold is not crossed though, another yet unobserved strong-field processes could still occur, the vacuum self-interaction of light. Even in the absence of real particle creation, intermediate electron-positron states indeed allow the electromagnetic field to interact with itself, giving rise to macroscopic effects akin to a "vacuum polarization". From a particle perspective this interaction translates into photons scattering off each other, towards final states possibly outside the initial coherent state spectrum. The detection of these photons has driven significant theoretical and experimental efforts during the last two decades, showing that possibilities to observe them exist within the current laser technological realm (see [3] and references therein).

A major difficulty for these observations is that for kinematic reasons, the scattering amplitudes are dominated by quasi-elastic channels, where photons are scattered close to the energy and direction of the incoming ones; as the required Petawatt class lasers typically comprise more than 10^{20} photons, discerning a scattering signal proves the main challenge in these experiments. The relevant quantity is therefore the number of "discernible photons" generated per shot, that is the ones satisfying a criterion of the form,

$$n_{\text{scattered}}(\mathbf{k}) > C N_{\mathcal{A}}(\mathbf{k}) \tag{1.32}$$

with $C > 0$, $n_{\text{scattered}}(\mathbf{k})$ and $N_{\mathcal{A}}(\mathbf{k})$ the phase space densities around momentum $\mathbf{k}$ respectively of scattered and initial field photons. State-of-the-art studies typically find tens of discernible photons in the collision of two or more laser fields [3] (see *e.g.* [297]). An experimental investigation of realistic photon detection and background filtering capabilities in this context has also been recently conducted [298].

These a priori very harsh constraints call for new schemes improving the signal to noise ratio, for which as will be shown RPM light proves very promising. A previous study had already demonstrated that collision of a low order harmonic beam with a fundamental frequency pulse could open sizeable inelastic channels, both in direction and frequency, producing robustly discernible photons [299].

- In chapter 8, we will present our own work on the use of RPM light for exploring vacuum light-by-light scattering, improving on former knowledge through an accurate modelling of RPM spectra and fields, made operational by the use of large scale computing infrastructures. The main results are first the possibility to produce as many discernible photons as with two exactly synchronized and aligned counter-propagating infrared pulses focused at diffraction limit, with a single RPM harmonic beam, thus considerably simplying the setup. Then, we proceeded to study the collision of the harmonics with an auxiliary pulse, which allowed us to confirm the existence of inelastic scattering channels in this case, resulting, all else being equal, in improvement of the attainable signal-to-noise ratios by several orders of magnitude over optical frequency configurations.

- This core study was completed by extensive numerical validation of the "Stimulated Vacuum Emission" algorithm, highlighting its behavior under many different options of implementation. Analytical estimate of the number of scattered photons in RPM beams as a function of the field harmonic spectrum could also be derived. Finally, a theoretical discussion of the different methods employing the Heisenberg-Euler action could be lead, and the correspondence between the Stimulated Vacuum Emission algorithm and the resolution of effective field equation fully detailed and clarified, putting forward a condensed view of previous knowledge on the matter. These studies are presented in part III.

1.4.2 Converting relativistic plasma mirror light into exotic matter processes and states

The above discussed physics relied on the assumption that strong fields propagate in a pure fermionic vacuum. However, there are many circumstances in which this might not be the case, be it from controlled operation, or physical contingency. In this section, we will expose our work on the physics of these situations where real initial particles are involved, in the various way they can be introduced. Each of them will be detailed in chapter 9.

A first possible scenario is the straightforward extension of vacuum propagation when Schwinger pair creation occurs. The sharp field dependence of the local rate Eq. 2.51 entails that, in a semi-classical kinetic picture, electron-positron pairs will typically be created at focus when the harmonic field peaks, possibly in several attosecond pulses as they successively cross the focal plane. At this point, the electromagnetic field is of the order of $F \sim 1.2\ F_S$, or $I \sim 6 \times 10^{29}$ W.cm^{-2}, so that these particles become relativistic in a fraction of their Compton time $\tau_C \simeq 8 \times 10^{-21}$ s. Under a Lorentz-force evolution, these particles are therefore instantly guided by the relativistic ponderomotive force along the local wavefronts normal direction, and conservatively estimating their quantum interaction parameter from the plane-wave case yields $\chi \simeq E/E_S$, where E is the electric field amplitude in the laboratory frame. As in this case we have $E/E_S \gtrsim 1$, sf-QED processes can occur, and QED cascades instantly start to develop. Moreover, the field is even locally not a plane wave and, as a consequence of the above, trajectories do not follow the Lorentz-force, all of which tends to favor higher χ parameters. This process leads to exponential growth of the particle number in the beam for at least as long as $E \gtrsim E_S$, concentrated in the attosecond high-field fronts and guided by them, which results in extremely high density globally neutral electron-positron sheets accelerated up to GeV energies.

☐ The final states of these configurations, in between relativistic quantum plasmas and ultrarelativistic particle beams, are very challenging to predict even numerically, particularly their maximum particle densities, as the corresponding plasma proper wavelength-frequency generically tend to exceed any computationally tractable resolution. Partial results could however be obtained, and lower bounds on the maximum density of the order of $\gtrsim 10^{29}$ cm^{-3} established, however these preliminary results will not be presented in this thesis.

A related physics could be observed when the field interacts with external particles from the beginning, all the more with an abundant particle source, which a priori provides strong motivations for studying the focusing of RPM fields on solid targets. Significant enhancement of sf-QED processes could then be evidenced, up to the formation of very high density, relativistic quantum plasma states.

- A first study was conducted with moderate intensity RPM light[22], where the focused intensity on target reached about $\sim 10^{25}$ W.cm^{-2} [300]. In this case, a relativistic quantum plasma was not properly formed, as the harmonics and target plasma fields determined the dynamics, however a significant increase in produced gamma photons and Breit-Wheeler pairs was demonstrated compared to direct infrared pulse irradiation for an equivalent energy. A striking feature of these interactions was the formation of a depleted channel in the wake of the harmonic beam, which could propagate inside the solid target on a distance of many wavelengths, due both to its high frequency content and relativistic transparency.
- In a more extreme RPM light of above $\sim 10^{27}$ W.cm^{-2} intensity, both these effects are magnified, leading to the formation of very high-density electron-positron plasma states. These dense particle clusters tend to be accelerated by the RPM field, up to GeV energies, and charge separation tends to occur under the influence of the ambient strong fields. The thereby formed gamma, electron and positron beams properties were studied through their spectra. Though not directly studied here, their subsequent interaction with matter should display interesting phenomena as well, providing dense, attosecond, high-energy particle sources.

Another way to study elementary strong-field processes is to collide very high energy particles with the pulse, allowing for very high χ parameters, possibly up to the "fully non-perturbative" regime of sf-QED. This configuration typically represents the collision of a high-energy electron beam with the RPM-light beam, and was also investigated.

- The interaction of electron beams with the RPM field was studied for the whole 10^{26} W.cm^{-2}–10^{29} W.cm^{-2} intensity range, with an electron beam energy of 10 GeV, and an angle of collision maximizing peak χ values. In these conditions, it is shown that the $\chi = 1600$ threshold can be exceeded from intensities of 10^{27} W.cm^{-2}, opening the perspective of testing the Ritus-Narozhny conjecture. Besides, such configurations also allow for prolific sf-QED processes, that could be observed through the emitted particle spectra, which we will detail.

---

[22] This could result from a sub-Petawatt primary laser, or sub-optimal generation conditions, *e.g.* angle of incidence or plasma mirror gradient.

Chapter 2

Theoretical and numerical methods

Accurate prediction of the expected effects when strong fields are achieved requires appropriate theoretical methods. As we know that qualitatively new phenomena will stem from quantum processes, they have to be grounded in Quantum Electrodynamics. For conceptual clarity as well as versatility, it would furthermore be desirable for the new framework to encompass at least the former one, classical relativistic kinetic theory, with an explicit connection. Ideally, there should exist a map between the old variables and the new, then highlighting how the latter extend the first and reduce back to them under suitable physical circumstances[1]. Such definitive theoretical framework is not currently in use, and research in this direction is still active[2].

Meanwhile, strong-field physics could progress from a combination of a few more specialized formalisms, well-suited to most studied configurations. In particular, many concepts and intuitions in the field gravitate around a semi-classical "Boltzmann-QED" model, which proves flexible, operational, and incidentally constitutes the basis for *ab initio* numerical simulations [301] (*cf.* Chapter 9). This model will be described first, including how it casts the historical "Furry picture" [302] into general configurations, from which different regimes of strong-field QED will be discerned. We will then be able to detail the principles of *ab initio* PIC-QED simulations, that numerically realize the Boltzmann-QED equations, and provide reference for the WarpX code used in the present thesis. Final sections will be devoted to a formalism aimed at computing effects of the electromagnetic self-interaction in a vacuum specifically[3], and the validation of its numerical implementation on massively parallel computing infrastructures. It is called "Stimulated Vacuum Emission" [303], and forms the basis for the work presented in Chapter 8.

2.1 An operational framework for strong-field Quantum Electrodynamics

In the most common formulation of QED, as for that matter of other quantum field theories, processes are conceived in the basis of free particle states, that are stable in time when interactions are discarded[4]. Physically, this means that only transitions from incoming non-interacting $n-$particles states in the asymptotically far past to outgoing $n'-$particles states in the asymptotically late future are relevantly modelled, so-called "scattering events". If such picture provides operational tools for the empirical context of high-energy accelerators in which it was forged, it seems unfit to the more general

---

[1] This is would be all the more relevant that actual experiments would typically produce such physical scenarios, *e.g.* the focusing of a pulse to a transient strong-field region (itself only weakly quantum in standard facilities), or the screening of driving fields by an electron-positron plasma followed by relaxation.

[2] Non-equilibrium Quantum Field Theory naturally solves the problem (App. B.2.5), but then requires to be cast in a computationally, if not analytically, tractable form.

[3] A connection with the Boltzmann-QED framework is derived in Chapter 5.

[4] See *e.g.* App. B for details and terminology.

macroscopic configurations previously envisioned in classical plasma physics. Incidentally, the electromagnetic field expectation value in any state with a definite number of photons vanishes.

As a matter of principle though, quantum theory must be able to fully encompass its classical counterpart. Besides, non-vanishing field expectation values naturally arise also in the quantum theory [304]. The above described asymptotic formalism can indeed be understood as the computation of specific observables (scattering amplitudes) at late times for few-particles initial states, that are in a sense "near to the vacuum"[5]. However, the most general questions of the expectation value of any observable at a finite time from an arbitrary – possibly mixed – initial state are in principle within reach, through methods gathered under the name of "Non-equilibrium Quantum Field Theory" [305, 306]. In particular, all correlation functions of a theory can be computed to a given accuracy at all times, from the data of their initial values. In view of the previously evoked consistent, versatile and computable theory, a systematic approximation procedure may then be followed so as to obtain *e.g.* a suitably extended kinetic formulation of Quantum Electrodynamics [116, 307].

The most extensive theoretical framework currently underlying strong-field Quantum Electrodynamics research is one such extension of classical kinetic theory. It was however built from the opposite direction, adding quantum corrections to the kinetic equations, in a "bottom-up" motivated approach. In this context, particles are described by 1-body distribution functions governed by Boltzmann equations, and the electromagnetic field is classical. All quantum phenomena are encapsulated into *i*) a collision operator for the 1-particle distribution functions and *ii*) additional terms in Maxwell's equations. The cross-sections entering the collision terms are then computed in an extension of the usual QED scattering theory that accounts for the presence of an electromagnetic field, called the "Furry picture" of sf-QED [302, 308]. In this section, our primary aim is to outline this formulation of sf-QED, grounding both intuition and quantitative results such as presented in Chapter 9. Introducing the Furry picture in a second part will allow defining the parameters governing QED processes, and hence classifying the different physical regimes of strong-field electrodynamics.

2.1.1 The Boltzmann model of strong-field QED

Classical relativistic kinetic theory Let us start from a classical depiction of systems to be described. They consist in the electromagnetic field interacting with matter particles, typically in very high number and collectively forming a plasma. Considering indeed an electron-ions plasma, as produced by ordinary matter interaction with lasers, the critical plasma density at $\lambda_0 = 800$ nm is $n_0 = 1.7 \times 10^{21}$ cm^{-3}, and matter configurations typically range from $n_e \sim 10^{-3} n_0$ for gas jets to $n_e \sim 10^{2-3} n_0$ for solid targets, generically resulting in more than 10^6 electrons in a 1 μm^3 volume. As a consequence, the exact system state is practically irrelevant and statistical methods must be used.

The canonical formalism of mechanics usually provides a sound definition of the statistical behavior of a system. If the system has $6N$ independent variables, say $\{\mathbf{x}_i = (\mathbf{q}_i, \mathbf{p}_i)\}_{i \in [\![1;N]\!]}$, and $f_N(\mathbf{x}_1, \ldots, \mathbf{x}_N)$ is the full system state, Liouville's equation translates

---

[5] See Comp. B.3.

in a system of coupled equations for reduced distribution functions[6] [309],

$$f_{N-k}(\mathbf{x}_1,\dots,\mathbf{x}_{N-k}) = \frac{N!}{k!}\int d\mathbf{y}_1\dots d\mathbf{y}_k f_N(\mathbf{y}_1,\dots,\mathbf{y}_k,\mathbf{x}_1,\dots,\mathbf{x}_{N-k}) \tag{2.1}$$

known as the "Bogolioubov-Born-Green-Kirkwood-Yvon hierarchy". When closed at order 1, for instance *via* a "molecular chaos hypothesis" $f_2(\mathbf{x_1},\mathbf{x_2}) \sim f_1(\mathbf{x_1})f_1(\mathbf{x_2})$, a Boltzmann equation for the "1-body" distribution function f_1 is obtained,

$$\textbf{Boltzmann (1-body)}\ \frac{\partial f_1}{\partial t} + \{f_1, H_1\} = \mathcal{C}_B[f_1] \tag{2.2}$$

where H_1 is the "1-body Hamiltonian", derived from the full one, and $\mathcal{C}_B[f_1]$ is called a "collision term". The (normalized) 1-body distribution f_1 has a simple interpretation in terms of density of (probability to find) particles at point $(\mathbf{q},\mathbf{p})$ in phase space.

Now, in a relativistic theory difficulties arise as physical variables are not all independent[7], so that the *constrained* canonical formalism should be used [310, 311]. In practice, this difficulty is most often circumvented by a more heuristic approach [309, 312–314]. Let us illustrate one such procedure[8] noticing that an exact ("pure") system state can be encoded in the following singular distribution on the 1-body phase space,

$$f_K(\mathbf{x},t) \equiv \sum_{i=1}^{N} \delta(\mathbf{x}-\mathbf{x}_i(t)) \tag{2.3}$$

As each particle trajectory can be assumed to be dictated by the Lorentz force, that is,

$$\begin{cases} \dot{\mathbf{q}}_i = \dfrac{\mathbf{p}_i}{m\gamma_i}\ \text{, with}\ \gamma_i = \sqrt{1+\dfrac{\mathbf{p}_i^2}{m^2c^2}} & (2.4)\\ \dot{\mathbf{p}}_i = q\left[\mathbf{E}_K(\mathbf{q}_i) + \dot{\mathbf{q}}_i\times\mathbf{B}_K(\mathbf{q}_i)\right] & (2.5)\end{cases}$$

where $\mathbf{E}_K, \mathbf{B}_K$ follow Maxwell's equations sourced by the exact currents, deriving Eq. 2.3 with respect to time and gathering terms we find the *Klimontovitch-Dupree* equation,

$$\textbf{Klimontovitch-Dupree}\ \boxed{\frac{\partial f_K}{\partial t} + \frac{\mathbf{p}}{m\gamma}\cdot\frac{\partial f_K}{\partial \mathbf{q}} + q\left[\mathbf{E}_K + \dot{\mathbf{q}}\times\mathbf{B}_K\right]\cdot\frac{\partial f_K}{\partial \mathbf{p}} = 0} \tag{2.6}$$

This equation is exact, but unsolvable as it is equivalent to the $6N$ equations system Eqs. 2.4-2.5. In order to relate is with more accessible quantities, one idea then is to decompose dynamical variables in,

$$f_K = f + \delta f \tag{2.7}$$
$$\mathbf{E}_K = \mathbf{E} + \delta\mathbf{E} \tag{2.8}$$
$$\mathbf{B}_K = \mathbf{B} + \delta\mathbf{B} \tag{2.9}$$

introducing average values $X \equiv \langle X_K \rangle$ with respect to possible realizations of the system preserving a certain set of observable ("macroscopic") quantities[9]. Typically, we wish to

---

[6] Particles are assumed identical so the choice of integration variables does not matter (f_N is totally symmetric). The prefactor simply allows unifying expressions for certain forms of observables [309].

[7] The momenta components for instance are related by $p_\mu p^\mu = m^2$.

[8] We refer to [315] for more details on this presentation.

[9] In a derivation of kinetic theory from quantum field theory, distribution functions simply are quantum expectation values.

consider averages such that f now coincides with the 1-body distribution function f_1 in its operational interpretation. Averaging Eq. 2.6 and injecting definitions Eqs. 2.7-2.9 we are then lead to,

$$\textbf{Boltzmann (average)}\ \boxed{\frac{\partial f}{\partial t} + \frac{\mathbf{p}}{m\gamma}\cdot\frac{\partial f}{\partial \mathbf{q}} + q\left[\mathbf{E} + \dot{\mathbf{q}}\times\mathbf{B}\right]\cdot\frac{\partial f}{\partial \mathbf{p}} = \mathcal{C}_K[f,\mathbf{E},\mathbf{B}]} \tag{2.10}$$

$$\text{with, } \mathcal{C}_K[f,\mathbf{E},\mathbf{B}] \equiv -q\left\langle\left[\delta\mathbf{E} + \dot{\mathbf{q}}\times\delta\mathbf{B}\right]\cdot\frac{\partial f_K}{\partial \mathbf{p}}\right\rangle \tag{2.11}$$

In these equations, the average electric and magnetic fields are now be computed from the averaged currents,

$$\textbf{Maxwell (average)}\ \begin{cases} \nabla\cdot\mathbf{E} = \dfrac{\rho}{\varepsilon_0} & (2.12)\\ -\dfrac{1}{c^2}\partial_t\mathbf{E} + \nabla\times\mathbf{B} = \mu_0\mathbf{j} & (2.13)\\ \nabla\cdot\mathbf{B} = 0 & (2.14)\\ \partial_t\mathbf{B} + \nabla\times\mathbf{E} = 0 & (2.15)\end{cases}$$

where,

$$\textbf{Sources (average)}\ \begin{cases} \rho(\mathbf{r}) = \sum_\alpha \int d\mathbf{p} q_\alpha f_\alpha(\mathbf{r},\mathbf{p},t) & (2.16)\\ \mathbf{j}(\mathbf{r}) = \sum_\alpha \int d\mathbf{p} q_\alpha \dfrac{\mathbf{p}}{m_\alpha\gamma_\alpha} f_\alpha(\mathbf{r},\mathbf{p},t) & (2.17)\end{cases}$$

introducing possibly multiple particle species distributions f_α defined by their mass m_α and charge q_α, each following Eq. 2.10.

Equations Eqs. 2.10-2.17 define a system of coupled partial differential equations. Once closed by the data of the functional $\mathcal{C}_K$, it allows computing variables $f, \mathbf{E}, \mathbf{B}$ and hence all classical 1-body properties of the system.

A system is well approximated by these quantities if dynamics is dominated by collective effects rather than few-particles contributions, seen as fluctuations in Eqs. 2.7-2.9. In plasma physics, introducing a mean kinetic energy u_e for the electrons (or other fast particles), this criterion typically translates into,

$$\Lambda = n_e\lambda_D^3 \gg 1 \tag{2.18}$$

$$\text{with } \lambda_D = \sqrt{\frac{\varepsilon_0 u_e}{e^2 n_e}} \text{ the Debye length} \tag{2.19}$$

$$\textit{i.e.}\ \lambda_D \sim \sqrt{\frac{u_e}{m_e c^2}}\lambda_p \text{ with } \lambda_p = 2\pi\sqrt{\frac{\varepsilon_0 m_e c^2}{e^2 n_e}} \text{ the plasma length} \tag{2.20}$$

In the case of strong fields and plasma interactions, collisions typically are all the more negligible that electron-field interaction energies are ultra-relativistic ($u_e \gg m_e c^2$).

Strong-field QED as collision processes The key idea to extend classical kinetic theory to the strong-field regime of electrodynamics is to embed quantum processes in the collision term $\mathcal{C}_K$. This is made possible by the large scale separation between $\lambda_{\mathcal{C},e} \simeq$

2.42×10^{-12} m, the electron Compton length, and the typical field-plasma scales $\lambda_0, \lambda_p \gtrsim 1 \times 10^{-8}$ m[10] [301].

As a consequence, one may assume that the coherence scale of quantum processes is small enough to treat them as punctual events in Eq. 2.10, while all particles behave classically in-between. Namely, they are described by on-shell 1-body distribution functions following the transport equation Eq. 2.10. The electromagnetic field then receives a dual description, with classical values $\mathbf{E}, \mathbf{B}$ corresponding to its quantum expectation values, and a photon distribution function f_γ describing particle-like variables of the quantum electromagnetic field[11]. Once again, consistency is ensured by the large gap between frequencies associated with the coherent field ($h\nu \lesssim 100$ eV) and emitted high-energy photons ($\varepsilon_\gamma \gtrsim 1$ MeV) [301].

The above assumptions on the scale of quantum processes naturally imply that the electromagnetic field in which they occur can be considered constant[12]. This assumption, known as the “Locally Constant Field Approximation”, takes many forms in strong-field QED and typically strongly constrains models beyond this semi-classical level. Besides, quantum processes typically become non-negligible when particles are ultra-relativistic, in which case the field can also be considered crossed[13]. All cross-sections in the collision kernels therefore correspond to QED scattering amplitudes in a constant crossed field. This explains their dependence on a single *quantum interaction parameter* χ defined in Eq. B.126, and the existence of exact analytical expressions for the differential cross-sections.

The most significant new processes are (non-linear) Compton scattering of an electron or positron emitting a photon, and (non-linear) Breit-Wheeler electron-positron pair creation from a photon in the strong-field. The core equations of the Boltzmann-QED kinetic model can thus finally be written as [315],

$$\boxed{\begin{aligned} \frac{\partial f_{e^\mp}}{\partial t} + \frac{\mathbf{p}}{m_e\gamma}\cdot\frac{\partial f_{e^\mp}}{\partial \mathbf{q}} \mp e\left[\mathbf{E} + \dot{\mathbf{q}}\times\mathbf{B}\right]\cdot\frac{\partial f_{e^\mp}}{\partial \mathbf{p}} &= \mathcal{C}_{\mathrm{CS}}[f_{e^\mp}] + \mathcal{C}_{\mathrm{BW}}[f_\gamma] \qquad (2.21)\\ \frac{\partial f_\gamma}{\partial t} + \mathbf{c}\cdot\frac{\partial f_\gamma}{\partial \mathbf{q}} &= \mathcal{C}_{\mathrm{CS}}[f_{e^-}] + \mathcal{C}_{\mathrm{CS}}[f_{e^+}] - \mathcal{C}_{\mathrm{BW}}[f_\gamma] \qquad (2.22)\end{aligned}}$$

together with an unchanged Maxwell part[14] Eqs. 2.12-2.17, and possibly additional particle species such as ions.

2.1.2 QED processes in strong fields

In view of the above described picture of QED processes as collision events, we will now simply draw the implications of the presence of a coherent field for QED scattering amplitudes. Actually, the heuristic formulation used in this part will allow to reach conclusions beyond the scope of the Boltzmann-QED model. In particular, we will be able to introduce

---

[10] Equivalently, between the photon-plasmon energies $\lesssim 100$ eV and the electron characteristic energy $m_e c^2 \simeq 0.511$ MeV.

[11] In a kinetic reduction of Quantum Electrodynamics, “field values” and “photon particles” would naturally stem respectively from the $1-$point and $2-$points functions [116] (*cf.* App. B.2.5).

[12] More refined arguments for defining this so-called “formation length” show that it generally depends on the local field strength, and decreases as the field increases (see *e.g.* [2, 4]).

[13] Indeed, $(c\mathbf{B})^2 - \mathbf{E}^2$ and $\mathbf{B}\cdot\mathbf{E}$ are Lorentz-invariant while $\mathbf{E}^2 + (c\mathbf{B})^2 \sim \gamma^2$.

[14] See Chapter 5 for the inclusion of vacuum electromagnetic self-interaction.

the Furry picture of strong-field QED, that is pivotal to virtually all current investigations as it leads to *exact* expressions for processes in plane-wave fields, and more generally allows at least for approximations beyond the LCFA.

Observables in a coherent state Consider an observable of interest $\mathcal{O}$, then vacuum QED would typically consist in computing its asymptotic expectation value,

$$\begin{aligned} \langle \mathcal{O} \rangle_0 &\triangleq \langle 0 \,|\, \mathcal{O}(t \to +\infty) \,|\, 0 \rangle \\ &= \left\langle 0 \,\middle|\, U(+\infty, -\infty)^\dagger \mathcal{O} U(+\infty, -\infty) \,\middle|\, 0 \right\rangle \end{aligned} \tag{2.23}$$

where we have introduced the vacuum state vector $|0\rangle$, $U(t, t_0)$ the evolution operator from t_0 to t and the $\dagger$ symbol to denote the adjoint (*cf.* App. A.4).

Now we aim at computing similar quantities but from a coherent initial state, encoding the non-vanishing expectation value of the electromagnetic field before the process takes place[15]. Let us denote $|\mathcal{A}\rangle$ the coherent state associated with the classical field $\mathcal{A}$, the new computation writes

$$\langle \mathcal{O} \rangle_{\mathcal{A}} \triangleq \langle \mathcal{A} \,|\, \mathcal{O}(t \to +\infty) \,|\, \mathcal{A} \rangle \tag{2.24}$$

We can reexpress $|\mathcal{A}\rangle$ from the (photon) vacuum state $|0\rangle$ introducing the "displacement operator" $D_{\mathcal{A}}$, expressed in terms of creation-annihilation operators $a^\dagger_{\mathbf{k},p}$, $a_{\mathbf{k},p}$, such that

$$|\mathcal{A}\rangle = D_{\mathcal{A}} \,|0\rangle \tag{2.25}$$

The canonical commutation relations then allow us to derive the relation[16],

$$D^\dagger_{\mathcal{A}} A(x) D_{\mathcal{A}} = A(x) + \mathcal{A}(x) \tag{2.26}$$

which together with unitarity of the displacement operator directly implies,

$$D^\dagger_{\mathcal{A}} \mathcal{O}(A) D_{\mathcal{A}} = \mathcal{O}(A + \mathcal{A}) \tag{2.27}$$

$$\triangleq \mathcal{O}_{\mathcal{A}} \tag{2.28}$$

for any operator $\mathcal{O}$ depending on the field operator A at any spacetime point. It follows that observable values in the presence of a field expectation value become,

$$\begin{aligned} \langle \mathcal{O} \rangle_{\mathcal{A}} &= \left\langle D^\dagger_{\mathcal{A}} \mathcal{O}(t \to +\infty) D_{\mathcal{A}} \right\rangle_0 \\ &= \left\langle D^\dagger_{\mathcal{A}} U(+\infty, -\infty)^\dagger \mathcal{O} U(+\infty, -\infty) D_{\mathcal{A}} \right\rangle_0 \\ &= \left\langle U_{\mathcal{A}}(+\infty, -\infty)^\dagger \mathcal{O}_{\mathcal{A}} U_{\mathcal{A}}(+\infty, -\infty) \right\rangle_0 \end{aligned} \tag{2.29}$$

Furry Lagrangian Therefore, the presence of a non-vanishing field expectation value affects the vacuum formalism only by shifting the photon field operator by its mean value. The essential changes are thus captured in a new Lagrangian for the non-zero field theory:

$$\begin{aligned} \mathcal{L}_{\mathcal{A}} = &-\frac{1}{4} (F_{\mu\nu} + F_{\mu\nu}[\mathcal{A}])(F^{\mu\nu} + F^{\mu\nu}[\mathcal{A}]) + \bar{\psi} \left[i\partial\!\!\!/ - e(A\!\!\!/ + \mathcal{A}\!\!\!/) - m \right] \psi \\ &- J^\mu (A_\mu + \mathcal{A}_\mu) + \mathcal{L}_J \end{aligned} \tag{2.30}$$

---

[15] Coherent state are quantum states entirely characterized by their field expectation value, and the fact that they realize the equality in the Heinseberg indeterminacy relations of conjugated field variables. In this sense, among others, they are "the most classical states" of the electromagnetic field, and provide a natural embedding of classical field configurations in QED [304, 316].

[16] We omit the identity symbol multiplying scalars in operator expressions.

where the J current terms assumed to be responsible for creating the coherent field are explicitly included for consistency, and the ψ operator is meant to account for the remaining fermionic degrees of freedom.

In practice this formalism is only useful when J and $\mathcal{A}$ are known, which implies they have to be specified in advance and therefore cannot account for the self-consistent interaction between the field expectation value and the quantum processes it triggers[17]. For this reason, they are said to be "external". In QED, J and $\mathcal{A}$ are related by Maxwell's type equations, $\partial_\mu F^{\mu\nu}[\mathcal{A}] = J^\nu$, so that,

$$\begin{aligned}\mathcal{L}_{\mathcal{A}} = &-\frac{1}{4}F_{\mu\nu}F^{\mu\nu} + \bar{\psi}\left[i\not{\partial} - e(\not{A} + \not{\mathcal{A}}) - m\right]\psi \\ &- \partial_\mu F^{\mu\nu}[\mathcal{A}]A_\nu - \frac{1}{2}F_{\mu\nu}F^{\mu\nu}[\mathcal{A}] \\ &- \frac{1}{4}F_{\mu\nu}[\mathcal{A}]F^{\mu\nu}[\mathcal{A}] - J^\mu\mathcal{A}_\mu + \mathcal{L}_J\end{aligned} \tag{2.31}$$

Now integrating by part,

$$\begin{aligned}-\partial_\mu F^{\mu\nu}[\mathcal{A}]A_\nu &= F^{\mu\nu}[\mathcal{A}]\partial_\mu A_\nu \\ &= \frac{1}{2}F^{\mu\nu}[\mathcal{A}]F_{\mu\nu}\ ,\ \text{by antisymmetry of } F_{\mu\nu}[\mathcal{A}]\end{aligned}$$

so that, after dropping the non-dynamical terms (third line in Eq. 2.31), we finally reach [302],

$$\textbf{Furry Lagrangian}\quad \boxed{\mathcal{L}_{\mathcal{A}} = -\frac{1}{4}F_{\mu\nu}F^{\mu\nu} + \bar{\psi}\left[i\not{\partial} - e(\not{A} + \not{\mathcal{A}}) - m\right]\psi} \tag{2.32}$$

called the "Furry Lagrangian".

The Furry picture of strong-field QED Reading last expression, we see that the only difference with respect to the vacuum Lagrangian (Eq. B.60) is the term $-e\bar{\psi}\not{\mathcal{A}}\psi$, coupling the fermions to the external field, and responsible for "insertion" type diagrams in the perturbative expansion[18]. Now, for perturbative theory to make sense, these diagrams have to be small with respect to the kinetic part. We can qualitatively estimate their relative magnitude at the Lagrangian level, introducing a characteristic momentum scale Q and field amplitude $\mathcal{A}_0$ for the physics at play we see that,

$$\begin{cases} i\bar{\psi}\not{\partial}\psi \sim Qj\ ,\ \text{denoting } \bar{\psi}\gamma^\mu\psi \sim j \\ -e\bar{\psi}\not{\mathcal{A}}\psi \sim e\mathcal{A}_0 j \end{cases} \tag{2.33}$$

and thus a perturbative expansion is meaningful if,

$$\frac{e\mathcal{A}_0}{Q} \lesssim 1 \tag{2.34}$$

Starting from a non-relativistic fermion configuration, we identify the parameter of the field strength expansion as,

$$\xi = \frac{e\mathcal{A}_0}{m} \tag{2.35}$$

---

[17] Non-equilibrium QFT provides a more systematic approach to this purpose (App. B.2.5).

[18] See App. B.2.4 for a discussion on the occurrence of such diagrams from non-vanishing field expectation values (there illustrated in the Schwinger-Dyson equations of a simple ϕ^3 theory).

This quantity is precisely the “normalized vector potential” in the classical theory, or “classical field strength parameter” introduced in sec. 1.1.2[19]. Though here given in terms of gauge field, it can be given a manifestly Lorentz and gauge invariant definition [24, 25]. If $\xi > 1$, the interaction of the fermions with the background field has to be treated non-perturbatively, which amounts to diagonalizing the modified kinetic term,

$$\mathcal{L}_{\mathcal{A},0} = -\frac{1}{4}F_{\mu\nu}F^{\mu\nu} + \bar{\psi}\left[i\not{\partial} - e\not{\mathcal{A}} - m\right]\psi \tag{2.36}$$

The resulting theory is known as the “Furry picture” of Strong-field Quantum Electrodynamics. It preserves the structure of perturbative QED in its particle content and interaction term, photons and so-called “dressed” electron-positron states[20] interact via the bare QED interaction vertex, but qualitatively differs from its vacuum equivalent due to the presence of an energy-momentum reservoir constituted by the “background” field. As a consequence, Furry theorem does not hold, and processes forbidden by energy-momentum conservation in a vacuum can now occur. This implies in particular that the vacuum as well as 1-particle states become quasi-stable only.

Regimes of strong-field Electrodynamics All new processes are controlled by the endogenous field strength scale $F_S = \frac{m^2}{e} \simeq 1,32.10^{18}$ V.m^{-1}, the Schwinger field, which physically marks the threshold of spontaneous fermionic vacuum decay into real electron-positron pairs. This scale together with Lorentz invariance lets us build adimensionnal quantities upon which the sf-QED processes depend, and which control their contribution to the physics. Considering a particle of momentum p^μ and a constant background field[21] $\bar{F}^{\mu\nu}$, these “quantum interaction parameters” write:

$$\boxed{\begin{array}{l}
\chi \triangleq \dfrac{1}{m}\dfrac{\sqrt{(p_\mu \bar{F}^{\mu\nu})^2}}{F_S} = \dfrac{\gamma}{F_S}\sqrt{(\mathbf{E}+\mathbf{v}\times\mathbf{B})^2 - (\mathbf{v}\cdot\mathbf{E})^2} \qquad (2.37)\\
\text{and,} \qquad (2.38)\\
\begin{cases}
\mathcal{F} \triangleq \dfrac{1}{4}\dfrac{\bar{F}_{\mu\nu}\bar{F}^{\mu\nu}}{F_S^2} = \dfrac{1}{2F_S^2}(\mathbf{B}^2 - \mathbf{E}^2)\\
\mathcal{G} \triangleq \dfrac{1}{4}\dfrac{\bar{F}_{\mu\nu}{}^*\bar{F}^{\mu\nu}}{F_S^2} = -\dfrac{1}{F_S^2}\mathbf{E}\cdot\mathbf{B}
\end{cases} \qquad (2.39)\\
\text{or equivalently,} \qquad (2.40)\\
\begin{cases}
\mathcal{E} \triangleq \sqrt{\sqrt{\mathcal{F}^2+\mathcal{G}^2} - \mathcal{F}}\\
\mathcal{B} \triangleq \sqrt{\sqrt{\mathcal{F}^2+\mathcal{G}^2} + \mathcal{F}}
\end{cases} \qquad (2.41)
\end{array}}$$

where ${}^*\bar{F}^{\mu\nu} = \frac{1}{2}\epsilon^{\mu\nu\sigma\rho}\bar{F}_{\sigma\rho}$ is the Hodge dual of the field strength tensor. The χ parameter is the electric field magnitude in Schwinger units in the rest frame of the particle, while

---

[19] We note that in international units $\xi = e\mathcal{A}_0/mc$, it does not involve the Planck constant and therefore does *a priori* not relate to quantum mechanics. However, the connection can be made introducing a typical field frequency ω, so that $\xi \equiv eE_0/\omega mc = eE_0\lambda_C/\hbar\omega$, and $\xi \gtrsim 1$ thus sets the threshold at which coherent multiphoton effects arise (more than one field photon absorption over a Compton length).

[20] As Eq. 2.36 only differs from the vacuum Lagrangian by its fermionic part, photon propagators are unaffected, while fermion propagators are now Green’s functions of the differential operator of Dirac equation in the presence of the background field (see Eq. B.117, see also $\Delta^{0\mathcal{A}}$ in Fig. B.7).

[21] Though we will study non-constant fields, they will be assumed to vary slowly on a Compton scale so that quantum coherency will be confined to spatiotemporal regions in which the field can be treated as constant (Locally Constant Field Approximation, “LCFA”, see *e.g.* [AdQED] for a discussion).

Formal regime	**Name**	**Parameters**	**Physics**
Perturbative in α No field	Vacuum QED	ξ , χ, $\mathcal{E}$, $\mathcal{B} = 0$	Particle scattering
Perturbative in α Perturbative in ξ	Background field QED	$\xi \lesssim 1$ χ, $\mathcal{E}$, $\mathcal{B} \sim 0$	Particle and field photons scattering
Perturbative in α ($\alpha\chi^{2/3}$?) Non-perturbative in ξ	Strong-field QED	$\xi > 1$ χ, $\mathcal{E}$, $\mathcal{B} < 1$	Relativistic many photons field-particles interaction
	Quantum dominated sf-QED	$\xi > 1$ $\chi > 1$ $\mathcal{E}$, $\mathcal{B} < 1$	Many particles creations/annihilations (QED cascades)
	Critical sf-QED	$\xi > 1$ $\chi > 1$ $\mathcal{E}$, $\mathcal{B} \gtrsim 1$	Vacuum polarization and coherent field decay (Schwinger process)
Non-perturbative in α ? Non-perturbative in ξ	Fully non-perturbative sf-QED	$\xi > 1$ $\chi \gtrsim \alpha^{-3/2} \approx 1600$ $\mathcal{E}$, $\mathcal{B} \gtrsim 0$	Breakdown of loop processes hierarchy (Ritus-Narozhny conjecture)

Table 2.1: **Summary of the different considered regimes of strong-field QED**. $\mathcal{E}$ and $\mathcal{B}$ correspond to the electric and magnetic field magnitude in the reference frame in which they are colinear (they vanish for a plane wave).

Let us finally note that the study of loop corrections to the two point functions in sf-QED with constant background fields has lead to the conjecture that the loop expansion is controlled by the parameter $\alpha\chi^{2/3}$ [317–320], instead of simply the fine structure constant α as in a vacuum. If this is true, the perturbative expansion of sf-QED is only relevant so long as $\chi \lesssim \alpha^{-3/2} \approx 1600$, past which one enters the so-called "fully non-perturbative" regime of QED. Little is known about this regime in which all-order loop diagrams would equally contribute to any given process, though one might expect collective effects to play an important role at this scale as the standard particle picture fails. Nevertheless, this scaling behavior technically remains a conjecture to this day, and the asymptotics of sf-QED amplitudes even more so in physical, finite energy background fields is still open [321, 322]. As of today, the high-χ limit therefore still stands as a frontier in the understanding of QED [3].

The presence of coherent photons states hence reveals a stratified structure of electro-

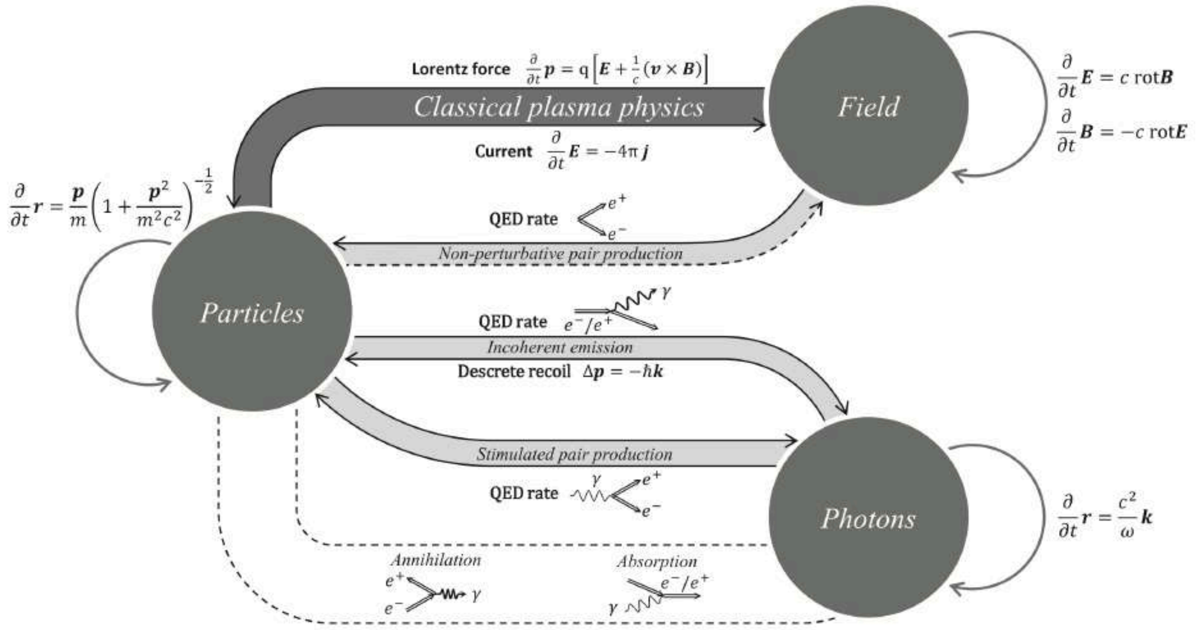

Figure 2.1: **Representation of physical variables and their interactions in a PIC-QED simulation (from [301]).** Circles represent the different mathematical-numerical objects to be computed, arrows show interactions entering in the system evolution. Matter particles and photons move according to their speed, and fields from Maxwell's equations. For charged matter, fields modify speeds through the Lorentz force, and particles generate sources for the fields. Quantum processes relate particles and photon directly, *via* local field values. Dashed arrows stand for discarded quantum processes due to negligible cross-sections (kinematic suppression).

dynamics, where qualitatively different physics succeed each other as the various invariant field strength parameters are increased. For convenience, this classification of the different regimes of electrodynamics is summed up in Table 2.1.

2.2 PIC-QED numerical simulations

The Boltzmann-QED model of strong-field QED has been introduced as a rather natural extension of relativistic classical kinetic theory, providing theoretical ground for an intuitive conception of general field-particles dynamics in strong-field QED. Most decisively, it also allows for numerical solving with virtually no further approximations, or so-called *ab initio* simulations. The underlying algorithm is known as the "Particle-in-Cell" (PIC) method. It has become standard in high-intensity laser research, now admits extensions to include QED events, which will be referred to as "PIC-QED" algorithms. This section will provide a summary of this numerical method. Though significant variations exist in the implementation, the main structure and functions of the algorithm remain quite stable, and will be described first. As the present thesis relied on the WarpX code [323], it will then be discussed briefly.

2.2.1 The PIC-QED algorithm

The general function of a PIC-QED algorithm is to produce numerical solutions to the closed system of partial differential equations Eqs. 2.12-2.17 and 2.21-2.22. An overview of the involved variables and their interactions is shown in Fig. 2.1. The principle of the algorithm is to solve the system by time discretization and iterative solving, allowing to compute quantities at later times from initial time data.

Objects of the algorithm The mathematical distinction between particle distribution functions and the electromagnetic field values numerically translates in two kinds of objects in the algorithm.

Fields values are attached to a discrete set of points in space forming a "grid". The definition of this grid sets the spatial extent of the simulation. Distribution functions are computed by the method of characteristics, that is,

$$f(u_{(t,t_0)}(\mathbf{x}_0),t) = f(\mathbf{x}_0,t_0) \tag{2.42}$$

$$i.e. \begin{cases} f(\mathbf{x},t) \equiv f_0(\mathbf{x}_0) \\ \text{with, } \dfrac{d\mathbf{x}}{dt} = \begin{pmatrix} \dot{\mathbf{r}}(t) \\ \dot{\mathbf{p}}(t) \end{pmatrix} = \begin{pmatrix} \mathbf{p}(t)/m\gamma(\mathbf{p}(t)) \\ q\left[\mathbf{E}(\mathbf{r}(t)) + \dot{\mathbf{r}}(t) \times \mathbf{B}(\mathbf{r}(t))\right] \end{pmatrix} \\ \text{and } \mathbf{x}(t_0) = \mathbf{x}_0 \end{cases} \tag{2.43}$$

Therefore, the distribution function at all times can be computed from the trajectories of a set of particles sampling the initial phase space of the system, weighted by the initial distribution values f_0. The sampling particles are called *macro-particles*[22], and enter the algorithm through the data of their instantaneous position (non-restricted to grid points), momenta components, and "weight" quantifying their contribution to the distribution function values. The value of f at all points is then approximated by interpolation of the macro-particles weight values, with a given interpolation function or "form factor".

Core evolution loop Time evolution is computed in discrete timesteps, chosen small enough for dynamics to be correctly resolved. At each time step, the same workflow is repeated, forming the loop represented in Fig. 2.2 by the yellow boxes (N/E/S/W directions). Let us summarize each of them,

i. **Particle pusher:** The field is known on the particles positions, hence the Lorentz force also. Positions and momenta are then updated *via* Eq. 2.43.

ii. **Current deposition:** The new particles configuration results in new sources for the electromagnetic field. Charges and current on the grid points are then computed with Eqs. 2.16-2.17, by interpolation of the macro-particles on grid points through their form factor.

iii. **Field solver:** Once currents are known on grid points, sources for the fields are as well, and field values at the next time can be computed. There exists different methods to perform this step, or "solvers", defined in terms of the fields directly or their Fourrier transforms.

---

[22] For brevity we will often simply call them "particles" in the following.

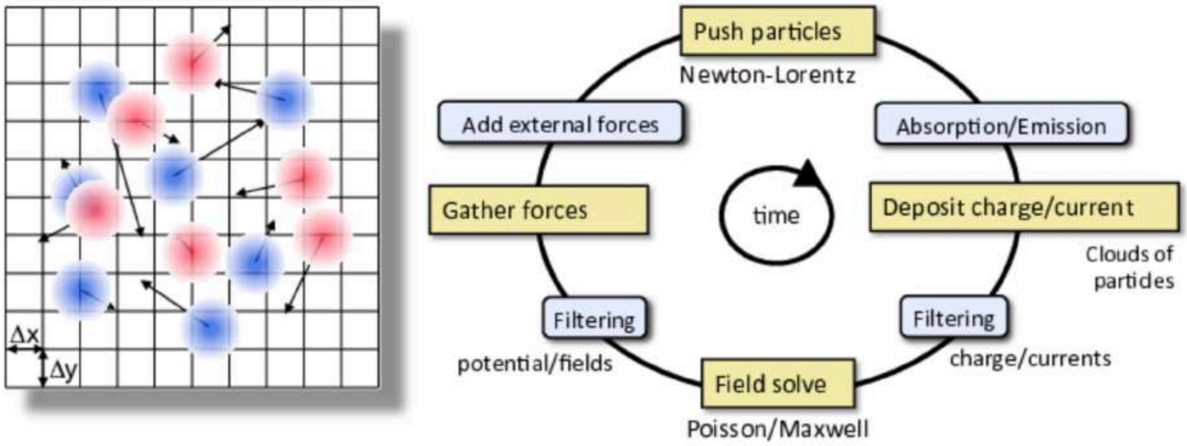

Figure 2.2: **Representation of numerical constituents and schematic workflow of a PIC algorithm (from [323]). (left)** Fields are computed on a set of points in space forming the nodes of a grid with finite resolution, while distribution functions are represented by macro-particles freely moving in space (blue/red dots). Interpolation between grid and macro-particles positions is performed thanks to a particle shape factor (shown in fading color scale). **(right)** Evolution is computed *via* an iterative loop, each represented step being performed in a sequence.

iv. **Field gathering:** The new field configuration results in new values of the Lorentz force on particles. Fields are therefore computed at each macro-particle position using the same interpolation method as in step ii.

Additional modules and QED processes Additional operations can be performed besides the core loop, for instance between each step. Looking at Fig. 2.1, we see that only the (matter) particles-field classical interaction has been described so far ("classical plasma physics", including macro-photons uniform motion at c). All other processes are computed in additional steps in the algorithms, encapsulated in code "modules" (NE/SE/SW/NW directions in Fig. 2.2). Regarding strong-field QED modules more specifically we can list,

a. **Compton scattering and Breit-Wheeler:** The two sf-QED processes expected to dominate are photon emission from an electron or positron (Compton scattering), and decay of a photon into an electron-positron pair (Breit-Wheeler). Both processes only involve one incoming particle and the local field values (LCFA), allowing to compute a probability of occurrence. As a result they can simply be implemented as a step following step i. Following such event if any, macro-particles are created and destroyed as appropriate.

b. **Schwinger pair production:** The process of pair creation from the coherent field directly rather than a high-energy photon, or Schwinger process, can also be accounted for in the PIC loop. Adopting the LCFA, local rates can be computed with an analytical expression. The only subtlety stems from the need to compute all field components at the same grid points, while staggered grids are typically used in PIC codes, motivating to place this step when the field solver acts[23]. When such process occurs, an electron and positron macro-particles are created.

---

[23] This is all the more true for Pseudo-spectral solvers, as fields are then Fourier transformed and can thus be trivially translated in space.

c. **Electromagnetic self-interaction:** One could also account for electromagnetic self-interaction through virtual electron-positron pairs in this framework using effective field equations (Chapter 5). In this case, Maxwell's equations are supplemented with additional source terms non-linear in the local field values. The resulting non-linear equations can then either be solved exactly in the field solver step [196], or linearized assuming the vacuum currents are small.

2.2.2 Implementation in the WarpX code

The WarpX code is an implementation of the PIC-QED algorithm amenable to high-performance computing on state-of-the-art infrastructures. In particular, it is compatible with GPU accelerated nodes. Different implementations of the core PIC loop are available in the code, most notably a Pseudo-Spectral solver, allowing dispersion-free propagation of the electromagnetic field. This last feature was crucial to the study lead in Chapter 9, as in particular the peak intensity reached by a beam comprising ~ 100 harmonics order would be very sensitive to any numerical dispersion.

The QED modules of Compton scattering, Breit-Wheeler and Schwinger pair production were all implemented and tested in the last three years. More detailed information on the QED library can be found in [324]. More general information on the code can be found at [323], and scientific documentation covering its critical features is available in [249–252, 324, 325].

2.3 "Stimulated Vacuum Emission" formalism

When a definite experimental context is given, a theoretical framework designed for it may be used, hopefully cutting in the complexity of the full theory. In this section, the situation we consider is the evolution of an harmonics beam in a vacuum, and we wish predict the effects of its self-interaction through the electron-positron field. Within some realistic conditions, it would be possible to derive an effective classical field theory capturing the electromagnetic evolution, eventually reducible to non-linear corrections to Maxwell's equation[24]. We here adopt another view called "Stimulated Vacuum Emission" (SVE) [303], based on photon creation transition amplitudes, which is simply and consistently defined in terms of fields obeying the classical Maxwell's equations. After presenting this formalism, we dedicate a second section to the definition of the classical data of the harmonics field, which itself proves non-trivial once computational tractability is factored in.

2.3.1 Stimulated Vacuum Emission formalism

A classical field configuration is naturally embedded in Quantum Electrodynamics under the form of a coherent state, and in free theory this correspondence commutes with time evolution [304, 316]. In particular, expectation values of the photon numbers in each mode, of momentum $\mathbf{k}$ and polarisation p, are encoded *via* the modulus of the Fourier coefficients of the classical field, which directly implies they are conserved quantities under Maxwell's action. Together with its experimental readiness, this property makes photon numbers an

---

[24] Chapter 5.

observable suited for detecting couplings to the quantum vacuum, and we therefore wish to compute

$$d^3N_{(p)}(\mathbf{k}) = \langle n_{(p)}(\mathbf{k})\rangle_{\chi_{\mathcal{A}}} - d^3N^{\mathcal{A}}_{(p)}(\mathbf{k}) \tag{2.44}$$

the change in the expectation value of the photon number operator $n_{(p)}(\mathbf{k})$ measured at asymptotically late times taking the coherent state $\chi_{\mathcal{A}}$ as the initial state, compared to the initial photon content $d^3N^{\mathcal{A}}_{(p)}(\mathbf{k})$ associated to the classical field with 4-potential $\mathcal{A}$. Following [303], we discard the marginal effects of coherent multi-photon emission and interference with the classical field to obtain

$$d^3N_{(p)}(\mathbf{k}) \equiv \frac{d\mathbf{k}}{(2\pi)^3}\left|S_{(p)}(\mathbf{k})\right|^2 \tag{2.45}$$

$$\text{with, } S_{(p)}(\mathbf{k}) = \langle\gamma_{(p)}(\mathbf{k})|\Gamma^{\mathcal{A}}_{\text{int}}\left[a(x)\right]|0\rangle \tag{2.46}$$

where $|\gamma_{(p)}(\mathbf{k})\rangle = a^\dagger_{(p)}(\mathbf{k})\,|0\rangle$ is the $(\mathbf{k}, p)$ mode 1-photon state vector, and $\Gamma^{\mathcal{A}}_{\text{int}}\left[a(x)\right]$ the effective interaction operator encoding couplings of the dynamical (operator-valued) photon field $a(x)$ with other fields for the initial state $\chi_{\mathcal{A}}$.

From orthogonality of the photon basis we can furthermore write [326],

$$S_{(p)}(\mathbf{k}) = \left\langle \gamma_{(p)}(\mathbf{k}) \left| \int d^4x \frac{\delta\Gamma^{\mathcal{A}}_{\text{int}}}{\delta a^\mu(x)}\right|_{a=0} a^\mu(x) \left| 0 \right.\right\rangle \tag{2.47}$$

or expressing a^μ in Lorenz gauge,

$$S_{(p)}(\mathbf{k}) = \frac{\varepsilon^{\mu *}_{(p)}(\mathbf{k})}{(2\pi)^3\sqrt{2\mathrm{k}}}\int d^4x e^{-i(\mathrm{k}t - \mathbf{k}\cdot\mathbf{x})}\left.\frac{\delta\Gamma^{\mathcal{A}}_{\text{int}}}{\delta a^\mu(x)}\right|_{a=0}, \text{ for } \mathrm{k} = \|\mathbf{k}\| \tag{2.48}$$

Within QED, in the limit of slowly varying classical electromagnetic fields, retaining only the dominant interaction with the electron field then leads to the identification of $\Gamma^{\mathcal{A}}_{\text{int}}$ with the 1-loop Heisenberg-Euler action [86, 327, 328], at first order in $\alpha = e^2/4\pi$ and nonperturbatively in the classical field strength $F_{\mathcal{A}}$. In such fields varying on characteristic spatio-temporal scales

$$\lambda \gg 1/m$$

subleading derivative corrections which scale as $\sim 1/(m\lambda)^2$ can be safely neglected, such that

$$\Gamma^{\mathcal{A}}_{\text{int}} \simeq \int d^4x \mathcal{L}^{\text{HE}}_{\text{int}}(F)|_{F\to F_{\mathcal{A}}(x)+f(x)}$$

with constant-field Heisenberg-Euler interaction Lagrangian $\mathcal{L}^{\text{HE}}_{\text{int}}$ and quantized photon field f. Taking as polarization vectors $\varepsilon^\mu_p(\mathbf{k}) = (0, \mathbf{e}_p(\mathbf{k}))$ with $p \in \{1, 2\}$ such that $(\mathbf{k}/\mathrm{k}, \mathbf{e}_1(\mathbf{k}), \mathbf{e}_2(\mathbf{k}))$ forms a direct orthonormal basis, the amplitudes reduce to

$$S_{(p)}(\mathbf{k}) = i\sqrt{\frac{\mathrm{k}}{2}}\int d^4x e^{-i(\mathrm{k}t-\mathbf{k}\cdot\mathbf{x})}\left[\mathbf{e}_p(\mathbf{k})\cdot\mathbf{P}(x) + \mathbf{e}_{p+1}(\mathbf{k})\cdot\mathbf{M}(x)\right] \tag{2.49}$$

with formal convention $\mathbf{e}_{p+2} = -\mathbf{e}_p$, and defining $\mathbf{P} = \frac{\partial\mathcal{L}^{\text{HE}}_{\text{int}}}{\partial\mathbf{E}}$ and $\mathbf{M} = \frac{\partial\mathcal{L}^{\text{HE}}_{\text{int}}}{\partial\mathbf{B}}$ the induced vacuum polarisation and magnetisation.

We finally restrict ourselves to field strengths $F \ll F_S$, so that up to $\mathcal{O}(F^2/F_S^2)$ corrections we have,

$$\mathcal{L}^{\text{HE}}_{\text{int}} \simeq \frac{m^4}{8\pi^2}\left(\frac{e}{m^2}\right)^4\left[4\mathcal{F}^2 + 7\mathcal{G}^2\right] \tag{2.50}$$

where we remind $\mathcal{F} = \frac{1}{2}(\mathbf{B}^2 - \mathbf{E}^2)$ and $\mathcal{G} = -\mathbf{B} \cdot \mathbf{E}$ are the gauge and Lorentz-invariants of the field.

The number of Schwinger pair creation events was besides estimated assuming no particles-field retro-action, by integrating the local production rate derived from the non-perturbative form of $\mathcal{L}_{\text{int}}^{\text{HE}}$ in the simulated space-time volume, as proposed *e.g.* in ref. [199, 296]:

$$N_S \equiv \frac{1}{4\pi^2} \lambda\!\!\!^{-}_C{}^{-4} \int d^4x \; \mathcal{E}\mathcal{B} \coth\left(\frac{\pi\mathcal{B}}{\mathcal{E}}\right) \exp\left(-\frac{\pi}{\mathcal{E}}\right) \tag{2.51}$$

where $\lambda\!\!\!^{-}_C = \hbar/mc$ is the reduced Compton length of the electron and

$$\mathcal{E} = \frac{1}{F_S}\sqrt{\sqrt{\mathcal{F}^2 + \mathcal{G}^2} + \mathcal{F}},\; \mathcal{B} = \frac{1}{F_S}\sqrt{\sqrt{\mathcal{F}^2 + \mathcal{G}^2} - \mathcal{F}} \tag{2.52}$$

The conditions of validity of this approach are further discussed in sec. 8.2.

2.3.2 Numerical implementation

The accurate estimation of the quantities of interest Eqs. 2.44 and 2.51 for arbitrary field configurations can be performed numerically. In order to achieve this we developed and optimized a code able to run on large scale parallel computing infrastructures.

Here, we give the general principle of this algorithm, similar in nature to the one presented in [297, 326]. Let us focus on the computation of Eq. 2.49, which amounts to a four dimensional on-shell ($k^0 = \|\mathbf{k}\|$) Fourier transform of third degree polynomials in the $\mathbf{E}$ and $\mathbf{B}$ fields values. We numerically estimate it by performing 3D space parallel fast Fourier transforms of the sources $\mathbf{P}$ and $\mathbf{M}$ from position to momentum space at each timestep t_j, followed by a 1D time integration of all these contributions multiplied by the appropriate phase factor, namely

$$S_{(p)}(\mathbf{k}) \equiv i\sqrt{\frac{\mathrm{k}}{2}}\left[\mathbf{e}_p(\mathbf{k}) \cdot \widetilde{\mathbf{P}}(\mathbf{k}) + \mathbf{e}_{p+1}(\mathbf{k}) \cdot \widetilde{\mathbf{M}}(\mathbf{k})\right] \tag{2.53}$$

$$\text{where } e.g.\ \widetilde{\mathbf{P}}(\mathbf{k}) \simeq \sum_{j=0}^{N_t} e^{-ikt_j} \mathrm{FFT}_3\left[\mathbf{P}(\mathbf{E}(t_j), \mathbf{B}(t_j))\right] \Delta t \tag{2.54}$$

Field values at time t_j are accessed by exact Maxwell propagation of an initial field configuration performed *via* 3D spatial Fourier transforms (plane wave decomposition). The computational cost of these simulations stems from the inherently tridimensional nature of the source fields $\mathbf{P}$ and $\mathbf{M}$, and from the necessity to resolve all spacetime scales from the total beam focusing length and pulse duration to the highest frequency content of the field. In the case of the harmonic beams, this imposes the use of a supercomputer[25].

Several observables of interest are finally extracted from the photon emission amplitudes that will be used as figures of merit for the different configurations:

- N_t, the total number of scattered photons
- $N_\perp$, the total number of photons emitted with polarization crossed to the main polarization direction of the driving beam, typically identifiable as its polarization direction at focus in all cases we consider

---

[25] Chapter 6.

- $N^{>}_{t,\perp}$, the corresponding quantities of *discernible* photons, generically defined as those emitted outside of the opening cones of the driving beams, as commonly done in this context [303, 326, 329], with some more detailed criteria that will be specified in each case of study.

2.3.3 A computationally tractable model of the harmonics field

The above described procedure involves an initialisation step, consisting in defining the field configuration in space at some given time and computing its amplitude for a given total energy. The careful definition of this initial condition is all the more important because, as explicit in Eq. 2.50, QED effects depend on the Lorentz invariants of the field, which can strongly reflect even minor variations in the field structure, as in particular they would strictly vanish for a plane wave. The investigation of the robustness of the simulation results upon specific choices in the numerical procedure details and involved approximations is carried out in Chapter 3. For our primary concern here, namely all simulations involving harmonics, initial beam configurations were defined by $A(\omega)$, the time spectrum of their main field component on-axis in a given plane $x = x_0$, under the assumption that each monochromatic component has a Gaussian spatial profile, given by the paraxial expressions of the Gaussian beam $E_{px}(\mathbf{x}, \omega)$ [330] and characterized by its waist and radius of curvature in plane $x = x_0$. The initial field is then reconstructed by summing over all monochromatic contributions,

$$E(\mathbf{x}, t_0) \equiv \sum_{\omega} e^{-i\omega t_0} E_{px}(\mathbf{x}, \omega) A(\omega) \tag{2.55}$$

The above field profiles being built from paraxial expressions, they do not exactly satisfy vacuum Maxwell's equations, we hence made the choice to project them on the exact solution space by dropping all longitudinal field components (*i.e.* making it divergence free) *via*,

$$\begin{cases} \mathbf{E}(\mathbf{k}) \equiv a_1(\mathbf{k})\mathbf{e}_1(\mathbf{k}) + a_2(\mathbf{k})\mathbf{e}_2(\mathbf{k}) \\ \mathbf{B}(\mathbf{k}) \equiv a_1(\mathbf{k})\mathbf{e}_2(\mathbf{k}) - a_2(\mathbf{k})\mathbf{e}_1(\mathbf{k}) \end{cases}, \text{ with } a_p(\mathbf{k}) = \mathbf{e}_p(\mathbf{k}) \cdot \mathbf{E}(\mathbf{k}) \tag{2.56}$$

Note that for accurate harmonics spectrum data, which can contain much more than a hundred frequency sampling points, equation (2.55) can prove computationally intensive. For 3-d field profiles, which are required as soon as non-symmetrical expressions for the field are used – *e.g.* the paraxial Lax series beyond order 0 – the induced overhead indeed prohibited any practical simulation for our most detailed spectral data. However it was found that, in our conditions, where in particular all initial configurations can be quantitatively well-approximated by summing 0-th order gaussian beams, the above-described procedure (2.56) projects configurations built from paraxial series expressions of any order on manifestly equivalent initial conditions. It therefore was possible to cut the initialization time drastically, by first computing (2.55) with 2-d 0-th order profiles, reconstruct the 3-d field by the assumed axisymmetry, and then apply (2.56).

Abstract of Part II

Our computation of vacuum processes is made possible in this part, *via* our study both of numerical and theoretical elements of vacuum strong-field Quantum Electrodynamics and relativistic plasma mirror light.

Chapter 3 presents an extensive numerical validation of our implementation of the Stimulated Vacuum Emission algorithm. Furthermore, seemingly equivalent numerical options were tested, evidencing a sizeable sensitivity in some cases.

Chapter 4 provides an explicit derivation of the analytical expression of the number of photons scattered in RPM light as a function of the harmonic spectrum (Eq. 8.2), leveraging on the solvable case of a Gaussian pulse.

Chapter 5 discusses the relation between our amplitude-based calculation of vacuum photon scattering and the resolution of effective field equations. Different types of expansions in quantum effective theories of electromagnetism are distinguished, specifying a role of non-perturbative solutions of approximate equations of motion.

Chapter 6 provides estimates of the computational cost of Stimulated Vacuum Emission simulations.

Chapter 7 provides lineouts of the PIC simulation field temporal spectra used to model RPM light in our work.

Part II

Theoretical and numerical studies for vacuum strong-field Quantum Electrodynamics

CHAPTER 3

Stimulated vacuum emission algorithm validation on reference configurations

For better comparison with existing literature [297, 326] and understanding of the RPM light case, results of our SVE code on four reference cases are presented in the following. As the expected results for each of our observables are known, we could use them to validate our algorithm, and in particular study the impact of different propagation and initialization procedures.

To that end, field values at any time are accessed using two different methods. Either explicit analytical expressions of the fields are used, derived from the paraxial series expansion [330] taken, unless explicitly specified otherwise, at fifth order and supplemented with a Gaussian time envelope; or by exact Maxwell propagation of an initial field configuration *via* 3D fast Fourier transforms, as described in previous section. In the following, we will refer to these mehtods as C_{px} and C_{ex} respectively[1]. In reference cases *i)*, *ii)* and *iv)* as defined in the introduction, purely numerical results have been supplemented with semi-analytical computations of the amplitudes C_{al}, where only a 1-dimensional space integral is left to perform numerically, providing another independent validation of the code.

All these procedures involve an initialisation step, consisting in defining the spatial field profile at some given time and computing its amplitude for a given total energy. For procedure C_{ex}, which involves exact Maxwell propagation, this step is used also to define the initial condition entering our Maxwell solver and therefore received further attention. For this purpose four different initialisation modes were tested, either in (f) or out (of) of focus, using either monochromatic paraxial expressions supplemented with a time-envelope, $E(\mathbf{x},t) = e^{-i\omega_0 t}E_{px}(\mathbf{x},\omega_0)a(t-x)$ (m), or defining the corresponding time spectrum and summing over all monochromatic contributions, $E(\mathbf{x},t) = \sum_\omega e^{-i\omega t}E_{px}(\mathbf{x},\omega)a(\omega)$ (p); we denote them respectively I_{m-f}, I_{p-f}, I_{m-of} and I_{p-of}. The projection prescription (2.56) was then applied in all cases. We note that procedure C_{ex}-I_{p-of} corresponds to the default one described in 2.3.3; it indeed stands as the most accurate and general, and is actually necessary to address all cases involving RPM beams.

3.1 Counterpropagating infrared pulses

Let us start with the reference case of two counter-propagating identical Gaussian pulses [297, 303, 326, 331, 332]. The importance of this configuration becomes clear noticing that the field invariants entering the Heisenberg-Euler Lagrangian Eq. 2.50 identically vanish for a plane wave, making the field of a single loosely focused laser *a priori* very

---

[1] The px and ex indices stand for "paraxial" and "exact" respectively.

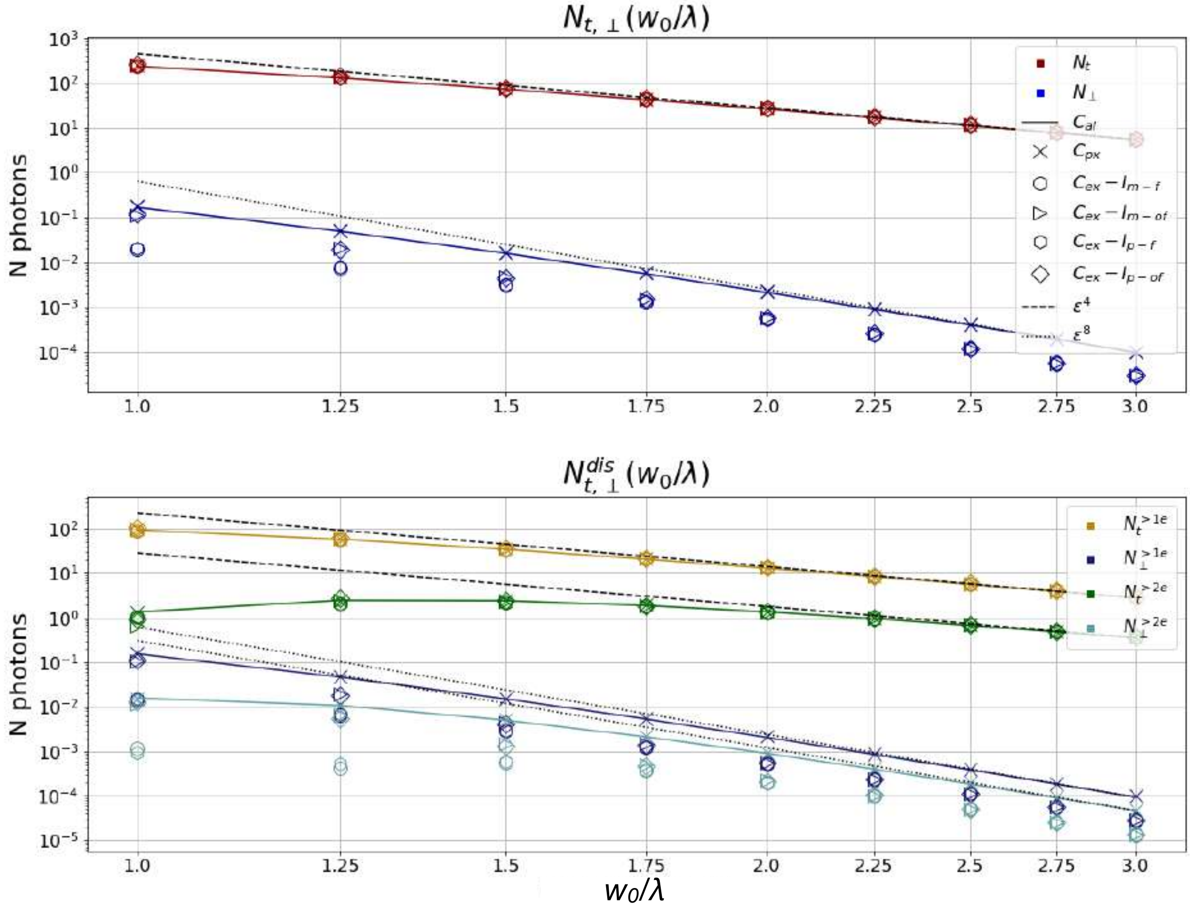

Figure 3.1: **Integrated photon numbers as a function of w_0 for two counter-propagating Gaussian pulses. (up)** Total number of photons N_t and photons with crossed-polarization $N_\perp$, for the different computation modes. **(bottom)** Total numbers of discernible photons, emitted outside of the $\theta = \arcsin(\varepsilon)$ (>1e) or $\theta = \arcsin(2\varepsilon)$ (>2e) cones directed along both pulses propagation directions.

sub-optimal for observing quantum vacuum effects. The transient standing wave obtained simply by crossing two such laser pulses on the opposite yields near maximal invariants for the same total energy, and therefore provides a landmark for the achievable signal in all-optical frequencies setups.

We considered two counterpropagating pulses with parameters typical of a Petawatt-class system [5], with the same linear polarization, wavelength $\lambda_0 = 800$ nm, $W = 25$ J respective energy, $\tau = 25$ fs duration considering a field time profile on-axis of the form:

$$E(t) \equiv E e^{-\frac{(t-x)^2}{(\tau/2)^2}} \tag{3.1}$$

and identical waist at focus $w_0 = \frac{\lambda_0}{\pi}\frac{1}{\varepsilon}$, where $\varepsilon \lesssim 1/\pi$ is the diffraction parameter.

The resulting values of the total and discernible photon numbers are plotted in Figure 3.1 for several waists at focus, using the different computation methods introduced in sec. 2.2. Here we define two discernible populations, respectively denoted by a >1e (>2e) superscript, scattered at an angle $\theta = \sphericalangle(\mathbf{e}_x, \mathbf{k})$ with the optical axis greater than $\theta_1 = \arcsin(\varepsilon)$ ($\theta_2 = \arcsin(2\varepsilon)$), which corresponds to a background laser photon density drop off of at least $1/e^2$ ($1/e^8$) in a gaussian pulse model. We observe a remarkable consistency between all methods for the polarization-insensitive photon number, from the analytical to the fully numerical calculations, with a standard deviation of 4.9 %, displaying the expected ε^4 scaling. This provides a first evidence for the validity of the code. Moreover, the maximum total photon number obtained in this case from $C_{ex} - I_{p-f}$, numerical Maxwell propagation with initialization at focus, is $N_t = 241.1$, consistent within 7 % error with the value $N_t = 260.4$ obtained by the authors of [297] with exactly the same method. The same holds true for the polarization-insensitive discernible photon numbers, now with standard deviations of 6.4 % and 6.5 % respectively, and maximum values of $N_t^{>1e} = 108.6$, $N_t^{>2e} = 2.756$ for $C_{ex} - I_{p-of}$. Comparing $N_t^{>1e}$ with the corresponding value computed in [326] gives a better than 1 % level agreement.

Regarding crossed-polarized photons, we again find agreement between the analytical and numerical calculation C_{px} where the paraxial expressions with time-envelope are used to define the field at each time step, including the asymptotic ε^8 dependency, for the total and discernible numbers, with standard deviations close to 0.5 % in each case. All C_{ex} computations however consistently display lower values at weak focusings for total and discernible photons, while maintaining the same ε scaling; at strong focusings, out of focus initialization procedures converge towards the common C_{al} and C_{px} result within at most 30 %, while numerical computations initialized at focus both give a value about one order of magnitude smaller. The common maximum crossed-polarized photon numbers obtained for the converging computations are, giving the $C_{ex-p-of}$ values for definiteness, $N_\perp = 1.176 \times 10^{-1}$, $N_\perp^{>1e} = 1.104 \times 10^{-1}$ (about 60 % of the value in [326]), $N_\perp^{>2e} = 1.321 \times 10^{-2}$. This illustrates the sensitivity of this problem to even minor field variations, here especially manifest for the crossed-polarization photons. Indeed, the analytical expressions reveal that while N_t and $N_\perp$ stem from the same field integral, $d^3 N_\perp$ is suppressed near axis by an additional factor $\propto \sin^4 \theta$, making it more dependent on the higher transverse modes of the source, or equivalently on the transverse field profiles details.

3.2 Single infrared pulse

We now consider the photon emission from a single focused Gaussian beam [297, 333], with wavelength $\lambda_0 = 800$ nm, duration $\tau = 25$ fs, and energy $W = 50$ J for easier comparison with the previous case. In this case the nonvanishing Lorentz invariants stem from field components beyond the main polarization direction, associated to higher powers of ε in the paraxial series expansion, and therefore to an overall much weaker signal than with *e.g.* two beams crossing at an angle. The results are depicted in Fig. 3.2. For the maximum total photon numbers we obtain, always giving the $C_{ex} - I_{p-of}$ value, $N_t = 4.196 \times 10^{-3}$ ($N_\perp = 7.275 \times 10^{-5}$), with a standard deviation of 28 % (17 %) between all the different methods at $w_0 = \lambda_0$. We once again find a very good agreement between paraxial and analytical calculations, of about 5 % standard deviation, recovering in particular the ε^8 scaling expected from the analytical calculation based on the order 2 paraxial field expression [330]. We note an agreement within one order of magnitude with previous results on this configuration [297], while an exact matching is made less likely in this case by the sensitivity to the field structure beyond zeroth order paraxial approximation; for the procedure $C_{ex} - I_{m-f}$ closest to the one described in this reference we nevertheless find a close to 20 % agreement on N_t. We also find consistency of the different C_{ex} results between themselves, and with C_{al} and C_{px} for the polarization-insensitive numbers, while the C_{ex} procedure gives smaller numbers of crossed-polarized photons at weak focusing.

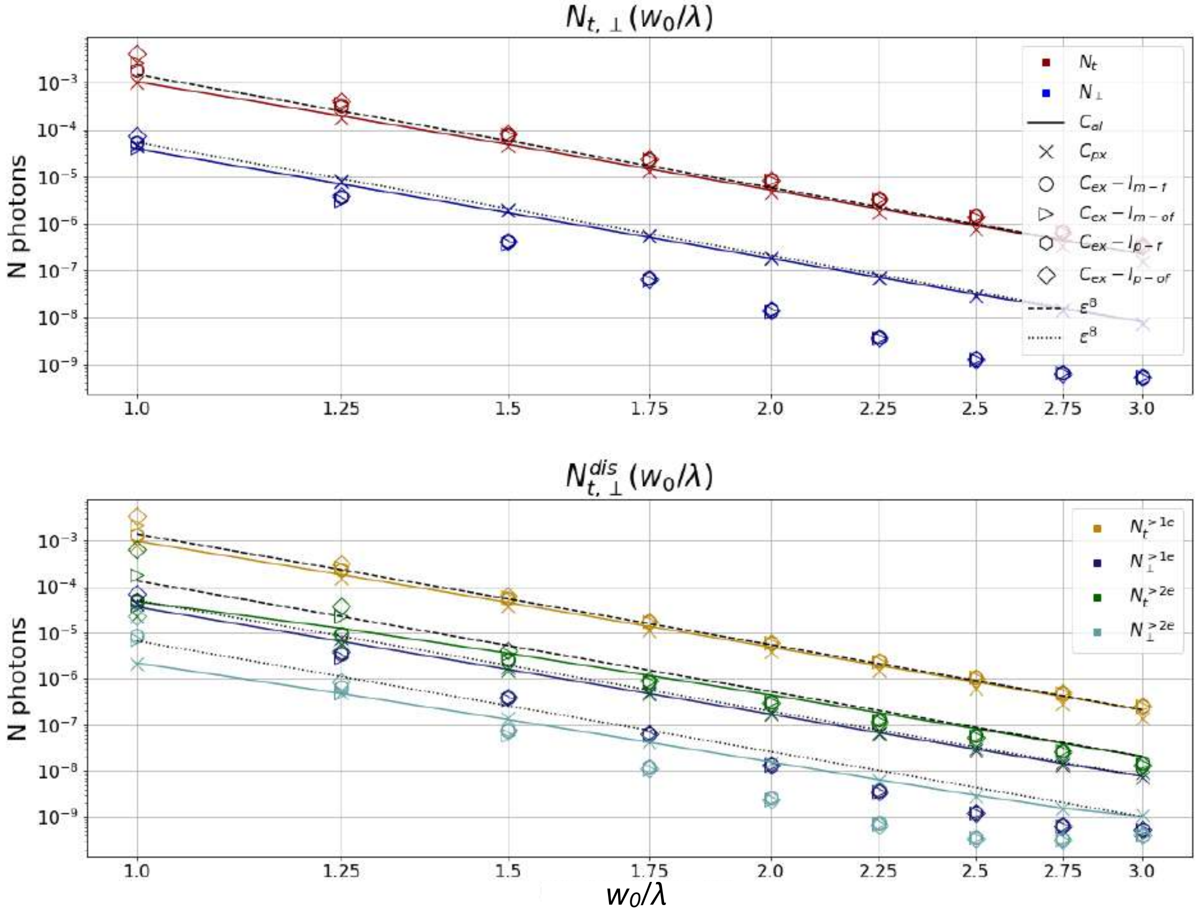

Figure 3.2: **Integrated photon numbers as a function of w_0 for a single Gaussian pulse. (up)** Total number of photons N_t and with crossed-polarization $N_\perp$, for the different computation modes. **(bottom)** Total numbers of discernible photons, emitted outside of the $\theta = \arcsin(\varepsilon)$ (>1e) or $\theta = \arcsin(2\varepsilon)$ (>2e) cones directed along the pulse propagation direction.

Defining discernible photons as in the two pulses case, we find at diffraction limit (*i.e.* $\varepsilon = 1/\pi$) $N_t^{>1e} = 3.492 \times 10^{-3}$ ($N_\perp^{>1e} = 7.032 \times 10^{-5}$), and $N_t^{>2e} = 6.486 \times 10^{-4}$ ($N_\perp^{>2e} = 2.286 \times 10^{-5}$).

Assuming a laser repetition rate comprised between 0.1 and 10 Hz, a realistic bound for upcoming Petawatt-class laser systems [5, 334], these results indicate that emitting a single discernible photon would require between a few minutes and several hours of accumulated operation time, so that building a clear signal in controlled conditions seems unfeasible with this single pulse configuration. In the following, we consider different ways to enhance this very low baseline signal without requiring the stringent space and time overlap of several focused ultra-intense sources.

3.3 Infrared pulse in a monochromatic wave

As a final reference case we consider a focused Gaussian pulse identical to the one of sec III.B, coupled to an ambient monochromatic plane wave. This setting aims at decorrelating the discernibility constraint from the intense field photon distribution, likely difficult to finely control, by trying to detect instead the photons of a well-controlled collimated source scattered off the intense field region. We consider the same focused beam as before, a Gaussian pulse of wavelength $\lambda_0 = 800$ nm, duration $\tau = 25$ fs, energy $W = 50$ J energy, and a plane wave of amplitude of $E = 5 \times 10^{-5} E_S$ which would correspond *e.g.* to a 200 TW laser focused at $w_0 = 3.32$ μm. Such configuration *a priori* depends non-trivially on the diffraction parameter of the focused beam, the angle $\theta_c = \sphericalangle(\mathbf{k}_0, \mathbf{k}_p)$ between the wave vector of each beam, and the frequency difference between them. In Fig. 3.3 we plot the dependence with respect to the angle and frequency, taking the focused beam at diffraction limit. The first feature of these results is the quasi-independence of the probe frequency and numbers of photons produced, very clear for the total photon numbers and more obfuscated in the discernible photon numbers due to higher variability of these calculations, although no alternative trend clearly appears. Regarding the collision angle dependence, for C_{ex} all photon numbers are maximized close to counter-propagation, while a maximum in crossed-polarized photon number is observed around $\theta_c \simeq 130°$ for the paraxial calculations, confirming similar observations in previous works [297]. Moreover, we note the very slow variation of the photon number around $\theta = 180°$, analytically found to follow $N_{t,\perp}(\theta_c) \overset{\theta_c \to \pi}{\sim} \sin^2 \frac{\theta_c}{2} . N_{t,\perp}|_{\theta_c = \pi}$, so that collision angles up to 135° can be considered to yield near-optimal photon signal. We obtain maximum photon numbers equal within less than 10 % for all probe frequencies, of $N_t = 376.6$ ($N_\perp = 1.507$), $N_t^{>1e} = 37.76$ ($N_\perp^{>1e} = 9.611 \times 10^{-1}$) and $N_t^{>2e} = 1.110$ ($N_\perp^{>2e} = 4.777 \times 10^{-2}$) giving the $C_{ex} - I_{p-of}$ values. However, we can only give credit to the relative values of these numbers, as the computation was done for a plane wave of infinite duration; we defer the numerical simulation of more realistic bounded field configurations to sec. 8.3.

3.4 Single multi-frequency beam

Regarding the photon number dependence with w_0, we observe seemingly the same trends as in the single frequency case, as Fig. 3.4 displays for $n = 2$ and $n_h = 3$. The enhancements factors with respect to the single frequency case are of $a_t^{n_h=2} = 3.17$ ($a_\perp^{n_h=2} = 6.04$) for two harmonics and of $a_t^{n_h=3} = 7.29$ ($a_\perp^{n_h=3} = 12.47$) for three. We once again find good agreement between the C_{px} and semi-analytical calculation for total photon numbers, which is lost for the discernible photon numbers though.

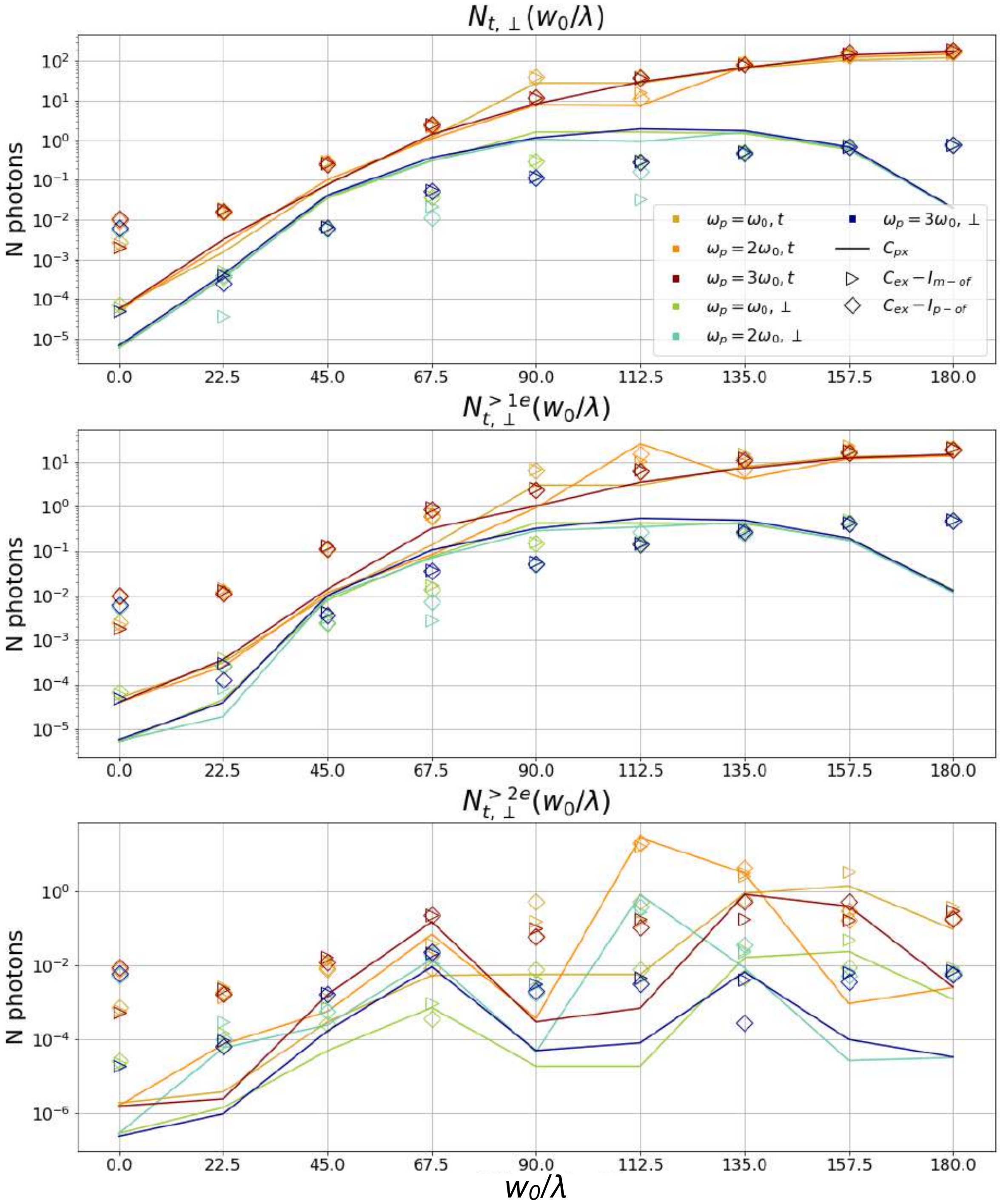

Figure 3.3: **Integrated photon numbers as a function of θ_c for a beam focused at diffraction limit in a plane wave. (up)** Total number of photons N_t or with crossed-polarization $N_\perp$, for the different computation modes. Total numbers of discernible photons, emitted outside of the $\theta = \arcsin(\varepsilon)$ **(middle)** or $\theta = \arcsin(2\varepsilon)$ **(bottom)** cones directed along the beam propagation direction.

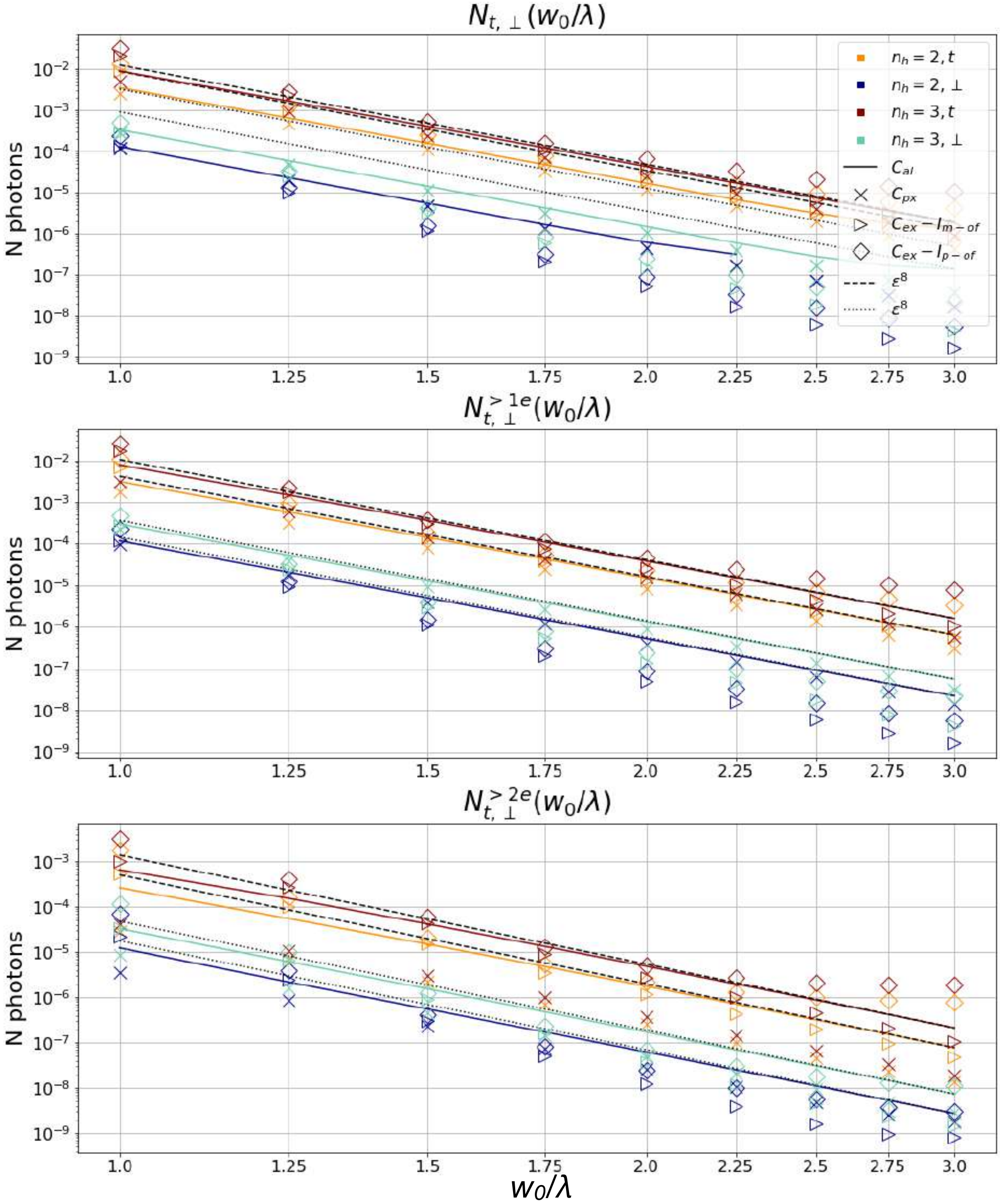

Figure 3.4: **Integrated photon numbers as a function of w_0 for a beam made of either two or three harmonics of its fundamental frequency, with equal amplitudes at focus.** **(up)** Total number of photons N_t or with crossed-polarization $N_\perp$, for the different computation modes. Total numbers of discernible photons, emitted outside of the $\theta = \arcsin(\varepsilon)$ **(middle)** or $\theta = \arcsin(2\varepsilon)$ **(bottom)** cones directed along the beam propagation direction.

Chapter 4

Analytical estimate of the RPM-light beam self-scattering

The full-scale numerical calculation of photon scattering within a focused plasma mirror generated beam is very computationally expensive, while the parameter space describing such RPM fields is at least as vast as the set of realistic spectra. As a consequence, a numerical derivation of scaling laws governing RPM-light self-scattering is practically impossible. On the other hand, an accurate analytical modelling of the field proves difficult as well, and the subsequent photon scattering amplitudes calculation rather deterring in any case.

We can nevertheless find guidance in analytical expressions adopting simple assumptions regarding the RPM light field, assimilated to a train of Gaussian pulses. Though quantitative predictions seem out of reach in this way, general trends can be derived for relevant quantities as a function of the beam parameters, including a quite flexible description of the RPM light spectral profile. This chapter exposes this calculation in detail. The self-scattering of a focused finite duration Gaussian pulse is presented first, the RPM light case is then treated leveraging on this result.

4.1 Study of a single focused Gaussian pulse

We primarily wish to compute the photon scattering amplitudes Eq. 2.49 for a single ultra-short laser pulse focused in a vacuum. This will here be achieved following the SVE method [303].

In the course of this calculation, the introduction of adimensional quantities will simplify some expression. We will therefore adopt the Lorentz-Heaviside units with $c = \hbar = 1$. The most general problem of vacuum QED photon emission only has one dimensional scale, the electron mass $m = 511$ keV $= 2,43.10^{-12}$ m $= 8,10.10^{-21}$ s, from which derives $E_S = \frac{m^2}{e} = 1,32.10^{18}$ V.m^{-1} $= 4,41.10^{9}$ T $(= 8,62.10^{5}$ keV$^2)$. Considering Gaussian pulses in particular, it is convenient to beside use the central wavenumber k_0 as the spatio-temporal scale. In the following, all quantities can be considered adimensionnalized in this way[1]. We finally introduce $\tilde{S} = k_0^{3/2} S$, the adimensional amplitudes such that $dN \propto |S|^2 d^3k = |\tilde{S}|^2 d^3\tilde{k}$.

4.1.1 Field and photon sources definition

In accordance with a widespread model of ultra-intense laser beams, we consider the field of a Gaussian beam under the paraxial approximation. Retaining the lowest order terms giving a non-zero contribution to the "stimulated vacuum emission", we will be working at second order in the paraxial expansion parameter, $\varepsilon = \frac{2}{k_0 w_0}$.

---

[1] Setting explicitly $\mathrm{k}_0 \equiv 1$ in expressions if needed.

A linearly polarized pulse along the z axis propagating along the growing x direction is then expressed as,

$$\mathbf{E} = E \left| \begin{array}{l} \varepsilon\xi c_1 \\ -\varepsilon^2\xi\nu s_2 \\ s_0 + \varepsilon^2\left[\xi^2 s_2 - \dfrac{\rho^4}{4}s_3\right] \end{array} \right. ;\ \mathbf{B} = E \left| \begin{array}{l} \varepsilon\nu c_1 \\ -s_0 - \varepsilon^2\left[\dfrac{\rho^2}{2}s_2 - \dfrac{\rho^4}{4}s_3\right] \\ 0 \end{array} \right. \tag{4.1}$$

$$\begin{aligned}
&\text{with, } E = E_0\frac{e^{-r^2/w^2}}{u},\ w = w_0\sqrt{1+x^2/x_R^2} \equiv w_0 u \\
&\qquad \xi = \frac{z}{w_0};\ \nu = -\frac{y}{w_0};\ \rho = \sqrt{\xi^2+\nu^2} \\
&\text{and, } \phi = -k_0(t-x) - \arctan(x/x_R) + \frac{xr^2}{x_R w^2} - \phi_0 \\
&\qquad \phi_g = -\arctan(x/x_R) \\
&\qquad c_n = \frac{1}{u^n}\cos(\phi + n\phi_g);\ s_n = \frac{1}{u^n}\sin(\phi + n\phi_g)
\end{aligned} \tag{4.2}$$

Let us then express the corresponding field invariants,

$$\begin{cases} \mathcal{F} \triangleq \dfrac{1}{2}\left(B^2 - E^2\right) & (4.3) \\ \mathcal{G} \triangleq -\mathbf{E}\cdot\mathbf{B} & (4.4) \end{cases}$$

First,

$$\begin{aligned}
\mathcal{F} = \frac{E^2}{2}\Bigg\{&\left(s_0 + \varepsilon^2\left[\frac{\xi^2+\nu^2}{2}s_2 - \frac{\rho^4 s_3}{4}\right]\right)^2 + \varepsilon^2\nu^2c_1^2 \\
&\qquad - \left(s_0 + \varepsilon^2\left[\xi^2 s_2 - \frac{\rho^4 s_3}{4}\right]\right)^2 - \varepsilon^2\xi^2c_1^2\Bigg\} \\
= \varepsilon^2 E^2 &\frac{\nu^2-\xi^2}{2}\left\{s_0 s_2 + c_1^2\right\}
\end{aligned}$$

Second,

$$\begin{aligned}
\mathcal{G} &= -E^2\left\{(\varepsilon\xi c_1).(\varepsilon\nu c_1) + \left(-s_0 - \varepsilon^2\left[\frac{\xi^2+\nu^2}{2}s_2 - \frac{\rho^4 s_3}{4}\right]\right).(-\varepsilon^2\xi\nu s_2)\right\} \\
&= -\varepsilon^2E^2\xi\nu\left\{s_0s_2 + c_1^2\right\}
\end{aligned}$$

Now, denoting $\phi_1 = \phi + \phi_g$,

$$\begin{aligned}
s_0s_2 &= \frac{1}{u^2}\left(\sin(\phi_1 - \phi_g)\sin(\phi_1 + \phi_g)\right) \\
&= \frac{1}{u^2}\left(\sin^2(\phi_1)\cos^2(\phi_g) - \cos^2(\phi_1)\sin^2(\phi_g)\right) \\
&= \frac{1}{u^2}\left(\sin^2(\phi_1) - \sin^2(\phi_g)\right) \\
c_1^2 &= \frac{1}{u^2}\cos^2(\phi_1) \\
\text{so that, } s_0s_2 + c_1^2 &= \frac{1}{u^2}\cos^2(\phi_g) \\
&= \frac{1}{u^4}
\end{aligned}$$

We therefore come to,

$$\begin{cases} \mathcal{F} = \varepsilon^2 E_0^2 \dfrac{e^{-2\frac{r^2}{w^2}}}{u^6} . \dfrac{y^2 - z^2}{2w_0^2} & (4.5) \\ \mathcal{G} = \varepsilon^2 E_0^2 \dfrac{e^{-2\frac{r^2}{w^2}}}{u^6} . \dfrac{yz}{w_0^2} & (4.6) \end{cases}$$

The associated polarization and magnetization fields write, in natural units,

$$\begin{cases} \mathbf{P} = -m^2 C_0 (4\mathcal{F}\mathbf{E} + 7\mathcal{G}\mathbf{B}) \\ \mathbf{M} = m^2 C_0 (4\mathcal{F}\mathbf{B} - 7\mathcal{G}\mathbf{E}) \end{cases} , \; C_0 = \frac{1}{90\pi}\sqrt{\frac{\alpha}{\pi}} \simeq 1,7.10^{-4} \tag{4.7}$$

we thus obtain,

$$\mathbf{P} = m^2 C_0 \varepsilon^2 E_0^3 \overbrace{\left| \begin{array}{l} \mathcal{O}(\varepsilon) \\ 7\dfrac{yz}{w_0^2} \\ -4\dfrac{y^2 - z^2}{2w_0^2} \end{array} \right. . \; \frac{e^{-3r^2/w^2}}{u^7} \sin\phi}^{\mathbf{p}} \tag{4.8}$$

$$\mathbf{M} = m^2 C_0 \varepsilon^2 E_0^3 \overbrace{\left| \begin{array}{l} \mathcal{O}(\varepsilon) \\ -4\dfrac{y^2 - z^2}{2w_0^2} \\ -7\dfrac{yz}{w_0^2} \end{array} \right. . \; \frac{e^{-3r^2/w^2}}{u^7} \sin\phi}^{\mathbf{m}} \tag{4.9}$$

Coming to the photon emission amplitudes, we manually add a time envelope $a(\varphi = \mathrm{k}_0(z - t))$ to the field profile, so that we can write,

$$S_p(\mathbf{k}) = i\sqrt{\frac{k}{2}} m^2 C_0 \varepsilon^2 E_0^3 \int d^4x \; e^{ik\cdot x} . a(\varphi)^3 \left(\mathbf{e}_p(\mathbf{k}) \cdot \mathbf{p}(x) + \mathbf{e}_{p+\pi/2}(\mathbf{k}) \cdot \mathbf{m}(x) \right) \tag{4.10}$$

4.1.2 Analytical expression of the amplitudes

Integrals reduction

With the latter conventions we can write the adimensional amplitudes in a spherical coordinate system aligned around the z axis,

$$\mathbf{e}_\theta(\mathbf{k}) = \left| \begin{array}{l} \cos\theta\cos\varphi \\ \cos\theta\sin\varphi \\ -\sin\theta \end{array} \right. ; \; \mathbf{e}_\varphi(\mathbf{k}) = \left| \begin{array}{l} -\sin\varphi \\ \cos\varphi \\ 0 \end{array} \right. \tag{4.11}$$

$$\begin{cases} S_1(\mathbf{k}) = K_0 . \mathrm{k}^{1/2} \left[\tilde{\mathbf{p}}(\mathbf{k}) \cdot \mathbf{e}_\theta(\mathbf{k}) + \tilde{\mathbf{m}}(\mathbf{k}) \cdot \mathbf{e}_\varphi(\mathbf{k}) \right] \\ \\ S_2(\mathbf{k}) = K_0 . \mathrm{k}^{1/2} \left[\tilde{\mathbf{p}}(\mathbf{k}) \cdot \mathbf{e}_\varphi(\mathbf{k}) - \tilde{\mathbf{m}}(\mathbf{k}) \cdot \mathbf{e}_\theta(\mathbf{k}) \right] \end{cases} \tag{4.12}$$

with $K_0 = \frac{i}{\sqrt{2}} \left(\frac{m}{\mathrm{k}_0} \right)^2 C_0 E_0^3 \varepsilon^2$, and tilde denoting on-shell four dimensional Fourier transforms.

According to (5,6) we can further write,

$$\tilde{\mathbf{p}}(\mathbf{k}) \triangleq \begin{vmatrix} 0 \\ 7I_2 \\ 4I_1 \end{vmatrix} \tag{4.13}$$

$$\tilde{\mathbf{m}}(\mathbf{k}) \triangleq \begin{vmatrix} 0 \\ 4I_1 \\ -7I_2 \end{vmatrix} \tag{4.14}$$

where,

$$\begin{cases} I_1 = \int d^4x \ e^{ik\cdot x}.\dfrac{z^2-y^2}{2w_0^2} a(\varphi)^3 \dfrac{e^{-3r^2/w^2}}{u^7} \sin(\phi) \\ I_2 = \int d^4x \ e^{ik\cdot x}.\dfrac{yz}{w_0^2} a(\varphi)^3 \dfrac{e^{-3r^2/w^2}}{u^7} \sin(\phi) \end{cases} \tag{4.15}$$

Now, changing variables as $(y', z') = R_{\pi/4}\left[(y, z)\right]$ in I_1, and taking note of $\mathbf{k}_\perp \cdot \mathbf{x}_\perp = R_\gamma\left[\mathbf{k}_\perp\right] \cdot R_\gamma\left[\mathbf{x}_\perp\right]$, it appears that

$$I_1(\mathbf{k}) = I_2(k_{||}, R_{\pi/4}\left[\mathbf{k}_\perp\right]) \tag{4.16}$$

One can therefore focus on $I_2 \equiv I$.

We further decompose I by shifting to the complex representation of the sine function,

$$\sin x = \frac{e^{ix} - e^{-ix}}{2i}$$

splitting the integral in two simpler ones. Specifically,

$$\begin{aligned} I &= \int d^4x \ e^{ik\cdot x} f(x). \sin\phi \\ &= \frac{1}{2i}\left(\int d^4x \ e^{ik\cdot x + i\phi} f(x) - \int d^4x \ e^{ik\cdot x - i\phi} f(x)\right) \\ &\triangleq \frac{1}{2i}\left(\tilde{I}(k) - \left[\tilde{I}(-k)\right]^*\right) \end{aligned} \tag{4.17}$$

where we used the real character of f for the last line. The calculation thereby comes down to evaluating the quantity $\tilde{I}$.

Explicitly,

$$\boxed{\begin{aligned} \tilde{I} = \int dx. \ \frac{e^{-i(\mathrm{k}_x - \mathrm{k}_0).x}}{\left[1 + x^2/x_R^2\right]^{8/2}}. (1 - ix/x_R) \int dt. e^{i(\mathrm{k} - \varepsilon \mathrm{k}_0).t} a^3(t - x) \\ \times \int dydz. \ \frac{yz}{w_0^2} e^{-\chi(x)/w_0^2.(y^2+z^2) - i\mathrm{k}_y.y - i\mathrm{k}_z.z} \end{aligned}} \tag{4.18}$$

with $\chi(x) = \left(3 - i\frac{x}{x_R}\right)\frac{1}{1+x^2/x_R^2}$.

Evaluation of the integrals

Let us first address the transverse variables y and z. The corresponding integral factorizes,

$$\tilde{I}_\perp = \int dy. \ \frac{y}{w_0} e^{-\chi(x)/w_0^2.y^2 - i\mathrm{k}_y.y} \int dz. \frac{z}{w_0} e^{-\chi(x)/w_0^2.z^2 - i\mathrm{k}_z.z} \tag{4.19}$$

besides,

$$\int du.\ u.e^{-a.u^2+ib.u} = i\frac{\sqrt{\pi}}{2}\frac{b.e^{-\frac{b^2}{4a}}}{a^{3/2}}$$

therefore,

$$\tilde{I}_\perp = \frac{i\sqrt{\pi}}{2w_0}\left(-\mathrm{k}_y\right)\frac{e^{-\frac{w_0^2\mathrm{k}_y^2}{4\chi(x)}}}{\chi(x)^{3/2}}w_0^3 \times \frac{i\sqrt{\pi}}{2w_0}\left(-\mathrm{k}_z\right)\frac{e^{-\frac{w_0^2\mathrm{k}_z^2}{4\chi(x)}}}{\chi(x)^{3/2}}w_0^3 \tag{4.20}$$

i.e.

$$\tilde{I}_\perp = -\frac{\pi}{4}w_0^4.\mathrm{k}_y\mathrm{k}_z\frac{e^{-\frac{w_0^2\mathrm{k}_\perp^2}{4\chi(x)}}}{\chi(x)^3} \tag{4.21}$$

with $\mathrm{k}_\perp^2 = \mathrm{k}_x^2 + \mathrm{k}_y^2$.

We then turn to the time integration, for this purpose we assume a Gaussian envelope of extent τ,

$$a(t-z) \doteq e^{-\frac{(t-x)^2}{\tau^2}} \tag{4.22}$$

so that we only have another Gaussian integral left,

$$\int dt.e^{i(\mathrm{k}-\mathrm{k}_0).t}a^3(t-x) = \int dt.e^{i(\mathrm{k}-\mathrm{k}_0).t-3\frac{(t-x)^2}{\tau^2}} \tag{4.23}$$

$$= e^{i(\mathrm{k}-\mathrm{k}_0).x}\tau\sqrt{\frac{\pi}{3}}e^{-\frac{\tau^2}{12}(\mathrm{k}-\mathrm{k}_0)^2} \tag{4.24}$$

Substituting these results in (18) we are led to,

$$\boxed{\begin{aligned}\tilde{I} = -\tau w_0^4\frac{\pi^{3/2}}{4\sqrt{3}}\mathrm{k}_y\mathrm{k}_z e^{-\frac{\tau^2}{12}(\mathrm{k}-\mathrm{k}_0)^2}\times \\ \int dx.\frac{e^{-i(\mathrm{k}_x-\mathrm{k}).x-\frac{w_0^2\mathrm{k}_\perp^2}{4\chi(x)}}}{(1+(x/x_R)^2)(3-ix/x_R)^3}.(1-ix/x_R)\end{aligned}} \tag{4.25}$$

$$\equiv -\tau w_0^4\frac{\pi^{3/2}}{4\sqrt{3}}\mathrm{k}_y\mathrm{k}_z e^{-\frac{\tau^2}{12}(\mathrm{k}-\mathrm{k}_0)^2}\times J \tag{4.26}$$

$$\text{with } \boxed{J = \int dx.\frac{e^{-i(\mathrm{k}_x-\mathrm{k}).x-\frac{w_0^2\mathrm{k}_\perp^2}{4\chi(x)}}}{(1+(x/x_R)^2)(3-ix/x_R)^3}.(1-ix/x_R)} \tag{4.27}$$

Amplitudes

As a final step we deduce I_1 and I_2 from the $\tilde{I}(k)$ *via* Eqs. 4.13-4.14, and the photon scattering amplitudes and probabilities follow according to,

$$S(\mathbf{k}) = K_0.\mathrm{k}^{1/2}\left|\begin{array}{c}4(\cos\varphi-\sin\theta).I_1 + 7\cos\theta\sin\varphi.I_2 \\ \\ -4\cos\theta\sin\varphi.I_1 + 7(\cos\varphi-\sin\theta).I_2\end{array}\right. \tag{4.28}$$

$$\left\{\begin{aligned}
d\mathrm{N}_{\mathrm{tot}} &= \frac{1}{2025}\frac{\alpha}{3}\left(\frac{m}{\mathrm{k}_0}\right)^4 .E_0^6\varepsilon^4\left(\frac{w_0}{2}\right)^8\tau'^2.\left(\frac{\mathrm{k}}{2}\right)^5 e^{-\frac{\tau'^2}{24}(\mathrm{k}-\mathrm{k}_0)^2} && (4.29)\\
&\times(1-\cos\theta)^2\sin^4\theta\left[n_{\mathcal{F}}^2+(n_{\mathcal{G}}^2-n_{\mathcal{F}}^2)\sin^2(2\varphi)\right]\\
&\times|J|^2\frac{d^3\tilde{\mathrm{k}}}{(2\pi)^3}\\
\\
d\mathrm{N}_{\perp} &= \frac{1}{2025}\frac{\alpha}{3}\left(\frac{m}{\mathrm{k}_0}\right)^4 .E_0^6\varepsilon^4\left(\frac{w_0}{2}\right)^8\tau'^2.\left(\frac{\mathrm{k}}{2}\right)^5 e^{-\frac{\tau'^2}{24}(\mathrm{k}-\mathrm{k}_0)^2} && (4.30)\\
&\times\frac{\sin^4\theta}{1-\sin^2\theta\sin^2\varphi}\Bigg[\frac{n_{\mathcal{F}}^2}{16}.\sin^4\theta\sin^2(4\varphi)\\
&\qquad\qquad+n_{\mathcal{G}}^2.(\cos\theta-1+\sin^2\theta\sin^2\varphi)^2\sin^2(2\varphi)\\
&\qquad\qquad+\frac{n_{\mathcal{F}}n_{\mathcal{G}}}{2}.\sin^2\theta(\cos\theta-1+\sin^2\theta\sin^2\varphi)\sin(2\varphi)\sin(4\varphi)\Bigg]\\
&\times|J|^2\frac{d^3\tilde{\mathrm{k}}}{(2\pi)^3}
\end{aligned}\right.$$

4.2 RPM light field as a train of Gaussian pulses

Let us model the RPM light field by a train of attosecond Gaussian pulses, each spaced by a period of the fundamental laser frequency. Then the amplitudes take the form,

$$S \equiv S\left[E_p\right]F_{N_p} \tag{4.31}$$

where F_{N_p} captures the interference effects between the different N_p pulses and depends on the modeling hypotheses, while $S\left[E_p\right]$ is the single pulse contribution that will be estimated.

4.2.1 Differential photon numbers

Following [299] we choose to model our field as a Gaussian pulse of duration $\tau_h \sim \tau_0/n_h$, waist $w_h \sim w_0/n_h$ and Rayleigh length $x_{Rh} \sim x_{R0}/n_h$, with n_h the harmonics order of the spectrum cut-off frequency $\mathrm{k}_h = n_h.\mathrm{k}_0$. We can besides adopt a generic model for the power spectrum setting,

$$\frac{\delta W_n}{W} \equiv \frac{n^{-2s}}{H_{2s}(n_h)} \tag{4.32}$$

where δW_n is the energy content of the n-th harmonic and W the total energy, while $H_q(n) \triangleq \sum_{k=1}^{n} 1/k^q$ is a generalized harmonic number. The field amplitude follows as,

$$\begin{aligned} E_h &= \sum_{n=1}^{n_h} E_{0n} \\ \text{with } E_{0n} &= \sqrt{\frac{\delta W_n}{\tau w_{0n}^2}} \\ &= E_0^g . \frac{n^{-s+1}}{(H_{2s}(n_h))^{1/2}} \text{ , denoting } E_0^g = \sqrt{\frac{W}{\tau w_0^2}} \qquad (4.33) \\ \text{so that } & \boxed{E_h = E_0^g . \frac{H_{s-1}(n_h)}{(H_{2s}(n_h))^{1/2}}} \qquad (4.34) \end{aligned}$$

Starting back from the single focused Gaussian beam scattered photons numbers Eqs. 4.29-4.30 we have,

$$\boxed{\begin{cases} n_t = c_t . \left|I_h\right|^2 . \mathrm{k}^5 \sin^4\left(\dfrac{\theta}{2}\right) \sin^4\theta . \left\{ n_{\mathcal{F}}^2 + (n_{\mathcal{G}}^2 - n_{\mathcal{F}}^2)\sin^2(2\varphi) \right\} & (4.35) \\ n_\perp = c_\perp . \left|I_h\right|^2 . \mathrm{k}^5 \sin^4\left(\dfrac{\theta}{2}\right) \sin^4\theta \dfrac{\sin^2(2\varphi)}{1 - \sin^2\theta \sin^2\varphi} & \\ \qquad \times \left\{ (n_{\mathcal{F}} - n_{\mathcal{G}})\cos(2\varphi)\cos^2\left(\dfrac{\theta}{2}\right) + 2n_{\mathcal{G}}^2 \sin^2\left(\dfrac{\theta}{2}\right) \right\}^2 & (4.36) \end{cases}}$$

for $c_{t,\perp}$ some constant factors, and where the integral factors write, after factoring out numerical constants,

$$\boxed{I_h \equiv \varepsilon^2 E_h^3 . \delta\tau_h w_{0h}^4 x_{Rh} . e^{-\frac{\delta\tau_h^2}{12}(\mathrm{k}-\mathrm{k}_h)^2} \tilde{J}_h} \qquad (4.37)$$

$$\tilde{J}_h = \int d\zeta . \frac{e^{-ix_{Rh}(k_x - \mathrm{k}).\zeta - \left(\frac{w_{0h}\mathrm{k}_\perp}{2}\right)^2 \frac{1+\zeta^2}{3-i\zeta}}}{(1+i\zeta)(3-i\zeta)^3} \qquad (4.38)$$

We then have to estimate the J integral. Switching to spherical coordinates we have,

$$\tilde{J}_h = \int d\zeta . \frac{e^{-i\frac{4}{\varepsilon^2}\frac{\mathrm{k}}{\mathrm{k}_h}\sin^2\left(\frac{\theta}{2}\right)\left[\frac{\zeta^2+1}{\zeta+3i}\frac{\mathrm{k}}{\mathrm{k}_h}\cos^2\left(\frac{\theta}{2}\right) - \zeta\right]}}{(1+i\zeta)(3-i\zeta)^3} \qquad (4.39)$$

Now it appears that the integrand has the form $j(\zeta) \equiv h(\zeta) e^{-i\frac{4}{\varepsilon^2}\frac{\mathrm{k}}{\mathrm{k}_h}\sin^2\left(\frac{\theta}{2}\right).f(\zeta,\theta)}$, where h has a pole at $\zeta = i$, and

$$\begin{aligned} f(\zeta,\theta) &\underset{|\zeta|\to\infty}{\sim} f_\infty(\theta)\zeta \qquad (4.40) \\ \text{with } f_\infty(\theta) &= \frac{\mathrm{k}}{\mathrm{k}_h}\cos^2\left(\frac{\theta}{2}\right) - 1 \qquad (4.41) \\ & \text{hence for } \mathrm{k} < \mathrm{k}_h,\ f_\infty(\theta) < 0\ \forall\theta \qquad (4.42) \end{aligned}$$

so that we can close the integration path in the upper complex plane and use the residue theorem to find,

$$\boxed{\tilde{J}_h = i\frac{\pi}{2^5}e^{-\frac{4}{\varepsilon^2}\frac{\mathrm{k}}{\mathrm{k}_h}\sin^2\left(\frac{\theta}{2}\right)}} \tag{4.43}$$

which by analytic continuation holds true also for $\mathrm{k} > \mathrm{k}_h$. Therefore,

$$I_h = \varepsilon^2 E_h^3.\delta\tau_h w_{0h}^4 x_{Rh}.e^{-\frac{\delta\tau_h^2}{12}(\mathrm{k}-\mathrm{k}_h)^2}.e^{-\frac{4}{\varepsilon^2}\frac{\mathrm{k}}{\mathrm{k}_h}\sin^2\left(\frac{\theta}{2}\right)} \tag{4.44}$$

so that,

$$\begin{cases} n_t = c_t.\varepsilon^4(E_0^g)^6.\tau_0^2 w_0^8 x_{R0}^2.\dfrac{1}{n_h^{12}}\dfrac{(H_{s-1}(n_h))^6}{(H_{2s}(n_h))^3}.\mathrm{k}^5 e^{-\frac{\delta\tau_h^2}{6}(\mathrm{k}-\mathrm{k}_h)^2} \\ \qquad \times\, e^{-\frac{4}{\varepsilon^2}\frac{\mathrm{k}}{\mathrm{k}_h}\sin^2\left(\frac{\theta}{2}\right)}\sin^4\left(\dfrac{\theta}{2}\right)\sin^4\theta.\left\{n_{\mathcal{F}}^2 + (n_{\mathcal{G}}^2 - n_{\mathcal{F}}^2)\sin^2(2\varphi)\right\} \\ n_\perp = c_\perp.\varepsilon^4(E_0^g)^6.\tau_0^2 w_0^8 x_{R0}^2.\dfrac{1}{n_h^{12}}\dfrac{(H_{s-1}(n_h))^6}{(H_{2s}(n_h))^3}.\mathrm{k}^5 e^{-\frac{\delta\tau_h^2}{6}(\mathrm{k}-\mathrm{k}_h)^2} \\ \qquad \times\, e^{-\frac{4}{\varepsilon^2}\frac{\mathrm{k}}{\mathrm{k}_h}}\sin^4\left(\dfrac{\theta}{2}\right)\sin^4\theta\dfrac{\sin^2(2\varphi)}{1-\sin^2\theta\sin^2\varphi} \\ \qquad\qquad \times\left\{(n_{\mathcal{F}} - n_{\mathcal{G}})\cos(2\varphi)\cos^2\left(\dfrac{\theta}{2}\right) + 2n_{\mathcal{G}}^2\sin^2\left(\dfrac{\theta}{2}\right)\right\}^2 \end{cases} \tag{4.45}$$

4.2.2 Total photon numbers

We can now integrate this differential signal intensities to find the total photon numbers. We see from the exponential factors that we can apply a small scattering angle approximation $\theta \ll \varepsilon$, so that expanding all trigonometric functions to lowest order in θ we find,

$$\int d^3k e^{-\frac{4}{\varepsilon^2}\frac{\mathrm{k}}{\mathrm{k}_h}}\sin^4\left(\frac{\theta}{2}\right)\sin^4\theta \propto \frac{\mathrm{k}_h^7}{\delta\tau_h}\varepsilon^{10} \tag{4.46}$$

So that,

$$\begin{cases} N_t = C_t.\varepsilon^4(E_0^g)^6.\mathrm{k}_0^7\tau_0 w_0^8 x_{R0}^2.\dfrac{1}{n_h^4}\dfrac{(H_{s-1}(n_h))^6}{(H_{2s}(n_h))^3}.\varepsilon^{10} \\ N_\perp = C_\perp.\varepsilon^4(E_0^g)^6.\mathrm{k}_0^7\tau_0 w_0^8 x_{R0}^2.\dfrac{1}{n_h^4}\dfrac{(H_{s-1}(n_h))^6}{(H_{2s}(n_h))^3}.\varepsilon^{10} \end{cases} \tag{4.47}$$

with $C_{t,\perp}$ some numerical constants. Finally making the diffraction parameters dependence explicit, we conclude that

$$\boxed{N_{t,\perp} = C_{t,\perp}.\mathrm{k}_0^3\frac{W^3}{\tau^2}.\frac{1}{(H_{2s}(n_h))^3}\left(\frac{H_{s-1}(n_h)}{n_h}\right)^4 \times (H_{s-1}(n_h))^2.\varepsilon^8} \tag{4.48}$$

If we consider the spectrum generated in optimal laser-plasma interaction conditions we can take $s \sim 1$ for the power spectrum, in which case the harmonics number scaling reduces to,

$$\boxed{N \propto n_h^2} \tag{4.49}$$

Chapter 5

Relation between Stimulated Vacuum Emission and effective classical field equations

---

The Stimulated Vacuum Emission formalism we used in this work is explicitly grounded in Quantum Electrodynamics. Nevertheless, it lead us to an expression of the number of photon observable Eqs. 2.45-2.49 in the purely classical terms of a radiated field spectrum. We here make explicit the possibility of the converse reasoning, starting from the equations of motion of the Heisenberg-Euler action, understood as a quantum effective action, so as to compute photon numbers defined from the classical field variables, understood as quantum field expectation values. This approach has also been pursued in the literature[1], with the benefit of a natural embedding in the reference Maxwell-Boltzmann framework, including PIC-QED numerical implementations allowing to numerically solve the self-consistent field equations without further approximation. In order to more clearly discern the predictive power of such methods, the equivalence domain with the amplitude-based calculation will be precised, and a typology of contributions beyond leading order highlighted, delineating the role of exact solutions to the effective equations of motion.

5.1 Heisenberg-Euler quantum effective theory

All predictions of a Quantum Field Theory are entirely encoded in its $n-$points functions and exact equations can be derived for them (*cf.* sec. B.2.3). In App. B we derived such relations, the Schwinger-Dyson equations Eq. B.94, simply from local commutation relations and the Euler-Lagrange equations satisfied by field operators. Now it turns out these equations can also be derived from a variational principle, formally identical to Hamilton's principle Eq. A.2. The generating functional Γ is then called the *quantum effective action* of the theory [307]. Considering for definiteness a real scalar field ϕ, this indeed means that there exists a functionnal Γ such that,

$$\frac{\delta\Gamma}{\delta f}=0;\ \frac{\delta\Gamma}{\delta G}=0;\ \frac{\delta\Gamma}{\delta G^{(3)}}=0;\dots\ \text{(“Quantum effective action”)} \tag{5.1}$$

whose solutions are the *exact* field expectation value f_x, propagator G and any higher-order correlation function $G^{(n)}_{1\dots n}$, for a given state ρ_0.

There is a second meaning of "effective action" in mechanics, conceptually distinct but physically related to the first in some contexts, including field theory. Namely, let us assume our system can be decomposed in two interacting subsystems $\{q_i\}=\{q_a\}_{a\in A}\cup\{q_b\}_{b\in B}$, then its action writes $S[q_i]=S_A[q_a]+S_{\text{int}}[q_a,q_b]+S_B[q_b]$. Now consider a configuration in which we can assume that the dynamics of q_b does practically not depend on the values of q_a. As a consequence q_b variables can be treated "non-dynamically", in the

---

[1] See *e.g.* [335–338], also dedicated section in [3] and references therein.

sense that their evolution can be determined considering system B in isolation. System A however is affected by system B and therefore obeys modified equations of motions, generated by a new action

$$S[q_a] \equiv S^{\text{eff}}_{AB}[q_a] \text{ (``effective action'')} \tag{5.2}$$

generically called an *effective action* for system A "integrating out" system B[2]. This effective action $S^{\text{eff}}_{AB}[q_a]$ has *a priori* no relation to the quantum effective action (*e.g.* Γ_A defining the quantum dynamics of S_A), and in particular does not share the defining property of generating exact equations of motion for correlation functions Eq. 5.1 upon extremization[3].

The Heisenberg-Euler action $\Gamma^{\text{HE}}[A]$ is defined as the "effective action" in the sense Eq. 5.2 of the electromagnetic field (A stands for the 4-potential) integrating out electron-positron dynamics (or any other charged fermionic particle), for a fermion field in the vacuum state, computed at first order in the fine-structure constant α (or "one-loop" order, diagrammatically) for a uniform electromagnetic field expectation value. Now it turns out that at this order in the loop expansion, this functional *coincides* with the electromagnetic part of the quantum effective action in the sense Eq. 5.1[4] [328], so that,

$$\frac{\delta}{\delta \mathcal{A}^\mu}\Gamma^{\text{HE}}[\mathcal{A}] = 0 \tag{5.3}$$

are the equations of motion of the electromagnetic potential expectation value $\mathcal{A}$ in QED at first order in α, with electron-positrons in the vacuum state.

In this section, we will examine more closely this approach to strong-field QED, that we choose to call "Heisenberg-Euler quantum effective theory" for definiteness. In particular, we will show how the scattered photon number Eq. 2.49 of the Stimulated Vacuum Emission formalism is then recovered.

5.1.1 Theory definition

We wish to consider the dynamics of the electromagnetic field expectation value (1-point function) coupled to a fermion field, in a fermionic vacuum state. Equations of motion are generated by a quantum effective action. For a field of frequencies $\omega \ll m$, we can adopt the locally constant field approximation and assume that, at first order in α, an effective action integrating out fermionic variables is provided by,

$$\Gamma^{\text{HE}}_{\mathcal{A}}[A] \equiv \int dx \mathcal{L}^{\text{HE}}_{\mathcal{A}(x)}(A(x)) \tag{5.4}$$

injecting the local electromagnetic field values in the Heisenberg-Euler Lagrangian (*cf* sec. 2.3.1)[5]. At first order in α, this functional coincides with the quantum effective action

---

[2] In classical theory we simply have $S^{\text{eff}}_{AB}[q_a] \equiv S_A[q_a] + S_{\text{int}}[q_a, \bar{q}_b]$ with $\bar{q}_b$ the known values of q_b. In quantum theory the expression is different but formally straightforward in terms of path integral [307].

[3] When a system A cannot be considered perfectly isolated, accounting for finer and finer effects in the quantum dynamics (*e.g. via* quantum effective actions of increasing order in a perturbative expansion) we may reach the point at which these contributions are of the same order of magnitude as the coupling of A with another system B. In this case, successful prediction requires considering the joint system AB, for instance *via* the second kind of "effective action" Eq. 5.2. This situation of (possibly weak) coupling between different kinds of variables is unavoidable in field theory (*e.g.* the Standard Model), so that in this sense both concepts of effective action are "physically" related in this context.

[4] This can be established *e.g.* showing that Γ^{HE} is the generator of 1-PI diagrams at one-loop order.

[5] In the following, corrections from non-uniformity of the field (*e.g.* in the form of derivative terms) will not be discussed further, relying on the vast gap between even X-UV frequencies and m to assume they can be neglected before other kinds of higher order contributions at the desired level of accuracy.

of the electromagnetic field in Quantum Electrodynamics with fermions,

$$\Gamma^{\text{HE}}_{\mathcal{A}} \equiv \Gamma^{(1)}_{\text{QED}}[\mathcal{A}] \tag{5.5}$$

$$\text{that is, } \mathcal{L}^{(1)}_{\text{QED}}(\mathcal{A}) \equiv \mathcal{L}_0(\mathcal{A}) + \mathcal{L}^{\text{HE}}_{\text{int}}(\mathcal{A}) \text{ , denoting } \mathcal{L}_0 \text{ Maxwell's Lagrangian} \tag{5.6}$$

Expanding $\mathcal{L}_{\text{int}}$ (with alleviated notations) at lowest order in normalized invariant field strengths $\mathcal{E}, \mathcal{B}$ Eqs. 2.41 we reach,

$$\boxed{\begin{aligned}
\mathcal{L}_0 &= -\mathcal{F} = -\frac{1}{2}\left[\mathbf{B}^2 - \mathbf{E}^2\right] && (5.7)\\
\mathcal{L}_{\text{int}} &= \frac{m^4}{8\pi^2}\frac{1}{45}\left(\frac{e}{m^2}\right)^4\left[4\mathcal{F}^2 + 7\mathcal{G}^2\right] && (5.8)\\
&= \frac{m^4}{8\pi^2}\frac{1}{45}\left(\frac{e}{m^2}\right)^4\left[\left(\mathbf{B}^2 - \mathbf{E}^2\right)^2 + 7\left(\mathbf{E}\cdot\mathbf{B}\right)^2\right]
\end{aligned}}$$

5.1.2 Equations of motion

Equations of motion are the Euler-Lagrange equations of the quantum effective action,

$$\partial_\mu \frac{\partial \mathcal{L}}{\partial(\partial_\mu \mathcal{A}_\nu)} - \frac{\partial \mathcal{L}}{\partial \mathcal{A}_\nu} = 0 \tag{5.9}$$

$$\textit{i.e. } \partial_\mu \frac{\partial \mathcal{L}_0}{\partial F_{\mu\nu}} = -\partial_\mu \frac{\partial \mathcal{L}_{\text{int}}}{\partial F_{\mu\nu}} \tag{5.10}$$

Let us rewrite them in tridimensional form, recalling,

$$F^{\mu\nu} = \begin{pmatrix} 0 & E^j \\ -E^i & \varepsilon^{ijk}B^k \end{pmatrix} \tag{5.11}$$

from which we deduce,

$$\begin{cases} \dfrac{\mathcal{L}_{\text{int}}}{\partial F_{0j}} = -\dfrac{1}{2}\dfrac{\mathcal{L}_{\text{int}}}{\partial E^j} \\ \dfrac{\mathcal{L}_{\text{int}}}{\partial F_{ij}} = \dfrac{1}{2}\varepsilon^{ijk}\dfrac{\mathcal{L}_{\text{int}}}{\partial B^k} \end{cases} \tag{5.12}$$

Then, for $\nu = 0$,

$$-\frac{1}{2}\partial_i F^{i0} = -\partial_i \frac{\partial \mathcal{L}_{\text{int}}}{\partial F_{i0}} \tag{5.13}$$

$$\Leftrightarrow \frac{1}{2}\partial_i E^i = -\frac{1}{2}\partial_i \frac{\partial \mathcal{L}_{\text{int}}}{\partial E_i} \tag{5.14}$$

$$\Leftrightarrow \nabla \cdot \mathbf{D} = 0 \tag{5.15}$$

$$\text{with } \mathbf{D} = \mathbf{E} + \mathbf{P}, \text{ and } \mathbf{P} \triangleq \frac{\partial \mathcal{L}_{\text{int}}}{\partial \mathbf{E}} \tag{5.16}$$

For $\nu = j$,

$$-\frac{1}{2}\left(\partial_0 F^{0j} + \partial_i F^{ij}\right) = -\left(\partial_0 \frac{\mathcal{L}_{\text{int}}}{\partial F_{0j}} + \partial_i \frac{\mathcal{L}_{\text{int}}}{\partial F_{ij}}\right) \tag{5.17}$$

$$\Leftrightarrow -\frac{1}{2}\left(\partial_0 E^j + \varepsilon^{ijk}\partial_i B^k\right) = -\frac{1}{2}\left(-\partial_0 \frac{\mathcal{L}_{\text{int}}}{\partial E^j} + \varepsilon^{ijk}\partial_i \frac{\mathcal{L}_{\text{int}}}{\partial B^k}\right) \tag{5.18}$$

$$\Leftrightarrow -\partial_t \mathbf{D} + \nabla \times \mathbf{H} = \mathbf{0} \tag{5.19}$$

$$\text{with } \mathbf{H} = \mathbf{B} - \mathbf{M}, \text{ and } \mathbf{M} \triangleq \frac{\partial \mathcal{L}_{\text{int}}}{\partial \mathbf{B}} \tag{5.20}$$

Besides, the definition of the electromagnetic field tensor F in terms of gauge field A remains unchanged, $F_{\mu\nu} = \partial_\mu \mathcal{A}_\nu - \partial_\nu \mathcal{A}_\mu$, so the homogeneous Maxwell's equations still follow. The electric and magnetic fields expectation values are therefore governed by,

Heisenberg-Euler field equations

$$\nabla \cdot \mathbf{D} = 0 \tag{5.21}$$

$$-\partial_t \mathbf{D} + \nabla \times \mathbf{H} = \mathbf{0} \tag{5.22}$$

$$\nabla \cdot \mathbf{B} = 0 \tag{5.23}$$

$$\partial_t \mathbf{B} + \nabla \times \mathbf{E} = \mathbf{0} \tag{5.24}$$

from which derive wave equations,

$$\begin{aligned}\Box \mathbf{E} &= \overbrace{-\nabla\left(\nabla \cdot \mathbf{P}\right) + \partial_t^2 \mathbf{P} + \partial_t \nabla \times \mathbf{M}}^{\mathbf{T}_E[\mathbf{E},\mathbf{B}]} \\ &= \nabla \rho_v + \partial_t \mathbf{j}_v \\ \Box \mathbf{B} &= \overbrace{-\nabla \times \left(\nabla \times \mathbf{M}\right) - \nabla \times \partial_t \mathbf{P}}^{\mathbf{T}_B[\mathbf{E},\mathbf{B}]} \\ &= -\nabla \times \mathbf{j}_v\end{aligned} \tag{5.25}$$

with $\rho_v = -\nabla \cdot \mathbf{P}$ and $\mathbf{j}_v = \partial_t \mathbf{P} + \nabla \times \mathbf{M}$ the induced "vacuum" charge and current[6].

5.1.3 Number of scattered photons

In order to be able to compute the photon number observable in the present framework, it should be expressible in terms of field expectation values. One may check that it is indeed the case, exactly for a coherent state, and neglecting some terms to a good approximation in a general strong-field state [304, 307]. This expectation value is then found to coincide with the pre-quantum correspondance rule between a photon and an energy-momentum unit of the electromagnetic field, in a given polarization. Formally[7],

$$N \equiv \int \frac{d^3k}{(2\pi)^3} \frac{|\mathbf{E}(\mathbf{k})|^2 + |\mathbf{B}(\mathbf{k})|^2}{2\mathrm{k}} \tag{5.26}$$

$$\text{and, } \frac{dN_p}{d^3k}(\mathbf{k}) \equiv \frac{1}{(2\pi)^3} \frac{|\mathbf{e}_p(\mathbf{k}) \cdot \mathbf{E}(\mathbf{k})|^2 + |\mathbf{e}_{p+1}(\mathbf{k}) \cdot \mathbf{B}(\mathbf{k})|^2}{2\mathrm{k}} \tag{5.27}$$

with polarization basis vectors as in sec. 2.3.1.

The non-free part of $\mathbf{E}$ is generated by the source $\mathbf{T}_E$, it can hence be expresed from it *via* a Green's function G, as $\mathbf{E} = G * \mathbf{T}_E$. We here wish to compute only photons radiated during the interaction, and thus use the radiative Green's function,

$$G^{\text{rad}} = G^{\text{ret}} - G^{\text{ad}} \tag{5.28}$$

We thereby find,

$$\frac{dN_p}{d^3k}(\mathbf{k}) = \frac{1}{(2\pi)^3} \frac{|\mathbf{e}_p(\mathbf{k}) \cdot \int d\tau G^{\text{rad}}(\mathbf{k}, \tau) \mathbf{T}_E(\mathbf{k}, t-\tau)|^2}{2\mathrm{k}} + (\mathbf{E}, p \leftrightarrow \mathbf{B}, p+1) \tag{5.29}$$

$$= \frac{1}{(2\pi)^3} \frac{|\mathbf{e}_p(\mathbf{k}) \cdot \int \frac{d\omega}{2\pi} e^{-i\omega t} G^{\text{rad}}(\mathbf{k}, \omega) \mathbf{T}_E(\mathbf{k}, \omega)|^2}{2\mathrm{k}} + (\mathbf{E}, p \leftrightarrow \mathbf{B}, p+1) \tag{5.30}$$

---

[6] Note we could trivially add classical currents as well in Eqs. 5.21-5.22, that could be understood as the expectation value of part of fermionic variables following a classical dynamics in some approximation. A systematic procedure to control such reduction can typically be found in a kinetic framework [116].

[7] Another form of the derivation can be found in [339].

Green's functions of the D'Alembertian are solution to the distribution equation,

$$(-\omega^2+\mathrm{k}^2)G(\mathbf{k},\omega)=1 \tag{5.31}$$

of general solution[340, 341], $G=\mathrm{Vp}\frac{1}{-\omega^2+\mathrm{k}^2}+\alpha\delta(\omega-\mathrm{k})+\beta\delta(\omega+\mathrm{k})$ with Vp the principal value. We can extract physically relevant values for the α,β coefficients by analytical continuation of $G(\omega)$ in the complex plane and choice of closing of the integration path on a contour when shifting to $G(\tau)$, leading to the prescriptions,

$$G^{\overset{\mathrm{ad}}{\mathrm{ret}}}=\lim_{s\to0^+}\frac{1}{2\mathrm{k}}\left[\frac{1}{-\omega+\mathrm{k}\pm is}+\frac{1}{\omega+\mathrm{k}\pm is}\right] \tag{5.32}$$

or, knowing that $\lim\limits_{y\to0^+}\frac{1}{x\pm iy}=\mp i\pi\delta(x)+\mathrm{Vp}\frac{1}{x}$,

$$G^{\overset{\mathrm{ad}}{\mathrm{ret}}}=\frac{1}{2\mathrm{k}}\left[\pm i\pi\delta(\omega-\mathrm{k})-\mathrm{Vp}\frac{1}{\omega-\mathrm{k}}\mp i\pi\delta(\omega+\mathrm{k})+\mathrm{Vp}\frac{1}{\omega+\mathrm{k}}\right] \tag{5.33}$$

$$\text{so that, } G^{\mathrm{rad}}=\frac{i\pi}{\mathrm{k}}\left(-\delta(\omega-\mathrm{k})+\delta(\omega+\mathrm{k})\right) \tag{5.34}$$

Injecting Eq. 5.34 in the computation of $\mathbf{E}(\mathbf{k})$ Eq. 5.30, we find,

$$\mathbf{E}(\mathbf{k})=\int\frac{d\omega}{2\pi}e^{-i\omega t}\frac{i\pi}{\mathrm{k}}\left(-\delta(\omega-\mathrm{k})+\delta(\omega+\mathrm{k})\right)\mathbf{T}_E(\mathbf{k},\omega) \tag{5.35}$$

$$=\frac{i}{2\mathrm{k}}\left(-\mathbf{T}_E(\mathbf{k},\mathrm{k})e^{-i\mathrm{k}t}+\mathbf{T}_E(\mathbf{k},-\mathrm{k})e^{i\mathrm{k}t}\right) \tag{5.36}$$

$$\text{hence, } |\mathbf{E}(\mathbf{k})|^2=\frac{1}{4\mathrm{k}^2}\left(|\mathbf{T}_E(\mathbf{k},\mathrm{k})|^2+|\mathbf{T}_E(\mathbf{k},-\mathrm{k})|^2\right) \tag{5.37}$$
$$-\frac{1}{2\mathrm{k}^2}\mathrm{Re}\left[\mathbf{T}_E(\mathbf{k},\mathrm{k})\cdot\mathbf{T}_E^*(\mathbf{k},-\mathrm{k})e^{-2i\mathrm{k}t}\right]$$

The term in the second line of Eq. 5.37 cancels out in the integral of N for $t\delta_T\omega\gg1$, where $\delta_T\omega$ is the characteristic variation scale in the spectrum of $\mathbf{T}_E$[8]. Besides, $\mathbf{T}_E(\mathbf{k},-\mathrm{k})=\mathbf{T}_E^*(-\mathbf{k},\mathrm{k})$, so that negative frequencies at $\mathbf{k}$ give a contribution identical to positive frequencies at $-\mathbf{k}$ when Eq.5.37 is integrated. From these conclusions Eq. 5.30 becomes,

$$\frac{dN_p}{d^3k}(\mathbf{k})\doteq\frac{1}{(2\pi)^3}\frac{1}{2\mathrm{k}}\left[\frac{1}{4\mathrm{k}^2}.2|\mathbf{e}_p(\mathbf{k})\cdot\mathbf{T}_E(\mathbf{k},\mathrm{k})|^2+\frac{1}{4\mathrm{k}^2}.2|\mathbf{e}_{p+1}(\mathbf{k})\cdot\mathbf{T}_B(\mathbf{k},\mathrm{k})|^2\right] \tag{5.38}$$

$$=\frac{1}{(2\pi)^3}\frac{1}{4\mathrm{k}^3}\left[|\mathbf{e}_p(\mathbf{k})\cdot\mathbf{T}_E(\mathbf{k},\mathrm{k})|^2+|\mathbf{e}_{p+1}(\mathbf{k})\cdot\mathbf{T}_B(\mathbf{k},\mathrm{k})|^2\right] \tag{5.39}$$

Now,

$$\mathbf{T}_E(\mathbf{k},\mathrm{k})=\mathbf{k}(\mathbf{k}\cdot\tilde{\mathbf{P}})-\mathrm{k}^2\tilde{\mathbf{P}}+\mathrm{k}(\mathbf{k}\times\tilde{\mathbf{M}}) \tag{5.40}$$

$$=-\mathrm{k}^2\left(\tilde{\mathbf{P}}_\perp-\mathbf{u_k}\times\tilde{\mathbf{M}}\right) \tag{5.41}$$

$$\text{with } \tilde{\mathbf{P}}_\perp=\tilde{\mathbf{P}}-(\mathbf{u_k}\cdot\tilde{\mathbf{P}})\mathbf{u_k} \tag{5.42}$$

$$\mathbf{T}_B(\mathbf{k},\mathrm{k})=\mathbf{k}\times(\mathbf{k}\times\tilde{\mathbf{M}})-\mathbf{k}\times(\mathrm{k}\tilde{\mathbf{P}}) \tag{5.43}$$

$$=-\mathrm{k}^2\left(\tilde{\mathbf{M}}_\perp+\mathbf{u_k}\times\tilde{\mathbf{P}}\right) \tag{5.44}$$

$$\text{noticing } \mathbf{u_k}\times\left(\tilde{\mathbf{M}}\times\mathbf{u_k}\right)=\tilde{\mathbf{M}}_\perp \tag{5.45}$$

with $\mathbf{u_k}=\mathbf{k}/\mathrm{k}$.

---

[8] That is if $t/\tau_T\gg1$ where $\tau_T\sim1/\delta_T\omega$ is the field source duration.

Then, using the geometrical identity $\mathbf{e}_p(\mathbf{k}) \cdot (\mathbf{u_k} \times \mathbf{v}) = -\mathbf{e}_{p+1}(\mathbf{k}) \cdot \mathbf{v}$,

$$\mathbf{e}_p(\mathbf{k}) \cdot \mathbf{T}_E(\mathbf{k}, \mathrm{k}) = -\mathrm{k}^2 \left(\mathbf{e}_p(\mathbf{k}) \cdot \tilde{\mathbf{P}} + \mathbf{e}_{p+1}(\mathbf{k}) \cdot \tilde{\mathbf{M}}\right) \tag{5.46}$$

$$\mathbf{e}_{p+1}(\mathbf{k}) \cdot \mathbf{T}_B(\mathbf{k}, \mathrm{k}) = -\mathrm{k}^2 \left(+\mathbf{e}_{p+1}(\mathbf{k}) \cdot \tilde{\mathbf{M}} - \mathbf{e}_{p+2}(\mathbf{k}) \cdot \tilde{\mathbf{P}}\right) \tag{5.47}$$

So that we finally come to,

$$\boxed{\frac{dN_p}{d^3k}(\mathbf{k}) = \frac{1}{(2\pi)^3}\frac{\mathrm{k}}{2}\left|\mathbf{e}_p(\mathbf{k}) \cdot \tilde{\mathbf{P}} + \mathbf{e}_{p+1}(\mathbf{k}) \cdot \tilde{\mathbf{M}}\right|^2} \tag{5.48}$$

which is formally identical to Eqs. 2.45-2.49.

5.2 Consistency beyond leading order contributions

It appears that effective equations of motion for the electromagnetic field together with a simple strong-field assumption allowed to retrieve exactly the SVE expression of the scattered photon number observable. At this point though, this result may appear as a mere coincidence. Besides, Eq. 5.48 actually is not exactly the same as Eqs. 2.45-2.49, for in the latter formula fields were conceived as expectation values in a free coherent state without mention of field equations Eqs. 5.21-5.24, and thus assumed to follow Maxwell's equations. In this section, we will define the equivalence domain between both approaches explicitly. Furthermore, as the Heisenberg-Euler quantum effective theory manifestly contains more information than the amplitude-based calculation, it is legitimate to ask for the precise extent of its predictive power. This will be discussed identifying three different kinds of contributions beyond the leading order. We will argue that in large interaction volumes, the local hierarchy of interaction terms can collapse due to high multiplicity interaction sequences; the role of exact solutions to the equations of motion then is identified as ensuring the consistency of approximations operated at the quantum effective action level, at all point in the system evolution.

5.2.1 Equivalence domain with Stimulated Vacuum Emission

Aside from shared assumptions regarding the expansion order of the effective action, or the validity of its locally constant field expression Eq. 5.4, we can identify two conditions for the equivalence of the direct perturbative expansion and effective equations for the computation of a given observable, or more specifically here the number of photons Eq. 2.44 in SVE and Eq. 5.27 in Heisenberg-Euler effective theory. Namely,

$$\text{i. } \langle \mathcal{O}(\phi) \rangle \overset{\text{strong fields}}{\equiv} \mathcal{O}(\langle \phi \rangle) + O(\text{higher orders in } \alpha) \tag{5.49}$$

$$\text{ii. } \langle \phi \rangle \simeq \phi_{\text{cl}}^{(1)} \text{ , with } \phi_{\text{cl}}^{(1)} = G * T[\phi_{\text{cl}}^{(\text{free})}] \tag{5.50}$$

and G the free propagator of field ϕ and T a source term stemming for quantum corrections to the classical equations of motion (*cf.* for instance Eqs. 5.25).

Decorrelation of observables in strong fields

The result Eq. 5.49 that at leading order in α observables can be obtained simply from the 1−point function is actually true in contexts more general than QED [307]. It can be established for instance by power counting, relating diagrammatic properties to the power of a graph in e and $\mathcal{A}$. In the context of QED with non-zero field expectation value, we can expect this property realized when $e\mathcal{A}/m > 1$, or $eE/\omega m > 1$.

First order solution to the effective field equations

The second condition Eq. 5.50 simply expresses that in the SVE calculation, the photon source terms are expressed in terms of the free fields. This is equivalent to expressing the solution to the effective field equation as a power series in the source (*e.g.* $\mathbf{E}$ as a series in $\mathbf{T}_E$) and truncating at first order. The outline of this procedure can be sketched more explicitly writing,

$$\begin{aligned}
&\Box\mathbf{E} = \mathbf{T}[\mathbf{E}] \Rightarrow \mathbf{E} \equiv \mathbf{E}^{(\text{free})} + \mathbf{E}^{(1)} + \mathbf{E}^{(2)} + \dots && (5.51)\\
\text{with } &\Box\mathbf{E}^{(\text{free})} = 0 && (5.52)\\
&\mathbf{E}^{(1)} = G * \mathbf{T}[\left(\mathbf{E}^{(\text{free})}\right)^3] \text{ , taking for instance a cubic source term} && (5.53)\\
&\mathbf{E}^{(2)} = 3G * \mathbf{T}[\left(\mathbf{E}^{(\text{free})}\right)^2, \mathbf{E}^{(1)}] = 3G * \mathbf{T}[\left(\mathbf{E}^{(\text{free})}\right)^2, G * \mathbf{T}[\left(\mathbf{E}^{(\text{free})}\right)^3]] && (5.54)\\
&\vdots
\end{aligned}$$

with $e^2 = 4\pi\alpha$. This highlights that the SVE formula simply gives the first order result in α, while solving the effective equations and computing *e.g.* photon numbers from Eq. 5.48 includes higher order terms stemming from the nonlinearity of the equations of motion.

5.2.2 Higher order terms hierarchy

The relevance of the higher order terms included in solving the equations of motion has to be examined more closely. All the above discussion of the “Heisenberg-Euler quantum effective theory”, in the sense defined below Eq. 5.3, was based on the leading order of a double expansion scheme of the full quantum effective action $\Gamma[\mathcal{A}]$ of the electromagnetic field in QED[9]. First, the quantum effective action was expanded in α and truncated at order one, where its expression coincides with the Heisenberg-Euler functional. Second, the resulting non-polynomial Heisenberg-Euler Lagrangian was expanded in the field strengths $\epsilon \equiv \max(\mathcal{E}, \mathcal{B})$, and again truncated at lowest order. Only then a third expansion could appear from the nonlinearity of the equations of motion, when solutions are written as a (classical) pertubative series Eq. 5.51 capturing the possible numbers of local interaction events. Calculations of chapter 8 could then be identified as the first order contribution of this last series.

We will here try and clarify the relevance of higher order contributions in all three expansions, either as corrections or source for qualitatively new effects, so as to better understand how consistent approximations can be obtained at a given level of accuracy. Simply writing the double expansion of the quantum effective action $\Gamma[\mathcal{A}]$ will first allow establishing a hierarchy in local interaction terms. For large interaction volumes, multiple scattering processes can alter this local ordering and break expansion Eq. 5.51, which will then be discussed.

---

[9] Effects beyond the LCFA open yet another dimension of possible extensions, that will however be left aside here.

Local interaction terms

Let us reason in the framework of the quantum effective action method again. If the electromagnetic field dynamics in QED with *e.g.* electron-positrons is described by an action $\mathcal{S}[\mathcal{A}]$, its exact expectation value in a given state ρ_0 can be obtained solving the equation of motion,

$$\frac{\delta}{\delta\mathcal{A}}\Gamma[\mathcal{A}] = 0 \tag{5.55}$$

where Γ is the quantum effective action. If the exact form of Γ is *a priori* out of reach, approximate expressions may be obtained through an expansion in the parameter α, which diagrammatically translates in a number of loops. This procedure can be sketched as,

$$\Gamma[\mathcal{A}] \equiv \sum_{l=0}^{\infty}\alpha^l\Gamma^{(l)}[\mathcal{A}], \text{ with } \Gamma^{(0)}[\mathcal{A}] = \mathcal{S}[\mathcal{A}] \tag{5.56}$$

and $\Gamma^{(l)}$ are known for $l \leq l_\Gamma$. Now in QED more specifically, the action actually depends on the gauge-invariant field strength tensor, appearing in Lorentz-invariant combinations. Furthermore, a consequence of gauge-invariance is the cancellation of diagrams with odd numbers of external photon lines (Furry theorem), so the action is expressed only from even powers of the field strength. Quantifying their invariant magnitude normalized to the Schwinger field with the above introduced parameter ϵ, we may then perform a weak field expansion,

$$\Gamma_{\text{int}}[\mathcal{A}] \equiv \sum_{l,p=1}^{\infty}\alpha^l\epsilon^{2(p+1)}\Gamma_{\text{int}}^{(l,p)}[\mathcal{A}] \tag{5.57}$$

denoting Γ_{int} the action term beyond Maxwell's.

The equations of motion Eq. 5.55 then take the form,

$$\frac{\delta}{\delta\mathcal{A}}\mathcal{S}[\mathcal{A}] = -\frac{\delta}{\delta\mathcal{A}}\Gamma_{\text{int}}[\mathcal{A}] \tag{5.58}$$

$$\Rightarrow \Box\mathbf{E} = \sum_{l,p=1}^{\infty}\alpha^l\epsilon^{2p}\mathbf{T}_{\text{int}}^{(l,p)}[\mathbf{E}^{2p+1}] \tag{5.59}$$

$$\text{with } \mathbf{T}_{\text{int}}^{(l,p)} \propto \frac{\partial\mathcal{L}_{\text{int}}^{(l,p)}}{\partial\mathbf{E}} \tag{5.60}$$

omitting the $\mathbf{B}$ field for better clarity of the argument, and where $\mathbf{E}$ should here be understood normalized such that its amplitude is captured in ϵ.

At this point it appears that in this context higher loop orders can not be expected to induce qualitatively new effects, but only refine the precision of the electromagnetic self-interaction terms appearing from order 1. On the opposite, higher order terms in the fields manifestly result in distinct phenomena such as harmonics generation at some frequencies differing according to their order in ϵ.

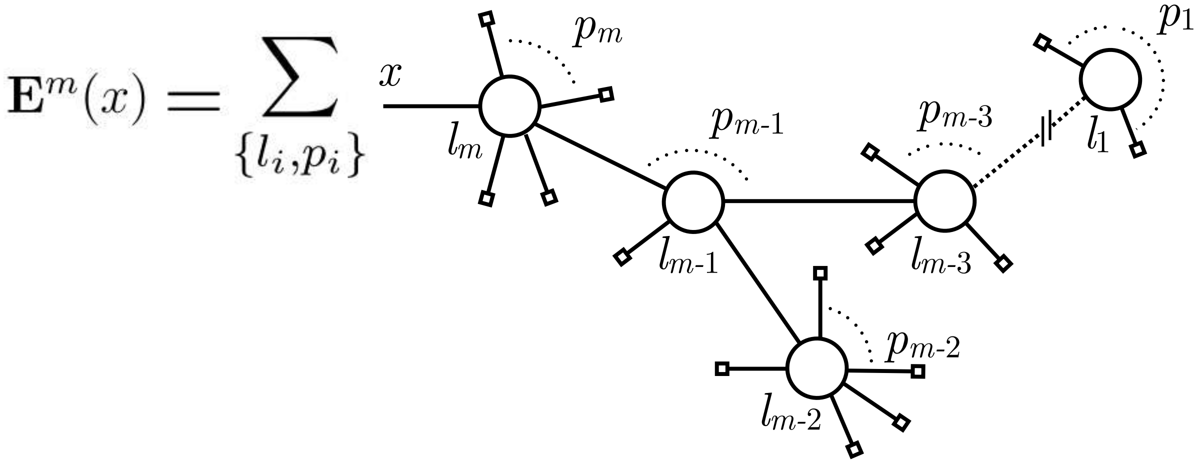

Figure 5.1: **Diagrammatic representation of the generic contributions to the multiplicity m component of the total field.** Lines are free Green's functions (propagators), vertices are represented by circles with two integers (l_i, p_i) specifying their type, and the leafs are free field insertions (the dotted line stands for the omitted part of the diagram). Integration over vertices positions is implied. The sum is over all possible tree diagrams with m vertices.

Propagation and terms mixing

Now expanding solutions to this field equation as well, in terms of number of interactions or "multiplicity", we are lead to,

$$\mathbf{E} \equiv \sum_{m=0}^{\infty} \mathbf{E}^m \tag{5.61}$$

$$\text{with } \mathbf{E}^m = \sum_{\{l_i,p_i\}_{i\in[\![1;m]\!]}} \alpha^{\sum_{i=1}^m l_i} \epsilon^{2\sum_{i=1}^m p_i} \times G * \mathbf{T}_{\text{int}}^{(l_m,p_m)}[\ldots, G * \mathbf{T}_{\text{int}}^{(l_{m-1},p_{m-1})}[\ldots], \ldots] \tag{5.62}$$

Though quite unwieldy analytically, the content of $\mathbf{E}^m$ may be more easily grasped in terms of tree diagrams[10]. The term of order m is comprised of the sum of all possible sequences of m interactions, represented by tree diagrams with m vertices, for all possible combination of vertex types as given by their orders in α and ϵ, specified by two integers l, p. The generic term of such sum is drawn in Fig. 5.1.

We have therefore decomposed the total field in a sum whose terms are indexed by a multiplicity m, denoting the number of interaction events, and a set of integers $\{l_i, p_i\}_{i\in[\![1;m]\!]}$ labelling the order in α (loop order) and ϵ (number of incoming fields) of each interaction point. Each term can thereby be assigned the local magnitude,

$$\boxed{\left|\mathbf{E}^m_{\{l_i,p_i\}}\right| \propto \alpha^{\sum_{i=1}^m l_i} \epsilon^{2\sum_{i=1}^m p_i}} \tag{5.63}$$

---

[10] A solution to a classical partial differential equation with a linear differential operator can indeed be represented by a sum of "tree diagrams", that is diagrams without loops, where lines are Green's function and vertices carry the coefficients of interaction terms. This can be understood from Green's method of solution applied in a perturbative expansion as illustrated in Eqs. 5.51, or diagrammatically drawing an integral form of the equation as illustrated *e.g.* in Fig. B.6-a.

This simply shows that leading order effects are provided by the one-loop interaction terms and multiplicity one contributions. Indeed, relevance of a term to a given observable, *e.g.* harmonics generation at specific frequencies, is expected to only be defined by the order p in ϵ. Therefore, a general multiplicity term contribution to this observable has magnitude $\alpha^{\sum_{i=1}^{m} l_i}\epsilon^{2p}$, besides $l_i \geq 1$, hence all contributions of multiplicity $m \geq 2$ are suppressed by at least a factor α with respect to the leading $m = 1$ term.

Furthermore, higher multiplicity terms contribute with a magnitude equal to lower multiplicity terms originating from higher loop order vertices. As a consequence, corrections beyond the leading order result cannot be consistently obtained only from higher multiplicities at a fixed loop order, but necessarily imply increasing the loop order of the quantum effective action calculation[11].

From there one may conclude that exact fully non-linear solutions of the equations of motion can never consistently give approximations better than a perturbative solution up to multiplicity $m = l_\Gamma$, where l_Γ is the loop order at which the quantum effective action is given. In particular, in the above one-loop Heisenberg-Euler quantum effective theory, we would not be more accurate than a fully linearized $m = 1$ solution, such as prescribed in the SVE formalism. This conclusion however has to be mitigated accounting for long distance propagation effects, as we will now suggest.

A consistency criterion for fully non-linear macroscopic field propagation with finite order local interactions

Let us try and define more precisely a situation where exact solutions to the equations of motion are relevant. The only subtlety stems from the approximate character of equations of motion themselves. For practical purposes one would indeed strongly favor a weak field expansion of the effective action over its $\epsilon-$nonperturbative expression, and its expressions are only known to low order in α[12]. For this reason, though Eq. 5.63 simply indicates that resummation of perturbative field components in multiplicity number would be required as soon as,

$$\begin{aligned} &\alpha^l \epsilon^{2p} \gtrsim 1 \text{ , for some integers } l, p && (5.65)\\ &\Leftrightarrow \epsilon \gtrsim \frac{1}{\alpha^{l/2p}} \\ &i.e.\ \epsilon \gtrsim 1 \text{ , keeping the broadest condition} && (5.66)\end{aligned}$$

at this point the effective action has to be kept in $\epsilon-$nonperturbative form as well. Effective field equations given by a finite weak field Lagrangian such as Eq. 5.8 do therefore not admit a consistent fully nonlinear strong field regime $\mathcal{E}, \mathcal{B} \sim E_S, B_S$.

However, starting back *e.g.* from Eq. 5.62, we see that the prefactor retained in Eq. 5.63 does not capture the full scaling of $\mathbf{E}^m_{\{l_i,p_i\}}$ components. Convolution by the propagator

---

[11] This rather natural result can also be understood diagrammatically, indeed we see *e.g.* in Fig. 5.1 that diagrams obtained from multiplicities higher than 1 are 1-particle reducible (they can be disconnected cutting one internal line, *cf.* sec. B.2.4), while it is clear that there also exists some 1-particle irreducible diagrams at any given loop order, which are generated by the quantum effective action of the corresponding loop order.

[12] For reference, at order 1 in α the total Heisenberg-Euler Lagrangian has the non-polynomial integral form [342],

$$\mathcal{L}^{\mathrm{HE}} = -\frac{m^4}{8\pi^2}\int_0^\infty \frac{ds}{s^3} e^{-s}\left\{\frac{\mathcal{E}\mathcal{B}}{\tanh(\mathcal{B}s)\tan(\mathcal{E}s)} - 1 - \frac{s^2}{3}\left(\mathcal{B}^2 - \mathcal{E}^2\right)\right\} \tag{5.64}$$

functions G can indeed be expected to modify the local terms hierarchy when interactions take place over large propagation volumes. Introducing the resulting factors as $\mathcal{D}$, of form to be precised in a given field configuration geometry, we can then write,

$$\boxed{\left|\mathbf{E}^{m}_{\{l_i,p_i\}}\right| \sim \mathcal{D}^m \alpha^{\sum_{i=1}^{m} l_i} \epsilon^{2\sum_{i=1}^{m} p_i}} \tag{5.67}$$

An actual multiplicity-nonperturbative regime threshold thus appears as,

$$\mathcal{D}\alpha^l \epsilon^{2p} \gtrsim 1 \text{ , for some integers } l, p \tag{5.68}$$

$$i.e. \ \boxed{\mathcal{D} \gtrsim \frac{1}{\alpha\epsilon^2}} \tag{5.69}$$

In these conditions, though field magnitudes remain below the Schwinger field and thus legitimate a weak field (and low α) expansion of the action, high interaction multiplicity components dominate in the final field so that the perturbative expansion Eq. 5.62 breaks down and equations of motions Eq. 5.60 (with series truncated at finite l_Γ, p_Γ) have to be solved exactly[13].

This situation in which consistent approximations can be obtained from an expansion of the action, but not of dynamical quantities, due to a collapse of the local interaction terms hierarchy from multiple interaction events over large evolution scales, is reminiscent of the general *secularity* issue in Non-equilibrium Qunatum Field Theory, as evoked in sec. B.2.3. In the discussed context of quantum effective theories of the electromagnetic field expectation value, exact solutions of the equations of motion can therefore not be conceived as approximations to the strong field regime $\epsilon \sim 1$ or higher order phenomena in α, both small expansion parameters of the effective action. Instead, the role of exact (multiplicity-nonperturbative) solutions of the nonlinear equations of motion is to ensure self-consistency of the approximation scheme[14] for evolution over any (spacetime) extent.

---

[13] This conclusion is in accordance with *e.g.* [335].

[14] Mathematically this would refer to a “uniform approximation” of the full dynamics.

Chapter 6

Computational volume of Stimulated Vacuum Emission simulations

---

The general lack of symmetry of the source terms in Eq. 2.49 makes the algorithm described in sec. 2 potentially very expensive from the computational point of view. Indeed, working with 3-dimensional numerical arrays we can infer memory needs of $\mathcal{M} \propto N_x N_y N_z$, while the time complexity stemming from the on-shell Fourier transform is $\mathcal{T} \propto N_t N_x N_y N_z \log(N_x N_y N_z)$. On the other hand, the resolved scales in each space-time dimension need to range from the field support characteristic length $1/L$, in order to simulate the whole relevant interaction volume, to $2 \times \nu_{max}$, in order to fulfil the Shannon criterion associated to the maximal field frequency, as scattering events with significant energy exchanges are suppressed in comparison to the elastic channels [303, 326]. For a focused monochromatic Gaussian pulse with waist at focus $w_0 \sim \lambda_0$ and duration $\tau \sim 10\lambda_0$, choosing a minimal (maximal) propagation time such that the "front" ("rear") of the pulse is at about three Rayleigh lengths from focus implies that fitting the whole pulse in the simulation space at all times requires a total longitudinal length of about $2 \times (\tau + 3z_R) \simeq 40\lambda_0$, and a transverse length close to $20\lambda_0$ as a consequence of the large divergence of a tightly focused beam. If we furthermore assume the need to work with about ten 3-dimensional double precision (8 Bytes) arrays at any given moment (*e.g.* from field components, Lorentz invariants, etc.), we are then led to,

$$\mathcal{M}_{Gaus} \sim 10 \times (2 \times \nu_0 \times 40\lambda_0) \times (2 \times \nu_0 \times 20\lambda_0)^2 \times 8 \text{ Bytes} \tag{6.1}$$

$$\sim 10 \text{ MB} \tag{6.2}$$

This is a rather modest memory requirement, making such configurations computable on a laptop. If we now consider a beam comprising harmonics up to order $n_h \sim 100$, the maximum frequency is of course $\nu_{max} \sim 100\nu_0$, while the field falling length is still bound to the global duration of the beam $\tau \sim 10\lambda_0$, including in the transverse dimensions again due to the large divergence of a very focused beam, which implies,

$$\mathcal{M}_h \sim 10 \times (2 \times 100\nu_0 \times 20\lambda_0) \times (2 \times 100\nu_0 \times 10\lambda_0)^2 \times 8 \text{ Bytes} \tag{6.3}$$

$$\sim 100 \text{ GB} \tag{6.4}$$

Combined with the time constraint, this amounts to a computational volume of about 2.5×10^4 CPUhours/run, and thus marks the need for a large scale computing infrastructure.

Chapter 7

Harmonic spectra from PIC simulations

Under suitable interaction conditions, an overdense plasma irradiated by an ultra-intense laser pulse effectively acts as a mirror of optical quality, affecting essentially only the time spectrum of the field from the Doppler effect caused by its relativistic oscillations, without inducing major optical aberrations [9, 12, 260, 272, 284, 343, 344].

In these conditions, it is legitimate to approximate the reflected field by a superposition of monochromatic components each having a Gaussian spatial profile. Then the field is entirely determined by the data of $w_p(\omega)$, $R_p(\omega)$ and $A(\omega)$, respectively the (frequency-dependent) beam waist, radius of curvature and time spectrum of the main component of the electric or magnetic field, all taken in the PM plane. In this work we assumed that w_p and R_p were the same for all frequencies, implying they only encode the opening angle of the RPM beams (the diffraction parameter then being equal to $\varepsilon = w_p/R_p$ if we assume $\omega w_p \gg 1$ for all frequencies ω). The non trivial information about the PM harmonics generation is then entirely contained in the frequency spectrum $A(\omega)$, including its maximal attainable amplitude for a given field energy. This critical data was provided by Particle-In-Cell simulations using the WarpX+PICSAR framework [249–251, 325], as presented in sec. 2.2.2.

As specified in the main text, we used two spectra in this study, corresponding either to sub-optimal or optimized parameters of the laser-plasma interactions generating the RPM field. In both cases, the simulated laser was of wavelength $\lambda_0 = 800$ nm, duration $\tau = 20$ fs and normalized vector potential amplitude $a_0 = 80$. The bulk to vacuum plasma (electronic) density profile is $n_e(x > 0) = n_{\max} e^{-x/L_p}$, with $L_p = \lambda_0/20$ and $n_{\max} = 240 n_c$, where n_c is the plasma critical density for wavelength λ_0; besides, $n_e(x < 0) = n_{\max}$. The only difference between those two cases is the angle of incidence, of 45° and 55° respectively for the sub-optimal and optimized case. Both simulations were run in one dimension in the Bourdier frame [345]. Extensive parametric scans in 1D and 2D, backed with some 3D simulations, indeed show that 1D spectra faithfully depict the 3D configuration as long as the waist on PM is larger than about 4 λ_0 [281].

The modulus of these numerical spectra is shown in Figure 7.2, in the PM plane and at focus. The PM plane data corresponds to the output of the PIC simulation. In order to extract the propagative component of the field from these simulations, field values are actually recorded in a plane away from the PM surface, and then backpropagated on PM surface by vacuum Maxwell's equations. Spectra at PM focus are calculated from the PM plane spectra assuming perfect focusing, *i.e.* $E(\omega)|_{x=x_{foc}} \propto \omega \times E(\omega)|_{x=x_{PM}}$. It then appears that slowly decaying spectra can be obtained, with roll-off parameters (see sec. 8.2) of $s = 7/5$ and $s = 3/5$, with harmonics numbers of the order of a few tens in PM plane, resulting in quasi-constant harmonics amplitude at PM focus up to an harmonic order of more than 50 in the optimal case.

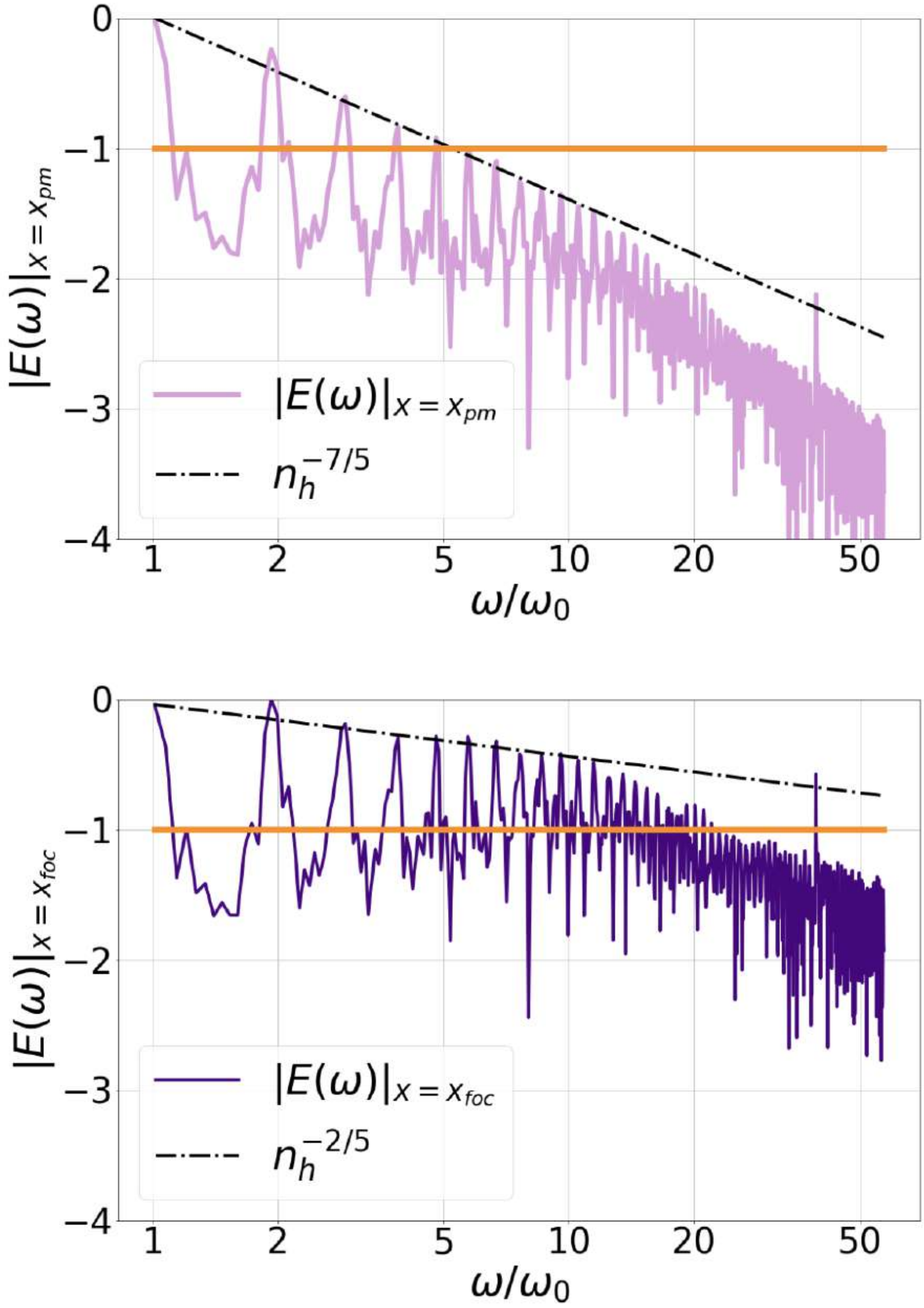

Figure 7.1: **Time spectrum of the main component of the electric field on-axis extracted from Particle-In-Cell plasma mirror simulations (logscale).** Original spectrum of the sub-optimal RPM beam recorded in the plasma mirror plane **(top)**, and the resulting spectrum at focus **(bottom)** assuming perfect focusing. The 10^{-1} level is shown (orange line) so as to provide a proxy for the cutoff harmonic order.

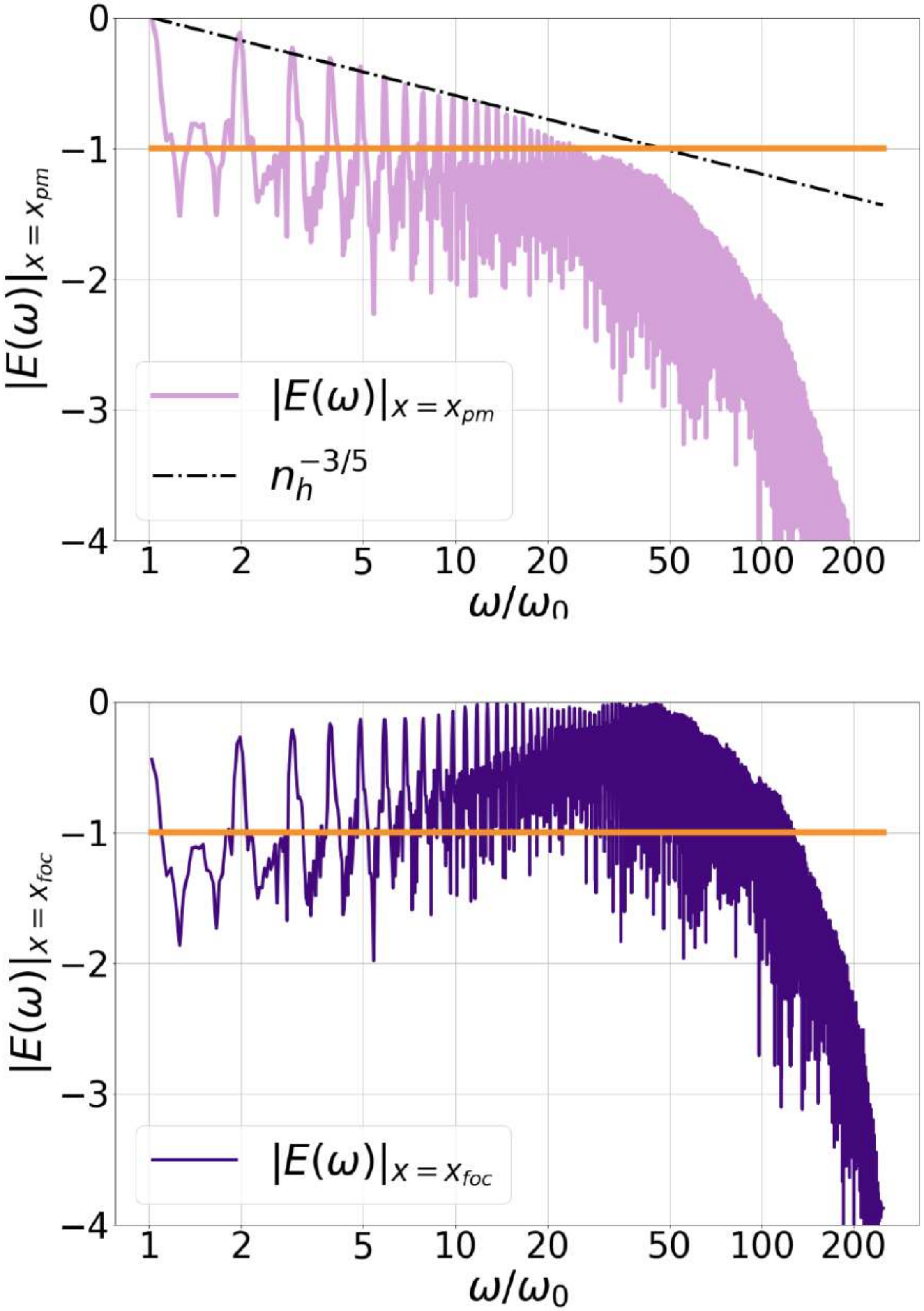

Figure 7.2: **Time spectrum of the main component of the electric field on-axis extracted from Particle-In-Cell plasma mirror simulations (logscale).** Original spectrum of the optimal RPM beam recorded in the plasma mirror plane **(top)**, and the resulting spectrum at focus **(bottom)** assuming perfect focusing. The 10^{-1} level is shown (orange line) so as to provide a proxy for the cutoff harmonic order.

Abstract of Part III

The results of our work on the physics of extremely intense relativistic plasma mirror light either in a vacuum or in the presence of matter are presented.

Chapter 8 details the effects of the electromagnetic field couplings with the electron-positron field in the absence of particles. More specifically, we compute spectra of photons scattered in the field in different configurations, and specify a power threshold for the occurrence of Schwinger pair creation in such fields.

Chapter 9 displays the outcome of the interaction of relativistic plasma mirror light with matter particles, present either in the form of an initially solid target, or of a high-energy electron beam. Distinct properties of the resulting macroscopic configurations are examined, as well as the involved individual elementary processes.

Part III

Quantum processes in the light of relativistic plasma mirrors

CHAPTER 8

Quantum vacuum processes in the light of relativistic plasma mirrors

In conceiving a "light beam", as in particular reflected from a plasma mirror, one often lends pictures from a well-defined configuration of the electric and magnetic fields in space. These originate from Maxwell's classical theory, which remarkably well describes macroscopic electromagnetic phenomena. In this framework, the field exists in all space, while matter is localized at some points and interactions are local. This allows conceiving a "vacuum" state where no matter is there, and all properties of the field derive from laws devoid of reference to any other physical system[1]. Formally, in classical theory the electromagnetic field in a vacuum is an isolated system.

Relativistic quantum theory however reveals that all fundamental degrees of freedom come in the form of fields permeating all space, and already quantum mechanics asserts their rest state, which cover the classical notion of absence of particles, can never be strictly assumed. Therefore an inert vacuum can in principle not exist, nor a single field be in perfect isolation. Since they can, each constantly interacts with all the other ones, be it through transitory – so-called "virtual" – states when no particles are observed. Considering, for our part, an excited electromagnetic field with all other fields at rest, this universal interaction can be logically displayed in three parts; endogenous evolution of photons, their direct coupling to charged fields, here *via* virtual states, and coupling of these fields to possibly neutral ones including the photon field. A self-interaction of light effectively results, persistently mediated through the other sectors. The empirical success of classical electrodynamics naturally implies such processes are extremely rare under usual circumstances. However, as unprecedented intensities are being reached, interaction of light with the quantum vacuum newly stands both as a tangible effect and a promising probe for fundamental physics.

In this chapter, we present results on the opportunity to use extremely intense, plasma mirror generated harmonics beams to this purpose. Details on the context of current efforts to detect the self-interaction of light will be given first. Computation of vacuum photon scattering from harmonics beam will then be presented, either from a single focused beam, in a second section, or using a secondary beam as a probe for the harmonics-polarized vacuum, in a third section.

8.1 The search for light-by-light scattering

According to the Standard Model, first deviations from free electromagnetic propagation stem from the coupling to the electron field, controlled by the electron mass m and the coupling constant e. Together they define the characteristic field scale of Quantum Electrodynamics, $F_S = m^2/e$ in Lorentz-Heaviside units with $c = \hbar = 1$, that is

---

[1] *e.g.* the free Maxwell's equations.

$F_S \simeq 1.32 \times 10^{18}$ V.m$^{-1} \simeq 4.4 \times 10^9$ T, which marks the onset of the spontaneous coherent field decay into real electron-positron pairs known as the nonperturbative Schwinger process [86, 327, 346]. Much below this threshold though, dynamics still bears the mark of this coupling through virtual electron-positron pairs, giving rise to an effective electromagnetic self-interaction with a perturbative component only suppressed by powers of F/F_S [327, 347–350]. Since the strongest macroscopic fields achievable to date, provided by femtosecond multi Petawatt-class lasers focused near diffraction-limit, reach $F_{\text{las}} \sim 10^{-3} \times F_S$, direct observation of fully nonperturbative vacuum processes such as pair creation seems precluded in a foreseeable future, while research efforts devoted to light-by-light scattering have pointed out the yet elusive nature of this process together with the exciting possibility to attain a discernible signal in several optimized configurations [176–196, 351] (see also [352] and references therein). These field configurations typically involve multiple colliding intense optical pulses, or in some cases coupling to a high-energy photon beam, providing existing and upcoming facilities with challenging experimental programs.

In this chapter, we examine how RPM sources compare in triggering these effects and present quantitative predictions on the quantum vacuum signatures produced by these extremely intense light sources. To achieve this, we developed and benchmarked at very large scale state-of-the-art numerical tools able to realistically simulate such field configurations.

The computational methods have been detailed in sec. 2.3. It consists for the most part in a parallel numerical implementation of the Stimulated Vacuum Emission theoretical framework introduced by the authors of [303]. Our plasma mirror generated harmonics beam model, which relies on the assumption that each monochromatic component of the field is Gaussian, has been exposed in sec. 2.3.3. The algorithm validation is presented in Chapter 3, from the results obtained in four simple reference cases: *i)* two counter-propagating Gaussian beams *ii)* a single focused Gaussian beam *iii)* a Gaussian beam colliding with a plane wave at an angle *iv)* an idealized harmonic beam made of $n_h = 2$ and 3 harmonics of a fundamental frequency of equal amplitude at focus. These reference cases provide, along with extensive analytical studies, both a benchmark for the code and a basis for understanding the more complex situation of a realistic harmonic beam produced from laser plasma interaction.

The results obtained with our numerical code applied to RPM generated harmonic beams are then presented below. In order to gain theoretical insight into the photon signal dependence upon the harmonic beam spectrum, the RPM beams results are compared with the idealized harmonic beams of Chapter 3 with $1 \leq n_h \leq 16$, and supplemented with analytical predictions derived from a simple model of these field configurations, detailed in Chapter 4.

Beyond maximizing the number of scattering events, in practice all-optical experiments for probing the quantum vacuum have to confront with the problem of clearly assessing the quantum origin of the detected photons. This may prove all the more crucial in the RPM configuration due to the possibly abundant emission of ”background photons” of non-quantum origin during the laser-plasma interaction. In view of identifying ways to relax the associated experimental constraints, two hybrid scenarios are finally presented in a third section, where the Doppler harmonics field plays the role of an ultra-intense pump while the polarized vacuum is probed by a controlled auxiliary source. We considered for the probe either a mildly focused PW-class infrared pulse, or a 100 TW-class green laser beam.

A conclusion of this study will finally be exposed along with a brief outlook.

8.2 Photon scattering in the focused harmonics field

We here turn to the study of plasma mirror generated fields as sources for the quantum vacuum processes of photon-photon scattering and Schwinger electron-positron pair creation. The most basic associated configuration is sketched in Figure 8.1. In the interaction of a relativistic-intensity laser (normalized vector potential $\xi = eE_0/(mc\omega_0) > 1$) with a sharp solid-density plasma surface, the electron population effectively acts as a "relativistic oscillating mirror" and thus converts by Doppler effect the incident laser pulse into a train of sub-wavelength pulses, equivalently described as a coherent superposition of harmonics of the initial laser beam, with effective harmonics orders up to $n_h \lesssim 100$ [9, 12, 260, 272, 284, 343, 344].

Although crucial to many applications including the present one, the analytical modelling of such fields remains very challenging to date, especially regarding the correct prediction of the spectrum amplitude and phase, and therefore of the associated maximum attainable field amplitude. We addressed this difficulty via first-principles kinetic Particle-In-Cell (PIC) simulations [353] of the harmonics time spectrum at a point near its region of generation. The numerical data obtained from these simulations allows us to fully reconstruct a realistic 3-dimensional harmonic field, under the hypotheses that *i)* the spatial profiles $E(\mathbf{x}, \omega)$ of the harmonic beams are well-described by the Gaussian paraxial field expressions at each frequency ω, and *ii)* all frequencies share the same waist w_p and radius of curvature R_p in the plane of generation, set to coincide with the plasma mirror plane of the original PIC simulation (see *e.g.* [12, 281] for a motivation from simulation results).

We studied two distinct harmonic fields, corresponding to two different conditions of generation of their original time spectrum. They are both generated by a multi-PW class laser of wavelength $\lambda_0 = 800nm$, duration $\tau = 20$ fs, normalized potential $a_0 = 80$ on the PM surface, waist on PM $w_p = 5\lambda_0$, with an optimized vacuum-plasma density gradient of $\lambda_0/20$ (see [12, 13, 281, 354] for details on optimal harmonics generation and Chapter 7 for simulation details and spectra), and only the incidence angle is varied. The choices employed here are either 45° or 55°. As the latter angle is found to be an optimum, we refer to the associated fields as optimal harmonic beams. On the other hand, an angle of 45° gives rise to a sub-optimal harmonic beam (see Chapter 7). In all studied cases, the initial field configuration was defined in the PM plane using zeroth order paraxial expressions [330] before projection (*cf.* sec. 2.3.3), and the total energy in the harmonic beam was set to $W = 50$ J.

8.2.1 Theoretical dependence of the scattered photon numbers over the harmonics beam parameters

For a single beam of frequency k_0, it has been shown [297, 333] (see also Chapter 4 for a detailed calculation) that the number of vacuum scattered photons increases with tighter focusing, demonstrating that the induced increase in field invariants overcomes the decrease in interaction volume. More specifically, analytical calculation of the photons emitted by a single frequency focused Gaussian pulse gives:

$$N_{t,\perp} \simeq C_{t,\perp} \left(\frac{\mathrm{k}_0}{m}\right)^3 \frac{1}{(m\tau)^2} \left(\frac{W}{m}\right)^3 \varepsilon^8 \tag{8.1}$$

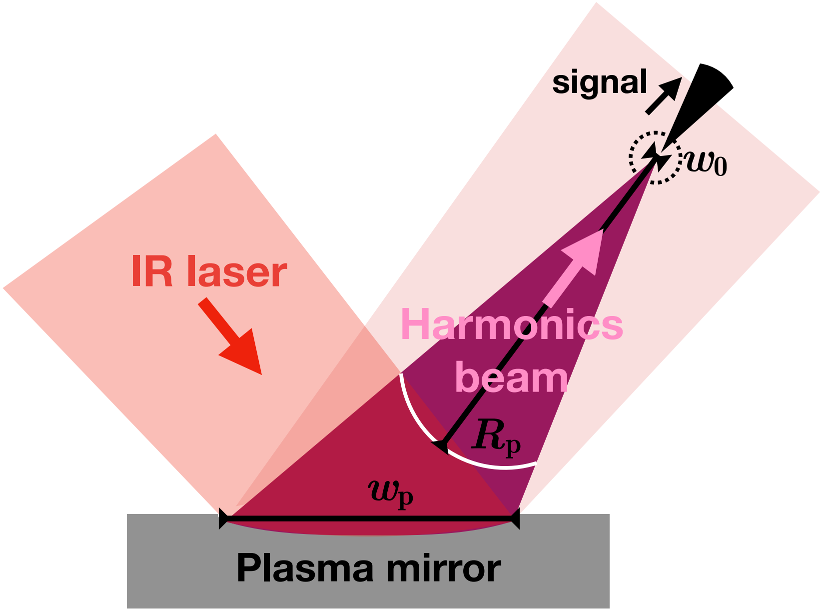

Figure 8.1: **Schematic representation of a RPM configuration.** The driving intense infrared laser impinges on the PM surface with waist w_p and is reflected as a focused harmonics beam with curvature radius R_p and waist at focus w_0. The signal photons are scattered around the direction of propagation of the harmonics beam.

where $C_{t,\perp}$ is a polarization-dependent constant, m the electron mass, τ its duration assuming a time profile of the form $E(t) = E_0 e^{-\frac{(t-x)^2}{(\tau/2)^2}}$, W its total energy, and $\varepsilon = 2/\mathrm{k}_0 w_0$ its diffraction parameter. The diffraction parameter being physically constrained to $\varepsilon \lesssim 1/\pi$, converting the beam to higher frequencies then appears as a straightforward way to increase the scattered photon number. The technique considered in this study for physically achieving this conversion involves generation of high-harmonics of the initial frequency, so that the energy ends up distributed among many different frequencies.

We can refine the calculation to account for this multiple frequency content along the line of [299]. This is done by assuming that $E_h = \sum_{n=1}^{n_h} E_{0n}$ with $E_{0n} = \sqrt{\frac{\delta W_n}{\tau w_{0n}^2}} = E_0^g \frac{n^{-s+1}}{(H_{2s}(n_h))^{1/2}}$ for a fundamental frequency Gaussian pulse amplitude $E_0^g = \sqrt{\frac{W}{\tau w_{01}^2}}$ and $H_q(n) = \sum_{m=1}^{n} m^{-q}$, where we have introduced the total beam duration τ, energy W, roll-off parameter of the power law spectrum s, and energy fraction δW_n and waist at focus w_{0n} of harmonic component of order n. Besides, in the limit $n_h \gg 1$ and $s \lesssim 2$ the field profile takes the form of a train of sub-wavelength pulses, whose individual profiles can then be approximated as Gaussian with $\tau_h \sim 1/n_h \mathrm{k}_0$, $w_h \sim w_0/n_h$, leading to

$$N_{t,\perp}^h = N_{t,\perp}^g \frac{1}{(H_{2s}(n_h))^3} \left(\frac{H_{s-1}(n_h)}{n_h}\right)^4 \times (H_{s-1}(n_h))^2 \tag{8.2}$$

with $N_{t,\perp}^g$ the photon number corresponding to a fundamental frequency Gaussian beam of same duration and energy up to a constant proportionality factor. In the case of optimal PM high-harmonics generation we have $s \simeq 1$, so that,

$$N_{t,\perp}^h \propto n_h^2 . N_{t,\perp}^g \tag{8.3}$$

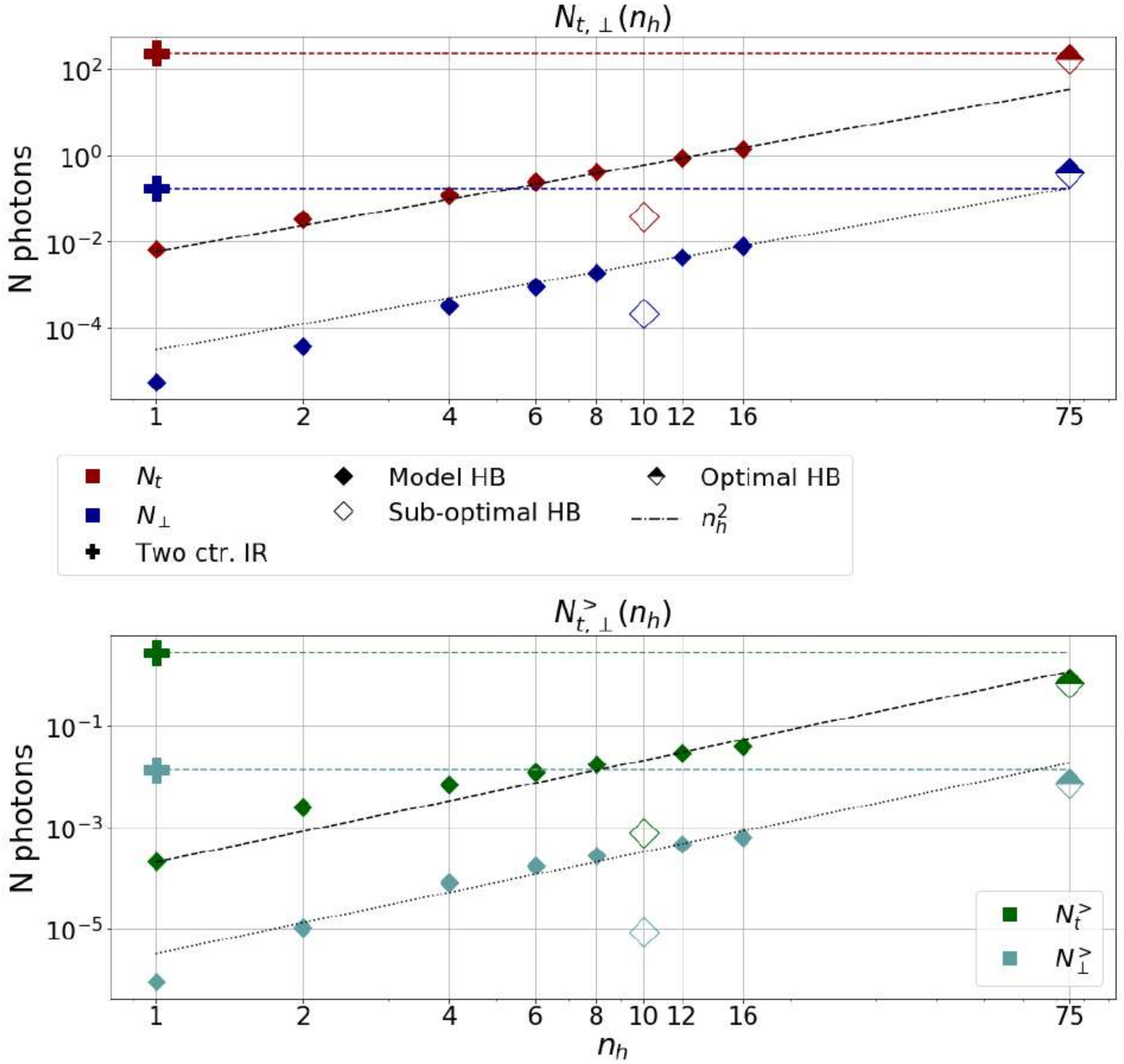

Figure 8.2: **Integrated photon numbers as a function of n_h for a model beam made of n_h harmonics of its fundamental frequency, with quasi-equal diffraction parameter ε, focal point and amplitude at focus, or PM-generated beams of effective number of harmonics n_h.** The case of two counterpropagating fundamental frequency pulses **(crosses)** is shown at $n_h = 1$ for comparison. **(top)** Total number of photons N_t or with crossed-polarization $N_\perp$. **(bottom)** Total numbers of discernible photons, emitted outside of the $\theta = \arcsin(2\varepsilon)$ cone directed along the beam propagation direction. All beams are at diffraction limit ($\varepsilon = 1/\pi$).

where $n_h \sim 100$, implying this method can *a priori* enhance the emitted photons number by 4 orders of magnitude over a single tightly focused infrared laser beam of same duration and energy.

As a first test of the viability of this prediction for PM-generated harmonics, we consider the simpler case of n_h harmonics at $s = 1$, *i.e.* such that the amplitude of each harmonic is equal at focus (*cf.* for instance [12, 281] and Chapter 7 for comparison with PM-generated spectra) for n_h ranging from 2 to 16. In view of the RPM scenario we simply considered that all harmonics are perfectly in phase in some plane at a finite distance from focus, and share the same waist $w_p = 5\lambda_0$ and radius of curvature R_p in this plane, so that they all approximately have the same diffraction parameter and focal point provided focusing is strong enough ($\lambda_0, w_0 \ll w_p$). The global duration and energy of the model beam are taken respectively as $\tau = 25$ fs (in practice by defining an $A(\omega)$ with peaks of appropriate spectral width, *cf.* sec. 2.3.3), chosen close to the effective duration of the harmonics pulses train, and $W = 50$ J.

In Fig. 8.2 we plot the number of scattered photons as a function of the harmonic number n_h for fixed other parameters. In particular, we take $R_p = \pi w_p$ so that all frequencies ω satisfying $\omega w_p/2 \gg 1$ are at diffraction limit. Besides, we define discernible photons as those scattered at an angle $\theta = \sphericalangle(\mathbf{e}_x, \mathbf{k})$ with the harmonic propagation direction greater than $\theta_2 = \arcsin(2\varepsilon)$, which corresponds to a background laser photon density drop off of at least $1/e^8$ in a Gaussian beam model. The corresponding numbers are denoted by a superscript $>$. The results confirm the increase in signal photons with the increase of harmonics number, and the scaling law reported in Eq. 8.3 at least for the total photon numbers. The crossed-polarized photons display an even faster increase with n_h at first, before converging to the n_h^2 trend. At $n_h = 16$, photon numbers reach $N_t = 1.443$ ($N_\perp = 8.152 \times 10^{-3}$), and $N_t^> = 3.955 \times 10^{-2}$ ($N_\perp^> = 6.311 \times 10^{-4}$), demonstrating enhancement factors of $a_t \equiv N_t/N_t^{n_h=1} = 2.1 \times 10^2$ ($a_\perp \equiv N_\perp/N_\perp^{n_h=1} = 1.5 \times 10^3$) for the total photon numbers, and $a_t^> = 1.8 \times 10^2$ ($a_\perp^> = 7.0 \times 10^2$) for the discernible signal. We note that the smaller increase of the discernible signal may be due to the discernibility criterion invoked here: as high-frequency photons tend to be more collimated, a frequency-independent exclusion cone generically disfavors configurations with a substantial high-frequency energy content.

For comparison, we also show the photon numbers attainable with PM-generated harmonic beams created in sub-optimal or optimal laser-plasma interaction conditions. In both cases we define their associated effective harmonics number as

$$n_h \equiv \sum_{n=1}^{\infty} |E_{foc}(n\omega_0)|/|E_{foc}(\omega_0)| \tag{8.4}$$

with E_{foc} the amplitude of harmonic order n at focus, consistently with the $s = 1$ hypothesis.

This already reveals that while sub-optimal RPM (sub-optimal HB in Fig. 8.2) allows for enhancement factors of $a_t = 5.9$ ($a_\perp = 3.9 \times 10^1$) and $a_t^> = 3.5$ ($a_\perp^> = 9.7$), it falls well below the values expected from our model due to the fast decrease of the spectrum in this case. On the opposite, the optimal harmonic beam results (optimal HB in Fig. 8.2) are much more closely in line with Eq. 8.3, and even exceed it in total photon numbers, as a consequence of the slight growth of the harmonics amplitudes at focus for the first dozen of harmonics orders (*cf.* Chapter 7).

The corresponding enhancement factors are $a_t = 2.5 \times 10^4$ ($a_\perp = 7.3 \times 10^4$) and $a_t^> = 3.1 \times 10^3$ ($a_\perp^> = 8.0 \times 10^3$), demonstrating the efficiency of RPM under these conditions, and therefore the importance of optimizing harmonic generation to obtain good photon signal. The resulting total photon numbers for a diffraction limited focusing ($\varepsilon = 1/\pi$) are respectively $N_t = 4.738 \times 10^{-2}$ ($N_\perp = 6.047 \times 10^{-3}$) for the sub-optimal beam, and $N_t = 170.3$ ($N_\perp = 4.088 \times 10^{-1}$) for the optimal beam. The discernible photon numbers are $N_t^> = 7.580 \times 10^{-4}$ ($N_\perp^> = 8.696 \times 10^{-6}$) for the sub-optimal beam, and $N_t^> = 1.110$ ($N_\perp^> = 4.777 \times 10^{-2}$) for the optimal beam, which implies about one discernible photon per shot.

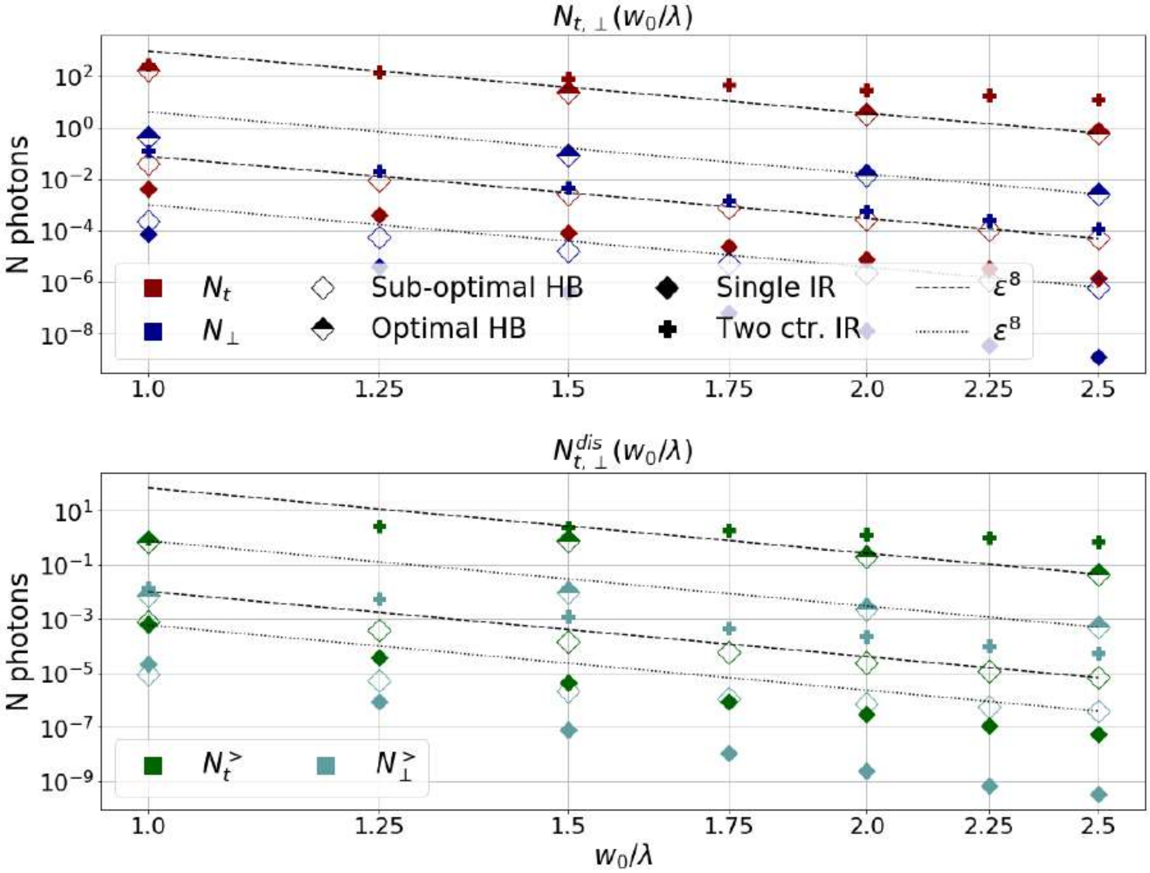

Figure 8.3: **Integrated signal photon numbers as a function of w_0/λ, the waist to wavelength ratio common to all frequencies. Here we present results for a relativistic PM-generated coherent harmonic beam (HB), a single fundamental frequency pulse (Single IR) and two counter-propagating fundamental frequency pulses (Two ctr. IR), focused in a vacuum. (top)** Total number of photons N_t or with crossed-polarization $N_\perp$. **(bottom)** Total numbers of discernible photons, emitted outside of the $\theta = \arcsin(2\varepsilon)$ cone directed along the beam propagation direction (both directions for **(Two ctr. IR)**).

8.2.2 Photon scattering results

Results regarding the photon numbers dependence on the beam diffraction parameter ε are plotted in Fig. 8.3. In all considered cases, the frequency-dependent waist at focus satisfies $w_0(\omega) \ll w_p$ for all frequencies, from which we can derive $\varepsilon = 1/\pi(w_0/\lambda) \simeq w_p/R_p$ so that the diffraction parameter is indeed nearly the same for all frequencies. We observe manifestly the same trends as in the cases of a single Gaussian beam [297, 333], namely a scaling with ε^8 of all photon numbers. This is fully consistent with the above described analytical estimates Eq. 8.1 for the single Gaussian beam, and Eq. 8.3 derived from a Gaussian pulse model of the individual harmonics pulses.

For reference, we can compare these results to the one obtained for the same total energy with two fundamental frequency pulses in head-on collision, each carrying half the total energy (Two ctr. IR in Fig. 8.2). The importance of this configuration has already been exposed in sec. 8.2. With our chosen parameters (50 J total energy, 25 fs duration, $\varepsilon = 1/\pi$)), the resulting values of the total and discernible photon numbers are

$N_t = 241.1$ ($N_\perp = 1.176 \times 10^{-1}$) and $N_t^> = 2.756$ ($N_\perp^> = 1.321 \times 10^{-2}$).

In the optimal case, it therefore appears that although a single beam photon signal is generically suppressed by at least ε^4 compared to counter-propagative beam configurations, individual PM-generated beams reach comparable signal levels, and hence allow bypassing the fine alignment and synchronisation conditions required to obtain sizable signals in multi-beam configurations. The final numbers remain admittedly low, so that the costs and benefits of each approach still has to be carefully determined. In particular, RPM alleviates the constraint of spatial and temporal synchronization at the micron and fs level of multiple focused high-power laser beams, demanding instead a fine control of the laser-plasma interaction conditions. While promising paths are being explored to this end, it may still happen that the background radiation inherent to the harmonics-generating plasma excitation overcomes the increase in signal photons, precluding a conclusive vacuum photon detection in the harmonic beam direction. In order to overcome this potential limitation, in sec. 8.3 we present a compromise scenario close to the one put forward in [299], where a second beam is used to build a vacuum photon signal out of the plasma radiation direction, while we leverage the extreme harmonic beam intensity to relax the focusing and intensity constraints on this secondary beam.

8.2.3 Schwinger pair creation

The peak intensity obtained when focusing the optimal harmonic beam with 100 J total energy is close to 1.4×10^{28} W cm^{-2}, corresponding to field amplitudes of 17 % of the Schwinger critical value. At such scales it becomes relevant to investigate electron-positron pair creation via the Schwinger process. Although strictly speaking the vacuum QED formalism used in this work does not hold in the event of one or more pair creation, requiring *e.g.* a self-consistent semi-classical evolution of fields and particles as done by PIC-QED algorithms [301, 355], it nevertheless allows determining the number of pairs produced assuming no field-particles retro-action. Under the same hypotheses as for vacuum photon emission, together with the Keldysh adiabatic condition $\gamma_K = 1/ml_E F_0^{-1} \ll 1$ [356, 357], where l_E is the field transverse space in the polarization direction and F_0 its characteristic amplitude in Schwinger field units, both safely met in our cases of study, this can be done integrating the local production rate (Eq. 2.51) in the full simulated spacetime volume [358] .

In Fig. 8.4 we show the resulting numbers for the field configurations of a single focused Gaussian pulse, two counter-propagating Gaussian pulses (all supplemented with Gaussian time envelopes as in previous section), and for the optimal harmonic beam. All beams are focused close to their diffraction limit ($\varepsilon = 1/\pi$) and only their energy (amplitude) is varied. In all cases the number of pairs grows exponentially with the intensity, and thus increases very fast past the one pair creation threshold. The corresponding threshold intensity however varies widely with the field configuration. For two counter-propagating Gaussian pulses, pair creation becomes significant at intensities of $I_0 \simeq 2.4 \times 10^{27}$ W.cm^{-2} ($E = 7.21 \times 10^{-2}\ E_S$), two orders of magnitude below the Schwinger intensity, in agreement with [197–200]. As noticed in the previous studies, this is possible in spite of the local production rate suppression, due to the macroscopic size of the interaction volume compared to the electron Compton scale. On the other hand, in a single beam configuration we find that intensities of $I_0 \simeq 7.5 \times 10^{28}$ W cm^{-2} ($E = 7.03 \times 10^{-1}\ E_S$) are required for a similar interaction volume, in agreement with [200, 359], as a consequence of the same invariants suppression discussed previously for photon-photon scat-

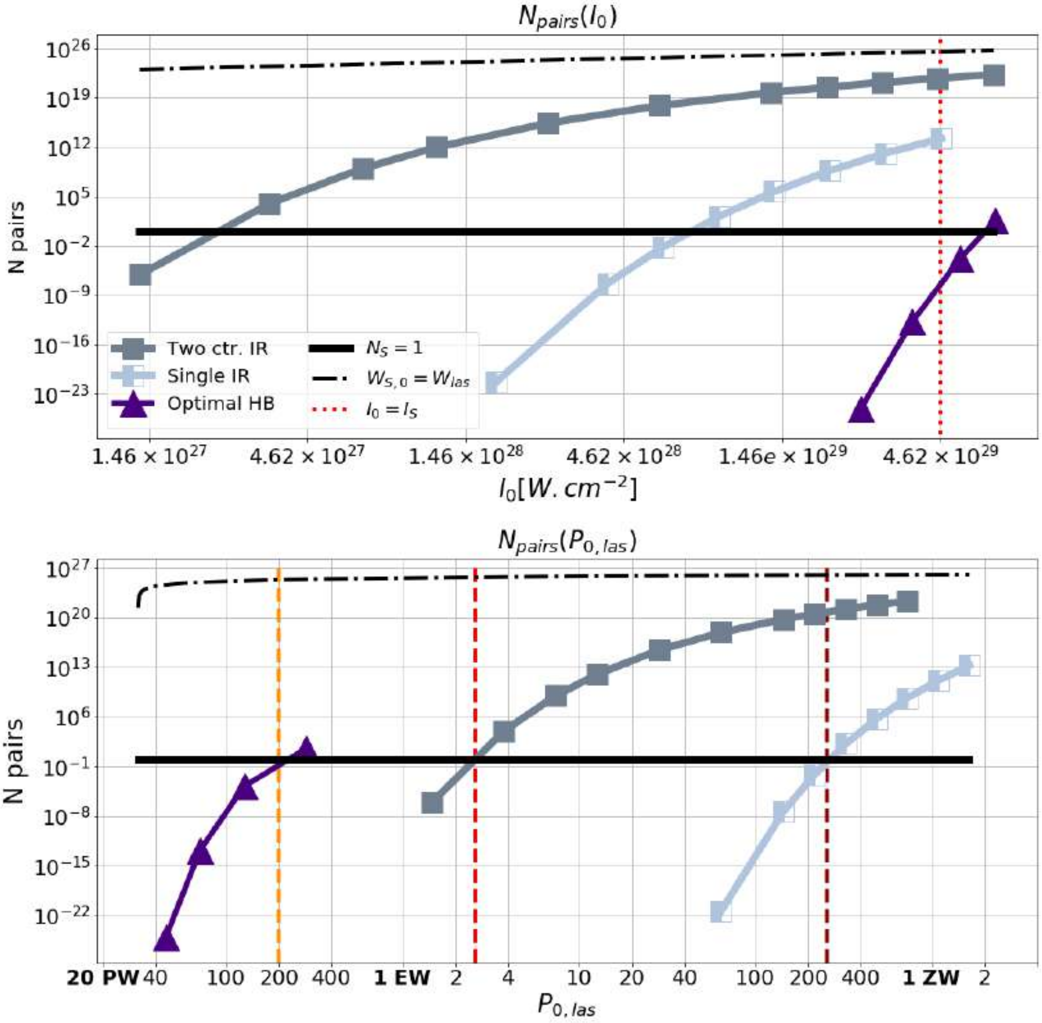

Figure 8.4: **Number of Schwinger electron-positron pairs created neglecting particles-field retroaction. (top)** Number of Schwinger pairs created as a function of peak intensity for the field configurations of two fundamental frequency pulses in head-on collision **(Two ctr. IR)**, a single one **(Single IR)** and an optimal PM-generated harmonic beam **(Optimal HB)**; all beams are focused at diffraction limit. The black lines show the thresholds of one created pair (solid) and pairs number corresponding to total field conversion to pairs mass energy (dashed). **(bottom)** Number of Schwinger pairs created as a function of driving beam power. In the harmonic beam scenario, power values stand for the laser incident on plasma mirror surface, accounting for reflection coefficients R_{pm} set to the realistic value of 70 % [281].

tering. In this regard the smaller interaction volume of the harmonic beam explains its even higher threshold of $I_0 \simeq 6.4 \times 10^{29}$ W cm^{-2} ($E = 1.18\ E_S$). For that matter, we note this value implies that exceeding the critical field value on macroscopic space extents is in principle possible within the RPM scheme. This is in contrast with other beam configurations tailored for enhancing vacuum pair production and subsequent QED cascades, such as counter propagation geometries, where efficient light to matter conversion once at least one pair is created effectively limits the intensity attainable with such fields [58, 59, 201–203].

Assuming fixed focusing at diffraction limit in all cases, we can then convert these intensity thresholds into requirements on the power of the driving beams, which offers a basic assessment of experimental feasibility. In order to avoid unnecessary modelling specifics we define power as $P_0 \equiv W/\tau$, where the total beam energy W is our simulation input and $\tau = 25$ fs, matching the duration of the considered Gaussian pulses, and the approximate harmonics train duration. The power values determined along these lines correspond either to the sum of the powers of the individual beams in the case of counterpropagating pulses, to the total beam power in the single pulse case, and to the hypothetical power of the laser pulse before PM interaction in the case of the harmonic beam, for a realistic reflection coefficient of 70 % [281]. We assume in particular that the harmonic spectrum remains independent of the total field energy. The latter assumption is an idealization of course, however it does not strictly rely on the invariance of laser-plasma interactions over a wide intensity range. Indeed one could in principle simply increase the laser waist on plasma mirror so as to maintain a quasi-constant incident intensity; for instance, a 200 PW laser with incident waist $w_p = 25\lambda_0$ reaches $a_0 \simeq 115$, only about 50 % more than a 3 PW laser with $w_p = 4.5\lambda_0$ ($a_0 \simeq 75$) as used in the PIC simulation from which the spectrum was extracted. From this perspective, RPM clearly emerges as the most favorable configuration, as Schwinger pair production first occurs for laser powers between 160 PW and 200 PW ($W_{las} \lesssim 5$ kJ at 25 fs), barely beyond reach of the most powerful facilities planned to date [5], and allowing a single-beam setup. According to our computation, achieving the same without harmonics conversion would require close to 2.6 EW cumulative power with two counter-propagating pulses ($W_{las} = 65$ kJ), a value that could potentially be reduced to 1.1 EW ($W_{las} = 27$ kJ) *via* the coherent combination of more individual beams in the so-called dipole wave setup [360]. The latter requirements remain about one order of magnitude beyond the currently envisioned facilities. Using a single optical pulse does not stand as a viable option in this respect, with a required power of 200 EW ($W_{las} = 6.4$ MJ).

8.3 Harmonics assisted secondary beam photon scattering

As demonstrated in [297] and consistently with analytical estimates, the numbers of signal photons emitted from a Gaussian beam colliding with a plane wave at an angle with the same linear polarization are maximized for a counter-propagating geometry, and vary as $(1 - \cos(\theta_{\text{collision}}))^4$ around this optimal collision angle [361]. Besides, as explicited in Chapter 3, a counter-propagating geometry gives rise to nonvanishing invariants, which strongly enhances photon emission over a single focused beam situation. We therefore investigate here the coupling of the focused PM-generated beam, thought of as a high-intensity “pump” for the quantum vacuum, with a loosely focused counter-propragating single frequency beam, thought of as a well-controlled “probe” to be scattered off the intense, strongly localized harmonic beam focal spot (see Figure 8.5). This can *a priori* help to increase the *discernible* photon number in two ways, namely *i)* by emitting some signal photons, which can be interpreted as scattered probe photons, away from the plasma mirror specular direction likely polluted by background plasma radiations, and *ii)* by increasing the scattering angles of the probe photons, due to the high transverse momenta of the harmonic photons. In a semi-classical picture the latter effect can be explained by diffraction of the probe beam off the intense pump field polarizing the quantum vacuum in a sub-wavelength region. For these reasons all photon numbers given in the following

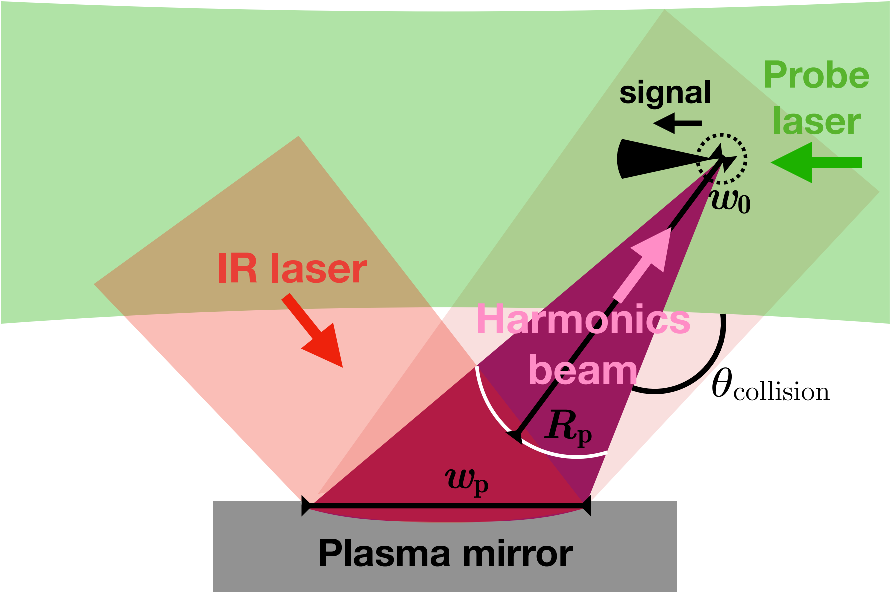

Figure 8.5: **Schematic representation of a secondary beam assisted RPM configuration.** A focused harmonics beam with curvature radius R_p and waist at focus w_0 is generated as in the basic RPM case, but is now made to collide with a well-controlled second pulse. Part of the signal photons are then scattered around the "probe" beam direction, which improves separation from the background photons.

correspond to "scattered probe photons", *i.e.* we completely discard photons scattered in the half ($\mathbf{k}-$)space around the harmonic beam propagation direction from the outset. We consider two different options for the probe, namely either (IR) a loosely focused Gaussian pulse with $\lambda_0 = 800$ nm, $\tau = 25$ fs, $I_0 = 2.5 \times 10^{21}$ W.cm^{-2} and $w_0 = 9\lambda_0$, or (Gr) an even less focused green laser with $\lambda_g = 527$ nm, $\tau = 100$ fs, $I_0 = 3.5 \times 10^{19}$ W.cm^{-2} and $w_0 = 14\lambda_g$. The first one can be thought of as a split part of a multi-Petawatt laser, whose second part would be driving the harmonic generation. The second option would typically involve an auxiliary 100 TW green laser close to the one suggested in [362]. In both cases, two polarizations of the probe beam are envisioned, both linear, with an angle $\psi = \sphericalangle(\mathbf{e}_{pr}, \mathbf{e}_h)$ with the harmonics polarization direction of either $\psi_t = \pi/2$ or $\psi_\perp = \pi/4$, aimed at maximizing the total or crossed-polarized photon numbers respectively [363] (in this context "crossed-polarized" means polarized in the direction perpendicular to the main polarization direction of the probe beam).

8.3.1 Theoretical dependence of the scattered photon numbers over the probe and harmonics beam parameters

In order to clarify to what extent can RPM improve over the single frequency beam signal in this configuration, we first computed the probe photon numbers scaling with the number n_h of harmonics, using the same model harmonic beam as in Chapter 3, colliding with the IR secondary beam.

These values show a slow increase in total numbers of photons, and a steeper increase in crossed-polarized photons; in the optimal harmonic beam case, N_t^p reaches levels comparable to the one of two counter-propagating beams at diffraction limit while $N_\perp^p$ exceeds those. Most importantly though, the number of discernible photons emitted outside of a

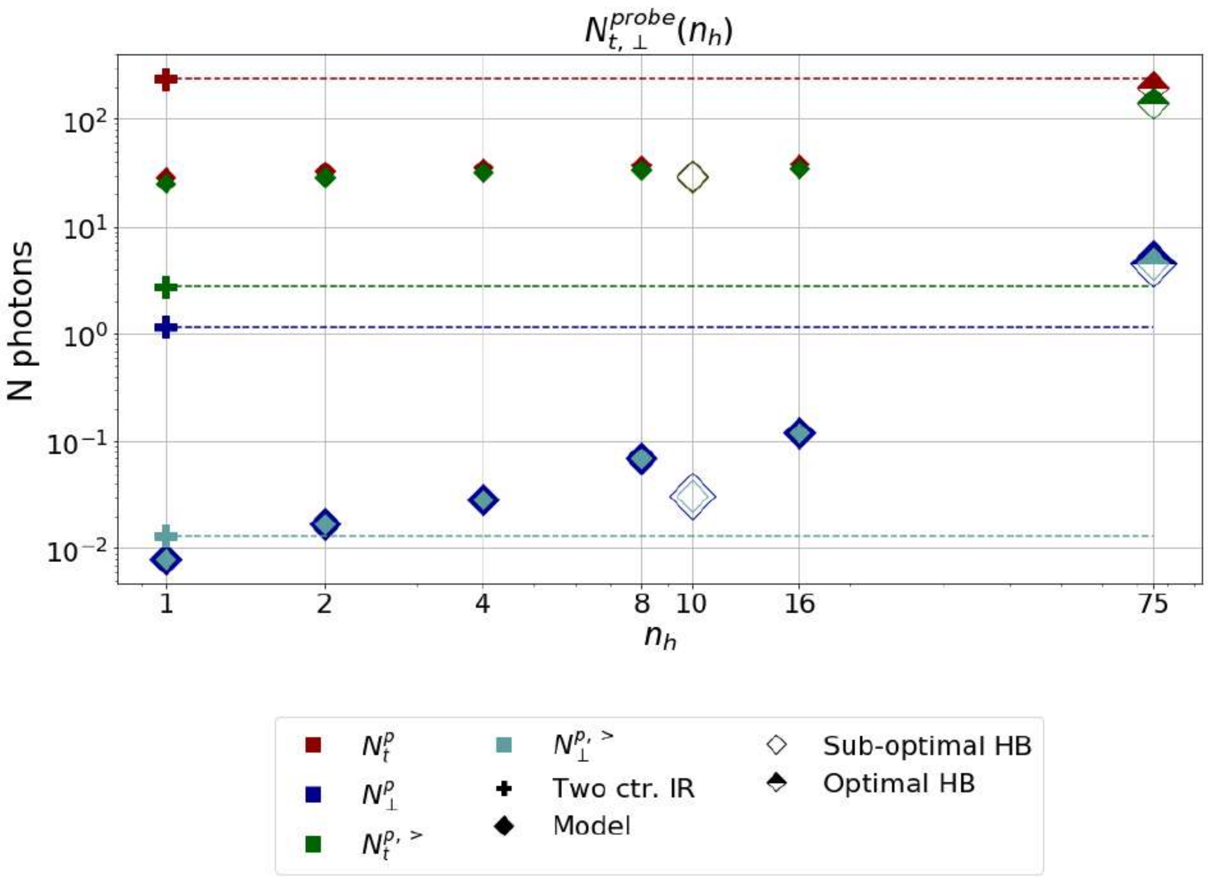

Figure 8.6: **Number of photons from a loosely focused beam scattered off a counter-propagating beam made of n_h harmonics of its fundamental frequency, or PM-generated beams with effective number of harmonics n_h, focused at diffraction limit.** Except from **(2 ctr. Gaus.)**, all shown number correspond to photons scattered in the half-space towards which the probe beam is directed, as denoted by a superscript p. The model beams are constructed as in sec. III. The PM-generated harmonic beams are linearly polarized at an angle $\psi_t = \pi/2$ compared to the probe beam main polarization direction.

$\theta = \arcsin(2\varepsilon_b)$ cone around the probe beam direction is almost equal to the total number of probe scattered photons. This is due mostly to the small probe beam opening angle, as the effect persists even in the single frequency case ($n_h = 1$ in Figure 8.6).

8.3.2 Numerical results and interpretation

The results for the PM-generated beams with varying probe beam parameters are displayed in Table 1. It confirms the very high number of probe photons scattered at large angles compared to the probe beam divergence, and shows that varying the probe beam polarization effectively allows to optimize total or crossed-polarized photon numbers in most cases.

The final numbers of discernible signal photons then appear significantly higher than in all the other configurations studied here. More specifically, resorting to RPM allows at most for a gain of almost two orders of magnitude in discernible photon numbers compared to directly using a split infrared pulse as both the pump and the probe for vacuum

HB spectrum	probe	$\sphericalangle(\mathbf{e}_{pr}, \mathbf{e}_h)$	N_t^p	$N_\perp^p$	$N_t^{p,>}$	$N_\perp^{p,>}$
sub-optimal	IR	ψ_t	29.6	3.11×10^{-1}	29.1	3.10×10^{-2}
		$\psi_\perp$	19.6	1.38	19.3	1.35
	Gr	ψ_t	1.43	7.72×10^{-3}	1.40	7.72×10^{-3}
		$\psi_\perp$	9.58×10^{-1}	7.49×10^{-2}	9.37×10^{-1}	7.34×10^{-2}
optimal	IR	ψ_t	199	4.58	$142 \mid 9.49_{2\omega_0}$	$4.58 \mid 2.61_{2\omega_0}$
		$\psi_\perp$	132	10.5	$94.2 \mid 6.31_{2\omega_0}$	$7.86 \mid 2.37_{2\omega_0}$
	Gr	ψ_t	24.7	4.16	$24.5 \mid 1.07_{\omega_g+\omega_0}$	$4.16 \mid 0.19_{\omega_g+\omega_0}$
		$\psi_\perp$	16.9	2.25	$16.8 \mid 0.70_{\omega_g+\omega_0}$	$2.22 \mid 0.14_{\omega_g+\omega_0}$

Table 8.1: **Number of probe beam photons scattered in the collision with a PM-generated harmonic beam, for different harmonics spectrum, probe beam and polarization directions.** The subscripts stand for numbers of probe photons emitted in the range $\Delta\omega = \omega_0/2$ around the indicated frequency.

polarization effects (comparing optimal HB and two ctr. Gaus. in Fig 8.6). Admittedly this achievement still has to be weighed against the additional experimental requirements of PM harmonics generation, however, we can identify two aspects in which the RPM scenario stands apart from simpler configurations.

First we note that the numbers of crossed-polarized photons benefits from even greater enhancements than the polarization insensitive photon numbers, reaching values higher than in any other configuration studied here by one to almost three orders of magnitude, respectively for the total and discernible populations (Figure 8.6).

Second and most importantly, a significant fraction of the probe photons undergo *inelastic* scattering with energy gains of $+\omega_0$, which corroborates the findings of [299]. In the case of the IR probe beam and optimal spectrum, this fraction can go up to 6.7 % in total, and 1.8 % of all the emitted photons are both crossed-polarized and have a $2\omega_0$ frequency, which amounts to more than 2 photons per shot. With the Gr probe beam and ψ_t polarization angle, more than one photon per shot is emitted in the $\omega_g + \omega_0 \simeq 2.5\omega_0$ range, and one every five shots adding the crossed-polarization constraint. Such photon signals are in principle detectable in experiments [298]. For reference, in the case of two counter-propagating pulses the proportion of inelastically scattered photons (at $3\omega_0$) is of the order of 0.01 %, and the model harmonic beam in collision with the IR probe yields about 0.3 % (at $2\omega_0$). This indicates that inelastic scattering in the probe beam direction is inherent to the interaction with a multi-frequency beam.

This property can potentially prove decisive for obtaining a signal discernible from the background of the driving laser photons beyond reasonable doubt. Indeed, the discernibility criterion used in our work as well as in many others [303, 326, 329] typically relies on the idealization of the photon distribution of the background beams as Gaussian, hence falling to negligible levels at a finite separation from their propagation direction. However, as there are about 20 orders of magnitude more background than signal photons, this assumption is extremely vulnerable to any laser imperfections or insufficient shielding against parasitic radiation [298], even at crossed-polarization. On the opposite, a large frequency separation could allow establishing the quantum origin of a photon on a much firmer ground.

8.4 Observing quantum vacuum dynamics through harmonics beams

Observing quantum vacuum processes with electromagnetic fields typically requires approaching the Schwinger field $F_S = 1.32 \times 10^{18}\ \mathrm{V\,m^{-1}} = 4.4 \times 10^{9}$ T, several orders of magnitude above current technological capabilities, and therefore pleads for any scheme maximizing the attainable field intensity. On the other hand, Lorentz invariance of the vacuum state implies that all the relevant expectation values depend on the Lorentz invariants of the field rather than on its amplitude, which generically explains their strong dependence upon the interaction geometry, and thus raises the question of the optimal configuration beyond achieved intensity. In this section, we have shown that optimal focusing of the harmonic beam produced in the reflection of a single Petawatt-class laser off a plasma mirror allows to generate as many vacuum photons as two perfectly counter-propagating Petawatt infrared pulses focused at diffraction limit and to significantly reduce the laser powers required to observe Schwinger pair creation.

The physical relevance of this result nevertheless crucially depends on the degree of control of the laser-plasma interactions achievable in an experiment. Besides the requirements of optimal harmonics generation and focusing [13], the level and nature of background plasma mirror emissions prevails as to which observations will be accessible. If the total radiated field after plasma mirror interaction can be consistently assimilated to the reflected harmonic beam, with sharp enough angular photon distribution, propagating in a vacuum, as we modelled it in this work, then it would be possible to detect vacuum photon scattering with the coherent harmonics focusing technique only. The coupling to a well controlled auxiliary beam significantly alleviates these constraints, only requiring low background emissions in the "probe" beam direction, which could be set close to counter-propagation with the harmonic beam. Furthermore, due to the high levels of inelastically scattered probe photons specific to this case, assessment of the quantum origin of the signal could then be made on a spectral basis, hence with potentially much higher confidence than solely on the basis of an angular discernibility criterion. As associated energy gains are of the order of $+\omega_0$, use of a $\omega_p \neq \omega_0$ frequency probe can result in even cleaner quantum vacuum signatures in the $\omega_p + \omega_0$ frequency range. Indeed, provided the probability of presence of residual charged particles in the overlap region of the beams can be made small enough such frequencies could not be generated by laser-matter interaction.

Irrespective of the chamber residual gas, whose density can be made small enough to empty the harmonics focal spot with high probability, the near-specular emission of relativistic electron beams directly from the plasma mirror surface is an experimentally established fact [260, 364], so that determining whether the above conditions can be met calls for a detailed study of these ejected electrons beyond the scope of this work. If these electrons are expelled from the harmonics field early enough, photon-photon scattering may still be observed. If on the opposite they radiate enough to preclude observation of photon-photon scattering, but do not trigger QED cascades, quantum vacuum processes could still be sought for at higher intensity in the form of Schwinger pair creation. If finally the electron beam dynamics results in prolific pair creation even before the Schwinger process can occur, detection of quantum vacuum effects from PM-generated beams would likely require more complex setups. Typically they would involve disentanglement of the generation and focusing steps, so as to refocus the harmonics beam using broadband visible-UV optics, either in a shielded part of the PM chamber or possibly even in another chamber [365]. In turn, direct interaction of the curved PM harmonics beam with matter, either in the form of beams or of a secondary target [300], would then open the way to yet unobserved regimes of plasma dynamics in strong-fields. This perspective is the focus of our next chapter.

CHAPTER 9

From relativistic plasma mirror light to extreme processes in matter

When charged matter particles are present in the strong field, sf-QED processes will deploy at a much wider scale than in the fermionic vacuum. Two simple factors directly concur to this fact. On the scale of elementary processes first, the relevant parameter quantifying the interaction of a particle of charge Q and mass M with momentum p with a coherent electromagnetic field F is,

$$\chi = \frac{Q\sqrt{(p_\mu F^{\mu\nu})^2}}{M^3} \tag{9.1}$$

$$\overset{\text{p.w.}}{=} \frac{Q}{e}\left(\frac{m}{M}\right)^2 \gamma \frac{E}{E_S}(1 + \beta \cdot \mathbf{u}_\text{k}) \tag{9.2}$$

where the second line is written for a plane wave of electric field amplitude E and propagation direction $\mathbf{u}_\text{k}$, with $\gamma = 1/\sqrt{1-\beta^2}$ the Lorentz factor of the particle. As the γ dependence indicates, for relativistic momenta this parameter can be orders of magnitudes above the field value in the laboratory frame, itself bounding the vacuum interaction parameters in some of the most favourable cases[1]. Furthermore, note that high particle momenta can arise from the field itself as a result of classical dynamics in macroscopic spacetime regions, or equivalently cumulative field photons absorption, represented by the elastic scattering process in sf-QED (depicted in Fig. 9.1-a). As a result, the probability of occurrence of elementary sf-QED processes can be increased dramatically, those involving the lightest particles above all others[2].

Secondly, on the macroscopic scale where many uncorrelated sf-QED processes can occur, there exists a chain of events leading to the exponential growth of fermion number, magnifying quantum effects in the overall dynamics. This directly derives from the structure of sf-QED, where single particle decays into two particles are allowed, already at tree-level[3]. Namely, a fermion can emit a photon (Compton scattering, CS, *c.f.* Fig. 9.1-b), which in turn can decay into a particle-antiparticle pair (Breit-Wheeler pair production, BW, *c.f.* Fig. 9.1-c), which can both emit a photon, forming a chain reaction known as a “QED cascade”. Note that from the CS step onwards, memory is lost of the initial particle nature, as from Eq. 9.1 the BW process will generically strongly favor electron-positron pair creation over any other channels simply from the mass difference. Combining these two aspects, it appears that, in the presence of matter, a coherent field strong enough upon large enough spacetime extents will spontaneously and massively decay into a system of many photons, electrons and positrons, through sequences known as QED cascades.

---

[1] *e.g.* in the case of two counterpropagating beams forming a transient standing wave at focus.

[2] In the standard model those are the electrons/positrons, by a mass ratio of about 200 to the muons.

[3] The lowest order in the sf-QED perturbative expansion in coupling parameter α (see Table 2.1).

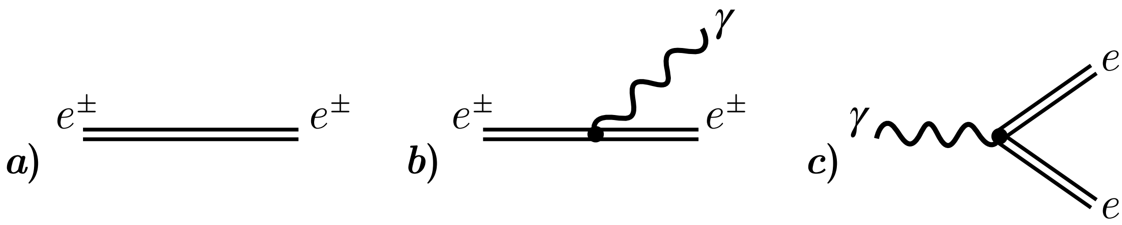

Figure 9.1: **Leading processes in a "QED cascade". a)** Field-dressed fermion propagators are represented by a double line, photon propagators by a wavy line, and interaction vertices by a dot (*cf.* sec. B.2.5). **b)** Photon emission by an electron or positron (Compton scattering); **c)** photon decay into an electron-positron pair (Breit-Wheeler).

In this section, we will present how this general scenario plays out in the field of RPM sources so as to predict general properties of resulting systems, identify observable signatures of the described regimes, and provide guidance for subsequent applications. Three different origins for the initial matter particles can be envisioned. In direct continuity with the previous chapter on vacuum interactions, pair production can proceed directly from the coherent field in the fermionic vacuum (Schwinger process). As the laser powers required to trigger such phenomenon presently remain out of reach, exogenous sources of matter remain of primary interest. In the optics of maximizing field-matter interaction while retaining experimental simplicity, focusing on a solid target is presented first. Due to the large number of seed particles, this configuration is found to allow extremely high electron-positron densities, possibly up to the formation of a quantum relativistic plasma in the form of quasi-neutral e^+e^- jets. We then turn to the collision of the RPM beam with high-energy electrons, producing instead remarkable microscopic processes through very high χ parameters. In suitable collision conditions, it is found that the attainable quantum interaction parameters exceed the Ritus-Narozhny regime threshold, which would be of significant theoretical interest. Both these RPM-light matter interaction scenarios entail significant numerical and theoretical challenges, towards which we will open in a final section.

9.1 RPM-light plasma interaction in solid targets

A common problem when trying to maximize the interaction of strong-fields with matter is that, in the relativistic regime, all charged particles are generically expelled from the highest field regions (*cf.* Eq. 1.14), so that only a fraction of the maximum quantum interaction parameter is achieved. Directing the pulse into a dense solid target provides a straightforward solution. Indeed, assuming *e.g.* that the ions move slow enough compared to electrons, the charge separation field then generically pulls electron populations back into the strong-field. The combination of such plasma dynamics with the shear number of involved electrons can thus be expected to significantly enhance both elementary sf-QED processes and subsequent relativistic quantum plasma effects.

In this section we will assess this idea for plasma mirror generated fields. In a first part we detail the overall plasma dynamics, and compare it with the laser-plasma interaction of infrared pulses. The microscopic properties of created photons, electrons and positrons will then be given, detailing their origin and final momenta. In the most favorable cases, corresponding to the highest intensities, the created electron-positron densities can be

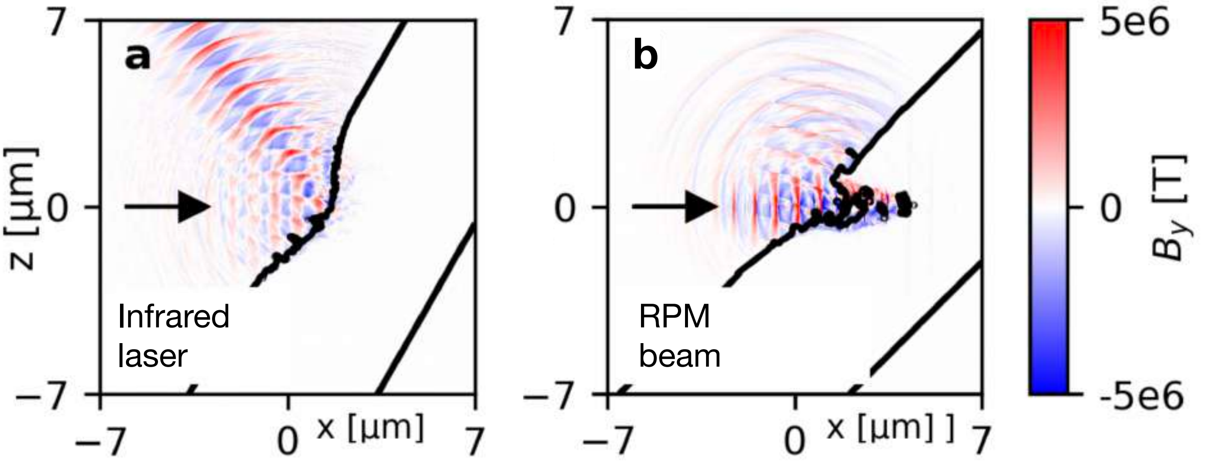

Figure 9.2: **Field and electrons distributions at mid-interaction between an incident beam and a solid plastics target.** (adapted from [300]) Black lines are electron isodensity curves $n_e = 100 n_c$, the magnetic field component in the normal direction is shown in blue and red, the black arrow indicates the incidence direction.

so high as to react on the incident RPM-light field, in which case they could form a macroscopic plasma. This limiting case will be examined in a third section. As the intensity range covered by such sources extends from at least 10^{24} W.cm^{-2} up to 10^{29} W.cm^{-2} [12, 13] in optimistic projections, all results will be given for both ends of this spectrum[4]. We may refer to each respectively as the "medium" and "extreme" intensity regimes, while the "critical regime" will denote the higher intensity limit $I \gtrsim 10^{29}$ W.cm^{-2} that will be found to coincide with our current numerical limitations[5].

9.1.1 RPM-light plasma dynamics

As sf-QED processes are generically suppressed in direct propagative electromagnetic waves interactions with free particles due to the repulsive ponderomotive force, solid targets may foster quantum processes under the effect of plasma fields. Elucidating the generic RPM-light plasma dynamics then appears as the primary task in order to fully take advantage of these configurations. In this section we will expose the general features of this interaction, with an emphasis on the difference with the infrared laser case. In particular, we will show that there exists a qualitative difference between both scenarios, resulting from the high-frequency spectrum of the RPM-light beam.

RPM-light versus infrared-laser interactions with a plasma The field and electron distributions about 10 fs after incidence of the beam peak on the target are shown in Fig. 9.2, both for an infrared laser pulse (a) and the RPM beam (b).

The infrared laser is here taken with a wavelength $\lambda_0 = 800$ nm, gaussian spatial and temporal profile with duration 20 fs, for a peak power of 10 PW. The waist on target is $w_0 = 2$ μm, corresponding to a peak intensity of $I_0 \simeq 1.6 \times 10^{23}$ W.cm^{-2}, which is a realistic figure at the current time. The laser incidence angle is taken at 30°, which has been shown to maximize sf-QED events [366].

---

[4] This parallels the logic of Chapter 8.

[5] We will expand on this point in Sec. 9.3.

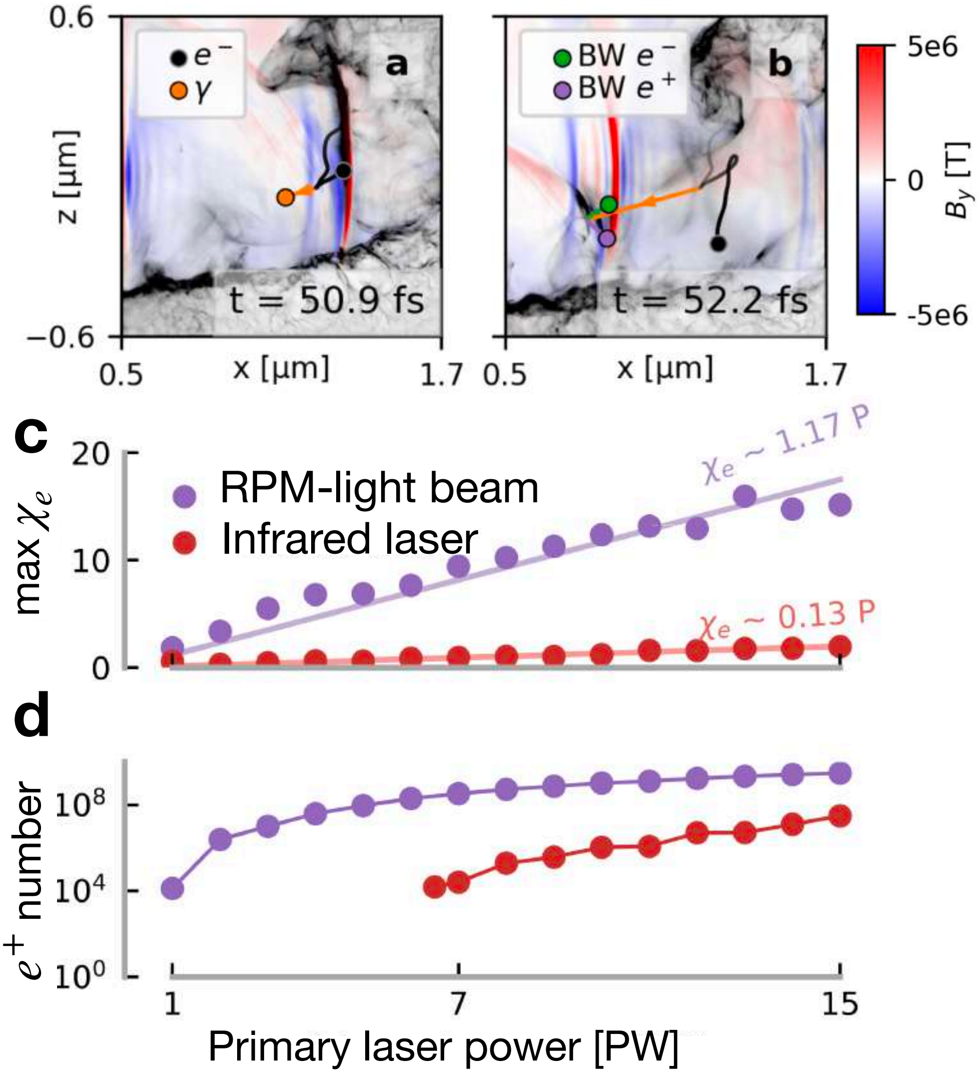

Figure 9.3: **Magnetic field and electrons distributions in the plasma channel; with trajectory of a pair creating electron.** (adapted from [300], WarpX simulations sec. 2.2.2) It appears that the axial plasma currents (a) generate a cylindrical magnetic fields in the channel (b), of the order of 1 MT for an RPM field of about 5 MT. **a)** A target electron is driven towards an attosecond pulse and emits a photon (CS); **b)** the emitted photon decays into an e^+e^- pair (BW) in the next pulse, which is accelerated by the local field front; **c**) maximum electron χ parameter; **d)** final positron number.

The RPM beam has a spectrum close to the “sub-optimal” beam studied in Chapter 8 (see also Chapter 7), resulting from an incidence angle on plasma mirror of 45° and plasma gradient length $\lambda_0/8$, close to the optimum [367]. In these conditions, the beam is focused down to a focal spot of $w_{0h} \sim 100$ nm on target and the intensity enhancement compared to the infrared pulse reaches about 1100, resulting in a peak intensity of $I_{0h} \simeq 1.8 \times 10^{26}$ W.cm^{-2}.

The target has the electron density of plastic in both cases that is $n_{0e} = 230 n_c$, where $n_c \simeq 1.8 \times 10^{21}$ cm^{-3} is the critical plasma density for a 800 nm wavelength.

The major difference between the two interactions can then be simply understood as follows. The infrared laser pulse curves the plasma surface but is efficiently reflected in the specular direction[6] (Fig. 9.2-a), while the RPM beam partially penetrates in the densest

---

[6] This is indeed the plasma mirror effect, though here not optimized for harmonics generation.

plasma regions, creating a channel (Fig. 9.2-b). The fact that part of the harmonic beam also is reflected suggests that this difference is explained by the high frequency content of the RPM beam. Indeed, the maximum plasma density can only reflects harmonics orders $k < \sqrt{n_{0e}/n_c} \approx 15$, while the spectrum extends beyond order 20. Then the reflected part can be interpreted as resulting from the low frequency content. Relativistic transparency only increases the overall transmitted part.

Characterization of the plasma channel When the RPM-light beam propagates in the target, electrons are totally depleted on its way, generating strong sources of electromagnetic plasma fields (Fig. 9.3). As visible in Fig. 9.3-b, the plasma fields reach values up to a fraction of the RPM-light field, therefore strongly deviating plasma electrons. At the considered medium intensity, the RPM-light field accelerates electrons to relativistic energies of the order of $\xi_e \approx 0.86 \times 100\ \text{nm}[\mu\text{m}]\sqrt{10^{26}\ \text{W.cm}^{-2}[10^{18}\ \text{W.cm}^{-2}]} \approx 1000$ (Eq. B.125), while for ions $\xi_i \equiv \xi_e/6 \times 1836 \approx 0.1$ so that the ponderomotive force only weakly acts on them and does essentially not displace them compared to the electrons. Accounting for the still shorter wavelengths achieved with the RPM harmonics spectra leading to the highest studied intensities, this situation would only change for $I_{0h} \gtrsim 5 \times 10^{28}$ W.cm^{-2}. When such ion relativistic threshold is exceeded they become subject to ponderomotive repulsion from the field as well. As a result charge separation fields may decrease, and therefore not suffice to efficiently bring electrons back into the strong field regions, so that the most intense pulses can end up reaching their focus in a near vacuum (Fig. 9.4-a). This effect can be simply compensated for by shifting the RPM-light focus deeper into the target by a few optical cycles (Fig. 9.4-b). The global plasma configuration remains similar on the whole studied intensity range though, with a well-formed central channel and some surrounding electrons driven in.

QED processes in the RPM and plasma fields As expected, the RPM-beam plasma interaction strongly enhances sf-QED processes compared to the infrared pulse (Fig. 9.3-c,d). This is due to the redirection of plasma electrons towards the strong field region, continuously fuelling the emission of high energy photons propagating against RPM-beam pulses, possibly decaying into a pair. As the pair is then quasi-instantly guided by the strong field fronts, this process leads to a localization of Breit-Wheeler electrons and positrons in the pulses and their direct acceleration up to high energies, with essentially no further sf-QED events as long as $E_{\text{lab}} < E_S$[7]. In all studied configurations the RPM field remains the vastly dominant source of sf-QED processes, with plasma fields mostly acting *via* Lorentz force. The total rate of particle creation is then simply modulated by the successive focalization of attosecond pulses (see Fig. 9.6), until the beam is totally absorbed or exits the plasma.

9.1.2 Electron-positron and photon radiations

The plasma electrodynamics of the RPM-beam-target system leads to a high number of sf-QED processes, resulting in specific distributions of created particles. In this section

---

[7] This can be understood from a plane wave calculation, where an electron initially at rest will experience $\chi_e \overset{\text{p.w.}}{\propto} E_{\text{lab}}/E_S$ whatever the energy gained in the wave. Qualitatively, one understands that all photons of a plane wave being exactly colinear, momentum gained by absorbing them can not influence interaction with another one.

we will examine their individual properties, through their process of creation, spectra, as well as their spatial configuration, critical to the onset of plasma effects.

Leading sequence of QED events Let us first identify the dominant sequence of events leading to pair creation. It can easily be understood reading Fig. 9.3 and Fig. 9.5. Indeed, the sequence leading to a single pair creation event is represented in the former, while the statistical representativity of this process can be inferred from the latter. Namely, an electron from the plasma encounters an RPM-beam pulse with a momentum component opposite to its propagation direction, resulting in a high χ parameter (Fig. 9.5-a,b,d), allowing CS photon emission in the same direction (Fig. 9.3-a). In crossing either the same RPM-beam pulse or one more upstream, this photon again acquires a high χ (Fig. 9.5-a,c,e), allowing a BW pair creation event (Fig. 9.3-b). At medium intensities $I_{0h} \lesssim 10^{28}$ W.cm^{-2}, this sequence is all the more transparent that virtually all pairs come from a photon emitted from a plasma electron rather than a BW electron (*cf.* Fig. 9.10).

Now the strong acceleration of BW pairs into the RPM field tends to align their momentum with the local field front normal $\mathbf{E} \times \mathbf{B}$, decreasing their χ parameter (see high p_x population in 9.5-d). More precisely, we know that in a plane wave $\chi_e \overset{\text{p.w.}}{\propto} E_{\text{lab}}/E_S$, therefore this dynamics can be expected to efficiently suppress subsequent sf-QED processes so long as $E_{\text{lab}} \ll E_S$. We can estimate this intensity threshold more precisely with the data of Fig. 9.10, showing what could be called the *degree* of a BW process, namely the number of CS processes preceding it. It is then found that pairs of degree higher than 1 only become significant for $I_{0h} \gtrsim 10^{28}$ W.cm^{-2}. At this point, the RPM field amplitude is high enough to trigger sf-QED processes from particles directly accelerated by it, which is sometimes called an “avalanche-like cascade” in the literature[8]. The spatial homogeneities of the tightly focused RPM pulses concur to lower this threshold below the $I_S = 4.64 \times 10^{29}$ W.cm^{-2} value expected for a plane-wave.

---

[8] Technically this regime can be characterized in terms of the Lorentz invariant ξ and χ parameters.

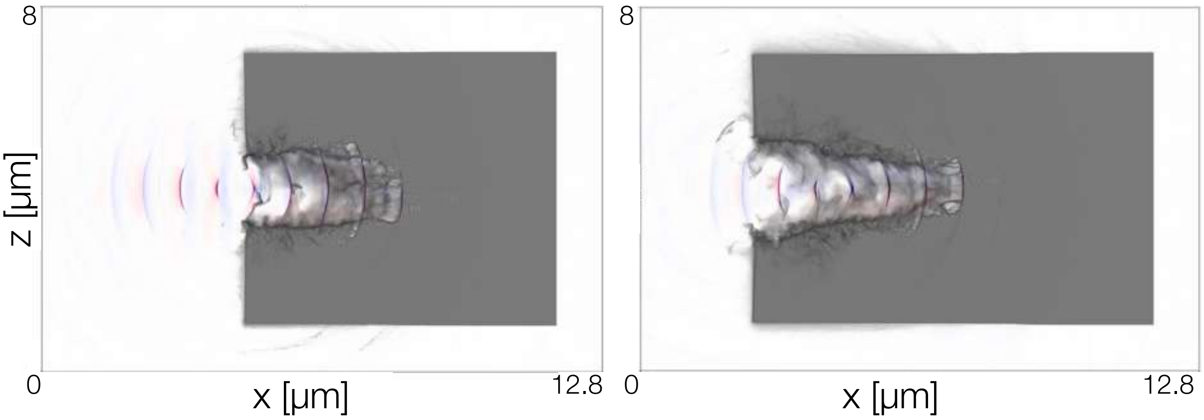

Figure 9.4: **Magnetic field and electrons distributions in the plasma channel for a 10^{29} W.cm^{-2} beam.** The focal spot is $w_{0h} \sim 40$ nm for a spectrum corresponding to the “optimal” beam (Chapter 7), plasma electron density is $n_{0e} = 200 n_c$. **a)** If the RPM-beam focus is set on the target surface, the ponderomotive force is efficient enough to strongly deplete the focal region as the main pulse focuses; **b)** this effect can be compensated by setting the RPM-beam focus inside the target, here at 2 μm.

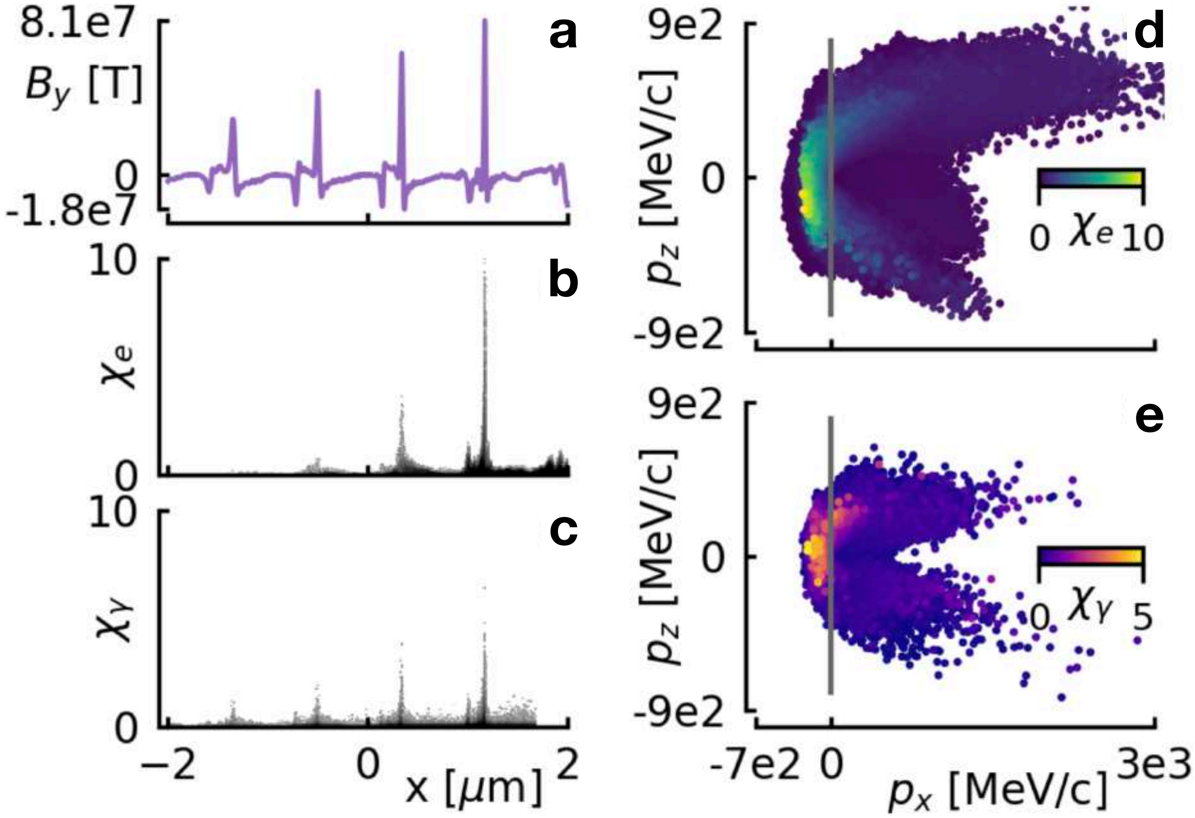

Figure 9.5: **Magnetic field and electrons distributions in the plasma channel for a 10^{29} W.cm^{-2} beam.** The focal spot is $w_{0h} \sim 40$ nm for a spectrum corresponding to the "optimal" beam (Chapter 7) **a)** If the RPM-beam focus is set on the target surface, the ponderomotive force is efficient enough to strongly deplete the focal region as the main pulse focuses; **b)** this effect can be simply compensated by setting the RPM-beam focus inside the target, here 2 μm away from the surface.

Spectra of created particles The final spectra of emitted CS photons and BW electrons are shown in Fig. 9.9 in the medium, extreme and critical intensity regimes. At all considered intensities, all created particles are globally accelerated in the RPM beam propagation direction, at energies of the order of a few GeV.

A clear distinction appears between electrons and positrons dynamics. The former are mostly accelerated along the optical axis, at energies about two times lower than that of the latter, which are also deviated in two directions at an angle with respect to the axis. This difference stems from the qualitative difference between their reaction to the plasma channel fields, from the electronic current and ionic charge, diverting positrons away from the axis towards the RPM-beam fronts, and dragging electrons inside the channel.

Spatial distribution of created particles Because pair creation occurs in the RPM pulses (that are focused on less than 100 nm transverse sizes and have longitudinal extents down to $c \times 50$ as ~ 15 nm) resulting matter densities can reach very high values at the time of focusing. At medium and extreme intensities, when the pulse then defocuses some particles remain concentrated in these field fronts, electrons and positrons separating due to the highly asymmetric field profile, creating very divergent attosecond electron and positron beams. However, electrons and positrons react differently in the plasma fields, leading to qualitatively distinct spatial distributions as shown in Fig. 9.7. Indeed, the

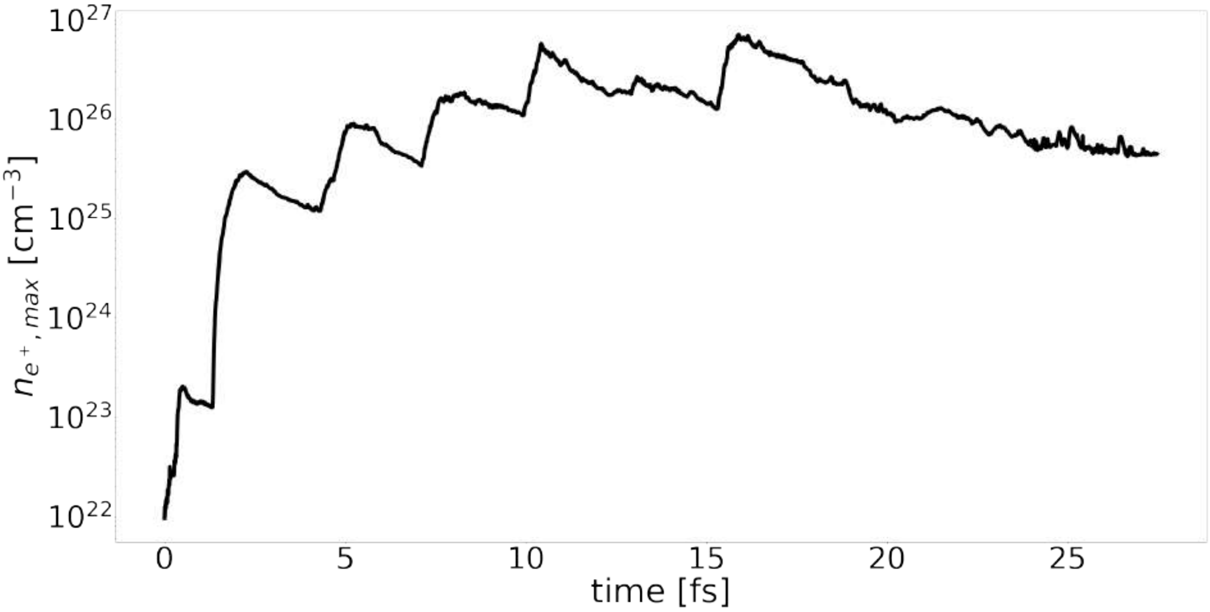

Figure 9.6: **Time evolution of the maximum positron density for a solid target.** Peak intensity here is 5.5×10^{28} W.cm^{-2}, electron target density is $n_{e0} = 200 n_c$.

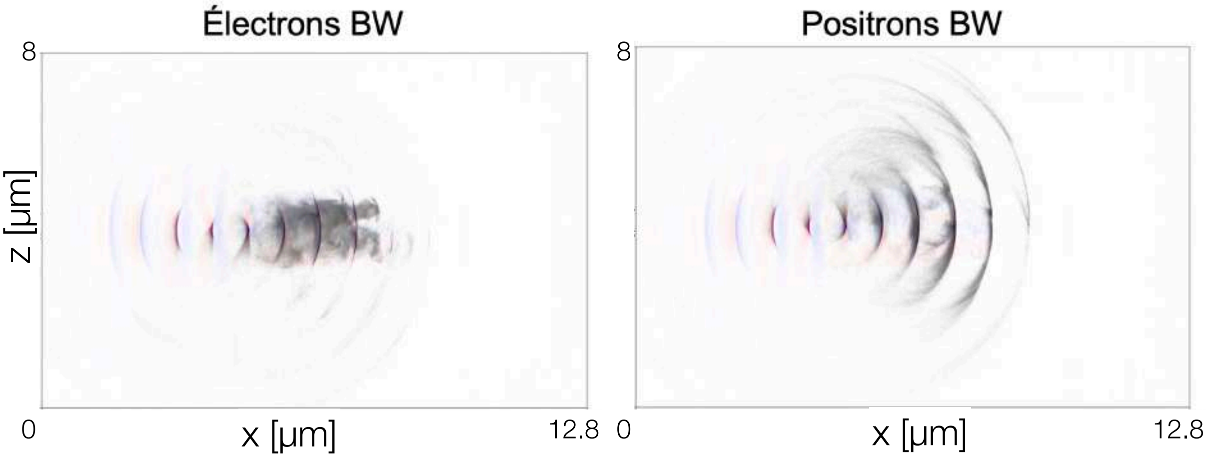

Figure 9.7: **Spatial configuration of Breit-Wheeler e^- and e^+ in an RPM-light solid interaction.** Peak intensity is 10^{28} W.cm^{-2}, electron target density is $n_{e0} = 200 n_c$.

plasma channel fields resulting from total electron depletion is focusing for the electrons, driving them away from the local field fronts, and defocusing for the positrons, pushing them in the same direction as the local field fronts. As a result, Breit-Wheeler electrons can disperse in-between attosecond pulses while positrons remain mostly concentrated in the field fronts.

9.1.3 Relativistic extremely dense e^+e^- plasma jets

At this point all macroscopic dynamics has been considered driven by the initially present particles, namely the RPM field and plasma, with created particles following trajectories dictated by the associated fields. However, as high densities are reached the electromagnetic current of created e^-e^+ particles may become large enough to act back on the ambient fields, resulting in plasma effects, in a relativistic and quantum regime. In this section we will devise a criterion for the presence of e^-e^+ plasma effects, evaluate it for various RPM-light intensities, and give some more details on the very high density configurations generated at extreme intensities.

A criterion for e^+e^- plasma dynamics A plasma is generically defined as a quasi-neutral system of charged particles whose interactions are dominated by the electromagnetic field they generate. In our case, where the dense electron-positron sheaths are immersed in an external coherent field, this definition could coincide with the limit in which this field is screened by the e^+e^- currents. We can however adopt a more flexible definition, requiring only that the particles own field influences their dynamics at least *at some point* in time. As we are now in the presence of an external field inducing charge separation, a necessary condition would typically be that the high density states last longer than a Langmuir plasma period. The only subtlety then comes from the fact that our system drifts with a mean velocity of Lorentz factor γ_0 in the laboratory frame where the field and matter quantities are computed.

In order to make sense of this proxy for plasma effects,

$$\tau_{ee} \geq \tau_p \tag{9.3}$$

with τ_{ee} the high-density state duration, we therefore have to relate it to a genuine plasma oscillation phenomenon of frequency τ_p, which may depend on γ_0. Reasoning on the case of a plasma interface with transverse translation invariance interacting with a plane wave in normal incidence, this is simply achieved *via* a Lorentz transformation from the laboratory frame $\mathcal{R}_{\rm lab}$ to the plasma rest frame $\mathcal{R}_{ee}$, where the configuration reduces to the well-known interaction between a plane wave and an infinite plasma at rest. In this frame, the plasma is indeed driven by the field to oscillate at characteristic frequency[9],

$$\nu_p\big|_{\mathcal{R}_{ee}} = 2\pi\sqrt{\frac{2\, n_e\big|_{\mathcal{R}_{ee}}\, e^2}{m_e\varepsilon_0}} = 2\pi\sqrt{\frac{2\, n_e\big|_{\mathcal{R}_{\rm lab}}\, e^2}{\gamma_0 m_e\varepsilon_0}} \tag{9.4}$$

In the laboratory frame, assuming stationary oscillation (plasma wave with wavevector $\mathbf{k} = \mathbf{0}$) we thus find[10],

$$\nu_p\big|_{\mathcal{R}_{\rm lab}} = \frac{1}{\gamma_0}\,\nu_p\big|_{\mathcal{R}_{ee}} = \frac{2\pi}{\gamma_0}\sqrt{\frac{2\, n_e\big|_{\mathcal{R}_{\rm lab}}\, e^2}{\gamma_0 m_e\varepsilon_0}} \tag{9.5}$$

$$i.e.\;\; \tau_p\big|_{\mathcal{R}_{\rm lab}} = \gamma_0^{3/2}\tau_{p0}\;,\text{ with } \tau_{p0} \equiv \frac{1}{2\pi}\sqrt{\frac{m_e\varepsilon_0}{2\, n_e\big|_{\mathcal{R}_{lab}}\, e^2}} \tag{9.6}$$

Now as maximum densities are achieved on durations of about an harmonic pulse focalization length, itself of the order of $\tau_0 = \lambda_0/c$ near diffraction limit, for λ_0 the initial pulse wavelength (Fig. 9.6), our criterion for plasma formation Eq. 9.3 simply translates into,

$$\tau_0 \geq \gamma_0^{3/2}\tau_{p0} \tag{9.7}$$

$$\Leftrightarrow \boxed{\frac{1}{\gamma_0^3}\frac{n_e}{n_{c,0}} \geq 1}\;,\text{ with } n_{c,0} = \frac{m_e\varepsilon_0}{8\pi^2\tau_0^2 e^2} \tag{9.8}$$

where n_e is the electron (or positron) density in $\mathcal{R}_{\rm lab}$ and $n_{c,0}$ is the critical electron-positron plasma density for wavelength λ_0.

---

[9] The factor 2 comes from the two-fluid e^- and e^+ motion compared to the ion-electron plasma case. We neglect relativistic transparency, rather ill-defined in this $\xi \gtrsim 100$ regime.

[10] This is simply the special relativistic "time dilation" effect.

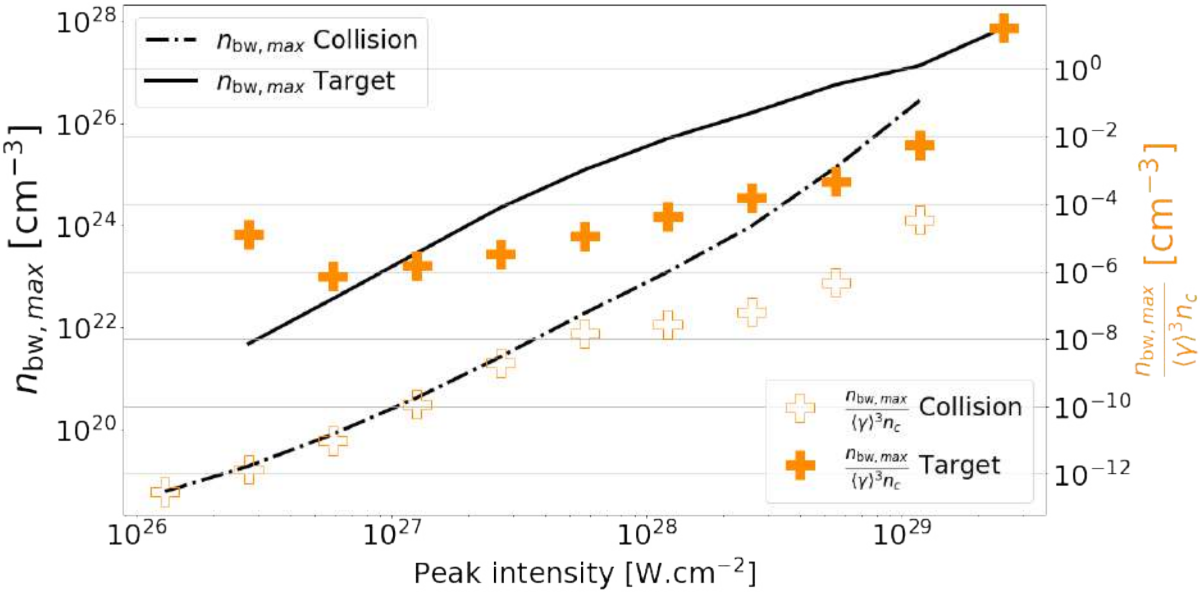

Figure 9.8: **Maximum positron density and plasma criterion for varying intensities.** The target electron density is $n_{e0} = 200n_c$. The Breit-Wheeler electron densities are within the same order of magnitude, but satisfy the plasma criterion sooner due to lower energies (Fig. 9.9).

Dynamics of the dense e^+e^- jets Let us then evaluate this criterion numerically on our full intensity range, for an RPM beam interacting with a $n_{e0} = 200n_c$ solid target. The results are displayed in Fig. 9.8. The maximum attained density increases exponentially with the peak intensity, from about $10n_c$ in a solid target at medium intensity up to about $10^7 n_c$ at extreme intensities. As created particles are accelerated on a wide spectrum up to GeV energies, the criterion Eq. 9.8 is only fulfilled at the highest intensities we were able to numerically simulate. Backreaction effects might become stronger past this threshold of $I \gtrsim I_S$, as then avalanche-like QED cascades continue developing, all the more that at $I \sim 10^{29}$ W.cm^{-2} already 80% of the beam energy is depleted in photon emission, resulting in a strong damping of the RPM field. Adopting a less stringent criterion $n_e/\gamma n_0 \geq 1$, *e.g.* following [368], one may even conclude that plasma-like effects can be observed from $I \gtrsim 10^{27}$ W.cm^{-2}.

These high intensities indeed mark the onset of the “critical regime”, where pairs can be generated by previously created pairs accelerated in the field, thus strongly enhancing the particle creation rate. This effect can be discerned in Fig. 9.10, showing the proportion of pairs generated from sequences of degree 4 or higher. This fraction is negligible below 10^{28} W.cm^{-2}, after which it quickly rises to represent nearly all pairs at 10^{29} W.cm^{-2}. At this point, densities actually seem to soar and result in local plasma frequencies impossible to resolve numerically, leading to the crash of corresponding WarpX simulations. This point will be further discussed in sec. 9.3.

In accordance with the plasma parameter values displayed in Fig. 9.8, the e^-e^+ dynamics mostly remains dictated by the RPM-light and target plasma fields up to $I \sim 10^{29}$ W.cm^{-2}. The resulting particle momenta near final state are shown in Fig. 9.9 for three different intensities.

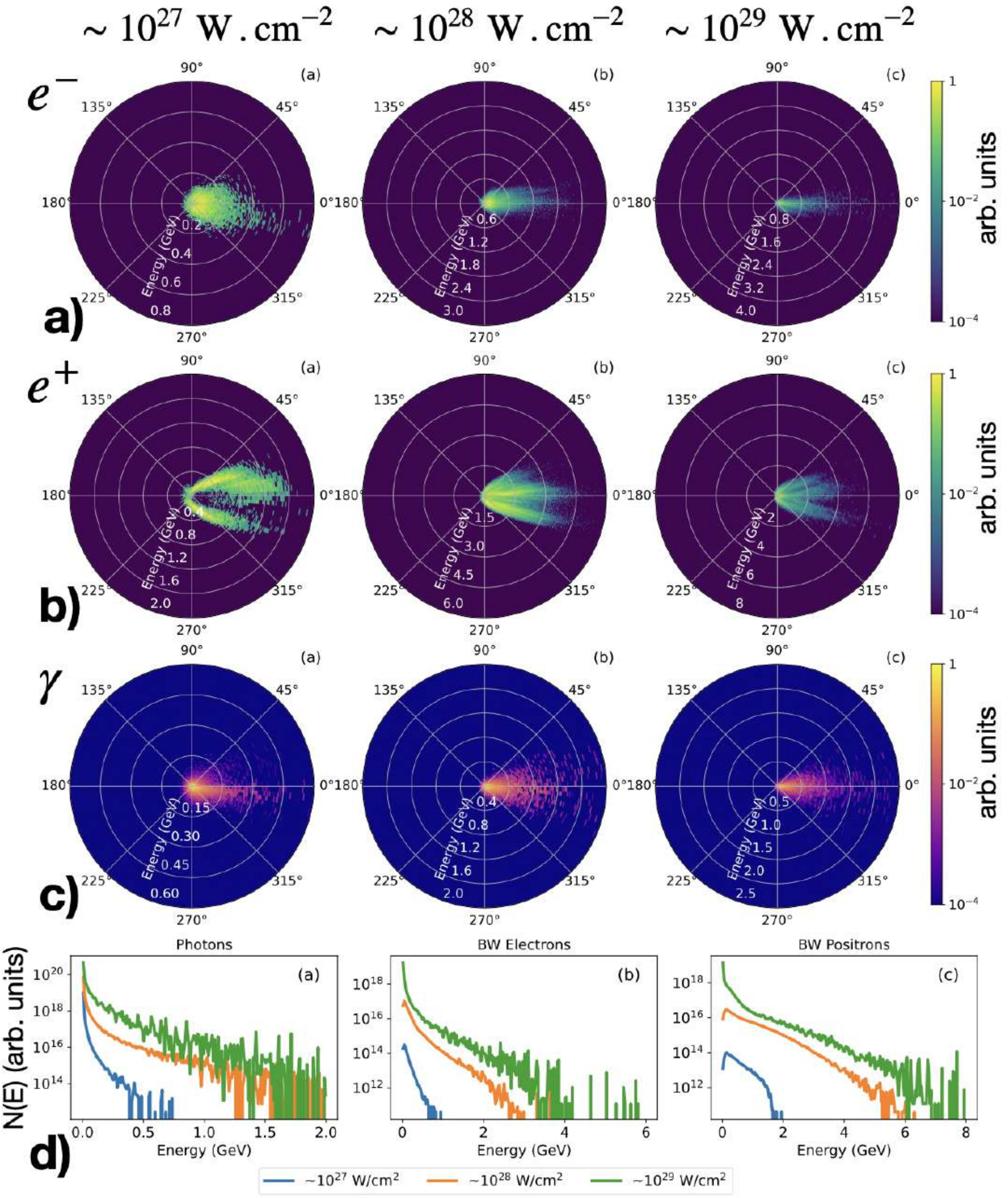

Figure 9.9: **Emitted electron, positron and photon spectra after RPM-light solid interactions. a)** BW electrons; **b)** BW positrons; **c)** CS photons; **d)** Integrated spectra. The target electron density is $n_{e0} = 200n_c$.

9.2 RPM-light and electron beam collision

As evoked in chapter 1, at this time the only way to trigger some sf-QED processes with conventional lasers is to make them collide with high energy electrons, so as to reach the Schwinger field in their rest frame. In last section we have seen that relativistic plasma mirrors essentially allow to lift these difficulties in a rather simple experimental setup of direct RPM-light solid interaction. Now it seems natural to investigate what physical regime would be reached combining both approaches, namely colliding high energy electrons with an RPM-light beam.

This section exposes results obtained along these lines, for medium to critical RPM-light intensities. The general characterisation of the different interaction processes and corresponding physical regimes is presented first. In the most favorable cases, the Ritus-Narozhny threshold of $\chi \geq \alpha^{-3/2} \approx 1600$ is exceeded, opening a window to the yet unexplored "fully non-perturbative" regime of Electrodynamics [317–320]. Some possible macroscopic signatures for these interactions in the system final states are then presented in a second section.

9.2.1 From cascades to the Ritus-Narozhny regime

Electron RPM-light interaction sequence The basic interaction scenario between a localized coherent field of classical strength parameter ξ and incoming ultra-relativistic electrons of Lorentz factor $\gamma_e \gg \xi$ is the strong deceleration of electrons in the field accompanied by high-energy radiation. This process is often referred to as "inverse Compton scattering", and is indeed leveraged on to efficiently convert electron energy into high energy electromagnetic beams. Depending on the classical and quantum interaction parameters, this process can be described either by Lorentz-Maxwell's equations, classical radiation reaction, or quantum Compton scattering in strong fields. At the envisioned intensities $I \geq 10^{26}$ W.cm^{-2}, counterpropagating electrons typically reach $\chi \gtrsim 1$ for $\gamma_e \gtrsim 100$, that is 50 MeV electron energies. On the other hand, current accelerators, including laser-plasma accelerators, routinely achieve beam energies between 100 MeV and 100 GeV, so that we can safely assume that radiation should be described by strong-field quantum Compton scattering.

As a consequence, an electron entering the field will be prone to high energy photon emission. At these energies, the emitted photon momentum is a significant fraction of the electron momentumand is emitted within a $1/\gamma_e$ angle in the initial electron propagation direction. In these conditions the photon χ parameter will remain high and Breit-Wheeler pair creation is favored. At high χ the BW cross-section is such that one of the two pairs tends to carry more energy than the other, however both typically hold a non-negligible fraction of the total [369]. These pairs hence are in a state comparable to that of the initial electron, only further in space and with a lower energy. If the initial energy is large enough, the created electron and (or) positron can themselves emit a photon, forming a QED cascade sometimes said of "shower type" by contrast with the avalanche type when particles are accelerated by the coherent field directly. As the cascade develops, the initial electron beam energy is depleted into pairs and photons escaping the strong fields, until either particle χ parameters fall below the CS or BW threshold, or particles exit the strong-field region. This scenario essentially captures how sf-QED processes are expected to be observed with optical lasers.

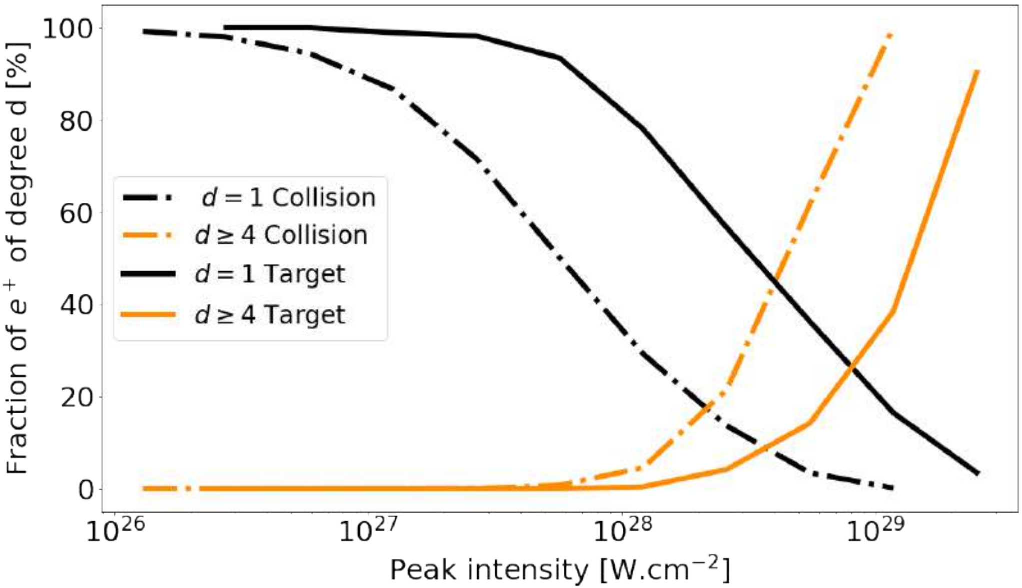

Figure 9.10: **Proportion of e^-e^+ pairs originating from a simple $e \overset{\text{CS}}{\to} \gamma \overset{\text{BW}}{\to} ee$ or a degree at least 4 $e \underset{\geq 4 \text{ times}}{\overset{\text{CS}}{\to} \dots} \overset{\text{BW}}{\to} ee$ sequence in the final state.** The degree 1 pairs fraction is nearly 100% at medium intensity, but quickly drops for $I_{0h} \gtrsim 10^{28}$ W.cm^{-2} when QED cascades start to develop, and higher degrees dominate. The solid target has $n_{e0} = 200 n_c$ density, and the electron beam collision angle is 45° angle.

Attainable quantum interaction parameter In our case, however, this fast energy depletion can play a very detrimental role by preventing electrons to reach the highest fields regions with their maximum momentum, and thus lower the effectively attainable quantum parameter χ. Indeed, for a 100 GeV electron beam the CS threshold $\chi \sim 1$ is reached at $I \sim 2.4 \times 10^{24}$ W.cm^{-2}, far from the maximum field of the RPM pulses even at medium intensity $I_{0h} \sim 10^{26}$ W.cm^{-2}. With this effect in mind, the question of the maximum attainable χ parameter given some field configuration becomes primordial and less trivial than it first appears.

In the case of a particle beam interacting with a focused field though, it has been demonstrated that simply adding an angle between the optical and particle beam axes is enough to recover almost the absolute maximum χ parameter [368]. The optimum angle is numerically found lying between $\pi/2$ and the field opening angle, which can be explained as χ geometrically decreases when the angle is increased (Eq. 9.1), implying a compromise. The situation is depicted in [220]. Fig. 9.12 shows the case of interaction at an optimum angle between RPM-light and particle beam axes.

In this situation the attained χ parameter reaches very high values, as depicted in Fig. 9.11 for various intensities, and the Ritus-Narozhny regime can be reached for $I_{0h} \gtrsim 1 \times 10^{27}$ W.cm^{-2}. Even below this threshold, χ values close to 10^3 are accessible, at which point new elementary processes could still manifest *e.g.* as radiative corrections in particle propagation and interactions.

9.2.2 Signatures in final states

Besides the sf-QED processes of shower type cascades, electrons in the field are subject to the Lorentz-force dynamics that can strongly affect the final state both of beam electrons and created particles. A characterization of the asymptotic particle properties after interaction is therefore desirable, all the more crucially in the Ritus-Narozhny regime where

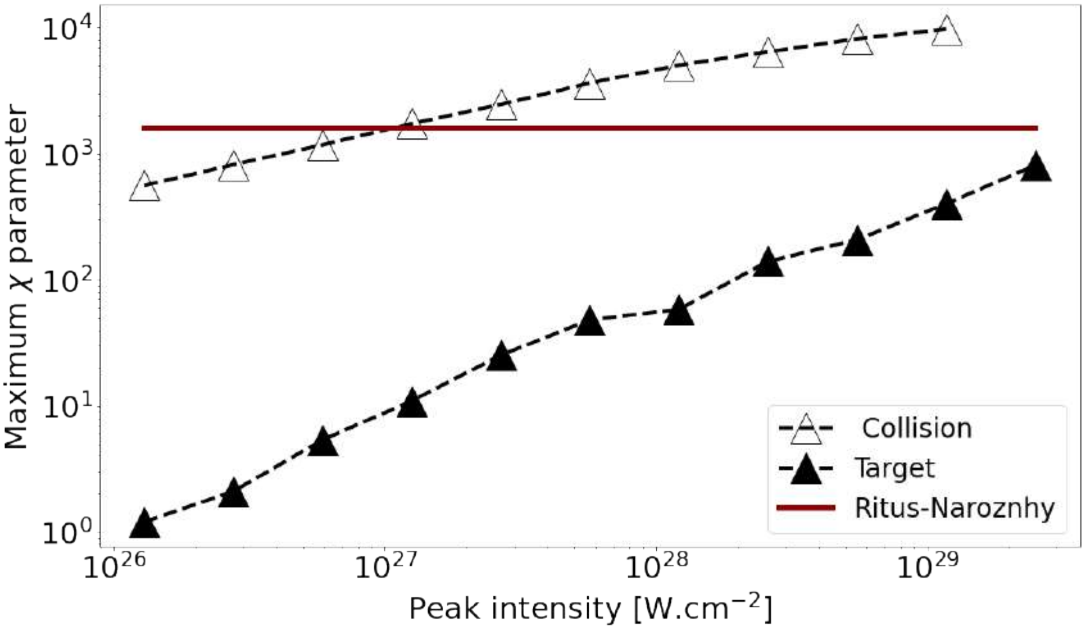

Figure 9.11: **Maximum χ parameter attained by electrons and positrons in the RPM field. Empty triangles)** correspond to 10 GeV electrons incoming on the RPM beam at a 45° angle; **Full triangles)** correspond to the RPM beam interaction with a $n_{e0} = 200n_c$ target, with focal point located 2 μm inside the target. The trend is steeper in RPM-light solid interactions as particles momenta also depend on field.

deviations from first order sf-QED computations would prove of high theoretical interest.

Dynamics intensity dependence Let us first try and discern some qualitatively different regimes of interaction depending on the RPM-light intensity. Regarding BW particles, we can asses their participation or not to further sf-QED processes. This information relates to the degree of created particles, as particles of degree higher than one originate from sf-QED processes involving BW particles. The proportion of degree 1 BW particles is shown in Fig. 9.10, revealing that more than 10% of BW pairs is of degree 2 of higher already at 10^{27} W.cm^{-2}. As photons can escape the field without decaying into a pair, this figure implies that an even higher fraction of BW pairs has undergone at least one CS process than visible in the degree 2 BW particle fraction, and we can thus conclude that sf-QED effects significantly affects created particles dynamics.

Another macroscopic information about the interaction can be obtained considering particle spatial distributions after collision with the RPM-light beam. The results are shown in Fig. 9.12, displaying a transition between almost no beam disruption at medium intensities to total beam depletion at critical intensity. The progressive transition between both configurations is interesting, as it implies a strong correlation between the maximum intensity at focus and the final particles angle-energy distributions.

Quantum interaction regime signatures We can then examine the particle final states more quantitatively through their energy-angle spectra. One should note that accessing the asymptotic properties of particles co-propagating with the field proves especially challenging though. Indeed, they can still undergo acceleration by the RPM-light field for some time as it defocuses. However including such process in the simulation is very computationally demanding. In particular, accounting for field defocusing effects would require three-dimensional simulations. In these simulations aimed at gaining a general understanding of RPM-light and high energy electrons interaction, we will simply assume that further energy gains do not affect conclusions drawn from distributions shortly after RPM-light focusing.

The resulting distributions are shown in Fig. 9.13. The reference momentum introduced by the incoming electron beam is again seen to induce a strong correlation of the final particle distributions with the RPM-light peak intensity. More specifically, some particles are injected in the beam and accelerated along the optical axis, while others persist in the electron beam direction, and the ratio between both populations depends on intensity. This may allow assess the intensity at interaction point experimentally, and hence trace back the achieved χ values.

Breit-Wheeler electrons and positrons differ only by opposite transverse momenta, in contrast with the plasma case. This is due to the simpler field form, approximately symmetric with respect to the optical axis, while field peaks are all of the same "phase"[11]. The pairs are accelerated in the field to maximum energies scaling linearly with the RPM-beam intensity, from about 1 GeV at $I \sim 10^{27}$ W.cm^{-2} to 15 GeV at $I \sim 10^{29}$ W.cm^{-2}.

In view of studying the elementary processes occurring at very high χ specifically, it would be desirable to be able to relate realistically observable quantities to the maximum χ value attained at interaction point. The stochastic character of particle dynamics in the cascade is an obstruction to such endeavour. Indeed, from the first photon emission resulting particles properties can overlap with properties of lower energy incoming electron. The strong dependence of the final energy-angle spectrum on intensity, on the other hand may at least help access the regime of interaction, and in particular the achied intensity at focus. A more refined numerical study of asymptotic momenta distributions, displaying sub-sampled angle-energy distributions for particles having reached a certain value of maximum χ, might help further disentangling different microscopic processes contributions. At the time of writing, the corresponding numerical diagnostics are yet to be implemented in the WarpX code.

---

[11] See Fig. 9.5. This contrasts with typical spectrally Gaussian pulses, symmetrical with respect to field sign inversion up to a "carrier-envelope phase".

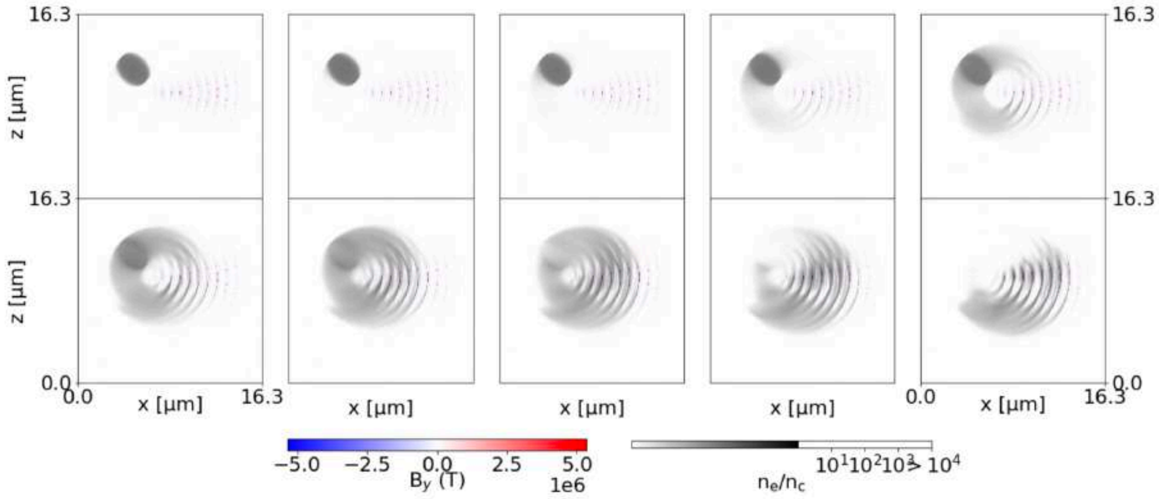

Figure 9.12: **Spatial electrons and transverse magnetic field distributions after interaction.** Each frame correspond to a given intensity, from left to right and top to bottom: $I_{0h}[\text{W.cm}^{-2}] \in \{1.3 \times 10^{26}; 2.8 \times 10^{26}; 5.9 \times 10^{26}; 1.3 \times 10^{27}; 2.7 \times 10^{26}; 5.7 \times 10^{27}; 1.2 \times 10^{28}; 2.6 \times 10^{28}; 5.5 \times 10^{28}; 1.2 \times 10^{29}\}$.

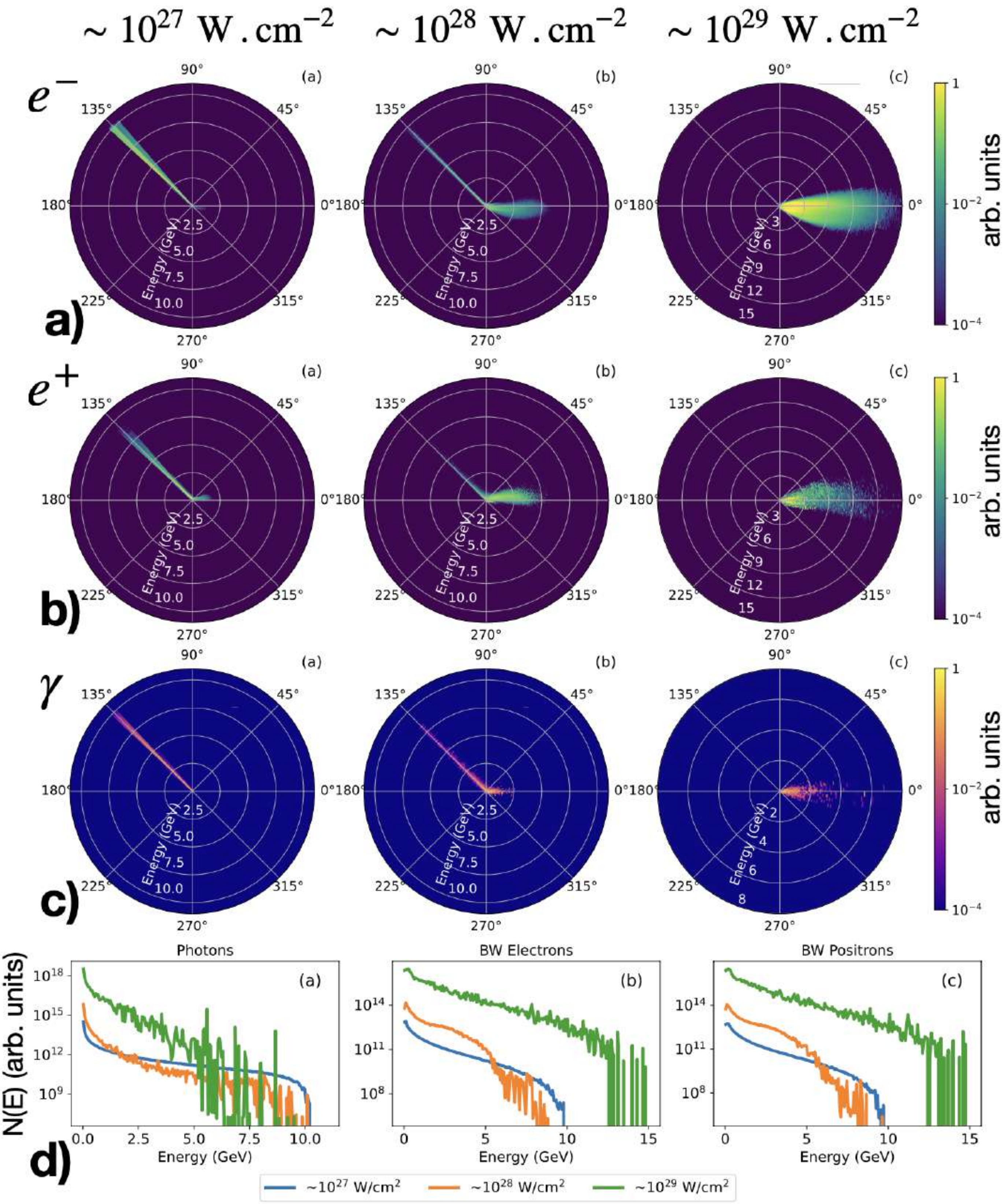

Figure 9.13: **Emitted electron, positron and photon spectra after RPM-light electron beam interactions. a)** Beam electrons; **b)** BW positrons; **c)** CS photons; **d)** Integrated spectra. The beam energy is 10 GeV, incoming at a 45° angle.

9.3 Theoretical and numerical challenges of extreme plasma states

All discussed simulations rely on the PIC-QED algorithm, which solves a Boltzmann-Maxwell system describing the self consistent evolution of the electromagnetic field and 1-body particles distribution functions, encapsulating sf-QED processes in collision terms. When simulating new physical regime, such as the extreme intensity RPM-light-matter interactions, it is legitimate to enquire about both the theoretical validity and computational viability of the model and its numerical implementation. In this section we will review and discuss the main issues identified along these lines during this work.

9.3.1 Numerical plasma simulation issues

The main difference of PIC-QED simulations in the deep quantum regime compared to the reference cold classical plasma configuration is the prolific particle creation process, resulting in extremely high densities. Both aspects have specific numerical consequences.

Resampling In PIC codes the electromagnetic field is computed at specific points on a grid, while each particle type is represented by a 1-body distribution function, that is sampled and evolved in time *via* the method of characteristics. The resulting sampling points are defined by a weight, position and momentum, allowing to identify them with "macro-particles", that can typically be interpreted as many individual particles tightly clustered together in phase space. As each macro-particle occupies some memory space and requires to be updated at each time step, the final computational expense of a PIC simulation strongly depends on the overall number of macro-particles.

Now in the PIC-QED algorithm, both Compton scattering and Breit-Wheeler processes convert one initial macro-particle ($e^{\mp}$ or γ) into two ($e^{\mp}\gamma$ or e^-e^+), so that QED cascades numerically result in an exponential growth of the total macro-particle number. Performing such simulations in the quantum-dominated regime of sf-QED therefore requires reducing the number of macro-particles, but without overly degrading the faithfulness of our distribution function sampling. This general problem is known as "resampling".

In our simulations, the retained resampling solution is referred to as a "thinning" method by contrast with "merging" methods, because it suppresses particles based on their individual properties rather than merges couples of similar particles. The detailed implementation corresponds to the "levelling thinning" algorithm described in [370]. The only modification was that thinning was only performed in cells with $N > 50$ macro-particles, as it was found to help preserving tails of the distribution[12]. This module, critical to the pursuit of high intensity simulations, was found to provide very satisfactory results with limited computational overhead. An illustration of its effect on particle distribution is provided in Fig. 9.14.

Local plasma scales When resampling allows taming the exponential macro-particle number growth, prolific QED cascades can be simulated, potentially leading to very high matter densities. This numerically results in high charge and current densities in Maxwell's equations, thereby directly affecting the fields. Numerical stability of this field-particles

---

[12] Note this could in principle be more than a corrective effect, as QED cascade can magnify the effects of a few seed particles in certain configurations.

dynamics requires at least that the local plasma period is always resolved by the space-time discretization scheme,

$$dt \overset{!}{<} \tau_p = \tau_0 \sqrt{\frac{n_c}{\|n_e\|_\infty}} \tag{9.9}$$

with $\tau_0 = \lambda_0/c = 2.6$ fs and $n_c = 1.7 \times 10^{21}$ cm^{-3} the critical plasma density at $\lambda_0 = 800$ nm. According to Fig. 9.8-a, densities as high as $10^7 n_c$ can be reached. This translates in local plasma periods of less than $10^{-3}\tau_0$, for a total simulation duration of the order of $10\tau_0$. In 2 spatial dimensions, this numerical instability prevented exploring the critical regime $I_{0h} \gtrsim 10^{29}$ W.cm^{-2}, where local plasma frequencies fell below the computationally maximum attainable resolution $dt \sim \tau_0 \times 10^{-4}$. In three spatial dimensions, such effect would severely restrict the study even of the extreme intensity regime.

Several attempts have been tried to circumvent this difficulty, such as numerical quanching of high-frequency longitudinal field components, with no satisfactory effects on the simulations. As of today, it seems the most promising path of progress would be the implementation of a non-uniform, possibly adaptive, grid for the electromagnetic field. This would allow finely resolving the focal area, where maximum densities are produced, while keeping the total number of grid points within reasonable bounds. The main challenge of such strategy in the context of an electromagnetic PIC code is to preserve the non-dispersive character of the propagation scheme, even at interfaces between different resolution domains. This general issue becomes critical in the study of strong field RPM beam, as the field profile is all the more sensitive to dispersion, and its peak intensity at focus especially. Besides, the exponential dependence of the maximum density with intensity would still make it difficult to enter the critical regime too deeply.

9.3.2 Relativistic quantum plasma modelling

The observation of new physical regimes, and possibly even of new elementary processes, is a key motivation to the study of strong fields. This naturally raises the question of the adequacy of the current theoretical framework in these configurations, first and foremost the one underlying *ab initio* PIC-QED simulations. In this section we will mention several directions in which this model may be extended.

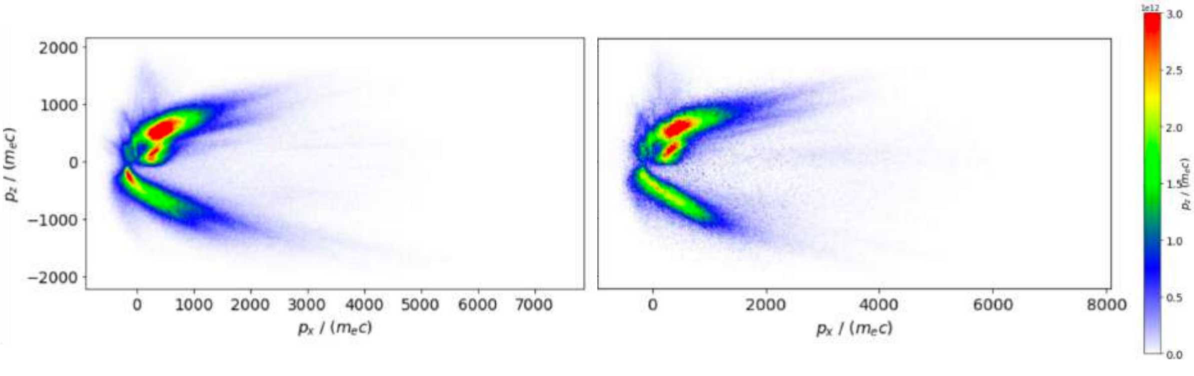

Figure 9.14: **Momentum positron distribution in RPM-light and matter seed interaction, with and without thinning algorithm. (left)** Momentum distribution without thinning; **(right)** Momentum distribution with thinning.

Higher multiplicity collision processes Considering again the distinctive feature of QED cascades in the RPM-light field, the generation of extremely high electron-positron densities, in a kinetic framework one natural expectation is the increase of collision rates. In these conditions, it becomes conceivable that scattering processes with more than one incoming particle become sizeable. Though such terms are *a priori* suppressed by at least a factor e compared to one particle processes, they scale in higher powers of particle density and could thus play a role in high density configurations. Relevant processes would be the two-particle scatterings $ee \to ee$, $e\gamma \to e\gamma$, and photon annihilation $\gamma\gamma \to ee$ [308, 371–373]. However, the rate of energy-momentum transferred in this manner should not only be compared to lower order scatterings, but to the Lorentz force exerted by the coherent field as well, which could still dominate in strong enough fields.

When individual particles quantum interaction parameter become of the order $\chi \sim 10^3$, even without entering the Ritus-Narozhny regime loop corrections to the electron and photon propagators could also affect sf-QED processes.

Degeneracy threshold Another source for deviations from a classical kinetic model when such electron-positron densities are reached is the rise of Fermi-statistics effects, that is the “quantum degeneracy” of the plasma. Though such thermodynamical notion is non-trivial to precisely apply to a system as far from equilibrium as the e^+e^- plasma formed in RPM-light-matter interactions, we can still gain insight in these effects by computing the local Fermi energy [374],

$$\varepsilon_F = mc^2\sqrt{\left(\frac{n_e}{n_\mathcal{C}}\right)^{2/3}+1} - 1 \tag{9.10}$$

$$\text{with, } n_\mathcal{C} = \frac{8\pi}{3}\frac{1}{\lambda_\mathcal{C}^3}\ , \ \textit{i.e. } n_\mathcal{C} \simeq 5.9\times 10^{29}\ \text{cm}^{-3} \tag{9.11}$$

where $\lambda_\mathcal{C}$ is the electron Compton length. Evaluating it from Fig. 9.8, we find that for all simulated intensities,

$$\varepsilon_F(I_{0h}) \lesssim mc^2 \tag{9.12}$$

As the typical energy spread of the electron-positrons is of the order of $\sim 10^3 mc^2$ (GeV), we conclude that degeneracy effects can still safely be neglected.

Extensions of the Boltzmann-QED framework There are other well-known assumptions on which the reference “Boltzmann-QED” picture is based, and many results were obtained in view of extending them. For instance, one of the most notable is the “Locally constant field approximation”, which could be relaxed or even lifted entirely in quite general configurations, for some specific processes[13]. One may conceive these lines of progress as “bottom-up” approaches, where the rich physics of strong-field electrodynamics is first grasped from the embedding of the Furry picture of sf-QED within a classical kinetic theory, and then progressively extended in several directions. A major merit of this approach is its very operational character, as it allows for computationally tractable simulations, and current experimental conditions usually strongly legitimate these approximations.

By contrast, an alternative “top-down” method would be to first formulate the exact theoretical framework fully encompassing the envisioned physical configurations, and then

---

[13] See *e.g.* [375–378] and references.

proceed to successive approximations until an operational formulation is reached. Though less direct, one may expect such approach to provide a systematic procedure of modelling, and control on the approximation error at each stage. In the present discussion such theory would be Non-equilibrium QED, such as defined *e.g.* by the equations of motion of a quantum effective action (*cf.* sec. B.2.5), and the approximation procedure its reduction to a kinetic theory with classical (on-shell) particle distribution functions.

However, one could then in principle stop at an earlier stage and use the resulting extension of the Boltzmann-QED model. Following [116], a kinetic description free of LCFA accounting for QED processes at order e^2 including off-shell effects can for instance be derived. Besides the usual situations where the LCFA fails, such model would typically be of use to consistently describe coherent field decay through the Schwinger process, or any more general particles backreaction on the coherent field.

Conclusion

Relativistic plasma mirrors may offer the opportunity to access the quantum dominated regime of strong-field Quantum Electrodynamics in a near future, *via* fields of intensities ranging between 10^{25} W.cm^{-2} and 10^{29} W.cm^{-2}. In this thesis, we have predicted the effects produced by such light in different configurations, either in a vacuum or in the presence of external particles.

Quantum vacuum processes were studied in chapter 8. Adopting the Stimulated Vacuum Emission formalism [303], we could compute the number of photons scattered in the RPM beam, for two different beam spectra, corresponding to different conditions of generation on the plasma mirror. We have shown that the focusing of a single RPM beam in a vacuum could produce as much scattered photons as the head-on collision of two 1 PW infrared pulses focused at diffraction limit, which may simplify the latter experimental setup. We also computed the number of photons in scattered in a probe beam when colliding with the RPM pulses, which revealed in particular that some photons could be scattered with energies absent of the initial colliding beams spectra, potentially significantly improving the signal-to-noise ratio, critical in these experiments. Finally, a threshold for Schwinger pair creation was found, indicating a laser required laser power of around 200 PW, which is high though much below the typical exawatt powers required in equivalent infrared configurations.

All these results were obtained through a numerical implementation of the Stimulated Vacuum Emission formalism, adapted to the large size of RPM field simulations, hence parallelized. This algorithm was extensively validated on known reference configurations, and against different modes of numerical implementation, as detailed in chapter 3. Guidance in the more complex case of the RPM beams could be gained *via* analytical estimates, whose detailed derivation was presented in chapter 4. We also worked towards more theoretical clarity by relating our approach with the resolution of effective field equations, also pursued in the literature, as summarized in chapter 5.

The interactions of RPM light with pre-existing matter was presented in chapter 9. In the case of interaction with a solid target, we could evidence that even at (comparatively) low intensities of 10^{25} W.cm^{-2} RPM beams enhance sf-QED signatures by several orders of magnitude compared to direct irradiation of the target with an infrared pulse of equivalent energy. We could also study dynamics at higher intensity, and find that very high density electron-positron clusters then form, and are accelerated to GeV energies. In the case of RPM light collision with a high-energy electron beam, we could compute the achieved χ parameter, and establish their relevance for physics around the Ritus-Narozhny regime of sf-QED, together with signatures of these interactions in the form of emitted particles spectra.

Abstract of Part IV

An outline of relativistic quantum theory is proposed. Specifically, we aim at a viewpoint encompassing both *i)* a proper delineation of strong-field Quantum Electrodynamics and *ii)* paths towards its, typically more familiar or operational, (semi-)classical aspects.

Chapter A summarizes the procedure of canonical quantization, highlighting a continuity between classical and quantum descriptions of physical systems.

Chapter B introduces the required elements of Quantum Field Theory at an heuristic level, with an emphasis on their relevance in view of the strong-field regime of Quantum Electrodynamics.

PART IV

– Appendix –
A primer in view of strong-field Quantum Electrodynamics

Appendix A

Landmarks from mechanics

We here motivate and clarify some terminology occurring in the main text with a brief summary of the canonical connection between the classical and quantum mechanics of a physical system. Emphasis is placed on the order of exposition rather than mathematical forms, however technical issues may hopefully be lifted from context, or from provided references. This material being standard we do not systematically give reference for the various results, but indicate our main sources at the beginning of each section, and wherever more specific derivations were reproduced.

A.1 Hamilton's principle

A.1.1 Lagrangian formulation

A physical system is a set of variables $\{q_i\}$ allowing to compute quantities that can in principle be observed. In the context of non-relativistic classical mechanics, typically $q_i \in \mathbb{R}$ and the problem amounts to determining their values at any time $q_i : t \mapsto q_i(t)$ given their values at some initial time $q(t_0) = q_0$.

Hamilton's principle states that there exists a functional of the form,

$$S[q_i] = \int_{t_0}^{t} d\bar{t} L\left(q_i(\bar{t}), \dot{q}_i(\bar{t})\right) \tag{A.1}$$

with $\dot{q} = dq/dt$, for which the physical trajectory is an extremal point. S is called the action and L the Lagrangian of the system. Considering an infinitesimal variation of the trajectories δq_i such that $\delta q_i(t_0) = \delta q_i(t) = 0$, the extremum condition writes[1],

$$\begin{aligned} \delta S[q_i] &= 0 & \text{(A.2)} \\ &= \int_{t_0}^{t} d\bar{t} \left[\frac{\partial L}{\partial q_i} - \frac{d}{dt}\left(\frac{\partial L}{\partial \dot{q}_i}\right)\right] \delta q_i + \left[\frac{\partial L}{\partial \dot{q}_i}\delta q_i\right]_{t_0}^{t} \ , \forall \delta q_i & \text{(A.3)} \end{aligned}$$

where integration by part has been used, which translates into,

$$\textbf{Euler-Lagrange:}\ \frac{\partial L}{\partial q_i} - \frac{d}{dt}\left(\frac{\partial L}{\partial \dot{q}_i}\right) = 0 \ , \forall i \tag{A.4}$$

called the Euler-Lagrange equations.

Thereby one recovers the usual vision of mechanics as the unfolding of trajectories in time according to differential equations. Such formulation already proves more fruitful than a simply differential view though, in that Eq. A.4 is invariant under any coordinate change $q_i \mapsto Q_i$. As partially displayed in the following, much beyond immediate uses it is empirically found to provide a unifying language for describing fundamental systems.

[†] Refs. A.1-A.2: [310, 379, 380]

[1] Summation over repeated indices is implied throughout the text: $a_i b_i \equiv \sum_i a_i b_i$.

A.1.2 Hamiltonian formulation

The Euler-Lagrange equations show that dynamics could be expressed as a differential system of the first order in the extended variables q_i, p_i, by defining,

$$p_i = \frac{\partial L}{\partial \dot{q}_i}(q_i, \dot{q}_i) \tag{A.5}$$

provided this expression can be inverted in $\dot{q}_i$. Equations of motions in the $\{(q_i, p_i)\}$ "phase space" are then generated by elimination of $\dot{q}_i$ in the action through the Legendre transform of L, called the Hamiltonian H[2],

$$S[\{q_i\}] = \int_{t_0}^{t} d\bar{t} \left[p_i \dot{q}_i - H(q_i(\bar{t}), p_i(\bar{t})) \right] \tag{A.6}$$

so that upon independent variation of q_i and p_i Hamilton's principle now writes,

$$0 = \int_{t_0}^{t} d\bar{t} \left[-\left(\dot{p}_i + \frac{\partial H}{\partial p_i} \right) \delta q_i + \left(\dot{q}_i - \frac{\partial H}{\partial p_i} \right) \delta p_i \right] + [p_i \delta q_i]_{t_0}^{t} \ , \forall \delta q_i, \delta p_i \tag{A.7}$$

and Hamilton's equations of motion follow as,

$$\textbf{Hamilton:} \begin{cases} \dot{q}_i = \dfrac{\partial H}{\partial p_i} \\ \dot{p}_i = -\dfrac{\partial H}{\partial q_i} \end{cases} , \forall i \tag{A.8}$$

A.2 From trajectories to observable values

A.2.1 Observables of definite states

The Hamiltonian formalism lends itself to a very operational view of mechanics. Because evolution is of first order in phase space, each point uniquely specifies the system state[3], and therefore any physical quantity can be expressed as a function defined on it, that is,

$$\textbf{Observable values:} \ \varphi(t) = \mathcal{O}(\mathbf{x}(t), t) \tag{A.9}$$

$$\triangleq O(\mathbf{x}_0, t) \tag{A.10}$$

with the abbreviation $\mathbf{x} = (q_i, p_i)$. Rephrasing in view of quantum mechanics, $\varphi(t)$ is the value taken by the "observable" $\mathbf{x} \mapsto \mathcal{O}(\mathbf{x}, t)$ measured on the system at time t, given initial data $\mathbf{x}(t_0) = \mathbf{x}_0$. As the second line suggests, for the purpose of computing φ time evolution can indifferently be cast in the state or the observables themselves. Indeed,

$$\begin{aligned} \frac{d}{dt} O(\mathbf{x}_0, t) &= \dot{\mathbf{x}} \cdot \frac{\partial O}{\partial \mathbf{x}} + \frac{\partial O}{\partial t} \\ &= \dot{q}_i \frac{\partial O}{\partial q_i} + \dot{p}_i \frac{\partial O}{\partial p_i} + \frac{\partial O}{\partial t} \\ &= \frac{\partial O}{\partial q_i} \frac{\partial H}{\partial p_i} - \frac{\partial O}{\partial p_i} \frac{\partial H}{\partial q_i} + \frac{\partial O}{\partial t} \end{aligned}$$

$$i.e. \ \boxed{\frac{dO}{dt} = \{O, H\} + \frac{\partial O}{\partial t}} \quad \textbf{Dynamics of observables} \tag{A.11}$$

---

[2] It coincides with the energy on known systems, and defines it in general.

[3] If $\partial H / \partial t \neq 0$ predicting evolution needs also the data of time. However, in a fundamental system data of $\{(q_i, p_i)\}$ exhausts all information by definition, so that in particular $H = H(q_i, p_i)$.

where we have introduced the *Poisson bracket*:

$$\textbf{Poisson bracket}\ \boxed{\{f,g\} \triangleq \frac{\partial f}{\partial q_i}\frac{\partial g}{\partial p_i} - \frac{\partial g}{\partial q_i}\frac{\partial f}{\partial p_i}} \tag{A.12}$$

This operator is at the core of the formal connection between quantum and classical mechanics. Let us nonetheless further prepare this shift by enlarging the set of admissible initial data.

A.2.2 Observables of general states

In the above discussion we considered that $\mathbf{x}(t_0) = \mathbf{x}_0$, meaning that the initial state of the system is known with certainty. However, successful prediction might require to alleviate this constraint, as for instance for systems with a large number of independent variables. This can be done introducing a probability density $f(\mathbf{x}, t)d\mathbf{x}$ for the system to be in state $\mathbf{x}$ at time t. An evolution equation for f is derived from probability conservation in a phase space volume $\Omega(t)$ comoving in time with phase space points considered as initial data:

$$\begin{aligned} P(t+dt) - P(t) = 0 & \\ &= \int_{\Omega(t+dt)} d\mathbf{x} f(\mathbf{x}, t+dt) - \int_{\Omega(t)} d\mathbf{x} f(\mathbf{x}, t) \\ &= \int_{\Omega(t)} d\mathbf{x} \left[\left| \frac{\partial u_{(t,t+dt)}(\mathbf{x})}{\partial \mathbf{x}} \right| f(u_{(t,t+dt)}(\mathbf{x}), t+dt) - f(\mathbf{x}, t) \right] \end{aligned}$$

where $u_{(t,t_0)} : \mathbf{x}_0 \mapsto \mathbf{x}(t)$ is the Hamiltonian flow, mapping a point $\mathbf{x}_0$ to the point $\mathbf{x}(t)$, solution to Hamilton's equations at time t for the initial data $\mathbf{x}(t_0) = \mathbf{x}_0$. By this definition, $\partial u_{(t,t_0)}/\partial t = \begin{pmatrix} \partial H/\partial p_i \\ -\partial H/\partial q_i \end{pmatrix}$. Besides, one demonstrates that the Jacobian of any Hamiltonian flow is one[4]. Proceeding accordingly,

$$\begin{aligned} 0 &= \int_{\Omega(t)} d\mathbf{x} \left(\frac{\partial f}{\partial t} + \frac{\partial u_{(t,t_0)}}{\partial t} \cdot \frac{\partial f}{\partial \mathbf{x}} \right) dt + O(dt^2) \\ \overset{dt \to 0}{\Longrightarrow}\ 0 &= \int_{\Omega} d\mathbf{x} \left(\frac{\partial f}{\partial t} + \{f, H\} \right) \ , \forall \Omega \end{aligned}$$

This establishes Liouville's equation,

$$\boxed{0 = \{H, f\} + \frac{\partial f}{\partial t}} \quad \textbf{Dynamics of the states} \tag{A.13}$$

$$\text{or, } \frac{df}{dt} = 0 \tag{A.14}$$

allowing to determine $f(\mathbf{x}, t)$ from an initial probability distribution $f_0(\mathbf{x})$.

---

[4] If $J(t) = \left| \frac{\partial u_{(t,t_0)}(\mathbf{x})}{\partial \mathbf{x}} \right| \equiv \left| \frac{\partial \mathbf{x}(t)}{\partial \mathbf{x}_0} \right|$, Jacobi formula gives its time derivative,

$$\begin{aligned} \dot{J} &= J(t)\mathrm{Tr}\left[\left(\frac{\partial \mathbf{x}(t)}{\partial \mathbf{x}_0} \right)^{-1} \frac{\partial \dot{\mathbf{x}}(t)}{\partial \mathbf{x}_0} \right] = J(t)\mathrm{Tr}\left[\left(\frac{\partial \mathbf{x}(t)}{\partial \mathbf{x}_0} \right)^{-1} \frac{\partial \dot{\mathbf{x}}(t)}{\partial \mathbf{x}(t)} \frac{\partial \mathbf{x}(t)}{\partial \mathbf{x}_0} \right] \\ &= J(t)\mathrm{Tr}\left[\frac{\partial \dot{\mathbf{x}}(t)}{\partial \mathbf{x}(t)} \right] = J(t) \left(\frac{\partial H}{\partial p_i \partial q_i} - \frac{\partial H}{\partial q_i \partial p_i} \right) = 0 \text{ , with use of cyclicity of the trace} \end{aligned}$$

and $J(t_0) = \left| \frac{\partial \mathrm{id}(\mathbf{x})}{\partial \mathbf{x}} \right| = 1$, so $J(t) = 1$.

All relevant quantities can then be expressed as the expectation value of an observable over a general system state,

$$\boxed{\langle \mathcal{O} \rangle_f = \int d\mathbf{x} f \mathcal{O}} \tag{A.15}$$

and we can again formulate two equivalent interpretations of the (expectation) value of an observable at time t[5],

$$\begin{aligned}
\bar{\varphi}(t) &= \langle \mathcal{O} \rangle_{f(t)} && \text{(A.16)}\\
&= \int d\mathbf{x} f(\mathbf{x}, t) \mathcal{O}(\mathbf{x}) && \text{(A.17)}\\
&= \int d\mathbf{x} f_0 \left(u^{-1}_{(t,t_0)}(\mathbf{x}) \right) \mathcal{O}(\mathbf{x}) \text{ , by Liouville's equation} \\
&= \int d\mathbf{x} f_0(\mathbf{x}) \mathcal{O}(u_{(t,t_0)}(\mathbf{x})) \text{ , using } \left| \frac{\partial u_{(t,t_0)}}{\partial \mathbf{x}} \right| = 1 \\
&= \int d\mathbf{x} f_0(\mathbf{x}) O(\mathbf{x}, t) && \text{(A.18)}\\
&= \langle O(t) \rangle_{f_0} && \text{(A.19)}
\end{aligned}$$

Either the system state evolves to f at time t when a fixed function $\mathcal{O}$ is measured, or the state merely encodes the initial data f_0 while all physical variables O evolve with time t. This transparently parallels the so-called Schrödinger and Heisenberg points of view in quantum mechanics.

Furthermore, the above reveals a duality between states and observables[6]. More specifically, any observable is fully determined by its values over a proper set of states, and conversely any state can be retrieved by the values that a proper set of observables take on it. This statement becomes trivial introducing "pure states" $f_{\mathbf{x}}(\mathbf{y}) \equiv \delta(\mathbf{y} - \mathbf{x})$, and what could be called "projections"[7] $\mathcal{O}_{\mathbf{x}}(\mathbf{y}) = \delta(\mathbf{y} - \mathbf{x})$. Either way, all necessary information about the physical system can explicitly be encoded in some set of observable values.

A.3 Algebraic aspects of physical observables

A.3.1 An algebra within classical mechanics

This procedure of abstraction of the structure underlying computation of measurement values can be pushed further, nearly closing the gap with its quantum generalization. Essentially, such structure crystallizes around the Poisson bracket. This symbol is formally interesting because it seems to allow rewriting mechanics only in terms of functions on phase space, that is general observables, independently of the specific variables (q_i, p_i) that initially defined it[8].

---

[5] We now consider an observable without explicit time dependence for better clarity of the argument.

[6] Mathematically, the expectation value is a scalar product and states are positive normalized linear forms on the vector space of observables.

[7] The analogue quantum objects mathematically are projection operators.

[†] Refs. A.3: [381]

[8] See *e.g.* Eq. A.11 or Eq. A.13; we notice in particular that canonical variables are observables themselves, and Hamilton's equations of motion Eqs. A.8 indeed write $\begin{aligned} \dot{q}_i &= \{q_i, H\} \\ \dot{p}_i &= \{p_i, H\} \end{aligned}$

This intuition finds ground in the notion of canonical transformation. Let us consider a change of variables $(q_i, p_i) \mapsto (\alpha_j, \beta_j)$ and see how the Poisson bracket transforms:

$$\{f,g\}_{qp} = \partial_{q_i} f \partial_{p_i} g - \partial_{q_i} g \partial_{p_i} f \text{ , denoting } \frac{\partial f}{\partial x} \equiv \partial_x f \tag{A.20}$$

$$\begin{aligned} &= \left(\partial_{q_i}\alpha_j \partial_{\alpha_j} f + \partial_{q_i}\beta_j \partial_{\beta_j} f\right)\left(\partial_{p_i}\alpha_k \partial_{\alpha_k} g + \partial_{p_i}\beta_k \partial_{\beta_k} g\right) \\ &\quad - \left(\partial_{q_i}\alpha_k \partial_{\alpha_k} g + \partial_{q_i}\beta_k \partial_{\beta_k} g\right)\left(\partial_{p_i}\alpha_j \partial_{\alpha_j} f + \partial_{p_i}\beta_j \partial_{\beta_j} f\right) \end{aligned} \tag{A.21}$$

$$\begin{aligned} &= \{\alpha_j, \alpha_k\}_{qp} \partial_{\alpha_j} f \partial_{\alpha_k} g + \{\alpha_j, \beta_k\}_{qp} \partial_{\alpha_j} f \partial_{\beta_k} g \\ &\quad - \{\alpha_k, \beta_j\}_{qp} \partial_{\alpha_k} g \partial_{\beta_j} f - \{\beta_k, \beta_j\}_{qp} \partial_{\beta_k} g \partial_{\beta_j} f \end{aligned} \tag{A.22}$$

Therefore, upon the condition that the canonical Poisson brackets are preserved[9],

$$\begin{array}{l|l} \textbf{Canonical} & \{\alpha_i, \alpha_j\}_{qp} = 0 \\ \textbf{Poisson} & \{\beta_i, \beta_j\}_{qp} = 0 \\ \textbf{brackets} & \{\alpha_i, \beta_j\}_{qp} = \delta_{ij} \end{array} \tag{A.23}$$

we find that the Poisson bracket does not change form,

$$\begin{aligned} \{f,g\}_{qp} &= \partial_{q_i} f \partial_{p_i} g - \partial_{q_i} g \partial_{p_i} f \\ &= \partial_{\alpha_i} f \partial_{\beta_i} g - \partial_{\alpha_i} g \partial_{\beta_i} f = \{f,g\}_{\alpha\beta} \end{aligned} \tag{A.24}$$

Transformation satisfying Eq. A.23 are called canonical. Restricting to such coordinate changes[10] the Poisson bracket acquires a coordinate-independent meaning, thus depending only on the structure of phase space.

A characterisation of mechanics can therefore *a priori* be sought for in the algebraic properties of $\{\cdot,\cdot\}$ considered as a binary operator on the space of observables, *i.e.* of real functions on phase space $\mathfrak{A}_{\mathrm{cl}} = C^\infty(\{(q_i, p_i)\}, \mathbb{R})$:

$$\text{linearity: } \{f, \lambda g + \mu h\} = \lambda\{f,g\} + \mu\{f,h\} \text{ , } \forall \lambda, \mu \in \mathbb{R} \tag{A.25}$$

$$\text{antisymmetry: } \{f,g\} = -\{g,f\} \tag{A.26}$$

$$\text{Jacobi identity: } \{f,\{g,h\}\} + \{h,\{f,g\}\} + \{g,\{h,f\}\} = 0 \tag{A.27}$$

$$\text{Leibniz rule: } \{f, gh\} = \{f,g\}h + g\{f,h\} \tag{A.28}$$

Together with the natural operations of pointwise addition and associative pointwise product, first three properties make $(\mathfrak{A}_{\mathrm{cl}}, \{\cdot,\cdot\})$ a Lie algebra, and the Leibniz rule, inherited from the differential nature of the Poisson bracket, a *Poisson algebra*.

A.3.2 Mechanics within Poisson algebras

Now to conclude at a complete characterization of mechanics, one should answer the converse question: does any real Poisson algebra correspond to the algebra of classical observables of a physical system? Though manifestly calling for a thorough mathematical treatment, such problem can shed light on the physical discussion by the following alleviated argument [382, 383]. Let us consider a Poisson algebra over a field $\mathbb{K}$ $(\mathfrak{A}_P, +, \cdot, \{\cdot,\cdot\})$, comprising a multiplicative unit $\mathbf{1}$. Then, for $a, b, u, v \in \mathfrak{A}_P$,

---

[9] Note those are the Poisson brackets of the initial canonical variables set.

[10] They are already much more general than the usual ones $q_i \mapsto Q_i$, as they allow mixing initial coordinates and conjugate momenta.

$$\begin{aligned}\{au,bv\} &= b\{au,v\}+\{au,b\}v\\ &= ba\{u,v\}+b\{a,v\}u+a\{u,b\}v+\{a,b\}uv\end{aligned} \tag{A.29}$$

by Leibniz rule on the right, then on the left. Proceeding in reverse order,

$$\begin{aligned}\{au,bv\} &= a\{u,bv\}+\{a,bv\}u\\ &= ab\{u,v\}+a\{u,b\}v+b\{a,v\}u+\{a,b\}vu\end{aligned} \tag{A.30}$$

we find equating the two,

$$\{a,b\}(uv-vu) = (ab-ba)\{u,v\} \ ,\ \forall a,b,u,v \in \mathfrak{A}_P \tag{A.31}$$

Now let us assume there exists at least one couple u, v such that $\{u,v\} \in \mathbf{1}\mathbb{K}$, by rescaling this is equivalent to $\{u,v\} = \mathbf{1}$, then using this property in Eq. A.31,

$$\{a,b\}[u,v] = [a,b] \ ,\ \forall a,b \in \mathfrak{A}_P \tag{A.32}$$

introducing the commutator symbol $[a,b] \triangleq ab - ba$. If another couple u', v' exists with a unit Poisson bracket, then writing Eq. A.31 for u, v, u', v' directly leads to,

$$[u,v] = [u',v'] \equiv Z \tag{A.33}$$

Furthermore,

$$\begin{aligned}\{a,Z\} &= \{a,[u,v]\}\\ &= [\{a,u\},v]+[u,\{a,v\}] \text{ , by Leibniz rule}\\ &= (\{\{a,u\},v\}+\{u,\{a,v\}\})\,Z \text{ , by Eq. A.32}\\ &= \{a,\{u,v\}\}\,Z \text{ , by antisymmetry and Jacobi identity}\\ &\text{but Leibniz rule implies that } \{a,\mathbf{1}\}=0\end{aligned}$$

$$\text{therefore, } \begin{cases}\{a,Z\}=0\\ \ [a,Z]=0\end{cases} ,\ \forall a \in \mathfrak{A}_P \tag{A.34}$$

This property makes the element Z a constant of the system, in the sense that it is invariant under any Hamiltonian flow Eq. A.11, and is uncorrelated to any other observable[11].

We have therefore shown that under the condition that at least one couple of variables is conjugated in the sense of classical mechanics, the defining properties of a Poisson bracket imply a direct link with the commutator of two elements via a unique constant in the centre of the Poisson algebra,

$$\boxed{\exists!\ Z \in Z(\mathfrak{A}_P) \text{ s.t. } \begin{cases}[a,b] = Z\{a,b\}\\ \{a,Z\}=0\end{cases} ,\ \forall a,b \in \mathfrak{A}_P} \tag{A.35}$$

Classical mechanics is then naturally distinguished as a special case in a wider framework, simply defined by,

$$\textbf{Classical mechanics: } \begin{cases} Z \equiv 0\\ i.e.\ [a,b]=0 \ ,\ \forall a,b \in \mathfrak{A}_P\end{cases} \tag{A.36}$$

A direct extension then appears as $Z = \lambda\mathbf{1}$ for $\lambda \in \mathbb{K}$. Together with a little more additional structure, quantum mechanics is recovered setting $\lambda \in i\mathbb{R}$, where $i^2 = -1$. Physically $\lambda \equiv i\hbar$, introducing Planck's constant, so that formally,

$$\textbf{Quantum mechanics: } \begin{cases} Z \equiv i\hbar\mathbf{1}\\ i.e.\ [a,b]=i\hbar\{a,b\} \ ,\ \forall a,b \in \mathfrak{A}_P\end{cases} \tag{A.37}$$

---

[11] For instance, in the algebra of classical mechanics these conditions would imply Z is a constant function on phase space, or in quantum mechanics that $Z = z\mathbf{1}$ for $z \in \mathbb{C}$ and $\mathbf{1}$ the identity operator.

The shift from Eq. A.36 to Eq. A.37 is called the *canonical quantization* of a system, usually summarized in the direct substitution rule $\{\cdot,\cdot\} \to -\frac{i}{\hbar}[\cdot,\cdot]$.

Expressed in terms of Poisson bracket, equations of mechanics are unchanged, as well as their operational interpretation. Of course, the mathematical realizations of the classical or quantum algebras may differ a lot in their individual parts[12]. However, their above described proximity at an abstract level is faithfully reflected in their global structure[13], or in a physical perspective when thought of in terms of observable values.

Two essential differences between classical and quantum mechanics quite often highlighted, the non-commutativity of observables and the seemingly necessary occurrence of complex numbers[14], appear at the same time in Eq. A.37. While commutative Poisson algebras directly lead to the geometric structures underlying classical mechanics known as symplectic manifolds, the former properties can be linked to so-called C^*-algebras, whose representations are known to coincide with operators on Hilbert spaces. From there follow all non-classical features of quantum mechanics[15], effectively rooting them in one equation.

In some views, it can be interpreted as conveying the "indeterminacy" of physical variables, generalizing probability theory to systems whose variables can not be assumed to all simultaneously have a value [385–388]. Alternatively one may require logically grounding physics on a set of motivated principles, then quantum mechanics can be rebuilt [389, 390] and Hamilton's principle, rather unsettling in this regard, explained as a consequence[16].

A.4 Observables in Quantum Mechanics

A.4.1 Mathematical represention

Let us conclude this section with a brief review of the realization of the quantum algebra of observables as self-adjoint operators[17] on a Hilbert space $\mathcal{H}$, that is $\mathfrak{A}_{\mathrm{q}} = \mathfrak{H}(\mathcal{H})$. States are linear forms $\omega : \mathfrak{H}(\mathcal{H}) \to \mathbb{R}$ satisfying $\omega(A^\dagger A) > 0$ and $\omega(\mathbf{1}) = 1$, which by Riesz representation theorem can be identified with operators $\rho \in \mathcal{S}(\mathcal{H})$ called state operators or density matrices. Using scalar product $A \cdot B \triangleq \mathrm{Tr}(A^\dagger B)$ for the representation, these operators satisfy,

$$\begin{array}{ll} & \rho^\dagger = \rho \\ \textbf{State operator} & \sigma(\rho) \subset \mathbb{R}^+ \text{ , denoting } \sigma(\rho) \text{ the spectrum of } \rho \\ & \mathrm{Tr}(\rho) = 1 \end{array} \tag{A.38}$$

The expectation value of an observable then writes,

$$\boxed{\langle \mathcal{O} \rangle_\rho = \mathrm{Tr}\left(\rho \mathcal{O}\right)} \tag{A.39}$$

For consistency, as we shall now explain, one furthermore postulates that the value o taken by a measured observable $\mathcal{O}$ belongs to its spectrum,

$$\textbf{Observable values: } \varphi = o \in \sigma(\mathcal{O}) \tag{A.40}$$

---

[12] Typically, comparing a collection of point particles coordinates with a wavefunction.

[13] Precisely because, in a mathematical sense, they are representations of algebraic structures that, in an informal sense, are found very similar (linked by a single parameter $\lambda \in \mathbb{C}$).

[14] Implying up to representations. See *e.g.* [384] and citations for an entry to this topic.

[15] *e.g.* superpositions, Heisenberg indeterminacy relations, entanglement, etc.

[16] See *e.g.* the "path-integral" expression of transition amplitudes for an explicit connection [22].

[†] Refs. A.4: [381, 385, 386]

[17] We denote the adjoint of A by $A^\dagger$, so that observables satisfy $\mathcal{O}^\dagger = \mathcal{O}$.

A.4.2 Quantum indeterminacy

From the defining properties, if $\rho_1, \rho_2 \in \mathcal{S}(\mathcal{H})$ and $\mu \in [0,1]$ then $\mu\rho_1 + (1-\mu)\rho_2 \in \mathcal{S}(\mathcal{H})$, so that states form a convex set. A state operator cannot be decomposed in such a way if and only if $\mathrm{Tr}(\rho^2) = 1$, in which case it is called a "pure state"[18] and is a one-dimensional projection operator: $\exists\, |\psi\rangle \in \mathcal{H}$ s.t. $\rho_{\text{pure}} \equiv \rho_\psi = |\psi\rangle\langle\psi|$, introducing Dirac notations. An important difference with the classical case is that observable values can never be all predicted with certainty[19], even in a pure state. Indeed [391],

$$\begin{aligned}
\langle(\mathcal{O} - \langle\mathcal{O}\rangle_\psi)^2\rangle_\psi &= \langle\mathcal{O}^2\rangle_\psi - \langle\mathcal{O}\rangle_\psi^2 \\
&= \mathrm{Tr}\left(|\psi\rangle\langle\psi|\mathcal{O}^2\right) - \mathrm{Tr}\left(|\psi\rangle\langle\psi|\mathcal{O}\right)^2 \\
&= \mathrm{Tr}\left(|\psi\rangle\,\langle\psi|\psi\rangle\,\langle\psi|\,\mathcal{O}^2\right) - \langle\psi|\,\mathcal{O}\,|\psi\rangle\,\langle\psi|\,\mathcal{O}\,|\psi\rangle \\
&= \mathrm{Tr}\left(\rho_\psi^2\mathcal{O}^2 - \rho_\psi\mathcal{O}\rho_\psi\mathcal{O}\right) \\
&= \frac{1}{2}\mathrm{Tr}\left([\rho_\psi, \mathcal{O}]^\dagger[\rho_\psi, \mathcal{O}]\right) \qquad \text{(A.41)}
\end{aligned}$$

where the self-adjointness of ρ_ψ and $\mathcal{O}$ have been used in the last line. Therefore, an observable is always measured equal to its expectation value in state ρ_ψ if and only if[20] it commutes with the projector $|\psi\rangle\langle\psi|$, that is if $|\psi\rangle$ is an eigenvector of $\mathcal{O}$.

This allows viewing the postulate Eq. A.40 in a new light. Let us indeed require that two immediately successive[21] measurements always give the same result, say $o'|_o = o$, and denote $\rho_{\psi'|_o}$ the system state after the first measurement. Then, by the above, this condition is equivalent to requiring that $\rho_{\psi'|_o}$ be a projector on an eigenvector of $\mathcal{O}$, implying that $o'|_o \in \sigma(\mathcal{O})$ and therefore o as well. This consistency requirement is sometimes referred to as the "(Von-Neumann) projection postulate".

Besides, let $\mathcal{O}^{(\prime)} = \sum_i o_i^{(\prime)} |\varphi_i^{(\prime)}\rangle\langle\varphi_i^{(\prime)}|$ be two non-commuting variables[22]. Then given ρ_ψ a general pure state and alleviating notations with $c_{i\psi} \equiv \langle\varphi_i|\psi\rangle$ and $c_{ij'} \equiv \langle\varphi_i|\varphi'_j\rangle$,

$$\langle\mathcal{O}\rangle_\psi = \mathrm{Tr}\left[\rho_\psi \sum_k o_k |\varphi_k\rangle\langle\varphi_k|\right] = \sum_k o_k P_{k|\psi}\ , \text{ with } P_{k|\psi} \equiv |c_{k\psi}|^2 \qquad \text{(A.42)}$$

$$\text{now, } P_{k|\psi} = c_{k\psi}c_{k\psi}^* = \sum_{l,p} c_{kl'}c_{l'\psi}\left(c_{kp'}c_{p'\psi}\right)^*\ \text{, using two times } \mathbf{1} = \sum_k |\varphi'_k\rangle\langle\varphi'_k|$$

$$\textit{i.e.}\ \boxed{P_{k|\psi} = \sum_l P_{k|l'}P_{l'|\psi} + 2\sum_{l<p}\mathcal{I}_{k|^{l'}_{p'}|\psi}}\ \text{, with } \mathcal{I}_{k|^{l'}_{p'}|\psi} \equiv \mathrm{Re}\left[c_{kl'}c_{l'\psi}\left(c_{kp'}c_{p'\psi}\right)^*\right] \qquad \text{(A.43)}$$

Unobserved values can therefore not simply be assumed existent but unknown as the first line could suggest, instead all potential values of any non-commuting observables "interfere" according to the generalized conditional probability formula Eq. A.43.

Together with the existence of an absolute scale of action $\hbar$, this specific form of indeterminacy can be used to capture the major qualitative aspects of quantum mechanics [386, 392, 393]. Because variables do not have and then take values the theory is *discrete*, according to Eq. A.41 this process is *random*, and potential (observable but unobserved) values of non-commuting variables bilinearly *interfere* in final probabilities Eq. A.43.

---

[18] It is said "mixed" otherwise. Pure states have maximum information, or lowest possible entropy, and thereby are the quantum counterpart of previously defined classical pure states $f_{\mathbf{x}} : \mathbf{y} \mapsto \delta(\mathbf{y} - \mathbf{x})$.

[19] Admitting the usual methodological principles pertaining to the relevance of limited (local) data, they should not be inferred to have *any definite* value in-between measurements [386–388], *cf.* also Eq. A.43.

[20] Recall that $A \mapsto \mathrm{Tr}(A^\dagger A)$ is a norm of $\mathcal{L}(\mathcal{H}, \mathcal{H})$ (upon appropriate mathematical restrictions).

[21] Hence indiscernible.

[22] Note they could simply be the same variable at two times, or after any other transformation.

A.4.3 Dynamics of states and observables

Dynamics is given by either mechanical equations Eq. A.11 or Eq. A.13 with the Poisson bracket defined by Eq. A.37, leading respectively to Heisenberg and Von-Neumann equations,

$$\boxed{\begin{cases} \textbf{Dynamics of observables :} & i\hbar\dfrac{dO}{dt} = [O,H] + i\hbar\dfrac{\partial O}{\partial t} \\ \text{(Heisenberg)} & \\ \textbf{Dynamics of the state :} & 0 = [\rho,H] + i\hbar\dfrac{\partial \rho}{\partial t} \\ \text{(Von-Neumann)} & \end{cases}} \qquad \begin{matrix}\text{(A.44)}\\[3em]\text{(A.45)}\end{matrix}$$

with H the Hamiltonian observable. Let us for instance consider the Heisenberg equation more closely, for an observable without extrinsic time-dependence,

$$\begin{aligned} \frac{dO}{dt} &= -\frac{i}{\hbar}OH + \frac{i}{\hbar}HO \\ &= \frac{dV}{dt}V^{-1}O + OU^{-1}\frac{dU}{dt} \\ &\text{introducing invertible operators } U,\ V \text{ s.t. } O(t) \equiv V(t)\mathcal{O}U(t) \\ &\qquad\qquad\qquad\qquad \text{with } O(t_0) = \mathcal{O} \end{aligned} \tag{A.46}$$

$$\begin{aligned} &\text{so that, } \begin{cases} \dfrac{dU}{dt} = -\dfrac{i}{\hbar}UH \\ \dfrac{dV}{dt} = \dfrac{i}{\hbar}HV \end{cases} \\ &\Leftrightarrow \begin{cases} \dfrac{dU}{dt} = -\dfrac{i}{\hbar}UH \ : \textbf{Evolution (differential)} \\ \dfrac{dV^\dagger}{dt} = -\dfrac{i}{\hbar}V^\dagger H \ , \text{ because as an observable } H^\dagger = H \end{cases} \end{aligned} \tag{A.47}$$

Time independence of the Hamiltonian of fundamental systems derives from anti-symmetry of the Poisson bracket and is therefore still true. By our definition we clearly have $U(t_0) = V(t_0) = \mathbf{1}$, so that the familiar expressions for the time evolution follow,

Evolution operator

$$\boxed{\begin{gathered} O(t) = U^\dagger(t,t_0)\mathcal{O}U(t,t_0) \\ \text{with, } U(t,t_0) = e^{-\frac{i}{\hbar}H(t-t_0)} \text{ the evolution operator} \end{gathered}} \tag{A.48}$$

The evolution operator is easily seen unitary as the Hamiltonian is hermitian, $U^\dagger U = \mathbf{1}$, conveying again conservation of total probability.

Equivalence of state or variables time evolution, Schrödinger or Heisenberg picture, is even more transparent than classically:

$$\begin{aligned} \bar{\varphi}(t) &= \langle \mathcal{O} \rangle_{\rho(t)} && \text{(A.49)} \\ &= \mathrm{Tr}\left(\rho(t)\mathcal{O}\right) && \text{(A.50)} \\ &= \mathrm{Tr}\left(U(t,t_0)\rho_0 U^\dagger(t,t_0)\mathcal{O}\right) \ , \text{ by Von-Neumann's equation} && \\ &= \mathrm{Tr}\left(\rho_0 U^\dagger(t,t_0)\mathcal{O}U(t,t_0)\right) \ , \text{ by cyclicity of the trace} && \\ &= \mathrm{Tr}\left(\rho_0 O(t)\right) && \text{(A.51)} \\ &= \langle O(t) \rangle_{\rho_0} && \text{(A.52)} \end{aligned}$$

A.4.4 Interaction formalism

In this discussion we have illustrated the invariance of mechanics so as to motivate the mathematical form of quantum theories, for which exact equations were pivotal. However a large part of the terminology used to describe quantum fields derives from approximation methods, almost always required for definite prediction. We will now present one link between these views.

Let us assume that the Hamiltonian of the system can be written as,

$$\textbf{Interaction form :}\ H = H_0 + \underbrace{gV_I}_{H_I} \tag{A.53}$$

where time-evolution generated by H_0 can be solved exactly[23] and $g \in \mathbb{R}$. In many contexts H_0 is called the "free" or "kinetic" Hamiltonian, H_I the "interaction" term and g the coupling parameter[24].

We can therefore decompose time evolution so as to isolate contributions from H_I,

$$\begin{cases} U(t,t_0) \equiv U_0(t,t_0)U_I(t,t_0) \\ \dfrac{dU_0}{dt} = -\dfrac{i}{\hbar}U_0H_0 \end{cases} \tag{A.55}$$

Substituting in the full equation Eq. A.47 we find,

$$\begin{aligned} i\hbar\frac{dU}{dt} &= UH \\ \Leftrightarrow i\hbar\left(\frac{dU_0}{dt}U_I + U_0\frac{dU_I}{dt}\right) &= U_0U_I\left(H_0+H_I\right) \\ \Leftrightarrow U_0H_0U_I + i\hbar U_0\frac{dU_I}{dt} &= \left(H_0+H_I\right)U_0U_I\ \text{, using } [U,H]=0 \\ \Leftrightarrow i\hbar\frac{dU_I}{dt} &= U_0^\dagger H_I U_0 U_I\ \text{, using } [U_0,H_0]=0 \end{aligned} \tag{A.56}$$

Now because $[H,U]=0$, the operators within the Hamiltonian of the first line can be written at any time. Choosing $H = H(\mathcal{Q},\mathcal{P})$, we have,

$$U_0^\dagger H_I U_0 \equiv H_I^0(t) = H_I(Q^0(t),P^0(t)) \tag{A.57}$$

$$\text{defining, } \boxed{O^0(t) \triangleq U_0^\dagger(t,t_0)\mathcal{O}U_0(t,t_0)} \tag{A.58}$$

---

[23] This means that $U_0(t,t_0) \equiv e^{-\frac{i}{\hbar}H_0(t-t_0)}$ can be expressed analytically, *e.g.* by diagonalization. Introducing a basis of the Hilbert space $\mathbf{1} = \int dq|q\rangle\langle q|$, that diagonalizes the operator Q such that $[Q,P]=i\hbar$, we can define $\psi : (q,t) \mapsto \langle q|U(t,t_0)|\psi_0\rangle$ for a given vector $|\psi_0\rangle \in \mathcal{H}$. Then by projection Eq. A.47 implies that,

$$\begin{aligned} i\hbar\frac{\partial\psi}{\partial t}(q,t) &= \int dq'\ \langle q|\,H(\mathcal{Q},\mathcal{P})\,|q'\rangle\,\psi(q',t) \\ &= H(q,-i\hbar\frac{\partial}{\partial q})\psi(q,t) \end{aligned} \tag{A.54}$$

where $\mathcal{Q}$ and $\mathcal{P}$ are the Q and P operators at initial time, and in the second line we have used the representation of $\mathcal{P}$ in the $|q\rangle$ basis, which is a consequence of the canonical commutation relation (*cf.* Weyl's form). Hence, finding $U_0(t,t_0)$ is equivalent to finding a basis of the solution space of Eq. A.54, the Schrödinger equation, for the Hamiltonian H_0.

[24] Note these notions are quite conventional, but nonetheless find ground in the fact that often H_0 stems from the evolution of two isolated systems, and H_I is required to describe their joint evolution.

Therefore,

Interaction evolution (differential)
$$\frac{dU_I}{dt} = -\frac{i}{\hbar}H_I^0 U_I \tag{A.59}$$

This equation is different from Eq. A.47 because now the operator H_I^0 depends on time, and does *a priori* not commute with itself at different times nor with U_I. A formal solution can however be written by integration and recursive substitution,

$$\begin{aligned} U_I(t,t_0) &= \mathbf{1} + \int_{t_0}^{t} d\bar{t}\frac{dU_I}{dt}(\bar{t}) \\ &= \mathbf{1} + \frac{1}{i\hbar}\int_{t_0}^{t} dt_1 H_I^0(t_1)U_I(t_0,t_1) \\ &= \mathbf{1} + \frac{1}{i\hbar}\int_{t_0}^{t} dt_1 H_I^0(t_1) \\ &\qquad + \left(\frac{1}{i\hbar}\right)^2 \int_{t_0}^{t} dt_1 \int_{t_0}^{t_1} dt_2 H_I^0(t_1)H_I^0(t_2)U_I(t_0,t_2) \\ &\;\vdots \\ &= \mathbf{1} + \sum_{k=1}^{\infty}\left(\frac{1}{i\hbar}\right)^k \int_{t_0}^{t} dt_1 \cdots \int_{t_0}^{t_{k-1}} dt_k H_I^0(t_1)\cdots H_I^0(t_k) \end{aligned} \tag{A.60}$$

Now let us examine more closely the successive integrals,

$$\int_{t_0}^{t} dt_1 \cdots \int_{t_0}^{t_{k-1}} dt_k H_I^0(t_1)\cdots H_I^0(t_k) = \int_{\substack{t_1,\ldots,t_k\in[t_0,t] \\ t_k\le t_{k-1}\le\cdots\le t_1}} dt_1 \ldots dt_k H_I^0(t_1)\cdots H_I^0(t_k) \tag{A.61}$$

so that we simply integrate over all products of operators $H_I^0(\bar{t})$ with $\bar{t}\in[t_0,t]$ arranged in order of decreasing time argument. We can rewrite this in terms of unconstrained time arguments $t_k\in[t_0,t]$ introducing the "time-ordering" symbol τ which returns any product of time-dependent operators in order of decreasing time argument[25]:

$$\int_{t_0}^{t} dt_1 \cdots \int_{t_0}^{t_{k-1}} dt_k H_I^0(t_1)\cdots H_I^0(t_k) \equiv \frac{1}{k!}\int_{t_1,\ldots,t_k\in[t_0,t]} dt_1 \ldots dt_k \tau\left[H_I^0(t_1)\cdots H_I^0(t_k)\right] \tag{A.62}$$

where division by the permutation number of k elements accounts for the redundancy induced by allowing all possible orderings of the integration variables $t_1,\ldots,t_k$.

Substituting in Eq. A.61 we find the so-called Dyson series expression of the interaction time evolution operator U_I,

$$U_I(t,t_0) = \mathbf{1} + \sum_{k=1}^{\infty}\frac{1}{k!}\left(\frac{1}{i\hbar}\right)^k \int_{t_1,\ldots,t_k\in[t_0,t]} dt_1 \ldots dt_k \tau\left[H_I^0(t_1)\cdots H_I^0(t_k)\right] \tag{A.63}$$

which can be compactly written as,

Interaction evolution operator
$$\boxed{U_I(t,t_0) = \tau e^{-\frac{i}{\hbar}\int_{t_0}^{t} d\bar{t} H_I^0(\bar{t})}} \tag{A.64}$$

---

[25] *e.g.* if $t_a < t_b < t_c$, then $\tau\left[B(t_b)C(t_c)A(t_a)\right] = A(t_a)B(t_b)C(t_c)$.

Now substituting in Eq. A.51 any expectation value can be written as,

$$\langle O(t)\rangle_{\rho_0} = \mathrm{Tr}\left(\rho_0 \bar{\tau} e^{-\frac{i}{\hbar}\int_t^{t_0} d\bar{t} H_I^0(\bar{t})} O^0(t) \tau e^{-\frac{i}{\hbar}\int_{t_0}^{t} d\bar{t} H_I^0(\bar{t})}\right) \tag{A.65}$$

where we have introduced the anti-time ordering symbol $\bar{\tau}$ to express $U_I^\dagger$. In this expression we notice that all operators are arranged in increasing time order until $O(t)$, after which they decrease again. We unite both introducing a contour $\gamma = [t_0, t] \oplus [t, t_0]$, and a "contour ordering" symbol τ_γ which orders operators in order of increasing argument on the the contour[26]. Then,

$$\boxed{\langle O(t)\rangle_{\rho_0} = \mathrm{Tr}\left(\rho_0 \tau_\gamma e^{-\frac{i}{\hbar}\int_\gamma dz g H_I^0(z)} O^0(t)\right)} \tag{A.66}$$

Naturally, this whole interaction formalism truly proves relevant when the interaction term can be considered small[27], typically for $g \ll 1$. In such instance, we can perform a *perturbative expansion* of the evolution operator U_I, which translates in a decomposition of all expectation values as power series in g:

$$\boxed{\begin{aligned}\langle O(t)\rangle_{\rho_0} \simeq \langle O^0(t)\rangle_{\rho_0} &- g\frac{i}{\hbar}\int_\gamma dz \langle \tau_\gamma V_I^0(z) O^0(t)\rangle_{\rho_0} \\ &+ g^2 \frac{1}{2!}\left(\frac{-i}{\hbar}\right)^2 \int_{\gamma_1}\int_{\gamma_2} dz_1 dz_2 \langle \tau_\gamma V_I^0(z_1) V_I^0(z_2) O^0(t)\rangle_{\rho_0} + \dots\end{aligned}} \tag{A.67}$$

Total evolution is thereby seen as a "free" part, generated by U_0, corrected by contributions from all possible numbers of "interaction events", appearing as products with V_I^0, of decreasing relative magnitude.

---

[26] This approach leads to the "Schwinger-Keldysh formalism" [307]. It naturally arises working with general states and extends scattering theory, restricted to the computation of transition amplitudes.

[27] In the sense *e.g.* of expectation value compared to that of H_0. Note that this condition therefore not only depends on g but also on the initial state and subsequent dynamics, which, in particular, is precisely why strong-field QED differs from the vacuum theory.

APPENDIX B

Landmarks in view of Quantum Field Theory and strong fields

We here present some elements of the extension of mechanics to relativistic quantum and possibly strong fields. More specifically, our aim is to provide motivation and references for concepts and methods relevant to an understanding of Quantum Field Theory irrespective of a specific context of application, though appropriate in view of strong-field Quantum Electrodynamics. For brevity as well as clarity, exposition will operate at an essentially heuristic level, while trying and preserve accurate enough mapping to the operational literature.

We will be proceeding through the following issues, in order of physical significance[1],

I – **Relativity and symmetries** Quantum fields are necessary parts of a fundamental theory insofar as they provide a realization of the principle of relativity. In a first section we will draw this connection, starting from the canonical formalism of mechanics. We will then be able to present how symmetry requirements dictate the form of physical variables, in particular some aspects of the field-particles duality, and eventually introduce the constituents of Quantum Electrodynamics.

II – **Fields observables and diagrammatic representation** In classical or quantum mechanics, canonical variables play the role of generating the algebra of observables defining a physical system. In systems of finite and small number of variables, this process often is obscured by the possibility to at least formally consider the joint evolution of a complete set of observables, possibly summarized in a state[2], and only then compute any quantity of interest. On the opposite, for systems of practically or conceptually infinite number of variables the efficient coordinatization of general observables by a generating subset proves crucial. In this section we will show how this idea is embedded in the fields $n-$points functions. The construction of finite order perturbation theory is presented first, introducing diagrammatic representations, followed by a motivation of exact relations more suited to general non-equilibrium contexts and thus strong fields in particular.

III – **Similarity classes of initial states** Prediction of observable values are produced in the form of expectation values, which encode all dependence on the initial data. Some formalisms, perturbative quantum field theory notably, however make extensive use of relations existing between intermediate quantities specifically for some initial state. In this section we briefly present how "reduction formula" unify methods within some sets of states, effectively defining equivalence classes, and how these distinctions tend to blur in the out-of-equilibrium initial values formulation.

---

[1] References are given as in App. A for the same reasons.

[2] In Quantum Mechanics, this would typically correspond to the computation of all coefficients of the state vector in a Hilbert space basis, the latter being given by the common eigenbasis of a "complete set of commuting observables".

B.1 Embedding of symmetry

The very notion of field can be understood as derived from the principle of locality, itself stemming from Einsteinian relativity of spacetime coordinates. Any fundamental physical theory therefore has to incorporate the underlying notion of invariance, also called "symmetry" in this context. Requiring *i)* actual invariance of physical predictions and *ii)* formal invariance of intermediate equations under a change of reference frame has strong technical implications, as can be guessed already in the above from the pervasive use of a distinguished time parameter. In an interesting turn, it occurs that the induced constraints are so strong they almost determine the physical variables and their interactions. In other words, a quantum mechanical theory consistent with few basic principles of *special relativity* is virtually driven to be a field(s) theory, whose forms and non-interacting dynamics are determined by a mass $m \in \mathbb{R}^+$ and spin $j \in \frac{1}{2}\mathbb{N}$, describing the evolution of bosonic or fermionic particles[3]. It has become a standard method also to generate interactions between fields *a priori* from extended symmetry principles[4], generalizing the notion of relativity.

The axiomatic derivation of QFT can proceed from an algebra of observables compatible with special relativistic locality, giving a primary role to "covariant local fields", as the generators of any observable, built through finite dimensional but non-unitary representations of the Poincaré group[5] [394]. Alternatively, one can consider the action of the Poincaré group on the Hilbert space of pure states, in which case unitary but infinite dimensional representations come first, defining the (multi-)particles Hilbert space (Fock space), and local covariant fields appear so as to enforce Poincaré-invariant dynamics [395]. Both are mathematically involved[6]. Here we will simply motivate some constituting elements of relativistic QFT at an heuristic level, based on these principles and the canonical formalism of mechanics.

B.1.1 From the Poincaré group to fields

- The set of all changes of inertial reference frame forms a group, called the Lorentz group $\mathfrak{L}$, its extension to include space and time translations is called the Poincaré group $\mathfrak{P}$. The Poincaré group is primarily defined as transformations on Minkowski space vector coordinates,

$$\begin{cases} x^\mu \xrightarrow{(\Lambda,a)} x^\mu = \Lambda^\mu{}_\nu x^{\nu\prime} + a^\mu \\ \Lambda^\rho{}_\mu \Lambda^\sigma{}_\nu \eta_{\rho\sigma} = \eta_{\mu\nu} \text{ , with } \eta = \mathrm{diag}(1,-1,-1,-1) \end{cases} \tag{B.1}$$

  where x^μ and $x^{\mu\prime}$ are interpreted as the coordinates of the same event respectively in the new and old reference frame. From general mechanics we know that Poincaré-

---

[†] Refs. B.1:[394–396]

[3] Together with unitarity, Lorentz-invariance even allows for excluding spins $j > 2$ and most couplings between the remaining ones in a fundamental theory (see results along the so-called "bootstrap" program).

[4] Most notably introducing local transformations of fields under a compact Lie group, known as a "gauge tranformation", resulting in "gauge theories" (Quantum Electrodynamics and Chromodynamics are two prominent examples).

[5] We will say more on the mathematical notion of "representation" below.

[6] For that matter, a rigorous mathematical definition of interacting quantum field theory is a notoriously open problem. One major obstruction is the existence of multiple inequivalent representations of the canonical commutation relations (*i.e.* Poisson brackets, see Eq. A.37) $[q_j, p_j] = i\hbar$ for an infinite number of variables [394].

invariant predictions would derive from a Poincaré-invariant action,

$$S' - S = 0 \tag{B.2}$$

$$i.e.\ \int_{\Omega'} d\tau L' - \int_{\Omega} d\tau L = 0\ ,\ \forall\Omega \tag{B.3}$$

where Ω is an undefined integration domain *a priori* encapsulating both the summation over physical variables and the boundaries that we wish to correlate. Now a natural way to enforce such condition appears to take Ω as a spacetime domain, for Poincaré transformations are simply given on Minkowski coordinates and by change of variable then,

$$\int_{\Omega'} dx\mathcal{L}'(x) = \int_{\Omega} dx\mathcal{L}'(\Lambda^{-1}(x-a))\ ,\ \text{using } |\det(\Lambda^{-1})| = 1\ (\textit{cf.}\ \text{Eq. B.1}) \tag{B.4}$$

introducing the "Lagrangian density" $\mathcal{L}$, and so Poincaré-invariance Eq. B.3 simply translates into,

$$\mathcal{L}'(\Lambda^{-1}(x-a)) = \mathcal{L}(x)\ ,\ \forall x$$

$$\Leftrightarrow \textbf{Lorentz-scalar: } \boxed{\mathcal{L}'(x) = \mathcal{L}(\Lambda x + a)} \tag{B.5}$$

This relation defines a "Lorentz scalar field", and simply reflects that the field values at the same event coincide in both reference frames.

In this context we note that kinematics (the set of physical variables) is not entirely transparently distinguished from dynamics (their transition from data to predicted values). The Lorentz-scalar condition inducing causality in the special relativistic sense, this distinction can be operated by considering a spacelike surface Σ crossing all timelike curves of Ω exactly once[7], for all predictions in Ω are then determined by appropriate data of the variables on Σ. We conclude that our physical variables are $\{q(x)\}_{x\in\Sigma}$, continuously indexed by a space of dimension 3, and thereby call them a *field*.

The canonical quantization of such system should then be a quantum and Poincaré-invariant theory. Before reviewing general conclusions, let us first illustrate this procedure in a simple case.

B.1.2 Illustration: canonical quantization of the free scalar field

- A Lagrangian density built from a Lorentz-scalar field evidently is a Lorentz-scalar itself. We therefore consider the real scalar field $\{\phi(\mathbf{x})\}_{\mathbf{x}\in\mathbf{R}^3}$, taking a simultaneity plane as our Cauchy surface. In order to include the field time-derivatives in the invariant Lagrangian, they should appear via scalar products[8] of the four derivative $\frac{\partial\phi}{\partial x^\mu} \equiv \partial_\mu\phi$. Considering a linear theory finally constrains the Lagrangian to,

$$\textbf{Scalar field (free): } \mathcal{L}(\phi, \partial_\mu\phi) = \frac{1}{2}\partial_\mu\phi\partial^\mu\phi - \frac{1}{2}m^2\phi^2 \tag{B.6}$$

---

[7] The existence of such Σ, called a "Cauchy surface", then being understood as part of the definition of Ω. The limiting case of a lightlike surface also is acceptable and actually finds uses, for instance in the context of so-called "light-front" quantization.

[8] Recall that Lorentz transforms preserve the Minkowski scalar product (*cf.* Eq. B.1): $(\Lambda x)\cdot(\Lambda y) = x\cdot y \triangleq \eta_{\mu\nu}x^\mu y^\nu \equiv x_\mu y^\mu$.

The Euler-Lagrange equations follow as before,

$$\begin{aligned}0 &= \int_\Omega dx\left[\mathcal{L}|_{\phi+\delta\phi}(x) - \mathcal{L}|_{\phi}(x)\right]\\ &= \int_\Omega dx\left[\frac{\partial\mathcal{L}}{\partial\phi}\delta\phi(x) + \frac{\partial\mathcal{L}}{\partial(\partial_\mu\phi)}\delta\partial_\mu\phi(x)\right]\\ &= \int_\Omega dx\left[\frac{\partial\mathcal{L}}{\partial\phi} - \partial_\mu\left(\frac{\partial\mathcal{L}}{\partial(\partial_\mu\phi)}\right)\right]\delta\phi(x) + \oint_{\partial\Omega} d\sigma_\mu\left[\frac{\partial\mathcal{L}}{\partial(\partial_\mu\phi)}\delta\phi(x)\right]\\ i.e.\ 0 &= \frac{\partial\mathcal{L}}{\partial\phi} - \partial_\mu\left(\frac{\partial\mathcal{L}}{\partial(\partial_\mu\phi)}\right) \quad \textbf{(Euler-Lagrange)} \qquad \text{(B.7)}\end{aligned}$$

For our scalar field we thus find,

$$\textbf{Klein-Gordon}\ \boxed{(\partial^2 + m^2)\phi(x) = 0} \qquad \text{(B.8)}$$

Shifting to the Hamiltonian formalism we have,

$$\pi(x) = \frac{\partial\mathcal{L}}{\partial(\partial_0\phi(x))} \equiv \partial_0\phi(x) \qquad \text{(B.9)}$$

so that performing the Legendre transform $\mathcal{H} = \pi\phi - \mathcal{L}$,

$$\mathcal{H}(\phi, \nabla\phi, \pi) = \frac{1}{2}\pi^2 + \frac{1}{2}(\nabla\phi)^2 + \frac{1}{2}m^2\phi^2 \qquad \text{(B.10)}$$

The equations of motion take the Hamiltonian form,

$$\textbf{(Hamilton)}\ \begin{cases}\partial_0\phi(x) = \{\phi(x), H\}\\ \partial_0\pi(x) = \{\pi(x), H\}\end{cases} \qquad \text{(B.11)}$$

with Hamiltonian $H = \int d\mathbf{x}\mathcal{H}(\mathbf{x})$, and Poisson bracket[9],

$$\{f, g\} = \int d\mathbf{x}\frac{\delta f}{\delta\phi(\mathbf{x})}\frac{\delta g}{\delta\pi(\mathbf{x})} - \frac{\delta g}{\delta\phi(\mathbf{x})}\frac{\delta f}{\delta\pi(\mathbf{x})} \qquad \text{(B.12)}$$

The field variables consequently have the equal-time Poisson brackets,

$$\begin{cases}\{\phi(x), \phi(y)\}_{x^0=y^0} = \{\pi(x), \pi(y)\}_{x^0=y^0} = 0\\ \{\phi(x), \pi(y)\}_{x^0=y^0} = \delta(x-y)\end{cases} \qquad \text{(B.13)}$$

However, by construction our action is invariant under Lorentz transformations, and it is a classical result of mechanics that symmetries of the action generate canonical transformations[10], so that,

$$\{f(x), g(y)\}_{\phi(z)\pi(z)} = \{f(x), g(y)\}_{\phi(\Lambda z)\pi(\Lambda z)} \qquad \text{(B.14)}$$

$$\text{that is, } \{f(x), g(y)\} = \{f(\Lambda x), g(\Lambda y)\} \qquad \text{(B.15)}$$

Therefore, the equal-time canonical relations actually hold for any spacetime points in the image of the equal-time plane by the Lorentz group, so that they are spacelike commutation relations indeed,

$$\text{Local Poisson Brackets}\ \boxed{\begin{cases}\{\phi(x), \phi(y)\}_{x\cdot y<0} = \{\pi(x), \pi(y)\}_{x\cdot y<0} = 0\\ \{\phi(x), \pi(y)\}_{x\cdot y<0} = \delta(x-y)\end{cases}} \qquad \text{(B.16)}$$

---

[9] The "functionnal derivative" is formally defined by *i)* $\frac{\delta uv}{\delta f(\mathbf{x})} = \frac{\delta u}{\delta f(\mathbf{x})}v + u\frac{\delta v}{\delta f(\mathbf{x})}$ and *ii)* $\frac{\delta f(\mathbf{y})}{\delta f(\mathbf{x})} = \delta(\mathbf{x}-\mathbf{y})$. We besides understand derivatives of delta in the usual sense of distributions, $f\nabla\delta(\mathbf{x}-\mathbf{y}) = -\delta(\mathbf{x}-\mathbf{y})\nabla f$.

[10] This equivalence is the Hamiltonian form of Noether's theorem, see [397–399] for explicit derivations.

- Canonical quantization provides the commutation relations of the quantum variables[11],

Commutation Relations (local)

$$\boxed{\begin{cases} [\phi(x),\phi(y)]_{x\cdot y<0} = [\pi(x),\pi(y)]_{x\cdot y<0} = 0 \\ [\phi(x),\pi(y)]_{x\cdot y<0} = i\delta(x-y) \end{cases}} \tag{B.17}$$

In order to proceed further, let us take advantage of the linearity of the equations of motion to express ϕ as a Fourier transform,

$$\phi(x) = \int dk \left(f(k)e^{-ik\cdot x} + f^\dagger(k)e^{ik\cdot x} \right) \tag{B.18}$$

where the hermitian conjugate part is a consequence of the real values (hermiticity) of ϕ. From the equations of motion we have the dispersion relation[12] $f(k) \propto \delta(k^2 - m^2)\theta(k^0)$, so that integrating over k^0 we find[13],

$$\begin{cases} \phi(x) = \int \frac{d\mathbf{k}}{2E_\mathbf{k}} \left(a(\mathbf{k})e^{-ik\cdot x} + a^\dagger(\mathbf{k})e^{ik\cdot x} \right) & \text{(B.19)} \\ \pi(x) = -i\int \frac{d\mathbf{k}}{2E_\mathbf{k}} E_\mathbf{k} \left(a(\mathbf{k})e^{-ik\cdot x} - a^\dagger(\mathbf{k})e^{ik\cdot x} \right) & \text{(B.20)} \end{cases}$$

where $k \equiv (E_\mathbf{k}, \mathbf{k})$ now satisfies the relativistic dispersion relation, and $a(\mathbf{k}), a^\dagger(\mathbf{k})$ still to be determined. These relations can be inverted,

$$\begin{cases} a(\mathbf{k}) = i\int d\mathbf{x} e^{ik\cdot x} \left[\pi(x) - iE_\mathbf{k}\phi(x)\right] & \text{(B.21)} \\ a^\dagger(\mathbf{k}) = -i\int d\mathbf{x} e^{-ik\cdot x} \left[\pi(x) + iE_\mathbf{k}\phi(x)\right] & \text{(B.22)} \end{cases}$$

and using the equal-time commutation relations we find the canonical commutation relations (CCR),

Commutation Relations (canonical)

$$\boxed{\begin{cases} [a(\mathbf{k}), a(\mathbf{k}')] = [a^\dagger(\mathbf{k}), a^\dagger(\mathbf{k}')] = 0 \\ [a(\mathbf{k}), a^\dagger(\mathbf{k}')] = 2E_\mathbf{k}\delta(\mathbf{k}-\mathbf{k}') \end{cases}} \tag{B.23}$$

These relations together with the existence of a lowest energy state $|0\rangle$ entirely determine the form of state space[14]. In particular, $a(\mathbf{k})|0\rangle = 0$, $\forall\mathbf{k}$ and $|0\rangle$ is called the vacuum. Defining $|\mathbf{k}_1 \ldots \mathbf{k}_n\rangle \triangleq a^\dagger(\mathbf{k}_1)\ldots a^\dagger(\mathbf{k}_n)|0\rangle$, we see that all possible such vectors form the so-called Fock space,

Fock space

$$\boxed{\begin{array}{l} \{|\mathbf{k}_1 \ldots \mathbf{k}_n\rangle\} \equiv \mathcal{F}_S = \mathcal{H}_0 \bigoplus_{n\geq 1} \left(\bigotimes_{\mathbf{k}\in\mathbb{R}^3} \mathcal{H}_\mathbf{k} \right)^{\otimes_S n} \\ \text{with } \dim(\mathcal{H}_0) = \dim(\mathcal{H}_\mathbf{k}) = 1 \end{array}} \tag{B.24}$$

where $\mathcal{H}^{\otimes n} = \overbrace{\mathcal{H}\otimes\ldots\otimes\mathcal{H}}^{n \text{ times}}$ and the S subscript stands for "symmetrized", as one easily sees from the commutation relations that states differing only by a permutation of their $\mathbf{k}$-vectors are identified, enforcing a bosonic statistics.

---

[11] We use natural units $\hbar = c = 1$.

[12] We denote the Heaviside step function $\theta(x) = 0$ if $x < 0$ and $\theta(x) = 1$ if $x \geq 0$.

[13] We use $\delta(f(x)) = \sum_{r_i} \delta(x - r_i)/|f'(r_i)|$ with $\{r_i\}$ the solutions of $f(x) = 0$.

[14] The detailed construction is sometimes referred to as the "ladder operator" method.

The CCR dictate the action of $a^\dagger(\mathbf{k})$ and $a(\mathbf{k})$ on Fock states,

$$\left\{\begin{aligned} a^\dagger(\mathbf{k})\,|\mathbf{k}_1\dots\mathbf{k}_n\rangle &= |\mathbf{k}\mathbf{k}_1\dots\mathbf{k}_n\rangle && \text{(B.25)}\\ a(\mathbf{k})\,|\mathbf{k}_1\dots\mathbf{k}_n\rangle &= \sum_{r=1}^{n} 2E_{\mathbf{k}_r}\delta(\mathbf{k}-\mathbf{k}_r)\,|\mathbf{k}_1\dots\mathbf{k}_{r-1}\mathbf{k}_{r+1}\dots\mathbf{k}_n\rangle && \text{(B.26)}\end{aligned}\right.$$

justifying their appellation respectively of “creation” and “annihilation” operator. The Fock basis therefore diagonalizes the “number operator” $n(\mathbf{k}) = a^\dagger(\mathbf{k})a(\mathbf{k})$, whose eigenvalues in a sense count the number of modes $\mathbf{k}$ in the state,

$$n(\mathbf{k})\,|\mathbf{k}_1\dots\mathbf{k}_n\rangle = \left(\sum_{r=1}^{n} 2E_{\mathbf{k}_r}\delta(\mathbf{k}-\mathbf{k}_r)\right)|\mathbf{k}_1\dots\mathbf{k}_n\rangle \tag{B.27}$$

We note that setting $\langle 0|0\rangle = 1$ the CCR induce the general scalar product,

$$\langle\mathbf{k}'_1\dots\mathbf{k}'_m|\mathbf{k}_1\dots\mathbf{k}_n\rangle = \delta_{mn}\sum_{s\in\mathfrak{S}_n}\prod_{l=1}^{n} 2E_{\mathbf{k}_l}\delta(\mathbf{k}_l-\mathbf{k}'_{s(l)}) \tag{B.28}$$

with $\mathfrak{S}_n$ the n elements permutation group. It is Lorentz-invariant, as seen *e.g.* by integration with the invariant measure $\frac{d\mathbf{k}}{2E_{\mathbf{k}}}$[15].

After some algebra, the total Hamiltonian $H = \int d\mathbf{x}\mathcal{H}$ can be reexpressed in terms of the creation and destruction operators as[16],

$$\boxed{H = \int d\mathbf{k}\left(\tilde{n}(\mathbf{k})E_{\mathbf{k}} + \frac{1}{2}\mathcal{V}\right)} \tag{B.29}$$

with $\tilde{n}(\mathbf{k}) = n(\mathbf{k})/2E_{\mathbf{k}}$, so its action on states is fully determined,

$$H\,|\mathbf{k_1}\dots\mathbf{k_n}\rangle = \left(\sum_{l=1}^{n} E_{\mathbf{k}_l}\right)|\mathbf{k_1}\dots\mathbf{k_n}\rangle \tag{B.30}$$

It therefore appears that the defining Fock space basis diagonalizes the Hamiltonian, hence in other words consists of definite energy states, that are stable in time.

■ We can further clarify this result by examining the effect of a spacetime translation l on states *via* the Lorentz-scalar property of fields,

$$\begin{aligned} a^\dagger(\mathbf{k}) &\xrightarrow{l} -i\int d\mathbf{x}e^{-ik\cdot x}\left[\pi'(x) + iE_{\mathbf{k}}\phi'(x)\right] && \text{(B.31)}\\ &= -i\int d\mathbf{x}e^{-ik\cdot x}\left[\pi(x+l) + iE_{\mathbf{k}}\phi(x+l)\right]\ \text{, by scalar property} &&\\ &= e^{ik\cdot l}a^\dagger(\mathbf{k})\ \text{, by injection of Eqs. B.19-B.20} && \text{(B.32)}\\ \text{hence}\ &\boxed{|\mathbf{k_1}\dots\mathbf{k_n}\rangle \xrightarrow{l} e^{i\left(\sum_{i=1}^{n}k_i\right)\cdot l}\,|\mathbf{k_1}\dots\mathbf{k_n}\rangle} && \text{(B.33)}\end{aligned}$$

The relativistic invariance property of fields hence determines the transformation of states under a translation. Let $U(l)$ denote the corresponding endomorphism of Fock space. By the above we see that $U(l)$ is diagonal in the Fock basis, hence

---

[15] We recall $\frac{d\mathbf{k}}{2E_{\mathbf{k}}} \equiv dk\delta(k^2-m^2)\theta(k^0)$, where the RHS manifestly is Lorentz-invariant.

[16] An infinite constant $\propto \mathcal{V} \equiv \delta(\mathbf{0})$ appears in this calculation, which would literally be the vacuum state energy, but has however no dynamical role in this context and therefore is eventually discarded.

linear, and manifestly unitary[17]. We can therefore write $U(l) = e^{iP^\mu l_\mu}$, where P_μ are called the *infinitesimal generators* of the envisioned transformation, here a spacetime translation. They are hermitian because U is unitary, and all commute as sharing a common diagonalization basis.

Of course Eq. B.33 allows to concretely determine the action of P^μ on states,

$$P^\mu \left|\mathbf{k_1} \dots \mathbf{k_n}\right\rangle = \left(\sum_{i=1}^{n} k_i^\mu\right) \left|\mathbf{k_1} \dots \mathbf{k_n}\right\rangle \tag{B.34}$$

We find that $P^0 = H$, consistently with the general definition of the Hamiltonian as the generator of time evolution, but also $\mathbf{P}\left|\mathbf{k_1} \dots \mathbf{k_n}\right\rangle = \left(\sum_{i=1}^{n} \mathbf{k}_i\right)\left|\mathbf{k_1} \dots \mathbf{k_n}\right\rangle$. In mechanics, the infinitesimal generator of space translations is identified with *kinetic momentum*[18], therefore Fock states also have definite kinetic momentum, found to coincide with the ϕ field Fourier modes (times $\hbar$ in IU). Besides, single-particle momenta components (Eq. B.34) satisfy $k_\mu k^\mu = m^2$. We can consequently interpret $\mathcal{F}$ as the space of all relativistic multi-particle states, with particle mass m.

Let us note that such conceptual move actually is a physical interpretation rather than a mathematical identification; it has to be, for particles as defined even in "relativistic" single-particle quantum mechanics (Dirac theory) violate relativistic locality [395]. However, non-relativistic particle mechanics is correctly recovered when $\|\mathbf{p}\|/m \ll 1$.

- The same line of thought applies to Lorentz transformations,

$$a^\dagger(\mathbf{k}) \xrightarrow{\Lambda} -i\int d\mathbf{x} e^{-ik\cdot x}\left[\pi'(x) + iE_{\mathbf{k}}\phi'(x)\right] \tag{B.35}$$

$$= -i\int d\mathbf{x} e^{-ik\cdot x}\left[\gamma\{\pi - \beta\cdot\nabla\phi\}(\Lambda x) + iE_{\mathbf{k}}\phi(\Lambda x)\right]$$

by scalar (vector) property of ϕ (π^μ), *i.e.* $\pi' \equiv \pi^{0\prime} = \Lambda^0{}_\nu \pi^\nu \equiv \Lambda^0{}_\nu \dfrac{\partial\mathcal{L}}{\partial(\partial_\nu\phi)}$

$$= -\gamma\left\{E_{\Lambda\mathbf{k}} + \beta\cdot\Lambda\mathbf{k}\right\}\frac{a(-\Lambda\mathbf{k}) - a^\dagger(\Lambda\mathbf{k})}{2E_{\mathbf{k}}} + \frac{a(-\Lambda\mathbf{k}) + a^\dagger(\Lambda\mathbf{k})}{2}$$

by Eqs. B.19-B.20, using $q\cdot\Lambda x = \Lambda^{-1}q\cdot x$ and change of variable $q' = \Lambda^{-1}q$

$= a^\dagger(\Lambda\mathbf{k})$, as the first factor is indeed $[\Lambda(-\beta)\Lambda(\beta)k]^0 \equiv k^0 = E_{\mathbf{k}}$ (B.36)

hence $\boxed{\left|\mathbf{k_1} \dots \mathbf{k_n}\right\rangle \xrightarrow{\Lambda} \left|\Lambda\mathbf{k_1} \dots \Lambda\mathbf{k_n}\right\rangle}$ (B.37)

where $\gamma = 1/\sqrt{1-\beta^2}$ is the Lorentz-factor of Λ and by abuse of notation $\Lambda\mathbf{u}$ is the spatial part of the four vector $\Lambda(u^0, \mathbf{u})$. Fock state P^μ eigenvalues therefore transform as (4-)vectors in a change of reference frame, consistently with an interpretation in terms of particle's momenta. Besides, nothing else changes under such Lorentz transform, which means we must assign spin 0 to these particles[19].

Introducing the transformation operator $U(\Lambda)$ as before we have, by Lorentz-invariance of the scalar product Eq. B.28,

$$\begin{aligned}\langle U(\Lambda)\mathbf{k}'_1 \dots \mathbf{k}'_m | U(\Lambda)\mathbf{k}_1 \dots \mathbf{k}_n\rangle &= \langle \Lambda\mathbf{k}'_1 \dots \Lambda\mathbf{k}'_m | \Lambda\mathbf{k}_1 \dots \Lambda\mathbf{k}_n\rangle \\ &= \langle \mathbf{k}'_1 \dots \mathbf{k}'_m | \mathbf{k}_1 \dots \mathbf{k}_n\rangle \end{aligned} \tag{B.38}$$

so $U(\Lambda)$ also is unitary.

---

[17] An operator is unitary if it preserves the scalar product, $\langle U\phi|U\psi\rangle = \langle\phi|\psi\rangle$, *i.e.* $U^\dagger U = UU^\dagger = \mathbf{1}$.

[18] *e.g.* in classical mechanics recall that $\{O, p_i\} = -\frac{\partial O}{\partial q_i}$, and take q_i a particle spatial coordinate.

[19] One could also compute the total angular momentum J^2 and find all states have eigenvalue 0 [395]

■ Let us now summarize the results obtained so far,

- From a mechanical point of view the principle of special relativity invites to consider a Poincaré-invariant action.

- It can naturally be realized by a three dimensional field system $\{A(x)\}_{x\in\Sigma}$ with Lorentz-scalar Lagrangian density, entailing a local Poisson bracket,

$$\begin{aligned}\text{Lorentz-scalar (field): } \mathcal{L}'(x) &\overset{(\Lambda,l)}{=} \mathcal{L}(\Lambda x + l)\\ \text{Locality: } \{A(x), A(y)\}_{x\cdot y<0} &= \{\pi_A(x), \pi_A(y)\}_{x\cdot y<0} = 0\\ \{A(x), \pi_A(y)\}_{x\cdot y<0} &= \delta(x-y)\end{aligned}$$

- Canonical quantization of a field governed by linear equations of motion results in a Fock structure of the Hilbert space. Considering the real Klein-Gordon equation, Fock basis can be interpreted as the set of all multi-particle states for particles of mass m and spin 0, satisfying the "mass shell" condition $k^2 = m^2$.

- Upon action of the Poincaré group, the Lorentz-scalar property of the field translates into a unitary operator in Fock space. Denoting the corresponding operator by $U(\Lambda, l)$, this double transformation law writes[a],

Lorentz-scalar (quantum field)
$$\boxed{U(\Lambda, l)\phi(x)U^\dagger(\Lambda, l) = \phi(\Lambda x + l)} \tag{B.39}$$

---

[a] Under a symmetry, if pure states transform as $|\psi\rangle \to U|\psi\rangle$ invariance of all expectation values translates into the operator transformation law $\mathcal{O} \to U\mathcal{O}U^\dagger$.

B.1.3 General Poincaré and gauge covariant local fields

■ The relation Eq. B.39 between the transformation of variables as a field on the one hand, and as an operator on the other hand, is the basis for the general embedding of special relativity into quantum mechanics. The underlying mathematical notion is that of group representation, meaning a group morphism,

$$\pi : \begin{cases} G \to \mathrm{Gl}(V) \\ g \mapsto \pi(g) \end{cases} \tag{B.40}$$

$$\text{s.t. } \forall g, h \in G,\ \pi(gh) = \pi(g)\pi(h) \tag{B.41}$$

for V some vector space and $\mathrm{Gl}(V)$ its linear group. A representation is said unitary if its image elements are, finite dimensional if V is, and irreducible if it comprises no subspace stable under all $\pi(G)$.

In quantum mechanics, a symmetry group representation must be unitary to preserve predictions, while regarding the algebra of variables it would be desirable to have only finitely many generators, hence acted on by finite dimensional representations. We can then read Eq. B.39 as establishing the connection between the unitary representation acting on operators, and the finite-dimensional representation acting on the algebra of physical variables. Determining all irreducible unitary and finite dimensional representations of the Poincaré group $\mathfrak{P}$[20] would therefore exhaust all possibilities for a relativistic and quantum system.

It turns out that the determination of all irreducible representations of $\bar{\mathfrak{P}}$ is a well-posed and solved mathematical problem[21] [400]. Because the Poincaré (and Lorentz) group is non-compact, unitary representations are all infinite dimensional, so finite dimensional ones are non-unitary. Unitary representations are entirely characterized by a mass $m \geq 0$ and a half-integer spin $j \in \frac{1}{2}\mathbb{N}$. Finite dimensional representations are characterized also by a mass m and two half-integers A, B, related to the total spin j of the representation by,

$$|A - B| \leq j \leq |A + B| \tag{B.42}$$

A Lorentz-scalar Lagrangian can then be built from any combination of *Lorentz-covariant* fields,

$$\textbf{Lorentz-covariance: } \boxed{U(\Lambda, l)\phi_n(x)U^\dagger(\Lambda, l) = M_{nm}(\Lambda)\phi_m(\Lambda x + l)} \tag{B.43}$$

with U some unitary representation of $\bar{\mathfrak{P}}$, M some finite-dimensional representation of $\bar{\mathfrak{L}}$, and where contraction of all Lorentz indices in the final Lagrangian confers it the Lorentz-scalar property.

A general linear covariant field then writes[22],

$$\phi_n(x) = \sum_\sigma \int \frac{d\mathbf{k}}{2E_\mathbf{k}} \left(u_n^{AB}(\mathbf{k}, \sigma)a(\mathbf{k}, \sigma)e^{-ik\cdot x} + v_n^{AB}(\mathbf{k}, \sigma)a^{c\dagger}e^{ik\cdot x}\right) \tag{B.44}$$

with $1 \leq n \leq (2A+1)(2B+1)$, A, B the defining numbers of the finite dimensional representation, u_n^{AB}, v_n^{AB} coefficient functions, $k^2 = m^2$ and $-j \leq \sigma \leq j$ denotes the spin degree of freedom of the induced unitary representation. Together with the locality condition,

$$\textbf{Locality: } \boxed{[\phi_n(x), \phi_m(y)]^{\mp}_{x\cdot y<0} = 0} \tag{B.45}$$

with $[a, b]^{\mp} = ab \mp ba$ the field (anti-)commutator to be precised shortly, the coefficients can be determined for any mass m and spin $|A - B| \leq j \leq |A + B|$. A linear relativistic field equation satisfied by the covariant field ϕ_n appears as a consequence[23]. Besides the non-trivial correspondence is implied,

$$\textbf{Spin-statistics: } \begin{cases} j \in \mathbb{N} \Rightarrow \text{Canonical CR: } [\cdot, \cdot]^- \\ j \in \mathbb{N} + \dfrac{1}{2} \Rightarrow \text{Canonical anti-CR: } [\cdot, \cdot]^+ \end{cases} \tag{B.46}$$

---

[20] Actually the representations of its *universal cover* $\bar{\mathfrak{P}} \simeq \mathrm{SL}(2, \mathbb{C}) \rtimes \mathbb{R}^4$, in bijective correspondence with the *projective* representations of $\mathfrak{P}$ relevant for quantum states, that are *rays* of Hilbert space (*i.e.* vectors defined up to phase and norm). This shift, clearly motivated by quantum mechanics, is well-known to be at the origin of non-integer spin representations, which are indeed non-classical in this sense [396].

[21] See [395] for details on the results to follow.

[22] We introduce the “antiparticle” annihilation operator $a^{c\dagger}$, which naturally appears as soon as one quantizes complex scalar fields. Indeed the canonical procedure then amounts to quantizing two real fields, hence two independent “creation/annihilation” operators pairs. Invariance of the Lagrangian under phase multiplication of the field however entails net particle minus antiparticle number conservation.

[23] For spin 0, one finds back the Klein-Gordon equation

One concludes only fermionic and bosonic statistics are allowed[24], corresponding respectively to non-integer and integer spin particles.

As an example let us write the Dirac field, probably the most common yet non-classical object of relativistic field theory. It is realized as the reducible representation[25] $(A = \frac{1}{2}, B = 0) \oplus (A = 0, B = \frac{1}{2})$, direct sum of the two irreducible dimension 2 spin $\frac{1}{2}$ representations of the Poincaré group, so itself is dimension 4 and spin $\frac{1}{2}$, sometimes called a "bi-spinor representation". Its Fock space describes massive spin $\frac{1}{2}$ (fermionic) particles and anti-particle. The field can be written as,

$$\psi = \begin{pmatrix} \psi_{\frac{1}{2}0} \\ \psi_{-\frac{1}{2}0} \\ \psi_{0\frac{1}{2}} \\ \psi_{0-\frac{1}{2}} \end{pmatrix} \tag{B.47}$$

with left and right indices respectively for the A and B spin indices. Substituting in the general solution to Eq. B.43 and Eq. B.45 yields,

$$\psi(x) = \sum_{\sigma \in \left\{-\frac{1}{2}, \frac{1}{2}\right\}} \int \frac{d\mathbf{k}}{2E_{\mathbf{k}}} \left(u(\mathbf{k}, \sigma) b(\mathbf{k}, \sigma) e^{-ik\cdot x} + v(\mathbf{k}, \sigma) d^{\dagger} e^{ik\cdot x} \right) \tag{B.48}$$

Here $u(\mathbf{k}, \sigma)$ and $v(\mathbf{k}, \sigma)$ form two 2-dimensional basis for the solution space respectively of,

$$(\not{k} - m) u(\mathbf{k}, \sigma) = 0 \tag{B.49}$$

$$(\not{k} + m) v(\mathbf{k}, \sigma) = 0 \tag{B.50}$$

introducing $\not{a} \triangleq \gamma^{\mu} a_{\mu}$ with $\gamma^0 = \begin{pmatrix} 0 & \mathbb{1}_2 \\ \mathbb{1}_2 & 0 \end{pmatrix}$, $\gamma^i = \begin{pmatrix} 0 & -\sigma^i \\ \sigma^i & 0 \end{pmatrix}$ the Dirac matrices and σ^i the Pauli matrices.

This finally entails a covariant field equation for ψ, with a generating Lagrangian,

$$\boxed{\begin{cases} \textbf{Dirac equation: } \left(i\not{\partial} - m\right) \psi = 0 \\ \textbf{Dirac Lagrangian: } \mathcal{L}_0^D(x) = \overline{\psi}(x) \left(i\not{\partial} - m\right) \psi(x) \end{cases}} \tag{B.51}$$

where $\overline{\psi} \triangleq \psi^{\dagger} \gamma^0$.

- The Poincaré group may not be the only symmetry of the action, and in practice requiring new symmetries provides one systematic way to generate Lagrangian with interacting physical variables. Let us briefly illustrate this general idea, grounding so-called "gauge theories", with the simple Dirac Lagrangian just written.

---

[24] This result relies on spacetime dimension 4.

[25] This seemingly non-trivial choice is justified by ruling out simpler possibilities for spin $\frac{1}{2}$ particles (*i.e.* representations $(\frac{1}{2}, 0)$ or $(0, \frac{1}{2})$) on the basis that they either are their own anti-particle, and therefore cannot carry electric charge, or massless [395]. Historically, it naturally appeared looking for the "square root" of Klein-Gordon equation (*e.g.* H s.t. $H^2\psi = (i\hbar)^2 \partial_0^2 \psi \Leftrightarrow$ (K-G)).

Performing $\psi \to e^{-iqa}\psi$ manifestly leaves $\mathcal{L}_0^D$ invariant for any $q, a \in \mathbb{R}$. Then, taking q as a constant and a in the infinitesimal limit,

$$\begin{aligned}\delta_a \mathcal{L}_0^D &= 0\\ &= \left[\frac{\partial \mathcal{L}_0^D}{\partial \psi} - \partial_\mu \left(\frac{\partial \mathcal{L}_0^D}{\partial(\partial_\mu \psi)}\right)\right]\delta_a\psi(x) + \partial_\mu\left[\frac{\partial \mathcal{L}_0^D}{\partial(\partial_\mu\psi)}\delta_a\psi(x)\right]\\ &+ \delta_a\overline{\psi}(x)\left[\frac{\partial \mathcal{L}_0^D}{\partial \overline{\psi}} - \partial_\mu\left(\frac{\partial \mathcal{L}_0^D}{\partial(\partial_\mu\overline{\psi})}\right)\right] + \partial_\mu\left[\delta_a\overline{\psi}(x)\frac{\partial \mathcal{L}_0^D}{\partial(\partial_\mu\overline{\psi})}\right]\\ &\overset{\text{E-L}}{=} \partial_\mu\left[\frac{\partial \mathcal{L}_0^D}{\partial(\partial_\mu\psi)}\delta_a\psi(x)\right]\\ &\text{where } \delta_a\psi = -iqa\psi \text{ , and } \delta_a\overline{\psi} = iqa\overline{\psi}\end{aligned} \tag{B.52}$$

using Euler-Lagrange equations, and noticing the second divergence term is zero. We hence obtain,

$$\boxed{\partial_\mu j^\mu = 0} \tag{B.53}$$

$$\text{with, } j^\mu = q\overline{\psi}\gamma^\mu\psi \tag{B.54}$$

The symmetry of the Lagrangian is thereby seen to imply the existence of a current conserved by the equations of motion[26], leading to a time-invariant charge,

$$\begin{aligned}Q &\equiv \int d\mathbf{x} j^0(x)\\ &= \int d\mathbf{x} q\psi^\dagger(x)\psi(x)\\ &= q\sum_{\sigma\in\left\{-\frac{1}{2},\frac{1}{2}\right\}}\int\frac{d\mathbf{k}}{2E_\mathbf{k}}\left(b^\dagger(\mathbf{k},\sigma)b(\mathbf{k},\sigma) - d^\dagger(\mathbf{k},\sigma)d(\mathbf{k},\sigma)\right)\\ &\equiv q(N_{\bar{p}} - N_p)\end{aligned} \tag{B.55}$$

where we have used the normalization relation of basis spinors[27], the canonical anti-commutation relation and discarded the resulting infinite constant. The total number operators $N_{\bar{p}}$ and N_p clearly correspond to the total numbers of anti-particles and particles respectively.

Now consider a local transformation $\psi(x) \overset{a}{\to} e^{-iqa(x)}\psi(x)$, in this case the Lagrangian changes due to the field derivative,

$$\mathcal{L}_0^D\Big|_{a(x)} - \mathcal{L}_0^D = \overline{\psi}(x)\left(-iq\partial\!\!\!/ a(x)\right)\psi(x) \tag{B.56}$$

Invariance under the local "gauge" transformation can thus be enforced introducing a vector field A_μ transforming as $A_\mu \overset{a}{\to} A_\mu + \partial_\mu a$, which allows defining a covariant derivative,

$$D_\mu \triangleq \partial_\mu + iqA_\mu \tag{B.57}$$

making $\overline{\psi}D_\mu\psi$ gauge-invariant. A gauge-invariant Lagrangian naturally follows,

$$\mathcal{L}^D(x) = \overline{\psi}(x)\left(iD\!\!\!\!/ - m\right)\psi(x) \tag{B.58}$$

---

[26] This is a simple illustration of Noether's theorem in Lagrangian form.

[27] $u^\dagger(\mathbf{k},\sigma)u(\mathbf{k}',\sigma') = v^\dagger(\mathbf{k},\sigma)v(\mathbf{k}',\sigma') = \delta_{\sigma\sigma'}2E_\mathbf{k}\delta(\mathbf{k}-\mathbf{k}')$

The introduced field A_μ manifestly transforms as a vector, hence is a spin 1 field. The Poincaré locality-covariance equations then naturally determine a kinetic Lagrangian, while gauge-invariance requires $m_A = 0$, hence the total gauge-invariant Lagrangian,

$$\mathcal{L}^{\mathrm{U}(1)}(x) = \overline{\psi}(x)\left(i\not{D} - m\right)\psi(x) - \frac{1}{4}F_{\mu\nu}(x)F^{\mu\nu}(x) \tag{B.59}$$

with $F_{\mu\nu} = \partial_\mu A_\nu - \partial_\nu A_\mu$ the "field strength tensor".

We thereby see how requiring invariance of the Dirac Lagrangian under local transformations, here generated by elements of U(1), translates into a theory of fermions interacting with the vector (*i.e.* spin 1, hence bosonic) "gauge field" A_μ carrying the infinitesimal generator of local gauge transformations, here $-iq$. Setting $q = e$ and $m = m_e$, we physically recognize the Lagrangian of electrons and positrons interacting with the electromagnetic field, and the conserved charge Eq. B.55 is identified with the total net electric charge. The Lagrangian may then be rewritten so as to more closely parallel its classical form,

Quantum Electrodynamics

$$\boxed{\mathcal{L}^{\mathrm{QED}} = \overline{\psi}\left(i\not{\partial} - m_e\right)\psi - A_\mu j^\mu - \frac{1}{4}F_{\mu\nu}F^{\mu\nu}} \tag{B.60}$$

with j^μ defined in Eq. B.54. The systematic generalization of this procedure, in particular to non-abelian symmetry groups, is called Yang-Mills theory.

■ The basic canonical formalism inspired from point-particle mechanics we used, though convenient in view of an ordered exposition, clearly reveals its limits at this stage. Trying to define the canonical Hamiltonian of Eq. B.60, one finds that,

$$\pi_{A_0} = \frac{\partial\mathcal{L}^{\mathrm{QED}}}{\partial(\partial_0 A_0)} = 0 \tag{B.61}$$

as $F_{00} = 0$, preventing a consistent formulation of Hamiltonian equations of motion.

Actually, we ran into an inconsistency already when anti-CCR were introduced for fermions, as an anti-commutator does not share the algebraic properties of the usual Poisson bracket, breaking the canonical quantization procedure we described.

Both problems can be addressed in an extended canonical formalism, said to describe systems with "constraints", the case of fermions furthermore requiring the introduction of a generalized Poisson bracket defined on algebras of anticommuting numbers[28] [311]. Alternatively, one might use a different approach to the "quantization" of a mechanical system, most notably the path-integral method leading to the "functionnal formalism" of quantum mechanics. In practice, the latter approach currently is the most widely used to circumvent these complications, providing both a very operational mathematical framework and some physically evocative expressions [307, 396, 401].

---

[28] They are called "Grassmann numbers".

B.2 Fields correlation functions

A second difference of field theory with elementary mechanics is the continuous infinity of physical variables, at least one per point of space[29]. Thinking in computational terms for a moment, quantum mechanics of a single variable $q \in \mathbb{E}$ has about the complexity of the classical mechanics of $\psi_q \in \mathrm{L}^2(\mathbb{E}, \mathbb{C})$[30], that is a complex field over the space of values of q. Now considering a typical field $\{q_{\mathbf{x}}\}_{\mathbf{x}\in\mathbb{R}^3} \in \mathrm{L}^2(\mathbb{R}^3, \mathbb{E})$, its quantum theory naively appears as the computation of $\psi_{q_{\mathbf{x}}} \in \mathrm{L}^2(\mathrm{L}^2(\mathbb{R}^3, \mathbb{E}), \mathbb{C})$. This exponential soar of complexity translates in the formal theory as the necessity to find a hierarchy in physical variables in order to perform any definite calculation. In particular, a state-centred approach aimed at computing the full "field wavefunction" appears especially hopeless.

The "$n-$points (fields correlation) functions" prove central in this regard, for a field $\phi(\mathbf{x}, x^0)$ they are generically defined by,

$$\begin{aligned} G^{(n)}(x_1, \dots, x_n) &\triangleq \langle \tau_\gamma \phi(x_1) \dots \phi(x_n) \rangle_{\rho_0} && \text{(B.62)} \\ &= \mathrm{Tr}\left[\rho_0 \tau_\gamma \phi(x_1) \dots \phi(x_n)\right] && \text{(B.63)} \end{aligned}$$

with τ_γ the contour-ordering operator appearing in Eq. A.66. As field operators generate the algebra of observables, one may in principle express any quantity of interest in terms of field expectation values, and a finite number of them at some given level of accuracy. For instance, free 2-points functions form the basis of perturbation theory and its evocative diagrammatic representation. Let us stress nonetheless that correlation functions are fundamental objects, they encode all physical predictions and exact equations can be derived for them. Though *a priori* unsolvable[31], these equations allow for approximation schemes other than scattering theory and more amenable to describing non-equilibrium states[32], for instance *via* a kinetic theory.

In this section our aim is to provide broad reference for these possible approaches. Specifically, the usual perturbative expansion based on the interaction picture is introduced so as to make contact with the familiar terminology of particle scattering and diagrammatic representations. We then present Schwinger-Dyson equations for exact $n-$points functions, and motivate some tools used for kinetic reduction.

B.2.1 Finite order perturbation theory

- ■ If the system's Lagrangian can be split as $\mathcal{L} \equiv \mathcal{L}_0 + \mathcal{L}_I$ and dynamics in $\mathcal{L}_0$ is exactly solvable, the interaction formalism provides a systematic approximation method for the full dynamics. Assuming that the interaction term does not contain field derivatives we have $\mathcal{H} = \mathcal{H}_0 - \mathcal{L}_I$ and Eq. A.66 directly rewrites,

$$\langle O(t) \rangle_{\rho_0} = \left\langle \tau_\gamma e^{i\int_\gamma dx \mathcal{L}_I^0(x)} O^0(t) \right\rangle_{\rho_0} \tag{B.64}$$

[†] Refs. B.2: [305–307, 396]

[29] More of course for realistic fields with internal degrees of freedom, like the four components electromagnetic potential.

[30] Say, for computing the system state after some finite time, as a vector encoded in the list of its coefficients in a Hilbert space basis (*e.g.* the eigenbasis of q).

[31] They typically take the form of infinite hierarchies of coupled (classical) field equations, whereby one recovers the computational complexity of a quantum field theory: the set of fundamental variables consists of all correlation functions.

[32] An equilibrium state is ρ_{eq} s.t. $[\rho_{\mathrm{eq}}, H] = 0$, or $\frac{\partial \rho_{\mathrm{eq}}}{\partial t} = 0$. Clearly all $\rho \equiv f(H)$ are (*e.g.* thermal states $\rho_T \propto e^{-H/k_B T}$), as well as H eigenvector pure states (*e.g.* vacuum or in the absence of interactions multi-particle states $\rho_{\mathbf{k}_1 \dots \mathbf{k}_n} \propto a^\dagger_{\mathbf{k}_1} \dots a^\dagger_{\mathbf{k}_n} |0\rangle\langle 0| a_{\mathbf{k}_1} \dots a_{\mathbf{k}_n}$).

where the integral is understood as extending over all space and running along the contour in the time direction. Under the common circumstance that $\mathcal{L}_I^0$ can be considered small and is a low degree polynomial in the fields, this expression can be expanded at a given order and any quantity expressed in terms of a finite sum of expectation values of finite products of fields,

$$\langle O^{(n)}(t)\rangle_{\rho_0} = \sum_{l=0}^{n} \frac{i^l}{l!} \int dx_1 \ldots \int dx_l \left\langle \tau_\gamma \mathcal{L}_I^0(x_1) \ldots \mathcal{L}_I^0(x_l) O^0(t) \right\rangle_{\rho_0} \tag{B.65}$$

However the real value of this formalism unfolds only when a further reduction is performed, through an identity known as Wick's theorem,

$$\begin{array}{|l}
\text{If, } \phi_x \equiv \phi_x^+ + \phi_x^- \\
\quad \text{with } \left[[\phi_x^-, \phi_y^+], \mathcal{O}\right] = 0,\ \forall \mathcal{O} \text{ and } [\phi_x^\pm, \phi_y^\pm] = 0 \\
\quad \text{We define the “normal ordered product”,} \\
\quad N\left[\phi_{x_1} \ldots \phi_{x_n}\right] = \phi_{x_1}^+ \ldots \phi_{x_n}^+ \phi_{x_1}^- \ldots \phi_{x_n}^- \\
\quad \text{and the “contraction” of two fields,} \\
\quad D_{xy}^0 = \theta(x_\gamma^0 - y_\gamma^0)[\phi_x^-, \phi_y^+] + \theta(y_\gamma^0 - x_\gamma^0)[\phi_y^-, \phi_x^+] \\
\text{Then,} \\
\boxed{\tau_\gamma\left[\phi_{x_1} \ldots \phi_{x_n}\right] = N\left[\phi_{x_1} \ldots \phi_{x_n} + \sum \left\{\begin{matrix}\text{all possible} \\ \text{contractions}\end{matrix}\right\}\right]} \left(\begin{matrix}\textbf{Wick's} \\ \textbf{theorem}\end{matrix}\right)
\end{array} \tag{B.66}$$

where x_γ^0, y_γ^0 are the time contour arguments, and the sum is over both the number of contractions and possible field pairings[33]. If the ± components split of free fields can be operated in such a way that normal ordered products have zero expectation value[34], then free field products expectation values take the particularly simple form,

$$\left\langle \tau_\gamma \phi_{x_1}^0 \ldots \phi_{x_{2m+1}}^0 \right\rangle_{\rho_0} = 0 \tag{B.67}$$

$$\left\langle \tau_\gamma \phi_{x_1}^0 \ldots \phi_{x_{2m}}^0 \right\rangle_{\rho_0} = \sum_{\text{pairings}} D_{x_{i_1} x_{j_1}}^0 \ldots D_{x_{i_m} x_{j_m}}^0 \tag{B.68}$$

$$\text{with, } D_{xy}^0 \equiv \left\langle \tau_\gamma \phi_x^0 \phi_y^0 \right\rangle_{\rho_0} \tag{B.69}$$

The quantity D_{xy}^0 is the free theory 2-points function, called the free field propagator. In principle, it allows computing any term of the perturbative expansion Eq. B.71. As we shall now simply illustrates, it also receives a very visual interpretation.

B.2.2 Illustration: perturbative expansion for ϕ^3 interactions

■ For definiteness, let us apply the above formalism to the following scalar field theory [396],

$$\mathcal{L} = \underbrace{\frac{1}{2}\left(\partial_\mu \phi\right)^2 - \frac{1}{2} m^2 \phi^2}_{\mathcal{L}_0} \underbrace{+ \frac{g}{3!} \phi^3}_{\mathcal{L}_I} \tag{B.70}$$

---

[33] This relation is easily found true for $n = 2$ and proved for higher ranks by mathematical induction.

[34] This is always possible for quadratic free hamiltonian and thermal states [402], including the vacuum ($T \to 0$) where the split simply corresponds to positive and negative frequencies of the momentum decomposition. In general, the state has to be gaussian and field operators centred ($\langle \phi \rangle_{\rho_0} = 0$) [403, 404]. For instance considering a coherent state $|\chi\rangle$ (s.t. $\langle \phi^0(x) \rangle_\chi = \chi(x)$), $\langle N\left[O(\phi^0)\right]\rangle_\chi = O(\chi(x))$ so expectation values of normal ordered products of centred field operators $\bar{\phi}^0 \equiv \phi^0 - \chi$ would indeed cancel.

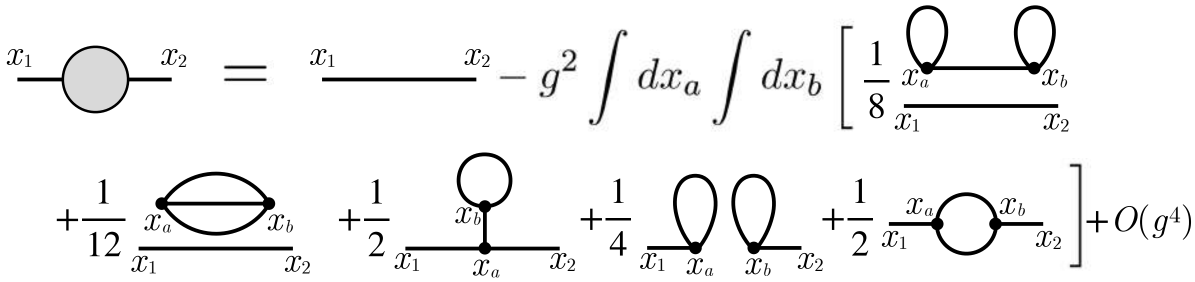

Figure B.1: **Diagrammatic representation of Eq. B.73.** The full 2-point function is represented by a circled line and expanded to order g^2 in the interaction formalism. Plain lines between x and y represent the free 2-points function D^0_{xy}, dots signal interaction vertices and their position is integrated over.

for a vacuum initial state $\rho_0 = |0\rangle\langle 0|$. We may calculate the 2-points function, at second order in the coupling g,

$$\begin{aligned}\langle \tau_\gamma \phi(x_1)\phi(x_2)\rangle_0 &= \langle \tau_\gamma \phi^0_{x_1}\phi^0_{x_2}\rangle_0 + \frac{ig}{3!}\int dx_a \left\langle \tau_\gamma \left(\phi^0_{x_a}\right)^3 \phi^0_{x_1}\phi^0_{x_2}\right\rangle_0 \\ &\quad -\frac{g^2}{2\times(3!)^2}\int dx_a\int dx_b \left\langle \tau_\gamma \left(\phi^0_{x_a}\right)^3\left(\phi^0_{x_b}\right)^3 \phi^0_{x_1}\phi^0_{x_2}\right\rangle_0 + O(g^3)\end{aligned} \tag{B.71}$$

using the free fields decomposition Eq. B.19, Wick's theorem results in[35],

$$\begin{aligned}\langle \tau_\gamma \phi(x_1)\phi(x_2)\rangle_0 = D^0_{12} &- \frac{g^2}{2\times(3!)^2}\int dx_a\int dx_b \Big[\\ &+ 9D^0_{12}D^0_{aa}D^0_{ab}D^0_{bb} + 6D^0_{12}\left(D^0_{ab}\right)^3 \\ &18D^0_{1a}D^0_{2a}D^0_{ab}D^0_{bb} + 9D^0_{1a}D^0_{2b}D^0_{aa}D^0_{bb} + 18D^0_{1a}D^0_{2b}D^0_{ab}D^0_{ab} \\ &+ 18D^0_{1b}D^0_{2b}D^0_{ab}D^0_{aa} + 9D^0_{1b}D^0_{2a}D^0_{aa}D^0_{bb} + 18D^0_{1b}D^0_{2a}D^0_{ab}D^0_{ab}\Big] + O(g^4)\end{aligned} \tag{B.72}$$

using the alleviated notation $D^0_{ij} \equiv D^0_{x_i x_j}$. As we integrate over x_a and x_b, the two last lines differing only by the permutation $a \leftrightarrow b$ are found identical, so that we can write,

$$\begin{aligned}\langle \tau_\gamma \phi(x_1)\phi(x_2)\rangle_0 = D^0_{12} &- g^2\int dx_a\int dx_b \Big[\frac{1}{8}D^0_{12}D^0_{aa}D^0_{ab}D^0_{bb} + \frac{1}{12}D^0_{12}\left(D^0_{ab}\right)^3 \\ &+ \frac{1}{2}D^0_{1a}D^0_{2a}D^0_{ab}D^0_{bb} + \frac{1}{4}D^0_{1a}D^0_{2b}D^0_{aa}D^0_{bb} + \frac{1}{2}D^0_{1a}D^0_{2b}\left(D^0_{ab}\right)^2\Big] + O(g^4)\end{aligned} \tag{B.73}$$

At this point, we can develop a diagrammatic interpretation of this expression. Let us notice that it depends only on doubly indexed quantities that can thereby be associated to the edges of a graph, linking vertices indexed by their argument. This result is drawn in Fig. B.1. Actually, we could bypass all the previous calculation by formalizing this diagrams-expressions correspondence, allowing to write down final

---

[35] As suggested already by this basic example the combinatorial procedure of pairing all elements of a finite set leads to a very fast growing number of terms (though still not of distinct diagrams here), namely $N_{\text{pairings}}(2m \text{ elements}) = \frac{(2m)!}{m!2^m}$. Diagrammatic methods alleviate the problem at low order of expansion and correlation function, as we shall discern shortly, but eventually also have to be supplanted by other tools [307]

perturbative expressions directly by listing all possible contributing diagrams of a given order[36].

We see that some diagrams have disconnected parts, factorizing in lower order correlation functions linking the end points[37]. Some even have "floating parts", unconected to any endpoints[38]. To understand the behavior of these so-called "vacuum diagrams"[39] consider,

$$\begin{aligned}
\langle \mathbf{1} \rangle_{\rho_0} &= \left\langle \tau_\gamma e^{i \int_\gamma dx \mathcal{L}_I^0(x)} \right\rangle_{\rho_0} \quad \text{, by Eq. B.64} \\
\Leftrightarrow \langle \mathbf{1} \rangle_{\rho_0} &= \langle \mathbf{1} \rangle_{\rho_0} + \sum_{l=1}^{n} \frac{(ig)^l}{l!(3!)^l} \int dx_1 \ldots \int dx_l \left\langle \tau_\gamma \left(\phi^0_{x_1}\right)^3 \ldots \left(\phi^0_{x_l}\right)^3 \right\rangle_{\rho_0} \\
\Leftrightarrow 0 &= \int dx_1 \ldots \int dx_l \left\langle \tau_\gamma \left(\phi^0_{x_1}\right)^3 \ldots \left(\phi^0_{x_l}\right)^3 \right\rangle_{\rho_0} \quad \text{, } \forall l \in \mathbb{N}^* \qquad \text{(B.74)}
\end{aligned}$$

We hence recognize that all vacuum diagrams cancel order by order. As a consequence, all terms containing them can simply be discarded in the perturbative expansion. Likewise, disconnected diagrams are clearly expressed in terms of lower order correlation functions. We therefore reach the conclusion that the relevant information is entirely contained in the set of connected diagrams.

In these diagrams some lines are attached to fixed locations (x_1 and x_2), they are called "external". Those directly relate to the variable whose expectation value is considered (here the correlation between ϕ field values at x_1 and x_2). Other lines are attached to vertices, whose position is integrated over the whole system volume and in the time-interval considered, they are called "internal" and receive a quite fruitful interpretation in terms of intermediate, unobserved processes. Interestingly, they allow developing an intuitive spatiotemporal understanding of the behavior of these integrands once that of D^0_{xy} is known. In the present theory, and quite generically, $D^0_{xy} \equiv D^0(m(x-y))$ displaying oscillations for $(x-y)^2 > 0$ and exponential fall off for $(x-y)^2 < 0$, all controlled by the field Compton scale $1/m$ [395].

In calculating transition probabilities between free particle states[40] specifically, the Fourier transform of these diagrams ("momentum space" diagrams) takes a particularly vivid interpretation. External lines indeed depend on the initial and final momenta, satisfying the relativistic dispersion relation, and hence label initial and final states, whereas internal lines momenta are integrated over irrespective of the "mass-shell" condition. They are then said to correspond respectively to "real" and "virtual" particles. Of course, such terminology reminiscent of classical images should not obscure the plain quantum mechanical structure of the theory. For that matter, similar interpretations can be drawn in related formalisms[41] without raising fundamental concerns.

---

[36] The result is called the "Feynman rules" of the theory.

[37] *cf.* the fourth term in the integral, factor of two 1-points functions.

[38] *cf.* the first and second terms in the integral.

[39] Note that in a general state ρ_0 these objects have nothing to do with the ground state of the Hamiltonian, also called "vacuum state".

[40] *i.e.* $\langle |\mathbf{k}_{1,f} \ldots \mathbf{k}_{m,f}\rangle\langle \mathbf{k}_{1,f} \ldots \mathbf{k}_{m,f}| \rangle_{\rho_0}$ for $\rho_0 = |\mathbf{k}_{1,0} \ldots \mathbf{k}_{n,0}\rangle\langle \mathbf{k}_{1,0} \ldots \mathbf{k}_{n,0}|$.

[41] Notably in statistical mechanics and non-relativistic quantum mechanics.

B.2.3 Exact equations of motion of fields $n-$points functions

- The above described perturbative expansion provides a systematic and well-proven computation method. However, it may appear restrictive in the following sense,

  i) **Interactions:** The interaction formalism is entirely grounded on the assumption that dynamics can be split into $\mathcal{L} = \mathcal{L}_0 + \mathcal{L}_I$, where $\mathcal{L}_0$ is solvable and $\mathcal{L}_I$ is small. Compatibility of both conditions is by no means generally granted. Though $\mathcal{L}_0$ is trivially solved including few enough terms, the reminder may well be large. Strong-field QED provides an example [2]:

  $$\mathcal{L}^{\text{sf-QED}} = \underbrace{-\frac{1}{4}F_{\mu\nu}F^{\mu\nu} + \overline{\psi}\left(i\not{\partial} - m_e\right)\psi}_{\mathcal{L}_0} \underbrace{-e\mathcal{A}_\mu j^\mu}_{\leftarrow ? \rightarrow} \underbrace{-ea_\mu j^\mu}_{\mathcal{L}_I} \tag{B.75}$$

  where $A_\mu \equiv a_\mu + \mathcal{A}_\mu$ with $\langle A_\mu \rangle_{\rho_0} = \mathcal{A}_\mu$. If $\mathcal{A}_\mu j^\mu \gtrsim 1/e$ the third term is not small, but in general $\mathcal{L}_0 - e\mathcal{A}_\mu j^\mu$ is not solvable.

  ii) **Secular terms:** Assuming the interaction formalism applies, in non-equilibrium states resulting quantities may still fail to provide good approximations at all times [305, 306]. This problem arises due to so-called “secular terms” growing in time, which can be traced back to the lack of “self-consistency” of the approximation scheme. Namely, quantities of a given order in the expansion are built from quantities of a lower order[42], instead of obeying equations of motion self-consistent in the sense of referring only to the same approximation order[43].

  iii) **Computation:** From a more practical point of view, the extreme versatility of the interaction formalism, that allows calculating virtually any observable at low expansion order, might generate costs without real profit. The cost is to solve the $\mathcal{L}_0$ dynamics for *all* operators. However, in many configurations data of the two or three first correlation functions of a system largely exhaust all information we may enquire about[44], let alone access experimentally [116, 305, 306]. Furthermore, such truncation of the infinite hierarchy of quantum field variables would ease contact with the classical limit, which is especially desirable in the strong-field context. Hopefully, it would eventually allow extending the extremely powerful and flexible numerical methods developed for classical fields and particles to some quantum regimes.

A promising starting point to address the above considerations may be to find equations governing $n-$points functions directly rather than the evolution operator. Then one could hope to close the system at some finite n, so as to obtain a uniform (self-consistent) approximation of the exact retained correlation functions. It turns out that exact equations can indeed be derived, leveraging on the field evolution equations.

For definiteness and simplicity we consider again a real scalar field ϕ. The exact equations of motion write (*cf.* Eq. A.44),

$$\textbf{eom (Hamilton):} \begin{cases} \partial_0\phi(x) = -i\left[\phi(x), H\right] \\ \partial_0\pi(x) = -i\left[\pi(x), H\right] \end{cases} \tag{B.76}$$

---

[42] *e.g.* in Eq. B.73 the 2-points function at order g^2 is built from “free” (order g^0) 2-points functions.

[43] See [305, 306] and references therein for a detailed exposition.

[44] *e.g.* 1-points functions provide the fields expectation values (at all points), 2-points functions relate to density, conductivity, or in a kinetic approximation to the full one-particle distributions in phase-space.

with the local commutation relations,

$$\begin{cases}[\phi(x),\phi(y)]_{x\cdot y<0}=[\pi(x),\pi(y)]_{x\cdot y<0}=0\\ [\phi(x),\pi(y)]_{x\cdot y<0}=i\delta(x-y)\end{cases} \tag{B.77}$$

Let us rewrite the equations of motion in a Lagrangian form [395]. First notice how the commutator of two canonically conjugate variables acts as a derivative:

$$\begin{aligned}[\phi(\mathbf{x}),\pi(\mathbf{y}_1)\pi(\mathbf{y}_2)]&=[\phi(\mathbf{x}),\pi(\mathbf{y}_1)]\,\pi(\mathbf{y}_2)+\pi(\mathbf{y}_1)\,[\phi(\mathbf{x}),\pi(\mathbf{y}_2)]\\ &\overset{\text{CCR}}{=}i\left(\delta(\mathbf{x}-\mathbf{y}_1)\pi(\mathbf{y}_2)+\pi(\mathbf{y}_1)\delta(\mathbf{x}-\mathbf{y}_2)\right)\\ &\equiv i\frac{\partial}{\partial\pi(\mathbf{x})}(\pi(\mathbf{y}_1)\pi(\mathbf{y}_2)) &&\text{(B.78)}\\ [\phi(\mathbf{x}),\nabla\pi(\mathbf{y}_1)\cdot\nabla\pi(\mathbf{y}_2)]&=[\phi(\mathbf{x}),\nabla\pi(\mathbf{y}_1)]\cdot\nabla\pi(\mathbf{y}_2)+\\ &\quad\nabla\pi(\mathbf{y}_1)\cdot[\phi(\mathbf{x}),\nabla\pi(\mathbf{y}_2)]\\ &\overset{\text{CCR}}{=}i\left(\nabla\delta(\mathbf{x}-\mathbf{y}_1)\cdot\nabla\pi(\mathbf{y}_2)+\nabla\pi(\mathbf{y}_1)\cdot\nabla\delta(\mathbf{x}-\mathbf{y}_2)\right)\\ &=-i\left(\delta(\mathbf{x}-\mathbf{y}_1)\nabla\cdot\nabla\pi(\mathbf{y}_2)+\delta(\mathbf{x}-\mathbf{y}_2)\nabla\cdot\nabla\pi(\mathbf{y}_1)\right)\\ &\equiv -i\nabla\cdot\frac{\partial}{\partial\nabla\pi(\mathbf{x})}(\nabla\pi(\mathbf{y}_1)\cdot\nabla\pi(\mathbf{y}_2)) &&\text{(B.79)}\end{aligned}$$

introducing partial derivatives acting as a formal derivation on the associated symbol all else fixed. By induction on both relations and reasoning similarly for π we deduce,

$$[\phi(\mathbf{x}),F(\phi,\pi)]=i\frac{\delta F}{\delta\pi(\mathbf{x})}=i\left(\frac{\partial F}{\partial\pi(\mathbf{x})}-\nabla\cdot\frac{\partial F}{\partial\nabla\pi(\mathbf{x})}\right) \tag{B.80}$$

$$[\pi(\mathbf{x}),F(\phi,\pi)]=-i\frac{\delta F}{\delta\phi(\mathbf{x})}=-i\left(\frac{\partial F}{\partial\phi(\mathbf{x})}-\nabla\cdot\frac{\partial F}{\partial\nabla\phi(\mathbf{x})}\right) \tag{B.81}$$

with use of the functional derivative symbol introduced in Eq. B.12. In order to insist on the symbolic relations let us now adopt the calculus notation [395],

$$\left.\frac{dF}{d\phi}\right|_{\pi}\triangleq\frac{\partial F}{\partial\phi}-\nabla\cdot\frac{\partial F}{\partial\nabla\phi} \tag{B.82}$$

so that we can rewrite,

$$\begin{cases}\partial_0\phi=\left.\dfrac{d\mathcal{H}}{d\pi}\right|_{\phi}\\ \partial_0\pi=-\left.\dfrac{d\mathcal{H}}{d\phi}\right|_{\pi}\end{cases} \tag{B.83}$$

However we know that our Hamiltonian derives from a Lagrangian, that is,

$$\pi=\frac{\partial\mathcal{L}}{\partial(\partial_0\phi)} \tag{B.84}$$

$$\mathcal{H}(\phi,\nabla\phi,\pi)=\pi\partial_0\phi-\mathcal{L}(\phi,\partial_\mu\phi) \tag{B.85}$$

Therefore the second Hamilton's equation of motion becomes,

$$\begin{aligned}
&\partial_0\left(\frac{\partial\mathcal{L}}{\partial(\partial_0\phi)}\right) = -\left(\frac{d\mathcal{H}}{d\phi} - \left.\frac{d\mathcal{H}}{d\pi}\right|_\phi \frac{d\pi}{d\phi}\right)\\
\Leftrightarrow &\partial_0\left(\frac{\partial\mathcal{L}}{\partial(\partial_0\phi)}\right) = \frac{d\mathcal{L}}{d\phi} - \left(\partial_0\phi - \left.\frac{d\mathcal{H}}{d\pi}\right|_\phi\right)\frac{d\pi}{d\phi}\\
\Leftrightarrow &\partial_0\left(\frac{\partial\mathcal{L}}{\partial(\partial_0\phi)}\right) = \frac{\partial\mathcal{L}}{\partial\phi} - \nabla\cdot\frac{\partial\mathcal{L}}{\partial\nabla\phi} \text{ , by first Hamilton's equation}\\
\Leftrightarrow &\boxed{\partial_\mu\left(\frac{\partial\mathcal{L}}{\partial(\partial_\mu\phi)}\right) = \frac{\partial\mathcal{L}}{\partial\phi}} \textbf{ : eom (Euler-Lagrange)}
\end{aligned} \tag{B.86}$$

This establishes that the Euler-Lagrange equations are preserved by canonical quantization, providing an alternative description of the dynamics of field operators. To complete the shift to a Lagrangian description, all canonical momenta π can be eliminated through Eq. B.84, leading to a new expression of the commutation relations,

$$\begin{cases}[\phi(x),\phi(y)]_{x\cdot y<0} = \left[\frac{\partial\mathcal{L}}{\partial(\partial_0\phi)}(x), \frac{\partial\mathcal{L}}{\partial(\partial_0\phi)}(y)\right]_{x\cdot y<0} = 0\\ \left[\phi(x), \frac{\partial\mathcal{L}}{\partial(\partial_0\phi)}(y)\right]_{x\cdot y<0} = i\delta(x-y)\end{cases} \tag{B.87}$$

With these two equations Eqs. B.86-B.87, we can derive equations of motions for the correlation functions themselves.

B.2.4 Illustration: Schwinger-Dyson equations for ϕ^3 interactions

- For better insight into the general $n-$points functions techniques, before reviewing conclusions we will first be deriving results for a real scalar field governed by the earlier Lagrangian Eq. B.70,

$$\mathcal{L} = \underbrace{\frac{1}{2}(\partial_\mu\phi)^2 - \frac{1}{2}m^2\phi^2}_{\mathcal{L}_0} + \underbrace{\frac{g}{3!}\phi^3}_{\mathcal{L}_I}$$

The equations of motion are,

$$(\partial_x^2 + m^2)\phi_x = \frac{g}{2!}\phi_x^2 \tag{B.88}$$

and the commutation relations write explicitly,

$$\begin{cases}[\phi_x,\phi_y]_{x\cdot y<0} = [\partial_0\phi_x,\partial_0\phi_y]_{x\cdot y<0} = 0\\ [\phi_x,\partial_0\phi_y]_{x\cdot y<0} = i\delta(x-y)\end{cases} \tag{B.89}$$

Taking contour-ordered expectation values the equation of motion directly yields,

$$(\partial_x^2 + m^2)\langle\phi_x\rangle_{\rho_0} = \frac{g}{2!}\langle\tau_\gamma\phi_x^2\rangle_{\rho_0} \tag{B.90}$$

$$\textit{i.e.}\ \textbf{Field expectation value: } \boxed{(\partial_x^2 + m^2)G_x^{(1)} = \frac{g}{2!}G_{xx}^{(2)}} \tag{B.91}$$

that is an equation of motion for $G^{(1)}$ in terms of $G^{(2)}$.

Let us then determine a similar equation for $G^{(2)}$. We wish to compute $(\partial_x^2 + m^2) G^{(2)}_{xx_1}$, the only subtlety comes from the θ functions enforcing contour-ordering in the expectation value. We can hence start by applying the time derivatives,

$$\begin{aligned}
\partial_{x^0} G^{(2)}_{xx_1} &= \partial_{x^0} \langle \tau_\gamma \phi_x \phi_{x_1} \rangle_{\rho_0} \\
&= \partial_{x^0} \Big(\theta(x^0_\gamma - x^0_{1\gamma}) \langle \phi_x \phi_{x_1} \rangle_{\rho_0} + \theta(x^0_{1\gamma} - x^0_\gamma) \langle \phi_{x_1} \phi_x \rangle_{\rho_0} \Big) \\
&= \langle \tau_\gamma \partial_{x^0} \phi_x \phi_{x_1} \rangle_{\rho_0} + \delta(x^0_\gamma - x^0_{1\gamma}) \langle [\phi_x, \phi_{x_1}] \rangle_{\rho_0} \\
&\overset{\text{CCR}}{=} \langle \tau_\gamma \partial_{x^0} \phi_x \phi_{x_1} \rangle_{\rho_0}
\end{aligned}$$

Applying a second time derivative this time we find,

$$\begin{aligned}
\partial^2_{x^0} G^{(2)}_{xx_1} &= \langle \tau_\gamma \partial^2_{x^0} \phi_x \phi_{x_1} \rangle_{\rho_0} + \delta(x^0_\gamma - x^0_{1\gamma}) \langle [\partial_{x^0} \phi_x, \phi_{x_1}] \rangle_{\rho_0} \\
&\overset{\text{CCR}}{=} \langle \tau_\gamma \partial^2_{x^0} \phi_x \phi_{x_1} \rangle_{\rho_0} - i\delta(x - x_1)
\end{aligned}$$

The other elements of our differential operator directly commute with the contour-ordered expectation value, so that finally,

$$\begin{aligned}
(\partial_x^2 + m^2) G^{(2)}_{xx_1} &= \langle \tau_\gamma (\partial_x^2 + m^2) \phi_x \phi_{x_1} \rangle_{\rho_0} - i\delta(x - x_1) \\
&= \frac{g}{2!} \langle \tau_\gamma \phi_x^2 \phi_{x_1} \rangle_{\rho_0} - i\delta(x - x_1)
\end{aligned}$$

$$\textit{i.e.}\ \textbf{Exact propagator:}\ \boxed{(\partial_x^2 + m^2) G^{(2)}_{xx_1} = \frac{g}{2!} G^{(3)}_{xxx_1} - i\delta(x - x_1)} \tag{B.92}$$

we hence obtain an equation for the exact 2-points function in terms of the exact three-points function. Note that in the absence of interactions, this implies for the free 2-points function,

$$\textbf{Free propagator:}\ \boxed{(\partial_x^2 + m^2) D^0_{xy} = -i\delta(x - y)} \tag{B.93}$$

meaning it is Green's function of the Euler-Lagrange differential operator, which substantiates its appellation of "free propagator".

Generalizing this result *e.g.* by induction we obtain,

$$\textbf{Schwinger-Dyson:}\ \boxed{\begin{aligned}(\partial_x^2 + m^2) G^{(n)}_{xx_1 \dots x_{n-1}} &= \frac{g}{2!} G^{(n+1)}_{xxx_1 \dots x_{n-1}} \\ &\quad - i\hbar \sum_{j=1}^{n-1} \delta(x - x_j) G^{(n-2)}_{x_1 \dots x_{j-1} x_{j+1} \dots x_n}\end{aligned}} \tag{B.94}$$

Interestingly from order 2 onward the equation differs from the Euler-Lagrange equations by δ terms. Reinstating $\hbar$ in this equation, we see that those terms indeed capture the quantum modifications to the classical form of these equations. In particular it is responsible for the appearance of loop diagrams in the context of perturbation theory (see *e.g.* [396]).

---

[46] Numerical prefactors are included in the Feynmann rules by dividing each diagram by its number of geometrical symmetries, and can therefore be omitted in diagram representations (see *e.g.* [307, 396, 401]).

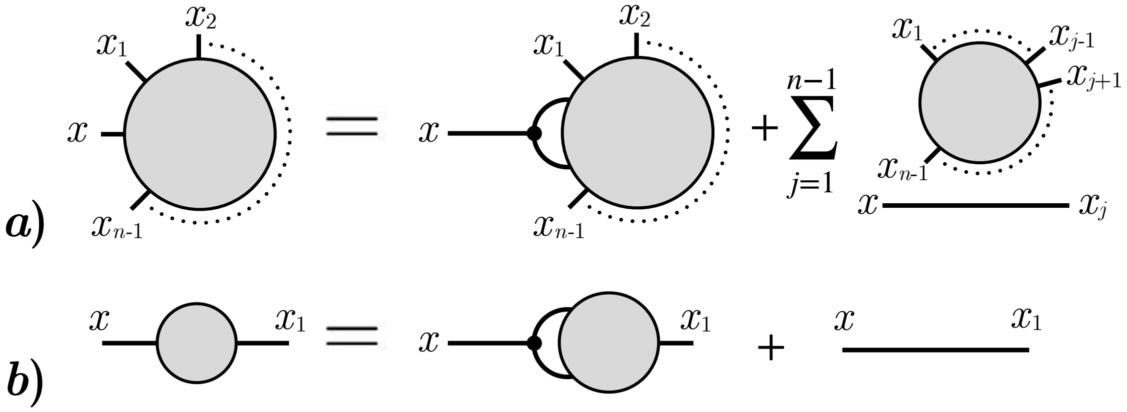

Figure B.2: **Diagrammatic representations of the Schwinger-Dyson equations for the ϕ^3 Lagrangian.** The full n-points functions are represented by disks with n outgoing lines, and dots signal interaction vertices, which contribute a factor ig and whose position is integrated over[46]. **a)** Representation of the general relation Eq. B.73; **b)** Representation of the exact propagator equation.

We can finally give a diagrammatic depiction of the Schwinger-Dyson equations, convoluting by iD^0 and using Eq. B.93 we find,

$$G^{(n)}_{xx_1\ldots x_{n-1}} = i\frac{g}{2!}D^0_{xy}G^{(n+1)}_{yyx_1\ldots x_{n-1}} + \sum_{j=1}^{n-1} D^0_{xx_j}G^{(n-2)}_{x_1\ldots x_{j-1}x_{j+1}\ldots x_n} \tag{B.95}$$

where integration over spacetime indices appearing in at least two different operators is implied. The corresponding diagram is drawn in Fig. B.2.

As becomes particularly clear comparing the exact 2-points functions equation Fig. B.2-b and the perturbative expansion Fig. B.1, the Schwinger-Dyson equations simply capture the structure of the interactions in the theory, hence of the perturbative expansion. Namely, a propagator line between two points either carry interactions or not, and in the former case it can only do so *via* one interaction vertex, followed by anything that can happen in-between the remaining points[47].

■ There are many different forms of these exact relations between the $n-$points functions[48]. All are equivalent at an exact level, but all do not prove equally fruitful so as to devise efficient approximation, or resolution schemes. This can be understood thinking of the different ways to organize the infinite diagram series summarized in Fig. B.2.

For instance, in the 3-points diagram appearing on the RHS of Fig. B.2-b, one knows either from algebra or direct diagrammatic reasoning that at least three qualitatively different kinds of terms can arise[49]. As vacuum diagrams cancel, external lines have to reach x and x_1, but in-between they can either be *i*) disconnected (*cf.* fifth term in B.1) *ii*) connected, with punctual insertion between external lines (fourth term)

---

[47] For our ϕ^3 interaction term, this translates in the $G^{(n+1)}$ term on the RHS of Eq. B.94

[48] Relating to many different names, *e.g.* "Dyson equations", "Kadanoff-Baym equations", "Martin-Schwinger hierarchy", "$n-$PI effective action equations of motion".

[49] *cf.* our derivation of Eq. B.73 in perturbation theory; in the following we assume that the initial state ρ_0 is such that Wick's theorem is valid (for centred field operators).

iii) connected, with two or more internal lines between external lines (sixth term). Disconnected graphs are easily seen to factorize in a product of two 1-point functions, so that in a sense they do not bring new information at the 2-points level. For this reason, it would be desirable to separate their contribution to the total 2-points function from the *connected* 2-points function.

This can be done again diagrammatically or algebraically. Opting for the latter approach and recalling that the 1-point function is the field expectation value $f_x \triangleq \langle \phi_x \rangle_{\rho_0}$, we can write,

$$\begin{aligned} G^{(2)}_{xx'} &= \langle \phi_x \phi_{x'} \rangle_{\rho_0} \\ &\equiv \langle (\varphi_x + f_x)(\varphi_{x'} + f_{x'}) \rangle_{\rho_0} \text{ , with } \langle \varphi_x \rangle_{\rho_0} = 0 \\ &= \langle \varphi_x \varphi_{x'} \rangle_{\rho_0} + f_x f_{x'} \\ \textit{i.e. } \mathcal{G}_{xx\prime} &\triangleq G^{(2)}_{xx'} - f_x f_{x'} \text{ is the connected 2-points function} \end{aligned} \tag{B.96}$$

Let us now inject the definition Eq. B.96 in the Schwinger-Dyson equation for $G^{(2)}$ Eq. B.92,

$$\begin{aligned} G^{(2)}_{xx'} &= D^0_{xx'} + \frac{ig}{2!} D^0_{xy} G^{(3)}_{yyx'} \\ \Leftrightarrow \mathcal{G}_{xx'} &= D^0_{xx'} - f_x f_{x'} + \frac{ig}{2!} D^0_{xy} \langle (\varphi_y + f_y)^2 (\varphi_{x'} + f_{x'}) \rangle_{\rho_0} \\ \Leftrightarrow \mathcal{G}_{xx'} &= D^0_{xx'} - \left[f_x - \frac{ig}{2!} D^0_{xy} \left(\mathcal{G}_{yy} + f_y^2 \right) \right] f_{x'} \\ &\quad + \frac{ig}{2!} D^0_{xy} \left\{ \mathcal{G}^{(3)}_{yyx'} + 2 f_y \mathcal{G}_{yx'} \right\} \end{aligned} \tag{B.97}$$

with $\mathcal{G}^{(3)}_{yyx'} \triangleq \langle \varphi_y^2 \varphi_{x'} \rangle_{\rho_0}$ the connected 3-points function. However, injecting Eq. B.96 in the Schwinger-Dyson equation for f_x Eq.B.91 we obtain,

$$f_x = \frac{ig}{2!} D^0_{xy} \left(\mathcal{G}_{yy} + f_y^2 \right) \tag{B.98}$$

so that Eq. B.97 becomes,

$$\mathcal{G}_{xx'} = D^0_{xx'} + \frac{ig}{2!} D^0_{xy} \left\{ \mathcal{G}^{(3)}_{yyx'} + 2 f_y \mathcal{G}_{yx'} \right\} \tag{B.99}$$

The corresponding diagram equation is,

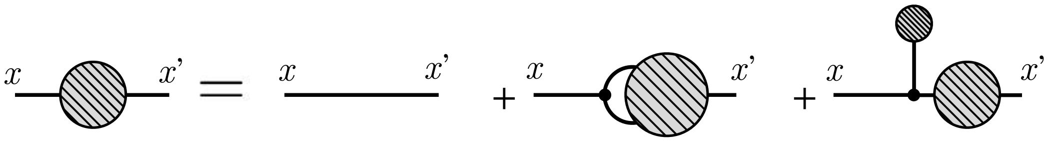

Figure B.3: **Schwinger-Dyson equation for the connected 2-points function.** The connected n-points functions are represented by hatched disks with n outgoing lines[51].

---

[51] The numerical factor in Eq. B.99 are accounted for by the symmetry factors in the Feynman rules.

Compared to Fig. B.2-b we see that only connected contributions remain on the RHS, of both kinds *ii*) (third term) and *iii*) (second term).

We can understand better the meaning of this equation by realizing that it is possible to factor out a connected 2-points function on the right of $\mathcal{G}^{(3)}$. Indeed, "all connected diagrams between y, y and x_1" can logically be decomposed as "all connected diagrams between y, y and y'"×"all connected diagrams between y' and x_1". In doing so we define what is called the "self-energy" Σ,

$$\mathcal{G}_{xx'} = D^0_{xx'} + \frac{ig}{2!} D^0_{xy} \left\{ \Sigma_{yyy'} + 2 f_y \delta_{yy'} \right\} \mathcal{G}_{y'x'} \tag{B.100}$$

$$\text{with } \mathcal{G}^{(3)}_{yyx'} \equiv \Sigma_{yyy'} \mathcal{G}_{y'x'} \tag{B.101}$$

At this point we alleviate notations by adopting an operator form for the convolution products, $AB \equiv A_{xy}B_{yz}$[52]. We can hence rewrite,

$$\begin{aligned} &\mathcal{G} = D^0 + D^0 \left\{ \tilde{\Sigma} + \tilde{f} \right\} \mathcal{G} \quad \text{with } \tilde{\Sigma} = \frac{ig}{2!}\Sigma \text{ and } \tilde{f} = igf \\ \Leftrightarrow\ &\mathcal{G} = \left[\mathbf{1} - D^0 \left\{ \tilde{\Sigma} + \tilde{f} \right\} \right]^{-1} D^0 \\ \Leftrightarrow\ &\mathcal{G} = \sum_{n=0}^{\infty} \left(D^0 \left\{ \tilde{\Sigma} + \tilde{f} \right\} \right)^n D^0 \end{aligned} \tag{B.102}$$

This form makes explicit that, in contrast with finite order perturbation theory, solving Dyson's equation automatically includes ("resums") an infinite number of diagrams. For the connected 2-points function they consist of $n \in \mathbb{N}$ occurrences of the exact interaction terms appearing on the RHS of Eq. B.100 each spaced by free propagation.

Now let us disentangle contributions of kinds *ii*) and *iii*) in $\mathcal{G}$. This seems *a priori* relevant, *e.g.* in view of some resolution *ansatz*, because of their different physical origins: one stems from local interactions with the mean field, the other from non-local coherent self-interaction[53]. They also clearly have distinct diagrammatic properties, which can be characterized by their remainder when external propagators are removed. For *ii*) it is a set of diagrams attached to a single point, we will call them "punctual". For *iii*) it is connected diagrams linking two points, such that they remain connected if one internal line is cut, this property is known as "1-particle irreducibility" (1-PI).

Simply reasoning diagrammatically again, we can decompose the full connected 2-points functions between all diagrams with no 1-PI contributions, and diagrams with at least one. In the latter case, we can factor out (on the left) all contributions before the 1-PI terms, which hence have no 1-PI contribution, as well as (on the right) all that is comprised after the 1-PI diagram. Denoting the 2-point function with only punctual interactions by $\mathcal{D}^f_{xx'}$, we conclude at the following decomposition,

$$\begin{cases} \mathcal{G} = \mathcal{D}^f + \dfrac{ig}{2!} \mathcal{D}^f \Sigma \mathcal{G} \\ \mathcal{D}^f = D^0 + ig D^0 f \mathcal{D}^f \end{cases} \tag{B.103}$$

---

[52] In our limited use ambiguities *e.g.* for more indices or δs should be lifted from context.

[53] Eventually perceived as "collisions" in a kinetic reduction.

Consistency of these relations with previous results can be checked explicitly with straightforward algebra, as they entail,

$$\begin{cases} \mathcal{G} = \sum\limits_{n=0}^{\infty} \left(\mathcal{D}^f \tilde{\Sigma}\right)^n \mathcal{D}^f \\ \mathcal{D}^f = \sum\limits_{n=0}^{\infty} \left(D^0 \tilde{f}\right)^n D^0 \end{cases} \tag{B.104}$$

Expanding the summand $\left(D^0 \left\{\tilde{\Sigma} + \tilde{f}\right\}\right)^n$ one sees that each term of the $\mathcal{G}$ series in Eq. B.104 is included in Eq. B.102, conversely expanding $\mathcal{D}^f$ in Eq. B.104 one finds back each term of Eq. B.102, hence both series are identical. In summing first $\mathcal{D}^f$ though, propagation is now expressed as a succession of exact streaming motion in the field, generated by punctual diagrams f, interspersed with $n \in \mathbb{N}$ self-interaction sequences, generated by 1-PI diagrams Σ. Diagrammatically we can draw,

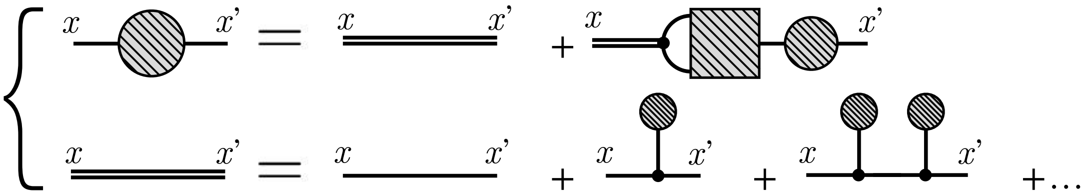

Figure B.4: **Exact propagator decomposition.** Self-energy is represented by a hatched square, and the field-dressed propagator by a double line.

As a final move to separate qualitatively different contributions, let us consider the internal structure of Σ. Pursuing the argument that allowed to define it[54], we understand that in order to obtain a connected 3-points function all three external lines have to join a common (connected) central diagram. In summing all the ways in which this centre can be reached, we can replace each external line by an exact 2-points function, resulting in the factorization,

$$\mathcal{G}^{(3)}_{xx'x''} \triangleq \mathcal{G}_{xy}\mathcal{G}_{x'y'}\mathcal{G}_{x''y''}\Gamma_{yy'y''} \tag{B.105}$$

The quotient 3-points function Γ is referred to as the “proper vertex”.

Furthermore thinking of all possible constituting diagrams it is clear that $\Gamma \equiv \Gamma[f, \mathcal{G}]$. However let us consider the f dependence more closely. Because Γ is connected a 1-point diagram has to be attached to a vertex. In our 3-points interaction theory we can then list all possibilities. If the two remaining end lines are closed together, it is a vacuum diagram and hence cancels. If they are attached to different points, then our 1-point diagram actually is connected to a 2-points diagram. If one end line is itself a 1-point function, then only one line remains which itself defines a 1-point diagram and we resume to the beginning of our reasoning. Therefore in the proper vertex all 1-point diagrams are actually attached to a 2-points diagram, so that $\Gamma[f, \mathcal{G}] \equiv \Gamma[\mathcal{G}] \equiv \Gamma[\mathcal{D}^f, \Sigma]$.

---

[54] Factorization of a connected 2-points function $\mathcal{G}$ out of a connected 3-points function $\mathcal{G}^{(3)}$

- We can gather our results at this point. The exact connected one and two points functions are governed by the relations[55],

$$\boxed{\begin{cases} (\partial_x^2 + m^2) f_x = \dfrac{g}{2!}\left(\mathcal{G}_{xx} + f_x^2\right) & \text{(B.106)} \\ (\partial_x^2 + m^2 - g f_x)\mathcal{G}_{xx'} = -i\delta_{xx'} \\ \qquad\qquad + \dfrac{g}{2!}\displaystyle\int_\gamma \mathcal{G}_{xa}\mathcal{G}_{xb}\Gamma_{abc}[D^f, \Sigma]\mathcal{G}_{cx'} & \text{(B.107)} \\ (\partial_x^2 + m^2 - g f_x)\mathcal{D}^f_{xx'} = -i\delta_{xx'} & \text{(B.108)} \end{cases}}$$

with $\int_\gamma A_x \equiv \int d\mathbf{x} \int_\gamma dz A(\mathbf{x}, z)$.

They form a system of coupled non-linear integro-differential equations which is not closed. The missing information is encapsulated in the unknown functional Γ. Of course, the proper vertex Γ obeys its own equation of motion, which could similarly be derived from the 3-points Schwinger-Dyson equation (Eq. B.94). Then again an unknown proper 4-points function Λ would appear, leading further still in the infinite correlation functions hierarchy. What has been achieved writing Eqs. B.106-B.108 though is a much clearer physical and mathematical picture of each term compared to the initial Schwinger-Dyson formulation Eq. B.94. As a consequence, it is easier to efficiently truncate the hierarachy from this point, depending on the physical configuration defined in ρ_0.

---

[55] We here reinstate explicit symbols where integration over repeated indices is intended.

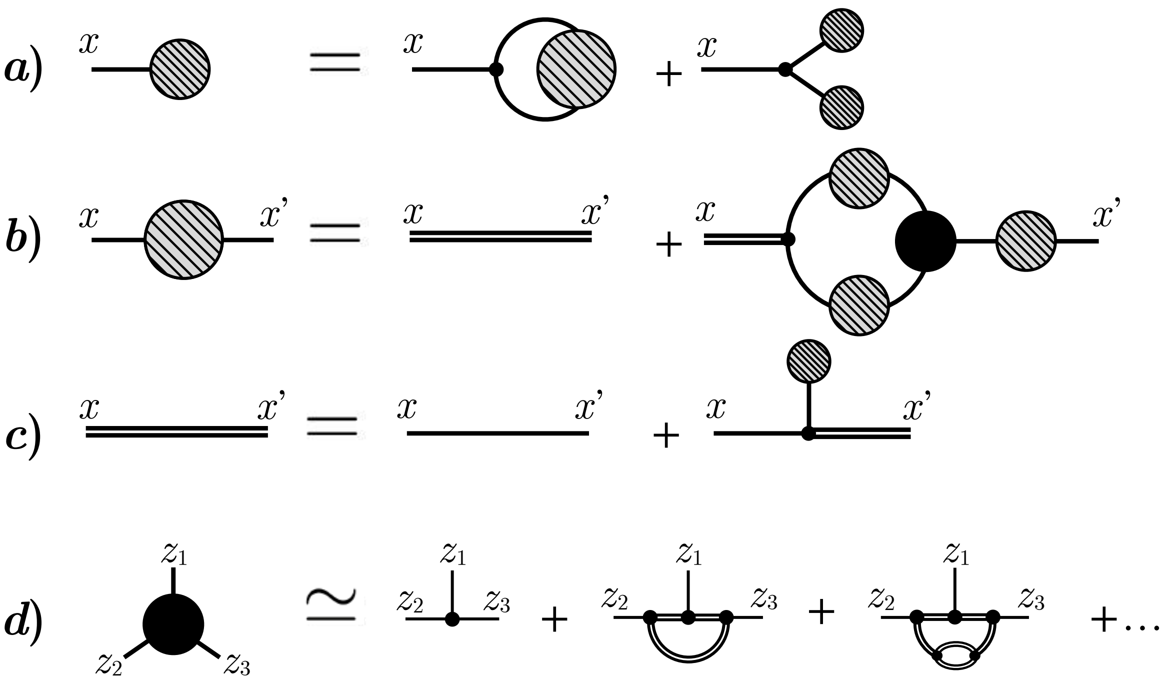

Figure B.5: **Schwinger-Dyson equations for the two first connected $n-$points functions.** The proper vertex is represented by a wide full circle. **a)** Field equation **b)** Propagator equation **c)** Field-dressed propagator equation **d)** First few terms of the proper vertex perturbative expansion, we notice their 1-PI property and expansion parameter $g^2\mathcal{D}^f$. Note for the connections with the proper vertex that $D^0 D^0 = D^0$.

This is illustrated in their diagrammatic representation Fig. B.5. The first three exact relations manifestly display more structural information on the solutions than Fig. B.2. For instance, Fig. B.5-c directly entails the explicit dependence on f of the field-dressed propagator $\mathcal{D}^f$, displayed in a series form. Besides, even the unknown proper vertex can be given an ordered perturbative expansion (Fig. B.5-d) based on its known functional dependence on $\mathcal{D}^f$ and 1-PI property.

Let us be more specific by imagining a closure scenario in a *strong-field* regime. We define it as $gf > 1$, so that the streaming motion in the field Eq. B.108 has to be solved exactly. In this context it would be desirable to simplify the field equations as well. In this regard we notice that on the RHS of Eq. B.106 the second term corresponds to the classical field equation, so that the first is a quantum correction that we may hope to neglect[56]. The quantum source term of the field equations can be interpreted as a local current density, so that neglecting it in a sense amounts to a "dilute medium" hypothesis. Assuming such condition holds, we enforce a decoupling of Eqs. B.106 and Eqs. B.107. Then truncating the proper vertex at lowest order we have $\Gamma \approx ig$, leading to,

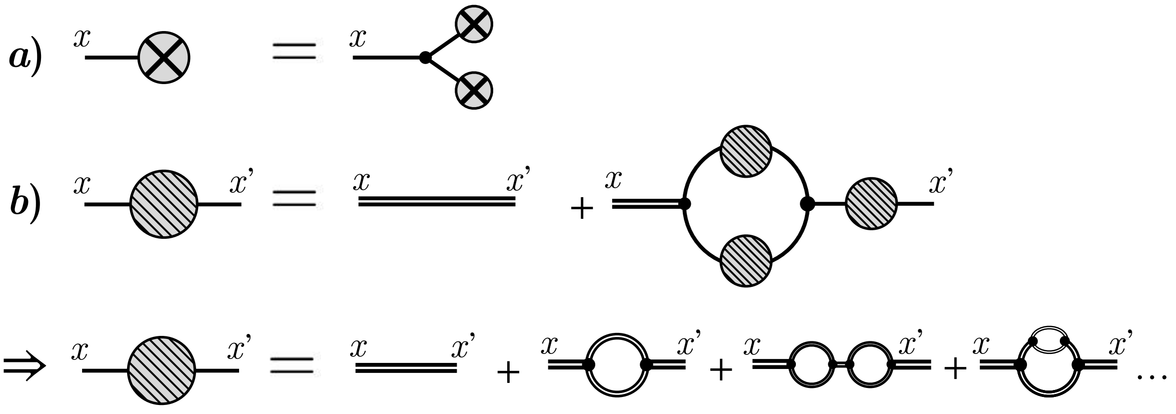

Figure B.6: **Schwinger-Dyson equations in a strong field approximation.** The diagrams included in a solution $\mathcal{G}$ are easily drawn by recursively injecting Fig. B.6-b into its RHS, as shown with the few first terms in the last line.

Even in these coarse approximations the equations of motion for the two first correlation functions f and $\mathcal{G}$ still encode a wealth of phenomena. This can be understood simply looking at the few first terms of the 2-points function Fig. B.6-b. The 1-body properties of the system appear to be computed in the field governed by its exact classical vacuum equations of motion, taking into account an infinite superposition of virtual processes of particle creation and recombination, without assuming quantum decoherence between each interaction event. The price is indeed a very high computational complexity. Nonetheless, as a systematic procedure to pursue the reduction down to kinetic theory is known, one is in principle free to find an adequate compromise between accuracy and tractability [116, 305, 306].

---

[56] *e.g.* on the intuitive grounds that strong fields correspond to high particle occupation numbers and hence globally classical behavior.

B.2.5 Opening remarks in view of non-equilibrium QFT

- As they rely solely on the Euler-Lagrange equations satisfied by the field operators, the Schwinger-Dyson relations clearly are extremely general. Without introducing superfluous complications we can take a glimpse at their general form assuming that,

  $$\mathcal{L}(\phi, \partial_\mu \phi) \equiv \mathcal{L}_0(\phi, \partial_\mu) + \mathcal{L}_I(\phi) \tag{B.109}$$

  where $\mathcal{L}_0$ leads to linear equations of motion[57], or in other words $\partial_\mu \left(\frac{\partial \mathcal{L}_0}{\partial(\partial_\mu \phi)}\right) - \frac{\partial \mathcal{L}_0}{\partial \phi} \equiv D_{\mathcal{L}_0}[\phi]$ is a linear functional of the field. Proceeding as before, the Euler-Lagrange equations imply an equation for the field correlation functions:

  $$\begin{aligned} D_{\mathcal{L}_0 x}[\langle \tau_\gamma \phi_x \phi_{x_1} \dots \phi_{x_n} \rangle_{\rho_0}] &= \left\langle \tau_\gamma \mathcal{L}'_I(\phi_x) \phi_{x_1} \dots \phi_{x_n} \right\rangle_{\rho_0} \\ &\quad - i \sum_{j=1}^{n-1} \delta_{x x_j} \langle \tau_\gamma \phi_{x_1} \dots \phi_{x_{j-1}} \phi_{x_{j+1}} \dots \phi_{x_n} \rangle_{\rho_0} \end{aligned} \tag{B.110}$$

  denoting $\partial \mathcal{L}_I / \partial \phi = \mathcal{L}'_I$.

  Now an actual derivation in this general setting would be much more accessible in a functional formulation of field theory [307] (introducing path integrals), which falls beyond our scope. Besides this exercise proves rather formal as physically predictive field theories generally feature non-zero spin fields, typically gauge-fields and fermions, so we will not pursue it further.

  Instead we show the (connected) Schwinger-Dyson equations of QED, as an example of a more interesting system. Retaining only the first two correlation functions, the system variables are,[58],

  $$\left\{ \begin{aligned} \mathcal{A}^\mu_x &= \langle A^\mu_x \rangle_{\rho_0} \text{ (Electromagnetic potential)} && \text{(B.111)} \\ \mathcal{D}^{\mu\nu}_{xx\prime} &= \langle \tau_\gamma A^\mu_x A^\nu_{x'} \rangle_{\rho_0} - \mathcal{A}^\mu_x \mathcal{A}^\nu_{x'} \text{ (Photon propagator)} && \text{(B.112)} \\ \Delta_{xx\prime} &= \langle \tau_\gamma \psi_x \overline{\psi}_{x'} \rangle_{\rho_0} \text{ (Electron-Positron propagator)} && \text{(B.113)} \end{aligned} \right.$$

  governed by the Schwinger-Dyson equations [45, 116, 405],

  $$\boxed{\left\{ \begin{aligned} \left(\eta^\mu{}_\sigma \partial^2_x - \left[1 - \xi^{-1}\right] \partial^\mu_x \partial_{x\sigma}\right) \mathcal{A}^\sigma_x &= -e \mathrm{Tr}\left[\gamma^\mu \Delta(x,x)\right] && \text{(B.114)} \\ \left(\eta^\mu{}_\sigma \partial^2_x - \left[1 - \xi^{-1}\right] \partial^\mu_x \partial_{x\sigma}\right) \mathcal{D}^{\sigma\nu}_{xx'} &= -i\eta^{\mu\nu} \delta_{xx'} \\ &\quad - e\gamma^\mu \int_\gamma \Delta_{xb} \Delta_{xc} \Gamma^\sigma_{abc}[\mathcal{D}^0, \Pi, \Delta^{0\mathcal{A}}, \mathcal{M}] \mathcal{D}_\sigma{}^\mu{}_{ax'} && \text{(B.115)} \\ \left(i\partial\!\!\!/_x - e\mathcal{A}\!\!\!/ - m\right) \Delta_{xx'} &= -i\delta_{xx'} \\ &\quad - e\gamma^\sigma \int_\gamma \mathcal{D}_{\sigma\rho xa} \Delta_{xb} \Gamma^\rho_{abc}[\mathcal{D}^0, \Pi, \Delta^{0\mathcal{A}}, \mathcal{M}] \Delta_{cx'} && \text{(B.116)} \\ \left(i\partial\!\!\!/_x - e\mathcal{A}\!\!\!/ - m\right) \Delta^{0\mathcal{A}}_{xx'} &= -i\delta_{xx'} && \text{(B.117)} \end{aligned} \right.}$$

  here written in Lorenz gauge with gauge fixing parameter ξ; where $\mathcal{M}$ (Π) is the fermion (photon) self-energy, and the trace acts on Dirac indices. Their diagrammatic representation is given in Fig. B.7.

---

[57] Hence is itself quadratic.

[58] This assumes that, as in vacuum, $\langle \overline{\psi}_x \rangle_{\rho_0} = \langle \psi_x \rangle_{\rho_0} = 0$.

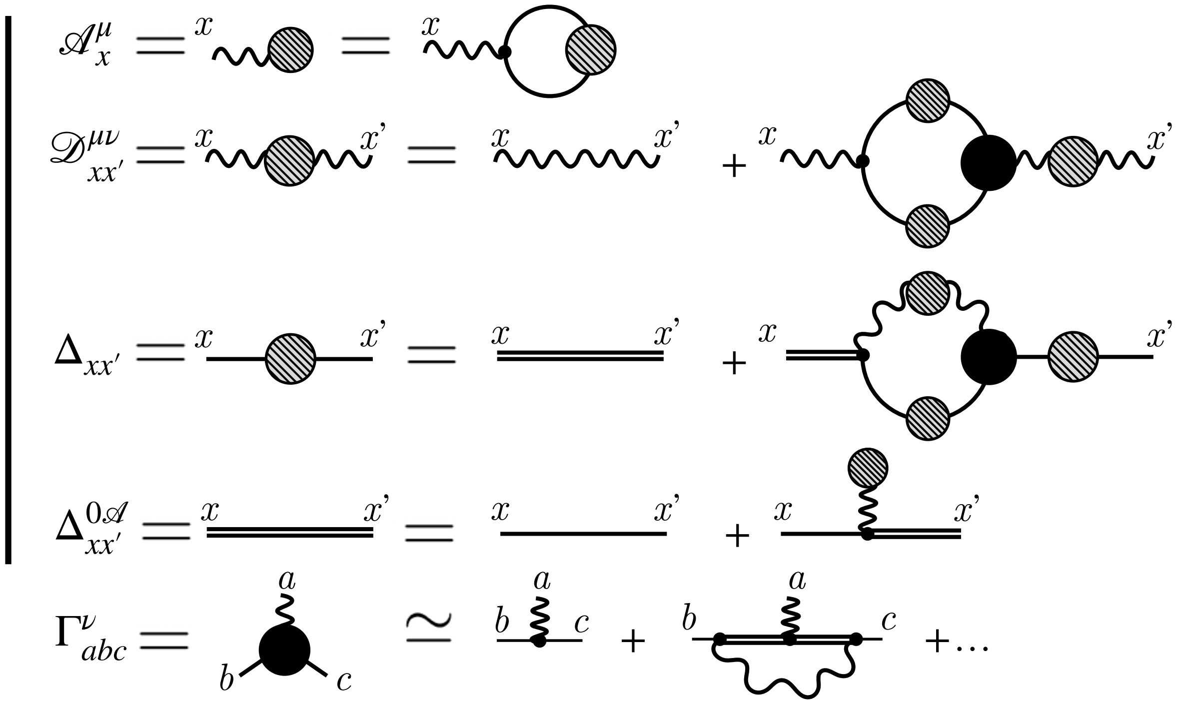

Figure B.7: **Schwinger-Dyson equations for the one and two points functions of Quantum Electrodynamics.** Wavy lines stand for connected free photon propagators $\mathcal{D}^{0\mu\nu}_{xx'} = \langle A^{0\mu}_{x} A^{0\nu}_{x'} \rangle_{\rho_0} - \mathcal{A}^{0\mu}_{x} \mathcal{A}^{0\nu}_{x'}$, and straight lines for connected electron-positron 2-points function $\Delta^{0}_{xx'} = \langle\rangle_{\rho_0} \overline{\psi}^{0}_{x} \psi^{0}_{x'}$. Dots are interaction vertices, with position integrated over and contributing a factor $-ie\gamma^{\mu}$ ($e^2 = 4\pi\alpha$ where α is the fine-structure constant).

The structural analogy with the previous ϕ^3 theory is manifest. The main differences are the presence of two interacting fields, leading to coupled equations of motion[59], and the absence of direct self-interaction of the electromagnetic field[60]. We will not push this discussion further, but refer the reader to [116] and references therein for an in-depth study of non-equilibrium QED and its kinetic reduction.

One major missing element so as to make this Schwinger-Dyson approach viable would be a general closure method of the system, granting fundamental properties such as self-consistency[61] of the approximated equations. It occurs that such controlled approximation procedure is provided by the notion of $n-$PI quantum effective actions of the system [305–307, 406]. Without entering into any more details, let us mention they prove a very efficient way of organising the diagrammatic information of the theory, a fraction of which we encountered and addressed "by hand" in our illustrative ϕ^3 study, and thus a relevant starting point for formulating Non-equilibrium Quantum Field Theory.

---

[59] Gauge freedom also adds some complexity, *e.g.* by the introduction of gauge-fixing terms.

[60] In other words photons do not have an electric charge. Non-abelian gauge bosons, *e.g.* gluons in Chromodynamics, do directly interact though (gluons have a colour charge).

[61] *cf.* introduction of this sec. B.2.3.

B.3 Similarity classes of initial states

Correlation functions allow computing any physical quantity, and some formalisms make use of their specific form[62]. However, being defined as expectation values it would seem these efforts have to be repeated for each possible initial state ρ_0. Fortunately, there are ways to avoid this duplication for some sets of related state operators, thereby defining formally equivalent classes of states. Probably the three most common families are the vacuum, thermal and coherent states, all accompanied by any finite number of additional particles.

In the context of scattering theory, a central technical tool concurring to such result for particle transition amplitudes is known as the Lehmann-Symanzik-Zimmermann reduction formula. In general (non-equilibrium) field theory, $n-$points function can be computed from their initial values, *e.g.* by Schwinger-Dyson equations, so that in a sense this formalism already is as state-independent as mechanics can be. However, actual computations typically need restricting to the few first $n \leq p-$points functions, by which initial conditions with irreducible correlations[63] of order no higher than p acquire a distinguished status [305, 306, 406]. In practice, one would often work only with field expectation values and propagators and therefore restrict to so-called *gaussian states*, with no irreducible correlations higher than 2.

B.3.1 Reduction of particle transition amplitudes

■ Following the methods presented in sec. B.2 we would be able to compute correlation functions in a given initial state. However in a given field theory one would like to calculate quantities for various initial states. For instance, considering the transition probability to a given (spin 0) particle state $|f\rangle \equiv |\mathbf{k}_1 \dots \mathbf{k}_{m_f}\rangle$, one computes,

$$P_{f|\rho_0}(t) = \langle |f\rangle\langle f|(t)\rangle_{\rho_0} \tag{B.118}$$

To be more specific still, in vacuum[64] scattering theory, the initial state is itself a pure particle state $\rho_0 \equiv |i\rangle\langle i|$ with $|i\rangle = |\mathbf{q}_1 \dots \mathbf{q}_{m_i}\rangle$, so that,

$$\begin{aligned} P_{f|i}(t) &= \mathrm{Tr}\left[|i\rangle\langle i|U^\dagger(t,t_0)|f\rangle\langle f|U(t,t_0)\right] \\ &= |\langle f|U(t,t_0)|i\rangle|^2 && \text{(B.119)} \\ &\triangleq |\langle f|i_{\mathrm{out}}\rangle|^2 && \text{(B.120)} \end{aligned}$$

Then of course repeating derivations for each possible particle state would be unmanageable. Hopefully this can be avoided *via* the standard result known as the

---

[†] Refs. B.3: [305–307]

[62] *e.g.* for writing the Feynmann rules in perturbation theory.

[63] We call a correlation function of order m irreducible if can not be expressed in terms of correlations of lower order (in the present context all considered at initial time).

[64] This terminology is to be justified shortly.

Lehmann-Symanzik-Zimmermann *reduction formula* [307, 396, 401],

Lehmann-Symanzik-Zimmermann

$$\begin{aligned}\langle \mathbf{k}_1 \dots \mathbf{k}_{m_f} | \mathbf{q}_1 \dots \mathbf{q}_{m_i \text{ out}} \rangle = i^{m_i+m_f} & \int \prod_{i=1}^{m_i} dx_i e^{-iq_i \cdot x_i} (\partial^2_{x_i} + m^2) \\ \times & \int \prod_{j=1}^{m_f} dy_j e^{ik_j \cdot y_j} (\partial^2_{y_j} + m^2) \\ & \langle 0 | \tau \phi_{x_1} \dots \phi_{x_{m_i}} \phi_{y_1} \dots \phi_{y_{m_f}} | 0_{\text{out}} \rangle \end{aligned} \qquad \text{(B.121)}$$

where τ is the simple time ordering operator. Therefore, the computation of particle transition amplitudes is entirely reduced to the computation of so-called "in-out" *vacuum* $n-$points functions. As this formula merely relies on the field expression of the Heisenberg creation and annihilation operators $a^\dagger_{\mathbf{k}}$ and $a_{\mathbf{k}}$, similar forms exist for non-zero spin fields.

For the most general problem of an arbitrary observable and initial state, we understand that similar reductions could be operated again leveraging on the field expression of the creation/annihilation operators. Let us simply sketch the first steps of such derivation. We consider a collection of initial particles $|\mathbf{q}_1 \dots \mathbf{q}_m\rangle$ added to a general state ρ_0, that is the modified initial state,

$$\rho_0 \oplus [\mathbf{q}_i]_1^m \triangleq \left(\prod_j^m a^\dagger_{\mathbf{q}_j} \right) \rho_0 \left(\prod_{j'}^m a_{\mathbf{q}_{j'}} \right) \qquad \text{(B.122)}$$

Then using Eq. B.21-B.22 together with the basic identity $f(t_0) = f(t) - \int_{t_0}^t \partial_t f$, repeating the algebra leading to the LSZ formula we obtain,

$$\begin{aligned}\langle O(t) \rangle_{\rho_0 \oplus [\mathbf{q}_i]_1^m} &= \left\langle \prod_j^m a_{\mathbf{q}_j} O(t) \prod_{j'}^m a^\dagger_{\mathbf{q}_{j'}} \right\rangle_{\rho_0} \quad \text{by cyclicity of the trace} \\ &= \left\langle \prod_j^m \left(a_{\mathbf{q}_j}(t) - i \int_\gamma dx_j \theta_+(x_j^0) e^{iq_j \cdot x_j} (\partial^2_{x_j} + m^2) \phi_{x_j} \right) \right. \\ &\times O(t) \\ &\times \left. \prod_{j'}^m \left(a^\dagger_{\mathbf{q}_{j'}}(t) - i \int_\gamma dy_{j'} \theta_-(y_{j'}^0) e^{iq_{j'} \cdot y_{j'}} (\partial^2_{y'_j} + m^2) \phi_{y_{j'}} \right) \right\rangle_{\rho_0} \end{aligned} \qquad \text{(B.123)}$$

where $\theta_\pm(z)$ is the step function that is one if z belongs to the forward (resp. backward) branch of the contour and 0 otherwise. This way we see that it would be possible to break the expectation value in the new state $(\rho_0 \,|\prod_i^m \mathbf{q}_i)$ down into $n-$points functions of the state ρ_0 and their derivatives.

B.3.2 Initial conditions in effective actions

- As already advocated in sec. B.2 in the most general case instead of a reduction formula of the kind Eq. B.123 one may directly compute correlation functions from their initial values, *via* some form of Schwinger-Dyson equations. In this case, as previously mentioned, the main concern is the degree of the highest irreducible initial correlation. A proper justification of this fact would require introducing the notion of $n-$PI effective action, which is hardly formulated outside the functional formalism. We refer the reader to [305, 306] and references therein for a recent introduction.

For our concern, it is sufficient to notice that appling Eq. B.123 at time t_0 and injecting Eqs. B.21-B.22, we find,

$$\begin{aligned}\langle O(t_0)\rangle_{\rho_0\oplus[\mathbf{q}_i]_1^m} &= (-1)^m \int \prod_j^m d\mathbf{x}_j e^{iq_j\cdot x_j} \int \prod_{j'}^m d\mathbf{y}_{j'} e^{iq_{j'}\cdot y_{j'}} \\ &\times \left\langle \left(\partial_0\phi_{\mathbf{x}_j} - iE_{\mathbf{q}_j}\phi_{\mathbf{x_j}}\right) O[\phi_{\mathbf{x}}] \left(\partial_0\phi_{\mathbf{y}_{j'}} - iE_{\mathbf{q}_{j'}}\phi_{\mathbf{y_{j'}}}\right)\right\rangle_{\rho_0} \qquad \text{(B.124)}\end{aligned}$$

where we denote $A_{\mathbf{x}} \equiv A_x|_{x^0=t_0}$ and substituted π by its expression in terms of ϕ and $\partial_0\phi$ (*cf.* Lagrangian formulation in sec. B.2.3). As a consequence, initial time correlators of the field and its derivatives in the modified state $\rho_0 \oplus [\mathbf{q}_i]_1^m$ can be expressed as a linear combination of initial time correlators of the field and its derivatives in state ρ_0. This implies that the degree of highest irreducible correlation function p is preserved by the addition of finitely many initial particles, so that the same effective action can be used with the updated initial correlation values.

Bibliography

[1] G. A. Mourou, T. Tajima, and S. V. Bulanov, “Optics in the relativistic regime”, Rev. Mod. Phys. **78**, 309–371 (2006).

[2] A. Di Piazza, C. Müller, K. Z. Hatsagortsyan, and C. H. Keitel, “Extremely high-intensity laser interactions with fundamental quantum systems”, Rev. Mod. Phys. **84**, 1177–1228 (2012).

[3] A. Fedotov, A. Ilderton, F. Karbstein, B. King, D. Seipt, H. Taya, and G. Torgrimsson, *Advances in qed with intense background fields*, arXiv:2203.00019, 2022.

[4] A. Gonoskov, T. G. Blackburn, M. Marklund, and S. S. Bulanov, “Charged particle motion and radiation in strong electromagnetic fields”, Rev. Mod. Phys. **94**, 045001 (2022).

[5] C. N. Danson, C. Haefner, J. Bromage, T. Butcher, J.-C. F. Chanteloup, E. A. Chowdhury, A. Galvanauskas, L. A. Gizzi, J. Hein, D. I. Hillier, and et al., “Petawatt and exawatt class lasers worldwide”, High Power Laser Science and Engineering **7**, e54 (2019).

[6] S. Gordienko, A. Pukhov, O. Shorokhov, and T. Baeva, “Coherent focusing of high harmonics: a new way towards the extreme intensities”, Phys. Rev. Lett. **94**, 103903 (2005).

[7] S. V. Bulanov, T. Z. Esirkepov, M Kando, and J Koga, “Relativistic mirrors in laser plasmas (analytical methods)”, Plasma Sources Science and Technology **25**, 053001 (2016).

[8] R. Lichters, J. Meyer-ter-Vehn, and A. Pukhov, “Short-pulse laser harmonics from oscillating plasma surfaces driven at relativistic intensity”, Physics of Plasmas **3**, 3425–3437 (1996).

[9] T. Baeva, S. Gordienko, and A. Pukhov, “Theory of high-order harmonic generation in relativistic laser interaction with overdense plasma”, Phys. Rev. E **74**, 046404 (2006).

[10] D. an der Brügge and A. Pukhov, “Enhanced relativistic harmonics by electron nanobunching”, Physics of Plasmas **17**, 033110 (2010).

[11] A. A. Gonoskov, A. V. Korzhimanov, A. V. Kim, M. Marklund, and A. M. Sergeev, “Ultrarelativistic nanoplasmonics as a route towards extreme-intensity attosecond pulses”, Phys. Rev. E **84**, 046403 (2011).

[12] H. Vincenti, “Achieving extreme light intensities using optically curved relativistic plasma mirrors”, Phys. Rev. Lett. **123**, 105001 (2019).

[13] F. Quéré and H. Vincenti, “Reflecting petawatt lasers off relativistic plasma mirrors: a realistic path to the schwinger limit”, High Power Laser Science and Engineering **9**, e6 (2021).

[14] E. T. Whittaker, *A history of the theories of aether and electricity: from the age of descartes to the close of the nineteenth century*, en (June 2015).

[15] F. A. Reuse, *Electrodynamique*, fr (PPUR Presses polytechniques, Oct. 2012).

[16]P. Gibbon, *Short pulse laser interactions with matter: an introduction*, en (Imperial College Press, London, England, Sept. 2005).

[17]J. W. Yoon, Y. G. Kim, I. W. Choi, J. H. Sung, H. W. Lee, S. K. Lee, and C. H. Nam, "Realization of laser intensity over 1023w/cm2", Optica **8**, 630–635 (2021).

[18]P. W. Milonni and J. H. Eberly, *Laser physics*, en (Wiley-Blackwell, Hoboken, NJ, Mar. 2010).

[19]D. Strickland and G. Mourou, "Compression of amplified chirped optical pulses", Optics Communications **56**, 219–221 (1985).

[20]A. Gonoskov, A. Bashinov, I. Gonoskov, C. Harvey, A. Ilderton, A. Kim, M. Marklund, G. Mourou, and A. Sergeev, "Anomalous radiative trapping in laser fields of extreme intensity", Phys. Rev. Lett. **113**, 014801 (2014).

[21]F Rohrlich, "Relativistic hamiltonian dynamics i. classical mechanics", Annals of Physics **117**, 292–322 (1979).

[22]J.-L. Basdevant, *Les principes variationnels en physique: cours, démonstrations & exercices corrigés*, fr (Feb. 2014).

[23]L. D. Landau and E. M. Lifschits, *The Classical Theory of Fields*, Vol. Volume 2, Course of Theoretical Physics (Pergamon Press, Oxford, 1975).

[24]H. R. Reiss, "Field intensity and relativistic considerations in the choice of gauge in electrodynamics", Phys. Rev. A **19**, 1140–1150 (1979).

[25]T. Heinzl and A. Ilderton, "A lorentz and gauge invariant measure of laser intensity", Optics Communications **282**, 1879–1883 (2009).

[26]E. Esarey, P. Sprangle, and J. Krall, "Laser acceleration of electrons in vacuum", Phys. Rev. E **52**, 5443–5453 (1995).

[27]G. Malka, E. Lefebvre, and J. L. Miquel, "Experimental observation of electrons accelerated in vacuum to relativistic energies by a high-intensity laser", Phys. Rev. Lett. **78**, 3314–3317 (1997).

[28]B. Quesnel and P. Mora, "Theory and simulation of the interaction of ultraintense laser pulses with electrons in vacuum", Phys. Rev. E **58**, 3719–3732 (1998).

[29]A. V. Arefiev, A. P. L. Robinson, and V. N. Khudik, "Novel aspects of direct laser acceleration of relativistic electrons", Journal of Plasma Physics **81**, 475810404 (2015).

[30]M. Thévenet, A. Leblanc, S. Kahaly, H. Vincenti, A. Vernier, F. Quéré, and J. Faure, "Vacuum laser acceleration of relativistic electrons using plasma mirror injectors", Nature Physics **12**, 355–360 (2016).

[31]H. R. Weller, M. W. Ahmed, H. Gao, W. Tornow, Y. K. Wu, M. Gai, and R. Miskimen, "Research opportunities at the upgraded his facility", Progress in Particle and Nuclear Physics **62**, 257–303 (2009).

[32]H. Utsunomiya, S. Hashimoto, and S. Miyamoto, "The -ray beam-line at newsubaru", Nuclear Physics News **25**, 25–29 (2015).

[33]S Gales, K. A. Tanaka, D. L. Balabanski, F Negoita, D Stutman, O Tesileanu, C. A. Ur, D Ursescu, I Andrei, S Ataman, M. O. Cernaianu, L D'Alessi, I Dancus, B Diaconescu, N Djourelov, D Filipescu, P Ghenuche, D. G. Ghita, C Matei, K Seto, M Zeng, and N. V. Zamfir, "The extreme light infrastructure—nuclear physics (eli-np) facility: new horizons in physics with 10 pw ultra-intense lasers and 20 mev brilliant gamma beams", Reports on Progress in Physics **81**, 094301 (2018).

[34]E. Esarey, C. B. Schroeder, and W. P. Leemans, "Physics of laser-driven plasma-based electron accelerators", Rev. Mod. Phys. **81**, 1229–1285 (2009).

[35]F. Albert, M. E. Couprie, A. Debus, M. C. Downer, J. Faure, A. Flacco, L. A. Gizzi, T. Grismayer, A. Huebl, C. Joshi, M Labat, W. P. Leemans, A. R. Maier, S. P. D. Mangles, P. Mason, F. Mathieu, P. Muggli, M. Nishiuchi, J. Osterhoff, P. P. Rajeev, U. Schramm, J. Schreiber, A. G. R. Thomas, J.-L. Vay, M. Vranic, and K. Zeil, "2020 roadmap on plasma accelerators", New Journal of Physics **23**, 031101 (2021).

[36]A. Macchi, M. Borghesi, and M. Passoni, "Ion acceleration by superintense laser-plasma interaction", Rev. Mod. Phys. **85**, 751–793 (2013).

[37]H. Daido, M. Nishiuchi, and A. S. Pirozhkov, "Review of laser-driven ion sources and their applications", Reports on Progress in Physics **75**, 056401 (2012).

[38]J Badziak, "Laser-driven ion acceleration: methods, challenges and prospects", Journal of Physics: Conference Series **959**, 012001 (2018).

[39]K. A. Tanaka, K. M. Spohr, D. L. Balabanski, S. Balascuta, L. Capponi, M. O. Cernaianu, M. Cuciuc, A. Cucoanes, I. Dancus, A. Dhal, B. Diaconescu, D. Doria, P. Ghenuche, D. G. Ghita, S. Kisyov, V. Nastasa, J. F. Ong, F. Rotaru, D. Sangwan, P.-A. Söderström, D. Stutman, G. Suliman, O. Tesileanu, L. Tudor, N. Tsoneva, C. A. Ur, D. Ursescu, and N. V. Zamfir, "Current status and highlights of the eli-np research program", Matter and Radiation at Extremes **5**, 024402 (2020).

[40]J. Li, J. Lu, A. Chew, S. Han, J. Li, Y. Wu, H. Wang, S. Ghimire, and Z. Chang, "Attosecond science based on high harmonic generation from gases and solids", Nature Communications **11**, 2748 (2020).

[41]M. Thévenet, A. Leblanc, S. Kahaly, H. Vincenti, A. Vernier, F. Quéré, and J. Faure, "Vacuum laser acceleration of relativistic electrons using plasma mirror injectors", Nature Physics **12**, 355–360 (2016).

[42]D. Papadopoulos, J. Zou, C. Le Blanc, G. Chériaux, P. Georges, F. Druon, G. Mennerat, P. Ramirez, L. Martin, A. Fréneaux, and et al., "The apollon 10 pw laser: experimental and theoretical investigation of the temporal characteristics", High Power Laser Science and Engineering **4**, e34 (2016).

[43]S. Weber, S. Bechet, S. Borneis, L. Brabec, M. Bučka, E. Chacon-Golcher, M. Ciappina, M. DeMarco, A. Fajstavr, K. Falk, E.-R. Garcia, J. Grosz, Y.-J. Gu, J.-C. Hernandez, M. Holec, P. Janečka, M. Jantač, M. Jirka, H. Kadlecova, D. Khikhlukha, O. Klimo, G. Korn, D. Kramer, D. Kumar, T. Lastovička, P. Lutoslawski, L. Morejon, V. Olšovcová, M. Rajdl, O. Renner, B. Rus, S. Singh, M. Šmid, M. Sokol, R. Versaci, R. Vrána, M. Vranic, J. Vyskočil, A. Wolf, and Q. Yu, "P3: an installation for high-energy density plasma physics and ultra-high intensity laser–matter interaction at eli-beamlines", Matter and Radiation at Extremes **2**, 149–176 (2017).

[44] B. Shen, Z. Bu, J. Xu, T. Xu, L. Ji, R. Li, and Z. Xu, "Exploring vacuum birefringence based on a 100 pw laser and an x-ray free electron laser beam", Plasma Physics and Controlled Fusion **60**, 044002 (2018).

[45] L. D. Landau, E. M. Lifshits, L. P. Pitaevski, and V. B. Berestetskii, *Physique théorique: électrodynamique quantique*, fr (Ellipses/Editions Mir, 2012).

[46] D. J. Griffiths, T. C. Proctor, and D. F. Schroeter, "Abraham–lorentz versus landau–lifshitz", American Journal of Physics **78**, 391–402 (2010).

[47] F. Rohrlich, "Classical self-force", Phys. Rev. D **60**, 084017 (1999).

[48] S. Parrott, *Comment on phys. rev. d 60 084017 "classical self-force" by f. rohrlich*, arXiv:gr-qc/0502029, 2005.

[49] J. Kijowski, "Electrodynamics of moving particles", General Relativity and Gravitation **26**, 167–201 (1994).

[50] H.-P. Gittel, J. Kijowski, and E. Zeidler, "The relativistic dynamics of the combined particle–field system in renormalized classical electrodynamics", Communications in Mathematical Physics **198**, 711–736 (1998).

[51] P. A. Sturrock, "A model of pulsars", The Astrophysical Journal **164**, 529 (1971).

[52] A. Philippov, A. Timokhin, and A. Spitkovsky, "Origin of pulsar radio emission", Phys. Rev. Lett. **124**, 245101 (2020).

[53] F. Cruz, T. Grismayer, A. Y. Chen, A. Spitkovsky, and L. O. Silva, "Coherent emission from qed cascades in pulsar polar caps", The Astrophysical Journal Letters **919**, L4 (2021).

[54] R. Hollebeek, "Disruption limits for linear colliders", Nuclear Instruments and Methods **184**, 333–347 (1981).

[55] P. Chen and K. Yokoya, "Disruption effects from the interaction of round e^+e^- beams", Phys. Rev. D **38**, 987–1000 (1988).

[56] R. Blankenbecler and S. D. Drell, "Quantum treatment of beamstrahlung", Phys. Rev. D **36**, 277–288 (1987).

[57] R. J. Noble, "Beamstrahlung from colliding electron-positron beams with negligible disruption", Nuclear Instruments and Methods in Physics Research Section A: Accelerators, Spectrometers, Detectors and Associated Equipment **256**, 427–433 (1987).

[58] E. N. Nerush, I. Y. Kostyukov, A. M. Fedotov, N. B. Narozhny, N. V. Elkina, and H. Ruhl, "Laser field absorption in self-generated electron-positron pair plasma", Phys. Rev. Lett. **106**, 035001 (2011).

[59] T. Grismayer, M. Vranic, J. L. Martins, R. A. Fonseca, and L. O. Silva, "Laser absorption via quantum electrodynamics cascades in counter propagating laser pulses", Physics of Plasmas **23**, 056706 (2016).

---

[60] A. Abada, M. Abbrescia, S. S. AbdusSalam, I. Abdyukhanov, J. Abelleira Fernandez, A. Abramov, M. Aburaia, A. O. Acar, P. R. Adzic, P. Agrawal, J. A. Aguilar-Saavedra, J. J. Aguilera-Verdugo, M. Aiba, I. Aichinger, G. Aielli, A. Akay, A. Akhundov, H. Aksakal, J. L. Albacete, S. Albergo, A. Alekou, M. Aleksa, R. Aleksan, R. M. Alemany Fernandez, Y. Alexahin, R. G. Alía, S. Alioli, N. Alipour Tehrani, B. C. Allanach, P. P. Allport, M. Altınlı, W. Altmannshofer, G. Ambrosio, D. Amorim, O. Amstutz, L. Anderlini, A. Andreazza, M. Andreini, A. Andriatis, C. Andris, A. Andronic, M. Angelucci, F. Antinori, S. A. Antipov, M. Antonelli, M. Antonello, P. Antonioli, S. Antusch, F. Anulli, L. Apolinário, G. Apollinari, A. Apollonio, D. Appelö, R. B. Appleby, A. Apyan, A. Apyan, A. Arbey, A. Arbuzov, G. Arduini, V. Arı, S. Arias, N. Armesto, R. Arnaldi, S. A. Arsenyev, M. Arzeo, S. Asai, E. Aslanides, R. W. Aßmann, D. Astapovych, M. Atanasov, S. Atieh, D. Attié, B. Auchmann, A. Audurier, S. Aull, S. Aumon, S. Aune, F. Avino, G. Avrillaud, G. Aydın, A. Azatov, G. Azuelos, P. Azzi, O. Azzolini, P. Azzurri, N. Bacchetta, E. Bacchiocchi, H. Bachacou, Y. W. Baek, V. Baglin, Y. Bai, S. Baird, M. J. Baker, M. J. Baldwin, A. H. Ball, A. Ballarino, S. Banerjee, D. P. Barber, D. Barducci, P. Barjhoux, D. Barna, G. G. Barnaföldi, M. J. Barnes, A. Barr, J. Barranco García, J. Barreiro Guimarães da Costa, W. Bartmann, V. Baryshevsky, E. Barzi, S. A. Bass, A. Bastianin, B. Baudouy, F. Bauer, M. Bauer, T. Baumgartner, I. Bautista-Guzmán, C. Bayındır, F. Beaudette, F. Bedeschi, M. Béguin, I. Bellafont, L. Bellagamba, N. Bellegarde, E. Belli, E. Bellingeri, F. Bellini, G. Bellomo, S. Belomestnykh, G. Bencivenni, M. Benedikt, G. Bernardi, J. Bernardi, C. Bernet, J. M. Bernhardt, C. Bernini, C. Berriaud, A. Bertarelli, S. Bertolucci, M. I. Besana, M. Besançon, O. Beznosov, P. Bhat, C. Bhat, M. E. Biagini, J. L. Biarrotte, A. Bibet Chevalier, E. R. Bielert, M. Biglietti, G. M. Bilei, B. Bilki, C. Biscari, F. Bishara, O. R. Blanco-García, F. R. Blánquez, F. Blekman, A. Blondel, J. Blümlein, T. Boccali, R. Boels, S. A. Bogacz, A. Bogomyagkov, O. Boine-Frankenheim, M. J. Boland, S. Bologna, O. Bolukbasi, M. Bomben, S. Bondarenko, M. Bonvini, E. Boos, B. Bordini, F. Bordry, G. Borghello, L. Borgonovi, S. Borowka, D. Bortoletto, D. Boscherini, M. Boscolo, S. Boselli, R. R. Bosley, F. Bossu, C. Botta, L. Bottura, R. Boughezal, D. Boutin, G. Bovone, I. BožovićJelisavić, A. Bozbey, C. Bozzi, D. Bozzini, V. Braccini, S. Braibant-Giacomelli, J. Bramante, P. Braun-Munzinger, J. A. Briffa, D. Britzger, S. J. Brodsky, J. J. Brooke, R. Bruce, P. Brückman De Renstrom, E. Bruna, O. Brüning, O. Brunner, K. Brunner, P. Bruzzone, X. Buffat, E. Bulyak, F. Burkart, H. Burkhardt, J. P. Burnet, F. Butin, D. Buttazzo, A. Butterworth, M. Caccia, Y. Cai, B. Caiffi, V. Cairo, O. Cakir, R. Calaga, S. Calatroni, G. Calderini, G. Calderola, A. Caliskan, D. Calvet, M. Calviani, J. M. Camalich, P. Camarri, M. Campanelli, T. Camporesi, A. C. Canbay, A. Canepa, E. Cantergiani, D. Cantore-Cavalli, M. Capeans, R. Cardarelli, U. Cardella, A. Cardini, C. M. Carloni Calame, F. Carra, S. Carra, A. Carvalho, S. Casalbuoni, J. Casas, M. Cascella, P. Castelnovo, G. Castorina, G. Catalano, V. Cavasinni, E. Cazzato, E. Cennini, A. Cerri, F. Cerutti, J. Cervantes, I. Chaikovska, J. Chakrabortty, M. Chala, M. Chamizo-Llatas, H. Chanal, D. Chanal, S. Chance, A. Chancé, P. Charitos, J. Charles, T. K. Charles, S. Chattopadhyay, R. Chehab, S. V. Chekanov, N. Chen, A. Chernoded, V. Chetvertkova, L. Chevalier, G. Chiarelli, G. Chiarello, M. Chiesa, P. Chiggiato, J. T. Childers, A. Chmielińska, A. Cholakian, P. Chomaz, M. Chorowski, W. Chou, M. Chrzaszcz, E. Chyhyrynets, G. Cibinetto, A. K. Ciftci, R. Ciftci, R. Cimino, M. Ciuchini, P. J. Clark, Y. Coadou, M. Cobal, A. Coccaro, J. Cogan, E. Cogneras, F. Collamati, C. Colldelram, P. Collier, J. Collot, R. Contino,

F. Conventi, and C. T. A. Cook, “Fcc-ee: the lepton collider”, The European Physical Journal Special Topics **228**, 261–623 (2019).

[61] J. L. Feng, “Dark matter candidates from particle physics and methods of detection”, Annual Review of Astronomy and Astrophysics **48**, 495–545 (2010).

[62] S. Villalba-Chavez and A. Piazza, “Axion-induced birefringence effects in laser driven nonlinear vacuum interaction”, JHEP **11**, 136 (2013).

[63] S. Villalba-Chávez, “Laser-driven search of axion-like particles including vacuum polarization effects”, Nucl. Phys. B **881**, 391–413 (2014).

[64] S. Shakeri, D. J. E. Marsh, and S.-S. Xue, *Light by light scattering as a new probe for axions*, 2020.

[65] S. Villalba-Chávez, T. Podszus, and C. Müller, “Polarization-operator approach to optical signatures of axion-like particles in strong laser pulses”, Phys. Lett. B **769**, 233–241 (2017).

[66] B. Dobrich and H. Gies, “Axion-like-particle search with high-intensity lasers”, JHEP **10**, 022 (2010).

[67] K. A. Beyer, G. Marocco, C. Danson, R. Bingham, and G. Gregori, “Parametric colinear axion photon instability”, (2021).

[68] S. Huang, B. Shen, Z. Bu, X. Zhang, L. Ji, and S. Zhai, “Axion-like particle generation in laser-plasma interaction”, Phys. Scripta **97**, 105303 (2022).

[69] D. A. Burton and A. Noble, “Plasma-based wakefield accelerators as sources of axion-like particles”, New J. Phys. **20**, 033022 (2018).

[70] S. Evans and J. Rafelski, “Virtual axion-like particle complement to Euler-Heisenberg-Schwinger action”, Phys. Lett. B **791**, 331–334 (2019).

[71] S. Villalba-Chávez, S. Meuren, and C. Müller, “Minicharged particles search by strong laser pulse-induced vacuum polarization effects”, Phys. Lett. B **763**, 445–453 (2016).

[72] H. Vogel and J. Redondo, “Dark radiation constraints on minicharged particles in models with a hidden photon”, Journal of Cosmology and Astroparticle Physics **2014**, 029–029 (2014).

[73] B. Dobrich, H. Gies, N. Neitz, and F. Karbstein, “Magnetically amplified tunneling of the 3rd kind as a probe of minicharged particles”, Phys. Rev. Lett. **109**, 131802 (2012).

[74] B. Döbrich, H. Gies, N. Neitz, and F. Karbstein, “Magnetically amplified light-shining-through-walls via virtual minicharged particles”, Phys. Rev. D **87**, 025022 (2013).

[75] S. Villalba-Chávez and C. Müller, “Light dark matter candidates in intense laser pulses I: paraphotons and fermionic minicharged particles”, JHEP **06**, 177 (2015).

[76] S. Villalba-Chávez and C. Müller, “Light dark matter candidates in intense laser pulses II: the relevance of the spin degrees of freedom”, JHEP **02**, 027 (2016).

[77] B. Acharya et al., “Search for magnetic monopoles produced via the Schwinger mechanism”, Nature **602**, 63–67 (2022).

[78] T. Kobayashi, “Monopole-antimonopole pair production in primordial magnetic fields”, Phys. Rev. D **104**, 043501 (2021).

[79] D. L. J. Ho and A. Rajantie, “Instanton solution for Schwinger production of ’t Hooft-Polyakov monopoles”, Phys. Rev. D **103**, 115033 (2021).

[80] D. L. J. Ho and A. Rajantie, “Classical production of ’t Hooft–Polyakov monopoles from magnetic fields”, Phys. Rev. D **101**, 055003 (2020).

[81] M. Born and L. Infeld, “Foundations of the new field theory”, Proc. Roy. Soc. Lond. A **144**, 425–451 (1934).

[82] J. Ellis, N. E. Mavromatos, and T. You, “Light-by-Light Scattering Constraint on Born-Infeld Theory”, Phys. Rev. Lett. **118**, 261802 (2017).

[83] A. Rebhan and G. Turk, “Polarization effects in light-by-light scattering: Euler–Heisenberg versus Born–Infeld”, Int. J. Mod. Phys. A **32**, 1750053 (2017).

[84] A. Ilderton, J. Lundin, and M. Marklund, “Strong Field, Noncommutative QED”, SIGMA **6**, 041 (2010).

[85] Z. Bai, T. Blackburn, O. Borysov, O. Davidi, A. Hartin, B. Heinemann, T. Ma, G. Perez, A. Santra, Y. Soreq, and N. T. Hod, *Luxe-npod: new physics searches with an optical dump at luxe*, arXiv:2107.13554, 2021.

[86] J. S. Schwinger, “On gauge invariance and vacuum polarization”, Phys. Rev. **82**, edited by K. A. Milton, 664–679 (1951).

[87] A. I. Nikishov and V. I. Ritus, “Quantum Processes in the Field of a Plane Electromagnetic Wave and in a Constant Field 1”, Sov. Phys. JETP **19**, 529–541 (1964).

[88] V. I. Ritus, “Quantum effects of the interaction of elementary particles with an intense electromagnetic field”, Journal of Soviet Laser Research **6**, 497–617 (1985).

[89] A. Kuznetsov and N. Mikheev, “Fermion propagator in an external electromagnetic field”, in *Springer tracts in modern physics*, Springer tracts in modern physics (Springer New York, New York, NY, 2004), page(s): 15–20.

[90] M. Ouali, M. Ouhammou, S. Taj, B. Manaut, and R. Benbrik, “Laser-assisted charged Higgs pair production in Inert Higgs Doublet Model (IHDM)”, Phys. Lett. B **823**, 136761 (2021).

[91] M. Ouhammou, M. Ouali, S. Taj, and B. Manaut, “Higgs-strahlung boson production in the presence of a circularly polarized laser field”, Laser Phys. Lett. **18**, 076002 (2021).

[92] S. J. Müller, C. H. Keitel, and C. Müller, “Higgs Boson Creation in Laser-Boosted Lepton Collisions”, Phys. Lett. B **730**, 161–165 (2014).

[93] M Baouahi, M Ouali, M Jakha, S Mouslih, Y Attaourti, B Manaut, S Taj, and R Benbrik, “Laser-assisted kaon decay and cpt symmetry violation”, Laser Physics Letters **18**, 106001 (2021).

[94] M. Ouali, M. Ouhammou, Y. Mekaoui, S. Taj, and B. Manaut, “Z-boson production via the weak process e+e→+ in the presence of a circularly polarized laser field”, Chinese Journal of Physics **77**, 1182–1196 (2022).

[95] H. Gies and R. Shaisultanov, “On the axial current in an electromagnetic field and low-energy neutrino - photon interactions”, Phys. Rev. D **62**, 073003 (2000).

[96] H. Gies and R. Shaisultanov, “Neutrino interactions with a weak slowly varying electromagnetic field”, Phys. Lett. B **480**, 129–134 (2000).

[97] S. Meuren, C. H. Keitel, and A. Di Piazza, “Nonlinear neutrino-photon interactions inside strong laser pulses”, JHEP **06**, 127 (2015).

[98]M. Formanek, S. Evans, J. Rafelski, A. Steinmetz, and C.-T. Yang, “Strong fields and neutral particle magnetic moment dynamics”, Plasma Physics and Controlled Fusion **60**, 074006 (2018).

[99]M. Dvornikov, “Spin-flavor oscillations of dirac neutrinos in a plane electromagnetic wave”, Phys. Rev. D **98**, 075025 (2018).

[100]M. Dvornikov, “Spin-flavor oscillations of dirac neutrinos in matter under the influence of a plane electromagnetic wave”, Phys. Rev. D **99**, 035027 (2019).

[101]M. Dvornikov, “Neutrino spin oscillations in external fields in curved spacetime”, Phys. Rev. D **99**, 116021 (2019).

[102]D. Kharzeev, K. Landsteiner, A. Schmitt, and H.-U. Yee, eds., *Strongly interacting matter in magnetic fields*, en, 2013th ed., Lecture notes in physics (Springer, Berlin, Germany, May 2013).

[103]K. Hattori and X.-G. Huang, “Novel quantum phenomena induced by strong magnetic fields in heavy-ion collisions”, Nuclear Science and Techniques **28**, 26 (2017).

[104]J. Berges, M. P. Heller, A. Mazeliauskas, and R. Venugopalan, “Qcd thermalization: ab initio approaches and interdisciplinary connections”, Rev. Mod. Phys. **93**, 035003 (2021).

[105]X.-G. Huang, “Electromagnetic fields and anomalous transports in heavy-ion collisions—a pedagogical review”, Reports on Progress in Physics **79**, 076302 (2016).

[106]K. Fukushima, “Evolution to the quark–gluon plasma”, Reports on Progress in Physics **80**, 022301 (2016).

[107]K. Fukushima, “Extreme matter in electromagnetic fields and rotation”, Progress in Particle and Nuclear Physics **107**, 167–199 (2019).

[108]F. Gelis, “Some aspects of the theory of heavy ion collisions”, Reports on Progress in Physics **84**, 056301 (2021).

[109]Z. Bern, J. J. Carrasco, M. Chiodaroli, H. Johansson, and R. Roiban, *The duality between color and kinematics and its applications*, 2019.

[110]C. D. White, “Double copy—from optics to quantum gravity: tutorial”, Journal of the Optical Society of America B **38**, 3319 (2021).

[111]A. G. Cohen and S. L. Glashow, *A lorentz-violating origin of neutrino mass?*, 2006.

[112]A. G. Cohen and S. L. Glashow, “Very special relativity”, Phys. Rev. Lett. **97**, 021601 (2006).

[113]A. Ilderton, “Very special relativity as a background field theory”, Phys. Rev. D **94**, 045019 (2016).

[114]P. Zhang, S. S. Bulanov, D. Seipt, A. V. Arefiev, and A. G. R. Thomas, “Relativistic plasma physics in supercritical fields”, Physics of Plasmas **27**, 050601 (2020).

[115]G. Brodin and J. Zamanian, “Quantum kinetic theory of plasmas”, Reviews of Modern Plasma Physics **6**, 4 (2022).

[116]G. Fauth, J. Berges, and A. Di Piazza, “Collisional strong-field qed kinetic equations from first principles”, Phys. Rev. D **104**, 036007 (2021).

[117]A. Ilderton and G. Torgrimsson, “Radiation reaction in strong field qed”, Physics Letters B **725**, 481–486 (2013).

---

[118] T. G. Blackburn, C. P. Ridgers, J. G. Kirk, and A. R. Bell, "Quantum radiation reaction in laser–electron-beam collisions", Phys. Rev. Lett. **112**, 015001 (2014).

[119] N. Neitz and A. Di Piazza, "Stochasticity effects in quantum radiation reaction", Phys. Rev. Lett. **111**, 054802 (2013).

[120] C. P. Ridgers, T. G. Blackburn, D. Del Sorbo, L. E. Bradley, C. Slade-Lowther, C. D. Baird, S. P. D. Mangles, P. McKenna, M. Marklund, C. D. Murphy, and et al., "Signatures of quantum effects on radiation reaction in laser–electron-beam collisions", Journal of Plasma Physics **83**, 715830502 (2017).

[121] M. Vranic, T. Grismayer, R. A. Fonseca, and L. O. Silva, "Quantum radiation reaction in head-on laser-electron beam interaction", New Journal of Physics **18**, 073035 (2016).

[122] F. Niel, C. Riconda, F. Amiranoff, R. Duclous, and M. Grech, "From quantum to classical modeling of radiation reaction: a focus on stochasticity effects", Phys. Rev. E **97**, 043209 (2018).

[123] A. V. Bashinov, A. V. Kim, and A. M. Sergeev, "Impact of quantum effects on relativistic electron motion in a chaotic regime", Phys. Rev. E **92**, 043105 (2015).

[124] C. S. Shen and D. White, "Energy straggling and radiation reaction for magnetic bremsstrahlung", Phys. Rev. Lett. **28**, 455–459 (1972).

[125] T. G. Blackburn, C. P. Ridgers, J. G. Kirk, and A. R. Bell, "Quantum radiation reaction in laser–electron-beam collisions", Phys. Rev. Lett. **112**, 015001 (2014).

[126] C. N. Harvey, A. Gonoskov, A. Ilderton, and M. Marklund, "Quantum quenching of radiation losses in short laser pulses", Phys. Rev. Lett. **118**, 105004 (2017).

[127] C. N. Harvey, A. Gonoskov, A. Ilderton, and M. Marklund, "Quantum quenching of radiation losses in short laser pulses", Phys. Rev. Lett. **118**, 105004 (2017).

[128] D. A. Burton and A. Noble, "Aspects of electromagnetic radiation reaction in strong fields", Contemporary Physics **55**, 110–121 (2014).

[129] Y. B. Zel'dovich, "Interaction of free electrons with electromagnetic radiation", Soviet Physics Uspekhi **18**, 79 (1975).

[130] L. L. Ji, A. Pukhov, I. Y. Kostyukov, B. F. Shen, and K. Akli, "Radiation-reaction trapping of electrons in extreme laser fields", Phys. Rev. Lett. **112**, 145003 (2014).

[131] J. G. Kirk, A. R. Bell, and I Arka, "Pair production in counter-propagating laser beams", Plasma Physics and Controlled Fusion **51**, 085008 (2009).

[132] A. Gonoskov, A. Bashinov, I. Gonoskov, C. Harvey, A. Ilderton, A. Kim, M. Marklund, G. Mourou, and A. Sergeev, "Anomalous radiative trapping in laser fields of extreme intensity", Phys. Rev. Lett. **113**, 014801 (2014).

[133] M. Jirka, O. Klimo, S. V. Bulanov, T. Z. Esirkepov, E. Gelfer, S. S. Bulanov, S. Weber, and G. Korn, "Electron dynamics and γ and e^-e^+ production by colliding laser pulses", Phys. Rev. E **93**, 023207 (2016).

[134] A. R. Bell and J. G. Kirk, "Possibility of prolific pair production with high-power lasers", Phys. Rev. Lett. **101**, 200403 (2008).

[135] S. S. Bulanov, V. D. Mur, N. B. Narozhny, J. Nees, and V. S. Popov, "Multiple colliding electromagnetic pulses: a way to lower the threshold of e^+e^- pair production from vacuum", Phys. Rev. Lett. **104**, 220404 (2010).

[136] A. M. Fedotov, N. B. Narozhny, G. Mourou, and G. Korn, “Limitations on the attainable intensity of high power lasers”, Phys. Rev. Lett. **105**, 080402 (2010).

[137] I. V. Sokolov, N. M. Naumova, J. A. Nees, and G. A. Mourou, “Pair creation in qed-strong pulsed laser fields interacting with electron beams”, Phys. Rev. Lett. **105**, 195005 (2010).

[138] S. S. Bulanov, C. B. Schroeder, E. Esarey, and W. P. Leemans, “Electromagnetic cascade in high-energy electron, positron, and photon interactions with intense laser pulses”, Phys. Rev. A **87**, 062110 (2013).

[139] A. Mironov, N. Narozhny, and A. Fedotov, “Collapse and revival of electromagnetic cascades in focused intense laser pulses”, Physics Letters A **378**, 3254–3257 (2014).

[140] M. Djebli, Zeitschrift für Naturforschung A **70**, 875–880 (2015).

[141] P. Goldreich and W. H. Julian, “Pulsar electrodynamics”, The Astrophysical Journal **157**, 869 (1969).

[142] R. Ruffini, G. Vereshchagin, and S.-S. Xue, “Electron–positron pairs in physics and astrophysics: from heavy nuclei to black holes”, Physics Reports **487**, 1–140 (2010).

[143] A. K. Harding and D. Lai, “Physics of strongly magnetized neutron stars”, Reports on Progress in Physics **69**, 2631 (2006).

[144] S. A. Olausen and V. M. Kaspi, “The mcgill magnetar catalog*”, The Astrophysical Journal Supplement Series **212**, 6 (2014).

[145] R. C. Duncan and C. Thompson, “Formation of very strongly magnetized neutron stars - implications for gamma-ray bursts”, The Astrophysical Journal **392**, L9 (1992).

[146] P. Goldreich and W. H. Julian, “Pulsar electrodynamics”, The Astrophysical Journal **157**, 869 (1969).

[147] P. A. Sturrock, “A model of pulsars”, The Astrophysical Journal **164**, 529 (1971).

[148] A. Y. Chen, F. Cruz, and A. Spitkovsky, “Filling the magnetospheres of weak pulsars”, The Astrophysical Journal **889**, 69 (2020).

[149] J. K. Daugherty and A. K. Harding, “Electromagnetic cascades in pulsars”, The Astrophysical Journal **252**, 337 (1982).

[150] A. N. Timokhin and A. K. Harding, “On the polar cap cascade pair multiplicity of young pulsars”, The Astrophysical Journal **810**, 144 (2015).

[151] S. L. Adler, “Photon splitting and photon dispersion in a strong magnetic field”, Annals of Physics **67**, 599–647 (1971).

[152] M. G. Baring and A. K. Harding, “Photon splitting and pair creation in highly magnetized pulsars”, The Astrophysical Journal **547**, 929 (2001).

[153] F. Cruz, T. Grismayer, and L. O. Silva, “Kinetic model of large-amplitude oscillations in neutron star pair cascades”, The Astrophysical Journal **908**, 149 (2021).

[154] K. Hirotani and H.-Y. Pu, “Energetic gamma radiation from rapidly rotating black holes”, The Astrophysical Journal **818**, 50 (2016).

[155] B. Crinquand, B. Cerutti, A. Philippov, K. Parfrey, and G. Dubus, “Multidimensional simulations of ergospheric pair discharges around black holes”, Phys. Rev. Lett. **124**, 145101 (2020).

[156] T. E. H. T. Collaboration, K. Akiyama, A. Alberdi, W. Alef, K. Asada, R. Azulay, A.-K. Baczko, D. Ball, M. Baloković, J. Barrett, D. Bintley, L. Blackburn, W. Boland, K. L. Bouman, G. C. Bower, M. Bremer, C. D. Brinkerink, R. Brissenden, S. Britzen, A. E. Broderick, D. Broguiere, T. Bronzwaer, D.-Y. Byun, J. E. Carlstrom, A. Chael, C. kwan Chan, S. Chatterjee, K. Chatterjee, M.-T. Chen, Y. Chen, I. Cho, P. Christian, J. E. Conway, J. M. Cordes, G. B. Crew, Y. Cui, J. Davelaar, M. D. Laurentis, R. Deane, J. Dempsey, G. Desvignes, J. Dexter, S. S. Doeleman, R. P. Eatough, H. Falcke, V. L. Fish, E. Fomalont, R. Fraga-Encinas, P. Friberg, C. M. Fromm, J. L. Gómez, P. Galison, C. F. Gammie, R. García, O. Gentaz, B. Georgiev, C. Goddi, R. Gold, M. Gu, M. Gurwell, K. Hada, M. H. Hecht, R. Hesper, L. C. Ho, P. Ho, M. Honma, C.-W. L. Huang, L. Huang, D. H. Hughes, S. Ikeda, M. Inoue, S. Issaoun, D. J. James, B. T. Jannuzi, M. Janssen, B. Jeter, W. Jiang, M. D. Johnson, S. Jorstad, T. Jung, M. Karami, R. Karuppusamy, T. Kawashima, G. K. Keating, M. Kettenis, J.-Y. Kim, J. Kim, J. Kim, M. Kino, J. Y. Koay, P. M. Koch, S. Koyama, M. Kramer, C. Kramer, T. P. Krichbaum, C.-Y. Kuo, T. R. Lauer, S.-S. Lee, Y.-R. Li, Z. Li, M. Lindqvist, K. Liu, E. Liuzzo, W.-P. Lo, A. P. Lobanov, L. Loinard, C. Lonsdale, R.-S. Lu, N. R. MacDonald, J. Mao, S. Markoff, D. P. Marrone, A. P. Marscher, I. Martí-Vidal, S. Matsushita, L. D. Matthews, L. Medeiros, K. M. Menten, Y. Mizuno, I. Mizuno, J. M. Moran, K. Moriyama, M. Moscibrodzka, C. Muller, H. Nagai, N. M. Nagar, M. Nakamura, R. Narayan, G. Narayanan, I. Natarajan, R. Neri, C. Ni, A. Noutsos, H. Okino, H. Olivares, T. Oyama, F. Özel, D. C. M. Palumbo, N. Patel, U.-L. Pen, D. W. Pesce, V. Piétu, R. Plambeck, A. PopStefanija, O. Porth, B. Prather, J. A. Preciado-López, D. Psaltis, H.-Y. Pu, V. Ramakrishnan, R. Rao, M. G. Rawlings, A. W. Raymond, L. Rezzolla, B. Ripperda, F. Roelofs, A. Rogers, E. Ros, M. Rose, A. Roshanineshat, H. Rottmann, A. L. Roy, C. Ruszczyk, B. R. Ryan, K. L. J. Rygl, S. Sánchez, D. Sánchez-Arguelles, M. Sasada, T. Savolainen, F. P. Schloerb, K.-F. Schuster, L. Shao, Z. Shen, D. Small, B. W. Sohn, J. SooHoo, F. Tazaki, P. Tiede, R. P. J. Tilanus, M. Titus, K. Toma, P. Torne, T. Trent, S. Trippe, S. Tsuda, I. van Bemmel, H. J. van Langevelde, D. R. van Rossum, J. Wagner, J. Wardle, J. Weintroub, N. Wex, R. Wharton, M. Wielgus, G. N. Wong, Q. Wu, A. Young, K. Young, Z. Younsi, F. Yuan, Y.-F. Yuan, J. A. Zensus, G. Zhao, S.-S. Zhao, Z. Zhu, J. Anczarski, F. K. Baganoff, A. Eckart, J. R. Farah, D. Haggard, Z. Meyer-Zhao, D. Michalik, A. Nadolski, J. Neilsen, H. Nishioka, M. A. Nowak, N. Pradel, R. A. Primiani, K. Souccar, L. Vertatschitsch, P. Yamaguchi, and S. Zhang, "First m87 event horizon telescope results. v. physical origin of the asymmetric ring", The Astrophysical Journal Letters **875**, L5 (2019).

[157] R. P. Mignani, V. Testa, D. GonzÃ¡lez Caniulef, R. Taverna, R. Turolla, S. Zane, and K. Wu, "Evidence for vacuum birefringence from the first optical-polarimetry measurement of the isolated neutron star RXÂ J1856.5â3754", Monthly Notices of the Royal Astronomical Society **465**, 492–500 (2016).

[158] L. M. Capparelli, A. Damiano, L. Maiani, and A. D. Polosa, "A note on polarized light from magnetars", The European Physical Journal C **77**, 754 (2017).

[159] CERN, *Cern yellow reports: monographs, vol 2 (2018): the compact linear e+e collider (clic) : 2018 summary report*, en, 1970.

[160] CERN, *Cern yellow reports: school proceedings, vol 3 (2017): proceedings of the cas-cern accelerator school on intensity limitations in particle beams*, en, 2017.

[161] F. Del Gaudio, T. Grismayer, R. A. Fonseca, W. B. Mori, and L. O. Silva, “Bright γ rays source and nonlinear breit-wheeler pairs in the collision of high density particle beams”, Phys. Rev. Accel. Beams **22**, 023402 (2019).

[162] P. Chen and K. Yokoya, “Disruption effects from the interaction of round e^+e^- beams”, Phys. Rev. D **38**, 987–1000 (1988).

[163] R. Hollebeek, “Disruption limits for linear colliders”, Nuclear Instruments and Methods **184**, 333–347 (1981).

[164] R. Blankenbecler and S. D. Drell, “Quantum treatment of beamstrahlung”, Phys. Rev. D **36**, 277–288 (1987).

[165] R. J. Noble, “Beamstrahlung from colliding electron-positron beams with negligible disruption”, Nuclear Instruments and Methods in Physics Research Section A: Accelerators, Spectrometers, Detectors and Associated Equipment **256**, 427–433 (1987).

[166] P. Chen and V. I. Telnov, “Coherent pair creation in linear colliders”, Phys. Rev. Lett. **63**, 1796–1799 (1989).

[167] T. Behnke, J. E. Brau, B. Foster, J. Fuster, M. Harrison, J. M. Paterson, M. Peskin, M. Stanitzki, N. Walker, and H. Yamamoto, *The international linear collider technical design report - volume 1: executive summary*, 2013.

[168] R. Blankenbecler and S. D. Drell, “Quantum beamstrahlung: prospects for a photon-photon collider”, Phys. Rev. Lett. **61**, 2324–2327 (1988).

[169] V. Yakimenko, S. Meuren, F. Del Gaudio, C. Baumann, A. Fedotov, F. Fiuza, T. Grismayer, M. J. Hogan, A. Pukhov, L. O. Silva, and G. White, “Prospect of studying nonperturbative qed with beam-beam collisions”, Phys. Rev. Lett. **122**, 190404 (2019).

[170] C. Bula, K. T. McDonald, E. J. Prebys, C. Bamber, S. Boege, T. Kotseroglou, A. C. Melissinos, D. D. Meyerhofer, W. Ragg, D. L. Burke, R. C. Field, G. Horton-Smith, A. C. Odian, J. E. Spencer, D. Walz, S. C. Berridge, W. M. Bugg, K. Shmakov, and A. W. Weidemann, “Observation of nonlinear effects in compton scattering”, Phys. Rev. Lett. **76**, 3116–3119 (1996).

[171] D. L. Burke, R. C. Field, G. Horton-Smith, J. E. Spencer, D. Walz, S. C. Berridge, W. M. Bugg, K. Shmakov, A. W. Weidemann, C. Bula, K. T. McDonald, E. J. Prebys, C. Bamber, S. J. Boege, T. Koffas, T. Kotseroglou, A. C. Melissinos, D. D. Meyerhofer, D. A. Reis, and W. Ragg, “Positron production in multiphoton light-by-light scattering”, Phys. Rev. Lett. **79**, 1626–1629 (1997).

[172] U. I. Uggerhøj, “The interaction of relativistic particles with strong crystalline fields”, Rev. Mod. Phys. **77**, 1131–1171 (2005).

[173] T. N. Wistisen, A. D. Piazza, H. V. Knudsen, and U. I. Uggerhøj, “Experimental evidence of quantum radiation reaction in aligned crystals”, Nature Communications **9** (2018).

[174] J. M. Cole, K. T. Behm, E. Gerstmayr, T. G. Blackburn, J. C. Wood, C. D. Baird, M. J. Duff, C. Harvey, A. Ilderton, A. S. Joglekar, K. Krushelnick, S. Kuschel, M. Marklund, P. McKenna, C. D. Murphy, K. Poder, C. P. Ridgers, G. M. Samarin, G. Sarri, D. R. Symes, A. G. R. Thomas, J. Warwick, M. Zepf, Z. Najmudin, and S. P. D. Mangles, “Experimental evidence of radiation reaction in the collision of a high-intensity laser pulse with a laser-wakefield accelerated electron beam”, Phys. Rev. X **8**, 011020 (2018).

---

[175] K. Poder, M. Tamburini, G. Sarri, A. Di Piazza, S. Kuschel, C. D. Baird, K. Behm, S. Bohlen, J. M. Cole, D. J. Corvan, M. Duff, E. Gerstmayr, C. H. Keitel, K. Krushelnick, S. P. D. Mangles, P. McKenna, C. D. Murphy, Z. Najmudin, C. P. Ridgers, G. M. Samarin, D. R. Symes, A. G. R. Thomas, J. Warwick, and M. Zepf, “Experimental signatures of the quantum nature of radiation reaction in the field of an ultraintense laser”, Phys. Rev. X **8**, 031004 (2018).

[176] E. B. Aleksandrov, A. A. Anselm, and A. N. Moskalev, “Double refraction of a vacuum in a field of intense laser radiation”, Zhurnal Eksperimentalnoi i Teoreticheskoi Fiziki **89**, 1181–1189 (1985).

[177] G. Kotkin and V. Serbo, “Polarization of high-energy γ-quanta traversing a bunch of polarized laser photons”, Physics Letters B **413**, 122–129 (1997).

[178] A. N. Luiten and J. C. Petersen, “Ultrafast resonant polarization interferometry: towards the first direct detection of vacuum polarization”, Phys. Rev. A **70**, 033801 (2004).

[179] A. N. Luiten and J. C. Petersen, “Detection of vacuum birefringence using intense laser pulses”, Physics Letters A **330**, 429–434 (2004).

[180] T. Heinzl, B. Liesfeld, K.-U. Amthor, H. Schwoerer, R. Sauerbrey, and A. Wipf, “On the observation of vacuum birefringence”, Optics Communications **267**, 318–321 (2006).

[181] A. Di Piazza, K. Z. Hatsagortsyan, and C. H. Keitel, “Light diffraction by a strong standing electromagnetic wave”, Phys. Rev. Lett. **97**, 083603 (2006).

[182] F. Karbstein, “Vacuum birefringence in the head-on collision of x-ray free-electron laser and optical high-intensity laser pulses”, Phys. Rev. D **98**, 056010 (2018).

[183] V. Dinu, T. Heinzl, A. Ilderton, M. Marklund, and G. Torgrimsson, “Vacuum refractive indices and helicity flip in strong-field QED”, Phys. Rev. D **89**, 125003 (2014).

[184] V. Dinu, T. Heinzl, A. Ilderton, M. Marklund, and G. Torgrimsson, “Photon polarization in light-by-light scattering: finite size effects”, Phys. Rev. D **90**, 045025 (2014).

[185] F. Karbstein, H. Gies, M. Reuter, and M. Zepf, “Vacuum birefringence in strong inhomogeneous electromagnetic fields”, Phys. Rev. D **92**, 071301 (2015).

[186] A. Ilderton and M. Marklund, “Prospects for studying vacuum polarisation using dipole and synchrotron radiation”, Journal of Plasma Physics **82**, 655820201 (2016).

[187] F. Karbstein and C. Sundqvist, “Probing vacuum birefringence using x-ray free electron and optical high-intensity lasers”, Phys. Rev. D **94**, 013004 (2016).

[188] H.-P. Schlenvoigt, T. Heinzl, U. Schramm, T. E. Cowan, and R. Sauerbrey, “Detecting vacuum birefringence with x-ray free electron lasers and high-power optical lasers: a feasibility study”, Physica Scripta **91**, 023010 (2016).

[189] Y. Nakamiya and K. Homma, “Probing vacuum birefringence under a high-intensity laser field with gamma-ray polarimetry at the gev scale”, Phys. Rev. D **96**, 053002 (2017).

[190] B. King and N. Elkina, “Vacuum birefringence in high-energy laser-electron collisions”, Phys. Rev. A **94**, 062102 (2016).

[191] S. Bragin, S. Meuren, C. H. Keitel, and A. Di Piazza, “High-energy vacuum birefringence and dichroism in an ultrastrong laser field”, Phys. Rev. Lett. **119**, 250403 (2017).

[192] S. Ataman, “Vacuum birefringence detection in all-optical scenarios”, Phys. Rev. A **97**, 063811 (2018).

[193] S. I. Tzenov, K. M. Spohr, and K. A. Tanaka, “Dispersion properties, nonlinear waves and birefringence in classical nonlinear electrodynamics”, Journal of Physics Communications **4**, 025006 (2020).

[194] S. Robertson, A. Mailliet, X. Sarazin, F. m. c. Couchot, E. Baynard, J. Demailly, M. Pittman, A. Djannati-Ataï, S. Kazamias, and M. Urban, “Experiment to observe an optically induced change of the vacuum index”, Phys. Rev. A **103**, 023524 (2021).

[195] M. Sangal, C. H. Keitel, and M. Tamburini, *Observing light-by-light scattering in vacuum with an asymmetric photon collider*, 2021.

[196] T Grismayer, R Torres, P Carneiro, F Cruz, R. A. Fonseca, and L. O. Silva, “Quantum electrodynamics vacuum polarization solver”, New Journal of Physics **23**, 095005 (2021).

[197] N. B. Narozhny and A. M. Fedotov, “Creation of electron-positron plasma with superstrong laser field”, The European Physical Journal Special Topics **223**, 1083–1092 (2014).

[198] N. B. Narozhny, S. S. Bulanov, V. D. Mur, and V. S. Popov, “On e+epair production by colliding electromagnetic pulses”, Journal of Experimental and Theoretical Physics Letters **80**, 382–385 (2004).

[199] S. S. Bulanov, N. B. Narozhny, V. D. Mur, and V. S. Popov, “Electron-positron pair production by electromagnetic pulses”, Journal of Experimental and Theoretical Physics **102**, 9–23 (2006).

[200] S. S. Bulanov, N. B. Narozhny, V. D. Mur, and V. S. Popov, “Electron-positron pair production by electromagnetic pulses”, Journal of Experimental and Theoretical Physics **102**, 9–23 (2006).

[201] A. R. Bell and J. G. Kirk, “Possibility of prolific pair production with high-power lasers”, Phys. Rev. Lett. **101**, 200403 (2008).

[202] A. M. Fedotov, N. B. Narozhny, G. Mourou, and G. Korn, “Limitations on the attainable intensity of high power lasers”, Phys. Rev. Lett. **105**, 080402 (2010).

[203] S. S. Bulanov, T. Z. Esirkepov, A. G. R. Thomas, J. K. Koga, and S. V. Bulanov, “Schwinger limit attainability with extreme power lasers”, Phys. Rev. Lett. **105**, 220407 (2010).

[204] C. Bamber, S. J. Boege, T. Koffas, T. Kotseroglou, A. C. Melissinos, D. D. Meyerhofer, D. A. Reis, W. Ragg, C. Bula, K. T. McDonald, E. J. Prebys, D. L. Burke, R. C. Field, G. Horton-Smith, J. E. Spencer, D. Walz, S. C. Berridge, W. M. Bugg, K. Shmakov, and A. W. Weidemann, “Studies of nonlinear qed in collisions of 46.6 gev electrons with intense laser pulses”, Phys. Rev. D **60**, 092004 (1999).

[205] H. Abramowicz, U. Acosta, M. Altarelli, R. Aßmann, Z. Bai, T. Behnke, Y. Benhammou, T. Blackburn, S. Boogert, O. Borysov, M. Borysova, R. Brinkmann, M. Bruschi, F. Burkart, K. Büßer, N. Cavanagh, O. Davidi, W. Decking, U. Dosselli, N. Elkina, A. Fedotov, M. Firlej, T. Fiutowski, K. Fleck, M. Gostkin, C. Grojean, J. Hallford, H. Harsh, A. Hartin, B. Heinemann, T. Heinzl, L. Helary, M. Hoffmann, S. Huang, X. Huang, M. Idzik, A. Ilderton, R. Jacobs, B. Kämpfer, B. King, H. Lahno, A. Levanon, A. Levy, I. Levy, J. List, W. Lohmann, T. Ma, A. J. Macleod, V. Malka, F. Meloni, A. Mironov, M. Morandin, J. Moron, E. Negodin, G. Perez, I. Pomerantz, R. Pöschl, R. Prasad, F. Quéré, A. Ringwald, C. Rödel, S. Rykovanov, F. Salgado, A. Santra, G. Sarri, A. Sävert, A. Sbrizzi, S. Schmitt, U. Schramm, S. Schuwalow, D. Seipt, L. Shaimerdenova, M. Shchedrolosiev, M. Skakunov, Y. Soreq, M. Streeter, K. Swientek, N. T. Hod, S. Tang, T. Teter, D. Thoden, A. I. Titov, O. Tolbanov, G. Torgrimsson, A. Tyazhev, M. Wing, M. Zanetti, A. Zarubin, K. Zeil, M. Zepf, and A. Zhemchukov, "Conceptual design report for the luxe experiment", The European Physical Journal Special Topics **230**, 2445–2560 (2021).

[206] K. Krajewska, "Frequency scaling law for nonlinear compton and thomson scattering: relevance of spin and polarization effects", Phys. Rev. A **90**, 052117 (2014).

[207] A. I. Titov, B. Kämpfer, H. Takabe, and A. Hosaka, "Breit-wheeler process in very short electromagnetic pulses", Phys. Rev. A **87**, 042106 (2013).

[208] A. I. Titov, H. Takabe, B. Kämpfer, and A. Hosaka, "Enhanced subthreshold e^+e^- production in short laser pulses", Phys. Rev. Lett. **108**, 240406 (2012).

[209] S. Tang, M. A. Bake, H.-Y. Wang, and B.-S. Xie, "Qed cascade induced by a high-energy γ photon in a strong laser field", Phys. Rev. A **89**, 022105 (2014).

[210] T. G. Blackburn and M Marklund, "Nonlinear breit–wheeler pair creation with bremsstrahlung rays", Plasma Physics and Controlled Fusion **60**, 054009 (2018).

[211] A. Hartin, A. Ringwald, and N. Tapia, "Measuring the boiling point of the vacuum of quantum electrodynamics", Phys. Rev. D **99**, 036008 (2019).

[212] A. J. Gonsalves, K. Nakamura, J. Daniels, C. Benedetti, C. Pieronek, T. C. H. de Raadt, S. Steinke, J. H. Bin, S. S. Bulanov, J. van Tilborg, C. G. R. Geddes, C. B. Schroeder, C. Tóth, E. Esarey, K. Swanson, L. Fan-Chiang, G. Bagdasarov, N. Bobrova, V. Gasilov, G. Korn, P. Sasorov, and W. P. Leemans, "Petawatt laser guiding and electron beam acceleration to 8 gev in a laser-heated capillary discharge waveguide", Phys. Rev. Lett. **122**, 084801 (2019).

[213] S. Kneip, S. R. Nagel, S. F. Martins, S. P. D. Mangles, C. Bellei, O. Chekhlov, R. J. Clarke, N. Delerue, E. J. Divall, G. Doucas, K. Ertel, F. Fiuza, R. Fonseca, P. Foster, S. J. Hawkes, C. J. Hooker, K. Krushelnick, W. B. Mori, C. A. J. Palmer, K. T. Phuoc, P. P. Rajeev, J. Schreiber, M. J. V. Streeter, D. Urner, J. Vieira, L. O. Silva, and Z. Najmudin, "Near-gev acceleration of electrons by a nonlinear plasma wave driven by a self-guided laser pulse", Phys. Rev. Lett. **103**, 035002 (2009).

[214] W. P. Leemans, A. J. Gonsalves, H.-S. Mao, K. Nakamura, C. Benedetti, C. B. Schroeder, C. Tóth, J. Daniels, D. E. Mittelberger, S. S. Bulanov, J.-L. Vay, C. G. R. Geddes, and E. Esarey, "Multi-gev electron beams from capillary-discharge-guided subpetawatt laser pulses in the self-trapping regime", Phys. Rev. Lett. **113**, 245002 (2014).

---

[215] X. Wang, R. Zgadzaj, N. Fazel, Z. Li, S. A. Yi, X. Zhang, W. Henderson, Y. Y. Chang, R. Korzekwa, H. E. Tsai, C. H. Pai, H. Quevedo, G. Dyer, E. Gaul, M. Martinez, A. C. Bernstein, T. Borger, M. Spinks, M. Donovan, V. Khudik, G. Shvets, T. Ditmire, and M. C. Downer, "Quasi-monoenergetic laser-plasma acceleration of electrons to 2 gev", Nature Communications **4**, 1988 (2013).

[216] M. Schnell, A. Sävert, B. Landgraf, M. Reuter, M. Nicolai, O. Jäckel, C. Peth, T. Thiele, O. Jansen, A. Pukhov, O. Willi, M. C. Kaluza, and C. Spielmann, "Deducing the electron-beam diameter in a laser-plasma accelerator using x-ray betatron radiation", Phys. Rev. Lett. **108**, 075001 (2012).

[217] S. Bulanov, T. Esirkepov, Y. Hayashi, M. Kando, H. Kiriyama, J. Koga, K. Kondo, H. Kotaki, A. Pirozhkov, S. Bulanov, A. Zhidkov, P. Chen, D. Neely, Y. Kato, N. Narozhny, and G. Korn, "On the design of experiments for the study of extreme field limits in the interaction of laser with ultrarelativistic electron beam", Nuclear Instruments and Methods in Physics Research Section A: Accelerators, Spectrometers, Detectors and Associated Equipment **660**, 31–42 (2011).

[218] F. Albert and A. G. R. Thomas, "Applications of laser wakefield accelerator-based light sources", Plasma Physics and Controlled Fusion **58**, 103001 (2016).

[219] G. Sarri, W. Schumaker, A. Di Piazza, M. Vargas, B. Dromey, M. E. Dieckmann, V. Chvykov, A. Maksimchuk, V. Yanovsky, Z. H. He, B. X. Hou, J. A. Nees, A. G. R. Thomas, C. H. Keitel, M. Zepf, and K. Krushelnick, "Table-top laser-based source of femtosecond, collimated, ultrarelativistic positron beams", Phys. Rev. Lett. **110**, 255002 (2013).

[220] T. G. Blackburn, A Ilderton, M Marklund, and C. P. Ridgers, "Reaching supercritical field strengths with intense lasers", New Journal of Physics **21**, 053040 (2019).

[221] J. Magnusson, A. Gonoskov, M. Marklund, T. Z. Esirkepov, J. K. Koga, K. Kondo, M. Kando, S. V. Bulanov, G. Korn, and S. S. Bulanov, "Laser-particle collider for multi-gev photon production", Phys. Rev. Lett. **122**, 254801 (2019).

[222] J. Magnusson, A. Gonoskov, M. Marklund, T. Z. Esirkepov, J. K. Koga, K. Kondo, M. Kando, S. V. Bulanov, G. Korn, C. G. R. Geddes, C. B. Schroeder, E. Esarey, and S. S. Bulanov, "Multiple colliding laser pulses as a basis for studying high-field high-energy physics", Phys. Rev. A **100**, 063404 (2019).

[223] I. Gonoskov, A. Aiello, S. Heugel, and G. Leuchs, "Dipole pulse theory: maximizing the field amplitude from 4π focused laser pulses", Phys. Rev. A **86**, 053836 (2012).

[224] C. Olofsson and A. Gonoskov, *Bi-dipole wave: optimum for attaining extreme regimes at matter-light colliders*, arXiv:2202.08251, 2022.

[225] I. Bassett, "Limit to concentration by focusing", Optica Acta: International Journal of Optics **33**, 279–286 (1986).

[226] A. Gonoskov, I. Gonoskov, C. Harvey, A. Ilderton, A. Kim, M. Marklund, G. Mourou, and A. Sergeev, "Probing nonperturbative qed with optimally focused laser pulses", Phys. Rev. Lett. **111**, 060404 (2013).

[227] E. G. Gelfer, A. A. Mironov, A. M. Fedotov, V. F. Bashmakov, E. N. Nerush, I. Y. Kostyukov, and N. B. Narozhny, "Optimized multibeam configuration for observation of qed cascades", Phys. Rev. A **92**, 022113 (2015).

---

[228] A. Gonoskov, A. Bashinov, S. Bastrakov, E. Efimenko, A. Ilderton, A. Kim, M. Marklund, I. Meyerov, A. Muraviev, and A. Sergeev, "Ultrabright gev photon source via controlled electromagnetic cascades in laser-dipole waves", Phys. Rev. X **7**, 041003 (2017).

[229] E. S. Efimenko, A. V. Bashinov, S. I. Bastrakov, A. A. Gonoskov, A. A. Muraviev, I. B. Meyerov, A. V. Kim, and A. M. Sergeev, "Extreme plasma states in laser-governed vacuum breakdown", Scientific Reports **8**, 2329 (2018).

[230] A. A. Muraviev, S. I. Bastrakov, A. V. Bashinov, A. A. Gonoskov, E. S. Efimenko, A. V. Kim, I. B. Meyerov, and A. M. Sergeev, "Generation of current sheets and giant quasistatic magnetic fields at the ionization of vacuum in extremely strong light fields", JETP Letters **102**, 148–153 (2015).

[231] E. S. Efimenko, A. V. Bashinov, S. I. Bastrakov, A. A. Gonoskov, A. A. Muraviev, I. B. Meyerov, A. V. Kim, and A. M. Sergeev, "Extreme plasma states in laser-governed vacuum breakdown", Scientific Reports **8**, 2329 (2018).

[232] I. Mukhin, A. Soloviev, E. Perevezentsev, A. Shaykin, V. Ginzburg, I. Kuzmin, M. Mart'yanov, I. Shaikin, A. Kuzmin, S. Mironov, I. Yakovlev, and E. Khazanov, "Design of the front-end system for a subexawatt laser of the xcels facility", Quantum Electronics **51**, 759 (2021).

[233] K. Landecker, "Possibility of frequency multiplication and wave amplification by means of some relativistic effects", Phys. Rev. **86**, 852–855 (1952).

[234] A Einstein, "Zu r elektrodynamik bewegter körper", Annalen der Physik. IV. Folge **17**, 891 (1905).

[235] S. V. Bulanov, T. Esirkepov, and T. Tajima, "Light intensification towards the schwinger limit", Phys. Rev. Lett. **91**, 085001 (2003).

[236] N. H. Matlis, S. Reed, S. S. Bulanov, V. Chvykov, G. Kalintchenko, T. Matsuoka, P. Rousseau, V. Yanovsky, A. Maksimchuk, S. Kalmykov, G. Shvets, and M. C. Downer, "Snapshots of laser wakefields", Nature Physics **2**, 749–753 (2006).

[237] S. V. Bulanov, T. Z. Esirkepov, M. Kando, A. S. Pirozhkov, and N. N. Rozanov, "Relativistic mirrors in plasma - new results and prospects", Success physical Sciences **183**, 449–486 (2013).

[238] S. S. Bulanov, A. Maksimchuk, C. B. Schroeder, A. G. Zhidkov, E. Esarey, and W. P. Leemans, "Relativistic spherical plasma waves", Physics of Plasmas **19**, 020702 (2012).

[239] M. Kando, Y. Fukuda, A. S. Pirozhkov, J. Ma, I. Daito, L.-M. Chen, T. Z. Esirkepov, K. Ogura, T. Homma, Y. Hayashi, H. Kotaki, A. Sagisaka, M. Mori, J. K. Koga, H. Daido, S. V. Bulanov, T. Kimura, Y. Kato, and T. Tajima, "Demonstration of laser-frequency upshift by electron-density modulations in a plasma wakefield", Phys. Rev. Lett. **99**, 135001 (2007).

[240] M. Kando, T. Z. Esirkepov, J. K. Koga, A. S. Pirozhkov, and S. V. Bulanov, "Coherent, short-pulse x-ray generation via relativistic flying mirrors", Quantum Beam Science **2**, 052117 (2018).

[241] A. S. Pirozhkov, J. Ma, M. Kando, T. Z. Esirkepov, Y. Fukuda, L.-M. Chen, I. Daito, K. Ogura, T. Homma, Y. Hayashi, H. Kotaki, A. Sagisaka, M. Mori, J. K. Koga, T. Kawachi, H. Daido, S. V. Bulanov, T. Kimura, Y. Kato, and T. Tajima, "Frequency multiplication of light back-reflected from a relativistic wake wave", Physics of Plasmas **14**, 123106 (2007).

---

[242] S. S. Bulanov, T. Z. Esirkepov, A. G. R. Thomas, J. K. Koga, and S. V. Bulanov, "Schwinger limit attainability with extreme power lasers", Phys. Rev. Lett. **105**, 220407 (2010).

[243] D. Habs, M. Hegelich, J. Schreiber, M. Gross, A. Henig, D. Kiefer, and D. Jung, "Dense laser-driven electron sheets as relativistic mirrors for coherent production of brilliant x-ray and -ray beams", Applied Physics B **93**, 349–354 (2008).

[244] V. V. Kulagin, V. A. Cherepenin, M. S. Hur, and H. Suk, "Theoretical investigation of controlled generation of a dense attosecond relativistic electron bunch from the interaction of an ultrashort laser pulse with a nanofilm", Phys. Rev. Lett. **99**, 124801 (2007).

[245] J. Meyer-ter Vehn and H. C. Wu, "Coherent thomson backscattering from laser-driven relativistic ultra-thin electron layers", The European Physical Journal D **55**, 433–441 (2009).

[246] T. Z. Esirkepov, S. V. Bulanov, M. Kando, A. S. Pirozhkov, and A. G. Zhidkov, "Boosted high-harmonics pulse from a double-sided relativistic mirror", Phys. Rev. Lett. **103**, 025002 (2009).

[247] A. Macchi, M. Borghesi, and M. Passoni, "Ion acceleration by superintense laser-plasma interaction", Rev. Mod. Phys. **85**, 751–793 (2013).

[248] M. Tamburini, A. Di Piazza, T. V. Liseykina, and C. H. Keitel, "Plasma-based generation and control of a single few-cycle high-energy ultrahigh-intensity laser pulse", Phys. Rev. Lett. **113**, 025005 (2014).

[249] J.-L. Vay, I. Haber, and B. B. Godfrey, "A domain decomposition method for pseudo-spectral electromagnetic simulations of plasmas", Journal of Computational Physics **243**, 260–268 (2013).

[250] H. Vincenti and J.-L. Vay, "Detailed analysis of the effects of stencil spatial variations with arbitrary high-order finite-difference Maxwell solver", Computer Physics Communications **200**, 147–167 (2016).

[251] H. Vincenti and J.-L. Vay, "Ultrahigh-order maxwell solver with extreme scalability for electromagnetic pic simulations of plasmas", Computer Physics Communications **228**, 22–29 (2018).

[252] H. Kallala, J.-L. Vay, and H. Vincenti, "A generalized massively parallel ultra-high order fft-based maxwell solver", Computer Physics Communications **244**, 25–34 (2019).

[253] J.-L. Vay, A. Huebl, A. Almgren, L. D. Amorim, J. Bell, L. Fedeli, L. Ge, K. Gott, D. P. Grote, M. Hogan, R. Jambunathan, R. Lehe, A. Myers, C. Ng, M. Rowan, O. Shapoval, M. Thévenet, H. Vincenti, E. Yang, N. Zaïm, W. Zhang, Y. Zhao, and E. Zoni, "Modeling of a chain of three plasma accelerator stages with the warpx electromagnetic pic code on gpus", Physics of Plasmas **28**, 023105 (2021).

[254] A. Myers, A. Almgren, L. Amorim, J. Bell, L. Fedeli, L. Ge, K. Gott, D. Grote, M. Hogan, A. Huebl, R. Jambunathan, R. Lehe, C. Ng, M. Rowan, O. Shapoval, M. Thévenet, J.-L. Vay, H. Vincenti, E. Yang, N. Zaïm, W. Zhang, Y. Zhao, and E. Zoni, "Porting warpx to gpu-accelerated platforms", Parallel Computing **108**, 102833 (2021).

[255] H. Vincenti, M. Lobet, R. Lehe, R. Sasanka, and J.-L. Vay, "An efficient and portable simd algorithm for charge/current deposition in particle-in-cell codes", Computer Physics Communications **210**, 145–154 (2017).

[256] H. C. Kapteyn, M. M. Murnane, A. Szoke, and R. W. Falcone, “Prepulse energy suppression for high-energy ultrashort pulses using self-induced plasma shuttering”, Opt. Lett. **16**, 490–492 (1991).

[257] G. Doumy, F. Quéré, O. Gobert, M. Perdrix, P. Martin, P. Audebert, J. C. Gauthier, J.-P. Geindre, and T. Wittmann, “Complete characterization of a plasma mirror for the production of high-contrast ultraintense laser pulses”, Phys. Rev. E **69**, 026402 (2004).

[258] B. Dromey, S. Kar, M. Zepf, and P. Foster, “The plasma mirror—a subpicosecond optical switch for ultrahigh power lasers”, Review of Scientific Instruments **75**, 645–649 (2004).

[259] S. Kahaly, S. Monchocé, H. Vincenti, T. Dzelzainis, B. Dromey, M. Zepf, P. Martin, and F. Quéré, “Direct observation of density-gradient effects in harmonic generation from plasma mirrors”, Phys. Rev. Lett. **110**, 175001 (2013).

[260] L. Chopineau, A. Leblanc, G. Blaclard, A. Denoeud, M. Thévenet, J.-L. Vay, G. Bonnaud, P. Martin, H. Vincenti, and F. Quéré, “Identification of coupling mechanisms between ultraintense laser light and dense plasmas”, Phys. Rev. X **9**, 011050 (2019).

[261] F. Dollar, P. Cummings, V. Chvykov, L. Willingale, M. Vargas, V. Yanovsky, C. Zulick, A. Maksimchuk, A. G. R. Thomas, and K. Krushelnick, “Scaling high-order harmonic generation from laser-solid interactions to ultrahigh intensity”, Phys. Rev. Lett. **110**, 175002 (2013).

[262] C. Rödel, D. an der Brügge, J. Bierbach, M. Yeung, T. Hahn, B. Dromey, S. Herzer, S. Fuchs, A. G. Pour, E. Eckner, M. Behmke, M. Cerchez, O. Jäckel, D. Hemmers, T. Toncian, M. C. Kaluza, A. Belyanin, G. Pretzler, O. Willi, A. Pukhov, M. Zepf, and G. G. Paulus, “Harmonic generation from relativistic plasma surfaces in ultrasteep plasma density gradients”, Phys. Rev. Lett. **109**, 125002 (2012).

[263] C. Thaury, F. Quéré, J. P. Geindre, A. Levy, T. Ceccotti, P. Monot, M. Bougeard, F. Réau, P. d’Oliveira, P. Audebert, R. Marjoribanks, and P. Martin, “Plasma mirrors for ultrahigh-intensity optics”, Nature Physics **3**, 424–429 (2007).

[264] J. A. Wheeler, A. Borot, S. Monchocé, H. Vincenti, A. Ricci, A. Malvache, R. Lopez-Martens, and F. Quéré, “Attosecond lighthouses from plasma mirrors”, Nature Photonics **6**, 829–833 (2012).

[265] S. Monchocé, S. Kahaly, A. Leblanc, L. Videau, P. Combis, F. Réau, D. Garzella, P. D’Oliveira, P. Martin, and F. Quéré, “Optically controlled solid-density transient plasma gratings”, Phys. Rev. Lett. **112**, 145008 (2014).

[266] A. Denoeud, L. Chopineau, A. Leblanc, and F. Quéré, “Interaction of ultraintense laser vortices with plasma mirrors”, Phys. Rev. Lett. **118**, 033902 (2017).

[267] A. Leblanc, A. Denoeud, L. Chopineau, G. Mennerat, P. Martin, and F. Quéré, “Plasma holograms for ultrahigh-intensity optics”, Nature Physics **13**, 440–443 (2017).

[268] M. Thévenet, A. Leblanc, S. Kahaly, H. Vincenti, A. Vernier, F. Quéré, and J. Faure, “Vacuum laser acceleration of relativistic electrons using plasma mirror injectors”, Nature Physics **12**, 355–360 (2016).

[269] K. Ta Phuoc, S. Corde, C. Thaury, V. Malka, A. Tafzi, J. P. Goddet, R. C. Shah, S. Sebban, and A. Rousse, “All-optical compton gamma-ray source”, Nature Photonics **6**, 308–311 (2012).

---

[270] M. Nakatsutsumi, A. Kon, S. Buffechoux, P. Audebert, J. Fuchs, and R. Kodama, "Fast focusing of short-pulse lasers by innovative plasma optics toward extreme intensity", Opt. Lett. **35**, 2314–2316 (2010).

[271] A Kon, M Nakatsutsumi, S Buffechoux, Z. L. Chen, J Fuchs, Z Jin, and R Kodama, "Geometrical optimization of an ellipsoidal plasma mirror toward tight focusing of ultra-intense laser pulse", Journal of Physics: Conference Series **244**, 032008 (2010).

[272] S. V. Bulanov, N. M. Naumova, and F. Pegoraro, "Interaction of an ultrashort, relativistically strong laser pulse with an overdense plasma", Physics of Plasmas **1**, 745–757 (1994).

[273] T. G. Blackburn, A. A. Gonoskov, and M. Marklund, "Relativistically intense xuv radiation from laser-illuminated near-critical plasmas", Phys. Rev. A **98**, 023421 (2018).

[274] B. Svedung Wettervik, M. Marklund, and A. Gonoskov, "Physics of the laser-plasma interface in the relativistic regime of interaction", Physics of Plasmas **26**, 053101 (2019).

[275] A. Debayle, J. Sanz, and L. Gremillet, "Self-consistent theory of high-order harmonic generation by relativistic plasma mirror", Phys. Rev. E **92**, 053108 (2015).

[276] M. Cherednychek and A. Pukhov, "Analytical approach to high harmonics spectrum in the nanobunching regime", Physics of Plasmas **23**, 103301 (2016).

[277] B. Dromey, D. Adams, R. Hörlein, Y. Nomura, S. G. Rykovanov, D. C. Carroll, P. S. Foster, S. Kar, K. Markey, P. McKenna, D. Neely, M. Geissler, G. D. Tsakiris, and M. Zepf, "Diffraction-limited performance and focusing of high harmonics from relativistic plasmas", Nature Physics **5**, 146–152 (2009).

[278] B. Dromey, S. Kar, C. Bellei, D. C. Carroll, R. J. Clarke, J. S. Green, S. Kneip, K. Markey, S. R. Nagel, P. T. Simpson, L. Willingale, P. McKenna, D. Neely, Z. Najmudin, K. Krushelnick, P. A. Norreys, and M. Zepf, "Bright multi-kev harmonic generation from relativistically oscillating plasma surfaces", Phys. Rev. Lett. **99**, 085001 (2007).

[279] S. V. Bulanov, T. Z. Esirkepov, M Kando, A. S. Pirozhkov, and N. N. Rosanov, "Relativistic mirrors in plasmas. novel results and perspectives", Physics-Uspekhi **56**, 429 (2013).

[280] G. Blaclard, H. Vincenti, R. Lehe, and J. L. Vay, "Pseudospectral maxwell solvers for an accurate modeling of doppler harmonic generation on plasma mirrors with particle-in-cell codes", Phys. Rev. E **96**, 033305 (2017).

[281] H. Vincenti, L. Fedeli, A. Sainte-Marie, N. Zaïm, and F. Quéré, "Novel methods for approaching the schwinger limit at the focus of curved relativistic plasma mirrors driven by a PW-class laser", Phys. Rev. A **90**, 052117 (in preparation).

[282] A. A. Solodov, V. M. Malkin, and N. J. Fisch, "Limits for light intensification by reflection from relativistic plasma mirrors", Physics of Plasmas **13**, 093102 (2006).

[283] A. Lévy, T. Ceccotti, P. D'Oliveira, F. Réau, M. Perdrix, F. Quéré, P. Monot, M. Bougeard, H. Lagadec, P. Martin, J.-P. Geindre, and P. Audebert, "Double plasma mirror for ultrahigh temporal contrast ultraintense laser pulses", Opt. Lett. **32**, 310–312 (2007).

[284] H. Vincenti, S. Monchocé, S. Kahaly, G. Bonnaud, P. Martin, and F. Quéré, "Optical properties of relativistic plasma mirrors", Nature Communications **5**, 3403 (2014).

[285] A. Leblanc, S. Monchocé, C. Bourassin-Bouchet, S. Kahaly, and F. Quéré, “Ptychographic measurements of ultrahigh-intensity laser–plasma interactions”, Nature Physics **12**, 301–305 (2016).

[286] L. Chopineau, A. Denoeud, A. Leblanc, E. Porat, P. Martin, H. Vincenti, and F. Quéré, “Spatio-temporal characterization of attosecond pulses from plasma mirrors”, Nature Physics **17**, 968–973 (2021).

[287] A. Leblanc, S. Monchocé, H. Vincenti, S. Kahaly, J.-L. Vay, and F. Quéré, “Spatial properties of high-order harmonic beams from plasma mirrors: a ptychographic study”, Phys. Rev. Lett. **119**, 155001 (2017).

[288] M. Yeung, S. Rykovanov, J. Bierbach, L. Li, E. Eckner, S. Kuschel, A. Woldegeorgis, C. Rödel, A. Sävert, G. G. Paulus, M. Coughlan, B. Dromey, and M. Zepf, “Experimental observation of attosecond control over relativistic electron bunches with two-colour fields”, Nature Photonics **11**, 32–35 (2017).

[289] M. Yeung, J. Bierbach, E. Eckner, S. Rykovanov, S. Kuschel, A. Sävert, M. Förster, C. Rödel, G. G. Paulus, S. Cousens, M. Coughlan, B. Dromey, and M. Zepf, “Noncollinear polarization gating of attosecond pulse trains in the relativistic regime”, Phys. Rev. Lett. **115**, 193903 (2015).

[290] J. Nees, N. Naumova, E. Power, V. Yanovsky, I. Sokolov, A. Maksimchuk, S. W. Bahk, V. Chvykov, G. Kalintchenko, B. Hou, and G. Mourou, “Relativistic generation of isolated attosecond pulses: a different route to extreme intensity”, Journal of Modern Optics **52**, 305–319 (2005).

[291] S. V. Bulanov, T. Esirkepov, and T. Tajima, “Light intensification towards the schwinger limit”, Phys. Rev. Lett. **91**, 085001 (2003).

[292] M. Kando, A. S. Pirozhkov, K. Kawase, T. Z. Esirkepov, Y. Fukuda, H. Kiriyama, H. Okada, I. Daito, T. Kameshima, Y. Hayashi, H. Kotaki, M. Mori, J. K. Koga, H. Daido, A. Y. Faenov, T. Pikuz, J. Ma, L.-M. Chen, E. N. Ragozin, T. Kawachi, Y. Kato, T. Tajima, and S. V. Bulanov, “Enhancement of photon number reflected by the relativistic flying mirror”, Phys. Rev. Lett. **103**, 235003 (2009).

[293] D. Kiefer, M. Yeung, T. Dzelzainis, P. S. Foster, S. G. Rykovanov, C. L. Lewis, R. S. Marjoribanks, H. Ruhl, D. Habs, J. Schreiber, M. Zepf, and B. Dromey, “Relativistic electron mirrors from nanoscale foils for coherent frequency upshift to the extreme ultraviolet”, Nature Communications **4**, 1763 (2013).

[294] I. J. Kim, K. H. Pae, C. M. Kim, H. T. Kim, H. Yun, S. J. Yun, J. H. Sung, S. K. Lee, J. W. Yoon, T. J. Yu, T. M. Jeong, C. H. Nam, and J. Lee, “Relativistic frequency upshift to the extreme ultraviolet regime using self-induced oscillatory flying mirrors”, Nature Communications **3**, 1231 (2012).

[295] H. P. Vincenti, “Génération d’impulsions attosecondes sur miroir plasma relativiste”, Theses (Ecole Polytechnique X, Dec. 2012), page(s): 052117.

[296] S. P. Gavrilov and D. M. Gitman, “Vacuum instability in slowly varying electric fields”, Phys. Rev. D **95**, 076013 (2017).

[297] A. Blinne, H. Gies, F. Karbstein, C. Kohlfürst, and M. Zepf, “All-optical signatures of quantum vacuum nonlinearities in generic laser fields”, Phys. Rev. D **99**, 016006 (2019).

---

[298] L. Doyle, P. Khademi, P. Hilz, A. Sävert, G. Schäfer, J. Schreiber, and M. Zepf, *Experimental estimates of the photon background in a potential light-by-light scattering study*, 2021.

[299] F. Karbstein, A. Blinne, H. Gies, and M. Zepf, "Boosting quantum vacuum signatures by coherent harmonic focusing", Phys. Rev. Lett. **123**, 091802 (2019).

[300] L. Fedeli, A. Sainte-Marie, N. Zaim, M. Thévenet, J. L. Vay, A. Myers, F. Quéré, and H. Vincenti, "Probing strong-field QED with doppler-boosted petawatt-class lasers", Phys. Rev. Lett. **127**, 114801 (2021).

[301] A. Gonoskov, S. Bastrakov, E. Efimenko, A. Ilderton, M. Marklund, I. Meyerov, A. Muraviev, A. Sergeev, I. Surmin, and E. Wallin, "Extended particle-in-cell schemes for physics in ultrastrong laser fields: review and developments", Phys. Rev. E **92**, 023305 (2015).

[302] W. H. Furry, "On bound states and scattering in positron theory", Physical Review **81**, 115–124 (1951).

[303] F. Karbstein and R. Shaisultanov, "Stimulated photon emission from the vacuum", Phys. Rev. D **91**, 113002 (2015).

[304] F. A. Reuse, *Electrodynamique et optique quantiques*, fr, Vol. 90 (PPUR presses polytechniques, 2007), page(s): 052117.

[305] J. Berges, "Introduction to nonequilibrium quantum field theory", AIP Conference Proceedings **739**, 3–62 (2004).

[306] J. Berges, *Nonequilibrium quantum fields: from cold atoms to cosmology*, arXiv:1503.02907, 2015.

[307] F. Gelis, *Quantum field theory*, Vol. 90 (Cambridge University Press, Cambridge, England, July 2019), page(s): 052117.

[308] A. Hartin, "Strong field qed in lepton colliders and electron/laser interactions", International Journal of Modern Physics A **33**, 1830011 (2018).

[309] A. Campa, T. Dauxois, D. Fanelli, and S. Ruffo, *Physics of Long-Range Interacting Systems*, Vol. 90 (Oxford University Press, Aug. 2014), page(s): 052117.

[310] O. Johns, *Analytical Mechanics for Relativity and Quantum Mechanics*, Vol. 90 (Oxford University Press, May 2011), page(s): 052117.

[311] M. Henneaux and C. Teitelboim, *Quantization of gauge systems*, Vol. 90 (Princeton University Press, Princeton, 2020), page(s): 052117.

[312] S. R. De Groot, *Relativistic Kinetic Theory. Principles and Applications*, edited by W. A. Van Leeuwen and C. G. Van Weert, Vol. 90 (American Physical Society, 1980), page(s): 052117.

[313] R. Hakim, *Introduction to relativistic statistical mechanics*, Vol. 90 (WORLD SCIENTIFIC, 2011), page(s): 052117.

[314] G. V. Vereshchagin and A. G. Aksenov, *Relativistic kinetic theory: with applications in astrophysics and cosmology*, Vol. 90 (Cambridge University Press, 2017), page(s): 052117.

[315] F. Niel, *Classical and quantum description of plasma and radiation in strong fields*, Vol. 90 (Springer International Publishing, 2021), page(s): 052117.

[316] R. Glauber, “Optical coherence and photon statistics”, in *Quantum theory of optical coherence*, Vol. 90 (John Wiley Sons, Ltd, 2014) Chap. 2, page(s): 23–182.

[317] N. B. Narozhny, “Radiation corrections to quantum processes in an intense electromagnetic field”, Phys. Rev. D **20**, 1313–1320 (1979).

[318] N. B. Narozhny, “Expansion parameter of perturbation theory in intense-field quantum electrodynamics”, Phys. Rev. D **21**, 1176–1183 (1980).

[319] D. Morozov, V. Ritus, and B. Narozhny, *Vertex function of electron in a constant electromagnetic field*, tech. rep. (CM-P00067564, 1981), page(s): 052117.

[320] A. Fedotov, “Conjecture of perturbative qed breakdown at 2/3 1”, Journal of Physics: Conference Series **826**, 012027 (2017).

[321] A. Ilderton, “Note on the conjectured breakdown of qed perturbation theory in strong fields”, Phys. Rev. D **99**, 085002 (2019).

[322] T. Podszus and A. Di Piazza, “High-energy behavior of strong-field qed in an intense plane wave”, Phys. Rev. D **99**, 076004 (2019).

[323] K. Krajewska, *Warpx documentation*, `https://warpx.readthedocs.io/en/latest/`, 2014.

[324] L. Fedeli, N. Zaïm, A. Sainte-Marie, M. Thévenet, A. Huebl, A. Myers, J.-L. Vay, and H. Vincenti, “Picsar-qed: a monte carlo module to simulate strong-field quantum electrodynamics in particle-in-cell codes for exascale architectures”, New Journal of Physics **24**, 025009 (2022).

[325] J.-L. Vay, D. P. Grote, R. H. Cohen, and A Friedman, “Novel methods in the particle-in-cell accelerator code-framework warp”, Computational Science & Discovery **5**, 014019 (2012).

[326] H. Gies, F. Karbstein, and C. Kohlfürst, “All-optical signatures of strong-field QED in the vacuum emission picture”, Phys. Rev. D **97**, 036022 (2018).

[327] W. Heisenberg and H. Euler, “Consequences of Dirac’s theory of positrons”, Z. Phys. **98**, 714–732 (1936).

[328] H. Gies and F. Karbstein, “An addendum to the Heisenberg-Euler effective action beyond one loop”, Journal of High Energy Physics **2017**, 108 (2017).

[329] H. Gies, F. Karbstein, and L. Klar, “Quantum vacuum signatures in multicolor laser pulse collisions”, Phys. Rev. D **103**, 076009 (2021).

[330] Y. I. Salamin, “Fields of a Gaussian beam beyond the paraxial approximation”, Applied Physics B **86**, 319 (2006).

[331] B King and C. H. Keitel, “Photon–photon scattering in collisions of intense laser pulses”, New Journal of Physics **14**, 103002 (2012).

[332] Y. Monden and R. Kodama, “Interaction of two counterpropagating laser beams with vacuum”, Phys. Rev. A **86**, 033810 (2012).

[333] Y. Monden and R. Kodama, “Enhancement of laser interaction with vacuum for a large angular aperture”, Phys. Rev. Lett. **107**, 073602 (2011).

[334] C. L. Haefner, A. Bayramian, S. Betts, R. Bopp, S. Buck, J. Cupal, M. Drouin, A. Erlandson, J. HorÃ¡Äek, J. Horner, J. Jarboe, K. Kasl, D. Kim, E. Koh, L. KoubÃkovÃ¡, W. Maranville, C. Marshall, D. Mason, J. Menapace, P. Miller, P. Mazurek, A. Naylon, J. NovÃ¡k, D. Peceli, P. Rosso, K. Schaffers, E. Sistrunk, D. Smith, T. Spinka, J. Stanley, R. Steele, C. Stolz, T. Suratwala, S. Telford, J. Thoma, D. VanBlarcom, J. Weiss, and P. Wegner, "High average power, diode pumped petawatt laser systems: a new generation of lasers enabling precision science and commercial applications", in Research using extreme light: entering new frontiers with petawatt-class lasers iii, Vol. 10241, edited by G. Korn and L. O. Silva (International Society for Optics and Photonics, 2017), page(s): 1 –5.

[335] P. Böhl, B. King, and H. Ruhl, "Vacuum high-harmonic generation in the shock regime", Phys. Rev. A **92**, 032115 (2015).

[336] A. P. Domenech and H. Ruhl, *An implicit ode-based numerical solver for the simulation of the heisenberg-euler equations in 3+1 dimensions*, `https://warpx.readthedocs.io/en/latest/`, 2016.

[337] T Grismayer, R Torres, P Carneiro, F Cruz, R. A. Fonseca, and L. O. Silva, "Quantum electrodynamics vacuum polarization solver", New Journal of Physics **23**, 095005 (2021).

[338] A. P. Domenech, "Simulation of quantum vacuum in higher dimensions" (2018), page(s): 052117.

[339] F. Karbstein, "Probing vacuum polarization effects with high-intensity lasers", Particles **3**, 39–61 (2020).

[340] W. Appel, *Mathematics for physics and physicists*, Vol. 90 (Princeton University Press, 2007), page(s): 052117.

[341] K. Krajewska, "Time-dependent green's functions", in *Green's functions in quantum physics*, Vol. 90 (Springer Berlin Heidelberg, Berlin, Heidelberg, 2006), page(s): 21–37.

[342] G. V. DUNNE, "Heisenberg–euler effective lagrangians: basics and extensions", in *From fields to strings: circumnavigating theoretical physics*, Vol. 90 (Springer Berlin Heidelberg, Berlin, Heidelberg, 2006), page(s): 445–522.

[343] U. Teubner and P. Gibbon, "High-order harmonics from laser-irradiated plasma surfaces", Rev. Mod. Phys. **81**, 445–479 (2009).

[344] A. Gonoskov, "Theory of relativistic radiation reflection from plasmas", Physics of Plasmas **25**, 013108 (2018).

[345] A. Bourdier, "Oblique incidence of a strong electromagnetic wave on a cold inhomogeneous electron plasma. relativistic effects", The Physics of Fluids **26**, 1804–1807 (1983).

[346] G. D. M. Fradkin E S and S. M. Shvartsman, *Quantum electrodynamics with unstable vacuum*, Vol. 90 (Springer Berlin Heidelberg, Berlin, Heidelberg, 1991), page(s): 21–37.

[347] V. Ritus, "Radiative corrections in quantum electrodynamics with intense field and their analytical properties", Annals of Physics **69**, 555–582 (1972).

[348] Z. Bialynicka-Birula and I. Bialynicki-Birula, "Nonlinear effects in quantum electrodynamics. photon propagation and photon splitting in an external field", Phys. Rev. D **2**, 2341–2345 (1970).

[349] W. Dittrich and M. Reuter, *EFFECTIVE LAGRANGIANS IN QUANTUM ELECTRODYNAMICS*, Vol. 220 (Springer Berlin Heidelberg, Berlin, Heidelberg, 1985), page(s): 21–37.

[350] W. Dittrich and H. Gies, *Probing the quantum vacuum. Perturbative effective action approach in quantum electrodynamics and its application*, Vol. 166 (Springer Berlin Heidelberg, Berlin, Heidelberg, 2000), page(s): 21–37.

[351] F. Karbstein, D. Ullmann, E. A. Mosman, and M. Zepf, "Direct accessibility of the fundamental constants governing light-by-light scattering", Phys. Rev. Lett. **129**, 061802 (2022).

[352] F. Karbstein, "Probing vacuum polarization effects with high-intensity lasers", Particles **3**, 39 (2020).

[353] T. D. Arber, K Bennett, C. S. Brady, A Lawrence-Douglas, M. G. Ramsay, N. J. Sircombe, P Gillies, R. G. Evans, H Schmitz, A. R. Bell, and C. P. Ridgers, "Contemporary particle-in-cell approach to laser-plasma modelling", Plasma Physics and Controlled Fusion **57**, 113001 (2015).

[354] M. R. Edwards and J. M. Mikhailova, "The x-ray emission effectiveness of plasma mirrors: reexamining power-law scaling for relativistic high-order harmonic generation", Scientific Reports **10**, 5154 (2020).

[355] E. Zoni, R. Lehe, O. Shapoval, D. Belkin, N. Zaïm, L. Fedeli, H. Vincenti, and J.-L. Vay, *A hybrid nodal-staggered pseudo-spectral electromagnetic particle-in-cell method with finite-order centering*, `https://warpx.readthedocs.io/en/latest/`, Berlin, Heidelberg, 2021.

[356] G. V. Dunne, "New strong-field qed effects at extreme light infrastructure", The European Physical Journal D **55**, 327 (2009).

[357] F. Karbstein, "Heisenberg-euler effective action in slowly varying electric field inhomogeneities of lorentzian shape", Phys. Rev. D **95**, 076015 (2017).

[358] T. D. Cohen and D. A. McGady, "Schwinger mechanism revisited", Phys. Rev. D **78**, 036008 (2008).

[359] A. M. Fedotov, "Electron-positron pair creation by a strong tightly focused laser field", Laser Physics **19**, 214–221 (2009).

[360] A. Gonoskov, I. Gonoskov, C. Harvey, A. Ilderton, A. Kim, M. Marklund, G. Mourou, and A. Sergeev, "Probing nonperturbative qed with optimally focused laser pulses", Phys. Rev. Lett. **111**, 060404 (2013).

[361] F. Karbstein, C. Sundqvist, K. S. Schulze, I. Uschmann, H. Gies, and G. G. Paulus, "Vacuum birefringence at x-ray free-electron lasers", Phys. Rev. A **23**, 095001 (2021).

[362] B. King, A. Di Piazza, and C. H. Keitel, "A matterless double slit", Nature Photonics **4**, 92–94 (2010).

[363] E. A. M. F. Karbstein, "X-ray photon scattering at a focused high-intensity laser pulse", Physical Review D **100**, 033002 (2019).

[364] M. Thévenet, A. Leblanc, S. Kahaly, H. Vincenti, A. Vernier, F. Quéré, and J. Faure, "Vacuum laser acceleration of relativistic electrons using plasma mirror injectors", Nature Physics **12**, 355–360 (2016).

[365] H. Motoyama, T. Sato, A. Iwasaki, Y. Takei, T. Kume, S. Egawa, K. Hiraguri, H. Hashizume, K. Yamanouchi, and H. Mimura, “Development of high-order harmonic focusing system based on ellipsoidal mirror”, Review of Scientific Instruments **87**, 051803 (2016).

[366] Z. Lécz and A. Andreev, “Diagnostics of peak laser intensity by pair production from thin foil target”, Laser Physics Letters **17**, 056101 (2020).

[367] C Thaury and F Quéré, “High-order harmonic and attosecond pulse generation on plasma mirrors: basic mechanisms”, Journal of Physics B: Atomic, Molecular and Optical Physics **43**, 213001 (2010).

[368] K. Qu, S. Meuren, and N. J. Fisch, “Signature of collective plasma effects in beam-driven qed cascades”, Phys. Rev. Lett. **127**, 095001 (2021).

[369] K. Krajewska, *Smilei documentation*, `https://smileipic.github.io/Smilei/Understand/multiphoton_Breit_Wheeler.html`, Berlin, Heidelberg, 2006.

[370] A. Muraviev, A. Bashinov, E. Efimenko, V. Volokitin, I. Meyerov, and A. Gonoskov, “Strategies for particle resampling in pic simulations”, Computer Physics Communications **262**, 107826 (2021).

[371] A. Hartin, “Second order qed processes in an intense electromagnetic field”, arXiv: High Energy Physics - Phenomenology **90**, 21–37 (2017).

[372] S. Bragin and A. Di Piazza, “Electron-positron annihilation into two photons in an intense plane-wave field”, Phys. Rev. D **102**, 116012 (2020).

[373] Y. He, T. G. Blackburn, T. Toncian, and A. V. Arefiev, “Dominance of -electron-positron pair creation in a plasma driven by high-intensity lasers”, Communications Physics **4**, 139 (2021).

[374] W. Greiner, L Neise, and H. Stocker, *Thermodynamics and statistical mechanics*, en, 1st ed., Vol. 90, Classical Theoretical Physics (Springer, New York, NY, July 2000), page(s): 21–37.

[375] A. Di Piazza, M. Tamburini, S. Meuren, and C. H. Keitel, “Improved local-constant-field approximation for strong-field qed codes”, Phys. Rev. A **99**, 022125 (2019).

[376] I. A. Aleksandrov, G. Plunien, and V. M. Shabaev, “Locally-constant field approximation in studies of electron-positron pair production in strong external fields”, Phys. Rev. D **99**, 016020 (2019).

[377] A. Di Piazza, “Wkb electron wave functions in a tightly focused laser beam”, Phys. Rev. D **103**, 076011 (2021).

[378] T. Heinzl, B. King, and A. J. MacLeod, “Locally monochromatic approximation to qed in intense laser fields”, Phys. Rev. A **102**, 063110 (2020).

[379] H. Goldstein, *Classical mechanics*, Vol. 90 (Addison-Wesley, Berlin, Heidelberg, 1980), page(s): 21–37.

[380] J.-M. Rax, *Mécanique analytique: adiabaticité, résonances, chaos*, fr, Vol. 90 (Springer Berlin Heidelberg, Berlin, Heidelberg, Feb. 2020), page(s): 21–37.

[381] N. P. Landsman, *Mathematical topics between classical and quantum mechanics*, en, 1998th ed., Vol. 90, Springer Monographs in Mathematics (Springer, New York, NY, Dec. 1998), page(s): 21–37.

---

[382] R. T. Prosser, “Poisson brackets and commutator brackets. I”, Proceedings of the American Mathematical Society **62**, 305–309 (1977).

[383] R. T. Prosser, “Poisson brackets and commutator brackets. II”, Proceedings of the American Mathematical Society **62**, 310–315 (1977).

[384] S. Aaronson, *Is quantum mechanics an island in theoryspace?*, arXiv:quant-ph/0401062v2, Berlin, Heidelberg, 2004.

[385] J. von Neumann, *Mathematical foundations of quantum mechanics*, edited by N. A. Wheeler, Vol. 90 (Princeton University Press, Princeton, NJ, Feb. 2018), page(s): 21–37.

[386] A. Peres, *Quantum theory: concepts and methods*, en, 1995th ed., Vol. 90, Fundamental Theories of Physics (Springer, Dordrecht, Netherlands, Oct. 1993), page(s): 21–37.

[387] W. Myrvold, M. Genovese, and A. Shimony, “Bell’s Theorem”, in *The Stanford encyclopedia of philosophy*, Vol. 90, edited by E. N. Zalta, Fall 2021 (Metaphysics Research Lab, Stanford University, Berlin, Heidelberg, 2021), page(s): 21–37.

[388] C. Held, “The Kochen-Specker Theorem”, in *The Stanford encyclopedia of philosophy*, Vol. 90, edited by E. N. Zalta and U. Nodelman, Fall 2022 (Metaphysics Research Lab, Stanford University, Berlin, Heidelberg, 2022), page(s): 21–37.

[389] L. Hardy, *Quantum theory from five reasonable axioms*, arXiv:quant-ph/0101012v4, Berlin, Heidelberg, 2001.

[390] G. M. D’Ariano, G. Chiribella, and P. Perinotti, *Quantum theory from first principles: an informational approach*, Vol. 90 (Cambridge University Press, Berlin, Heidelberg, 2017), page(s): 21–37.

[391] R. I. A. Davis, R Delbourgo, and P. D. Jarvis, “Covariance, correlation and entanglement”, Journal of Physics A: Mathematical and General **33**, 1895 (2000).

[392] J. Schwinger, *Quantum mechanics, symbolism of atomic measurements*, en, edited by B.-G. Englert and C. Schwinger, 1st ed., Vol. 90 (Springer, Berlin, Germany, Feb. 2001), page(s): 21–37.

[393] F. Laudisa and C. Rovelli, “Relational Quantum Mechanics”, in *The Stanford encyclopedia of philosophy*, Vol. 90, edited by E. N. Zalta, Winter 2021 (Metaphysics Research Lab, Stanford University, Berlin, Heidelberg, 2021), page(s): 21–37.

[394] R. Haag, *Local quantum physics*, en, 2nd ed., Vol. 90, Theoretical and Mathematical Physics (Springer, Berlin, Germany, Aug. 1996), page(s): 21–37.

[395] A. Duncan, *The Conceptual Framework of Quantum Field Theory*, Vol. 90 (Oxford University Press, Berlin, Heidelberg, Aug. 2012), page(s): 21–37.

[396] M. D. Schwartz, *Quantum Field Theory and the Standard Model*, Vol. 90 (Cambridge University Press, Berlin, Heidelberg, Mar. 2014), page(s): 21–37.

[397] R. E. Peierls, “The commutation laws of relativistic field theory”, Proceedings of the Royal Society of London. Series A. Mathematical and Physical Sciences **214**, 143–157 (1952).

[398] F. Gieres, “Covariant canonical formulations of classical field theories”, `https://smileipic.github.io/Smilei/Understand/multiphoton_Breit_Wheeler.html`, working paper or preprint, Berlin, Heidelberg, Sept. 2021.

---

[399] W. Greiner and J. Reinhardt, *Field quantization*, Vol. 90 (Springer Berlin Heidelberg, Berlin, Heidelberg, 1996), page(s): 21–37.

[400] E. Wigner, "On unitary representations of the inhomogeneous lorentz group", Annals of Mathematics **40**, 149–204 (1939).

[401] M. E. Peskin and D. V. Schroeder, *An introduction to quantum field theory*, en, Vol. 90 (Westview Press, Philadelphia, PA, Sept. 1995), page(s): 21–37.

[402] T. Evans and D. Steer, "Wick's theorem at finite temperature", Nuclear Physics B **474**, 481–496 (1996).

[403] P. Blasiak, A. Horzela, K. A. Penson, A. I. Solomon, and G. H. E. Duchamp, "Combinatorics and boson normal ordering: a gentle introduction", American Journal of Physics **75**, 639–646 (2007).

[404] H Casini and M Huerta, "Entanglement entropy in free quantum field theory", Journal of Physics A: Mathematical and Theoretical **42**, 504007 (2009).

[405] C. Itzykson and J.-B. Zuber, *Quantum field theory*, Vol. 90, Dover Books on Physics (Dover Publications, Mineola, NY, Feb. 2006), page(s): 21–37.

[406] J. Berges, "n-particle irreducible effective action techniques for gauge theories", Phys. Rev. D **70**, 105010 (2004).

Contents

Résumé détaillé

L'interaction électromagnétique imprègne essentiellement tous les phénomènes sensibles, et cette réalité est élucidée depuis plus d'un siècle. Cependant, cette connaissance ne pouvait se matérialiser pleinement comme force pratique qu'avec l'invention du laser, offrant un degré de contrôle sans précédent sur le champ électromagnétique, et ainsi sur ses interactions avec la matière. Les systèmes laser se sont depuis lors déployés vers toutes les sphères de la production, dont la science fondamentale. Cette thèse présente les résultats promis dans ce domaine, tant dans ses dimensions théorique qu'instrumentale, par l'application de l'effet de «miroir plasma relativiste »à l'obtention de sources de lumière d'intensité extrême, propres à provoquer des phénomènes inobservés à ce jour. Cette section en propose un résumé détaillé, en français, s'attachant à préciser son contexte et la substance des onze chapitres qui la composent.

Introduction et plan de la thèse

La frontière de la physique à ultra-haute intensité

Parmi la diversité des systèmes laser et de leurs usages, les deux dernières décennies ont vu émerger un champ de recherche structuré autour de la «physique à ultra-haute intensité », étudiant les interactions des impulsions laser aux plus hautes intensités réalisables avec la matière, alors convertie en particules et plasmas. Ces efforts ont pu révéler des phénomènes d'une grande richesse, donnant lieu à de multiples applications [1]. Quoique bénéficiant des progrès continus de la technologie laser, portant une élévation progressive des intensités laser, ces méthodes ont pu s'appuyer sur un ensemble qualitativement bien défini de processus physique élémentaires, tous décrits par la mécanique classique des champs et de particules à cinématique relativiste [1].

La situation actuelle est cependant susceptible de marquer un tournant, car les infrastructures de dernière génération, les lasers d'une puissance de crête supérieure à un pétawatt (10^{15} W), ont le potentiel de révéler des processus radicalement nouveaux. Tous découleraient de l'aspect quantique des particules et des champs et délimiteraient collectivement le domaine physique de l'*Électrodynamique quantique en champs forts* (EDQ-cf, ou sf-QED dans la littérature anglophone) [2]. L'accès à de tels phénomènes s'avérerait d'une valeur à la fois fondamentale et pratique, permettant de tester empiriquement des théories établies ou spéculatives [3], et de générer des sources exotiques de rayonnement et de particules [4]. Cette frontière de la physique des lasers a par conséquent fait l'objet d'une attention croissante et alimente aujourd'hui l'activité régulière de nombreux scientifiques ainsi que la mise en service d'installations expérimentales ambitieuses.

Néanmoins, si les premières signatures de ces effets pourront être détectées dans un avenir proche [3, 4], le chemin vers des régimes plus profonds d'EDQ-cf semble malheureusement beaucoup plus escarpé que ses rives. Considérons par exemple un processus central de l'EDQ-cf, la conversion d'un photon en une paire électron-positron. Si les installations prévues à ce jour peuvent s'attendre à détecter quelques positrons créés, une forte attrition du champ par la création d'un plasma électron-positron associé à un fort rayonnement photonique, produisant une dynamique physique qualitativement nouvelle, ne se produiraient qu'à des intensités encore dix à cent fois plus élevées. Cependant, les infrastructures de plusieurs pétawatts approchent maintenant des échelles industrielles, ce qui implique une ingénierie laser de plus en plus complexe, de sorte qu'un mur technologique ne peut pas être exclu à court terme [5]. Par conséquent, la recherche de schémas alternatifs en vue d'atteindre les champs les plus élevés est d'ores et déjà activement poursuivie [4].

Électrodynamique quantique dans la lumière extrêmement intense de miroirs plasma relativistes

Les miroirs plasma relativistes apparaissent comme un moyen très prometteur d'atteindre les champs les plus élevés possibles avec les lasers actuels [6–11]. Lorsqu'une impulsion intense atteint une interface solide nette, elle la transforme en un plasma dense qui oscille à des vitesses proches de celle de la lumière, réfléchissant ainsi l'impulsion tout en la comprimant par effet Doppler. En jouant correctement de cette interaction, notamment à très haute intensité, l'impulsion réfléchie peut également être naturellement focalisée à des tailles focales uniquement limitées par sa longueur d'onde désormais réduite, concentrant la lumière dans des volumes beaucoup plus restreints que ceux permis par la longueur d'onde laser initiale, ce qui se traduit par des augmentations d'intensité focale de deux à cinq ordres de grandeur [12, 13]. Les champs correspondants s'approcheraient de la valeur critique à laquelle un champ se décompose spontanément en paires électron-positron, connue sous le nom de champ de Schwinger, ce qui pourrait permettre d'étudier des effets critiques de la l'EDQ-cf tels que l'auto-interaction de la lumière, et faciliterait sans aucun doute l'entrée dans le régime quantique profond de l'EDQ-cf. Le cœur de mon travail a consisté à spécifier les principaux phénomènes physiques attendus au point d'interaction de telles sources miroirs plasma relativistes (MPR).

Présentation du plan

La partie I présente l'état de l'art de la physique en champs forts auquel contribue la thèse. Le contexte évoqué ci-dessus est ainsi exposé au chapitre 1, avec une discussion des motivations pour atteindre le régime de l'EDQ-cf. Dans cette thèse, je présente les prédictions dérivées d'une étude approfondie de différents scénarios d'interaction. Les outils théoriques et numériques mobilisés à cette fin sont introduits au chapitre 2.

La partie II aborde les études théoriques et numériques préalables à la caractérisation des processus d'interaction de champs MPR avec le vide fermionique. Le chapitre 3 présente une validation numérique complète de notre implémentation de l'algorithme d'«Émission du Vide Stimulée »[303]. De surcroît, des options numériques apparemment équivalentes ont été testées, démontrant une sensibilité non-négligeable des résultats à ces choix dans certains cas. Le chapitre 4 fournit une démonstration explicite de l'expression analytique du nombre de photons diffusés dans la lumière MPR en fonction du spectre harmonique (Eq. 8.2), en s'appuyant sur le cas résoluble d'une impulsion gaussienne. Le chapitre 5 traite de la relation entre notre calcul basé sur l'amplitude de probabilité de diffusion des photons dans le vide et la résolution d'équations du champ classiques effectives. Nous distinguons différents types de développement en série dans les théories quantiques effectives de l'électromagnétisme, en précisant le rôle des solutions nonperturbatives des équations perturbatives du mouvement. Le chapitre 6 fournit des estimations du coût en ressources de calcul des simulations d'émission stimulée du vide. Le chapitre 7 montre les spectres temporels du champ issus de simulation PIC utilisés pour modéliser la lumière MPR dans notre travail.

La partie III est consacrée aux résultats de nos travaux sur la physique de la lumière extrêmement intense issue de miroirs plasma relativistes, soit dans le vide, soit en présence de matière. Le chapitre 8 détaille les effets des couplages du champ électromagnétique avec le champ électron-positron en l'absence de particules. Plus précisément, nous calculons les spectres des photons diffusés dans le champ électromagnétique lui-même dans différentes configurations, et spécifions un seuil de puissance pour l'occurrence de la création de paires de Schwinger dans de tels champs. Le chapitre 9 montre le résultat de l'interaction de la lumière du miroir plasma relativiste avec des particules de matière, initialement présentes soit sous la forme d'une cible initialement solide, soit sous la forme d'un faisceau d'électrons à haute énergie. Les propriétés distinctes des configurations macroscopiques résultantes sont examinées, ainsi que les processus élémentaires individuels impliqués. En particulier, les cibles solides pourraient permettre la formation de jets de plasma électron-positron quantique relativiste et extrêmement dense, tandis que les collisions de faisceaux de particules à haute énergie avec les impulsions lumineuses pourraient permettre de tester la conjecture de Ritus-Narozhny, relative au comportement de l'électrodynamique quantique à champ fort dans un régime où la validité théoriques des notions usuelles de particules, photons, électrons et positrons, s'effondre.

La partie finale IV propose une synthèse du cadre de la théorie quantique des champs, avec un soin particulier porté à la pertinence en vue de l'électrodynamique en champs forts, et à ses réductions (semi-)classiques. Le chapitre A offre un résumé de la correspondance classique-quantique canonique. Le chapitre B introduit des éléments de théorie quantique des champs, notamment hors d'équilibre, à un niveau heuristique.

Résumé détaillé par chapitre

Partie I – État de l'art et objectifs

Chapitre 1 – La physique des lasers ultra-intenses aujourd'hui

- La notion d'*intensité lumineuse* I, exprimée en W.cm^{-2}, désigne la quantité d'énergie transmise par le champ électromagnétique par unité de temps à travers une unité de surfac donnée. Par conséquent, elle quantifie directement les changments que peut apporter une configuration électromagnétique donnée à d'autres systèmes, et à quel rythme, définissant donc largement les *processus* physiques qui auront lieu. Les lasers ultra-intense atteignent couramment 10^{18} W.cm^{-2}, à laquelle un atome de carbone est entièrement ionisé par simple suppression de la barrière de potentiel [16], et un électron initialement au repos devient relativiste en 4×10^{-16} s environ, soit une fraction de la période optique du laser. À l'intensité la plus élevée actuellement atteinte, de $I = 1 \times 10^{23}$ W.cm^{-2} [17], ce temps diminuerait à environ 3×10^{-18} s et même les protons approcheraient la vitesse de la lumière en un cycle optique. La physique des lasers et de la matière à ultra-haute intensité consiste donc en l'interaction de champs électromagnétiques avec des particules chargées ou des états plasma, généralement d'énergies cinétiques relativistes.

- En pratique, les lasers conçus pour atteindre les intensités les plus élevées émettent généralement une lumière visible ou en proche infrarouge d'une longueur d'onde centrée autour de $\lambda = 800$ nm, ce qui correspond à une période laser $\delta t \simeq 2.67 \times 10^{-15}$ s $\equiv 2.67$ fs ("femtosecondes") et une durée totale d'environ dix cycles $\tau \simeq 25$ fs, définissant la classe des "laser ultracourts". Le milieu lasant le plus couramment utilisé est constitué de cristaux de saphir dopés aux ions de titane (Ti:Sa) [16]. Les dernières installations construites délivrent généralement des impulsions d'énergie totale de 20 J à 100 J pour des intensités focalisées d'environ 10^{22-23} W.cm^{-2}, le record actuel étant de 1×10^{23} W.cm^{-2} [17]. La plupart des installations en projet envisagent des énergies supérieures à 100 J, mais ne dépasseraient pas 10^{24} W.cm^{-2}, bien qu'une exception notable affiche l'ambition d'une énergie de $1,5$ kJ en 15 fs (SEL), ce qui se traduirait par des intensités d'environ 2×10^{24} W.cm^{-2}.

- Dans un champ électromagnétique de fréquence donnée, un électron gagne une impulsion générique de l'ordre de $p \sim mc\xi$, avec m la masse de l'électron, c la vitesse de la lumière et [4]:

$$\xi \simeq 0.86\lambda_0[\mu\text{m}]\sqrt{I_0[10^{18}\ \text{W.cm}^{-2}]} \tag{B.125}$$

  où λ_0 est la longueur d'onde du faisceau central et I_0 l'intensité maximale au foyer, ξ est appelé le *paramètre de force de champ classique*. Par conséquent, la dynamique doit effectivement être décrite par la mécanique relativiste dès que $I_0 \geq I_{\text{rel}} = 2 \times 10^{18}$ W.cm^{-2} pour la longueur d'onde typique du laser $\lambda_0 = 800$ nm. Lorsque les intensités relativistes sont atteintes, les interactions avec la matière, *i.e.* les particules et les plasmas, deviennent fortement non linéaires, laissant place à des phénomènes physiques tels que l'accélération de particules à haute énergie ou la génération d'harmoniques de champ. Il s'agit du domaine classique de la physique à haute intensité, particulièrement exploré au cours des deux dernières décennies.

- Cet ensemble relativement bien défini de méthodes et de phénomènes physiques a permis de stabiliser la notion de «régime relativiste»des interactions laser-matière [1]. Cette situation est toutefois en train de changer avec la mise en service récente d'installations laser de plusieurs pétawatts (1 PW = 10^{15} W), éventuellement couplées à des accélérateurs conventionnels [33, 42–44] (*cf.* également Fig. 1.1). Ces infrastructures ouvrent la perspective de détecter pour la première fois des signatures de phénomènes de «champ fort », tels que le recul des électrons par émission de rayonnement, la création de paires électron-positron ou des non-linéarités optiques dans le vide, définissant ainsi un nouveau régime physique d'*électrodynamique quantique en champ fort* [2]. Tous ces effets sont contrôlés par une échelle de champ appelée *champ de Schwinger*,

Champs de Schwinger

$$\boxed{\begin{cases} E_S \simeq 1.32 \times 10^{18}\ \text{V.m}^{-1} \\ B_S = \dfrac{E_S}{c} \simeq 4.40 \times 10^{9}\ \text{T} \end{cases}}$$

se traduisant par une intensité (pour une onde plane) de,

Intensité de Schwinger $\boxed{I_S = c\varepsilon_0 E_S^2 = \simeq 4.62 \times 10^{29}\ \mathrm{W.cm^{-2}}}$

Plus précisément, si l'on considère les processus impliquant une particule massive chargée, électron ou positron, le paramètre d'interaction pertinent est le champ dans le cadre du repos de la particule, c'est-à-dire [4],

Paramètre quantique d'interaction $$\boxed{\chi = \frac{\sqrt{-(F_{\mu\nu}p^{\nu})^2}}{mcE_S} = \gamma\frac{\sqrt{(\mathbf{E}+\mathbf{v}\times\mathbf{B})^2-(\mathbf{v}\cdot\mathbf{E}/c)^2}}{E_S}} \tag{B.126}$$

Si $\chi \gtrsim 1$, les effets de champ fort deviennent importants. Lorsque les électrons/positrons sont accélérés directement par le champ laser (*e.g.* configurations laser-cible), on trouve la loi d'échelle [4],

$$\chi \simeq 0.09\lambda[\mu\mathrm{m}]I_0[10^{23}\ \mathrm{W.cm^{-2}}] \tag{B.127}$$

Si, au contraire, leur énergie initiale est importante par rapport à celle fournie par le laser (*e.g.* configurations laser-accélérateur), on trouve [4],

$$\chi \simeq 0.18\mathcal{E}_0[\ \mathrm{GeV}]\sqrt{I_0[10^{21}\ \mathrm{W.cm^{-2}}]} \tag{B.128}$$

Quoi qu'il en soit, nous comprenons pourquoi les effets de champ fort ne commencent à se manifester qu'à l'intensité la plus élevée possible à ce jour, et seulement à peine encore. Les miroirs plasma relativistes pourraient permettre d'entrer beaucoup plus profondément dans le régime dominé par le champ fort.

■ Les oscillations collectives non linéaires des populations d'électrons aux interfaces entre le vide et un plasma de densité solide irradié par laser peuvent se rapprocher d'une réalisation de l'effet de miroir relativiste [233], notamment en termes d'effet d'amplification. Ces «miroirs plasma relativistes»(MPR) sont potentiellement les sources de champs libres les plus intenses à portée de la technologie actuelle. L'utilisation d'un laser de classe Petawatt comme faisceau pilote pourrait permettre simultanément de générer des harmoniques efficacement, c'est-à-dire la compression temporelle de chaque cycle optique incident en impulsions d'une durée de plusieurs dizaines d'attosecondes, et la focalisation à des tailles focales limitées en longueur d'onde, ce qui se traduirait par des gains d'intensité de deux à cinq ordres de grandeur [12]. Les champs correspondants $I \sim 10^{25-29}\ \mathrm{W.cm^{-2}}$ s'approcheraient de la valeur critique dans le cadre du laboratoire, ce qui pourrait permettre d'étudier des effets critiques de la sf-QED tels que l'auto-interaction de la lumière, et faciliterait clairemetn l'entrée dans le régime à dominante quantique de l'EDQ-cf.

Chapitre 2 – Méthodes théoriques et numériques

- Le cadre théorique le plus complet qui sous-tend actuellement la recherche sur l'électrodynamique quantique en champ fort est une extension de la théorie cinétique classique. Il a été construit par une approche heuristique, en ajoutant des corrections quantiques aux équations cinétiques. Dans ce contexte, les particules sont décrites par des fonctions de distribution à un corps régies par les équations de Boltzmann, et le champ électromagnétique est classique. Tous les phénomènes quantiques sont encapsulés dans *i*) un opérateur de collision pour les fonctions de distribution à un corps et *ii*) des termes supplémentaires dans les équations de Maxwell. Les sections efficaces entrant dans les termes de collision sont alors calculées dans une extension de la théorie de la diffusion en Électrodynamique quantique, qui tient compte de la présence d'un champ électromagnétique, appelée la représentation de Furry de l'EDQ-cf [302, 308]. Les nouveaux processus les plus significatifs sont la diffusion Compton (non linéaire) d'un électron ou d'un positron émettant un photon, et la création de paires électron-positron de Breit-Wheeler (non linéaire) à partir d'un photon dans le champ fort. Les équations fondamentales du modèle cinétique Boltzmann-EDQ peuvent donc finalement être écrites comme suit [315],

  $$\begin{aligned}\frac{\partial f_{e^\mp}}{\partial t} + \frac{\mathbf{p}}{m_e\gamma}\cdot\frac{\partial f_{e^\mp}}{\partial \mathbf{q}} \mp e\left[\mathbf{E}+\dot{\mathbf{q}}\times\mathbf{B}\right]\cdot\frac{\partial f_{e^\mp}}{\partial \mathbf{p}} &= \mathcal{C}_{\mathrm{CS}}[f_{e^\mp}] + \mathcal{C}_{\mathrm{BW}}[f_\gamma]\\ \frac{\partial f_\gamma}{\partial t} + \mathbf{c}\cdot\frac{\partial f_\gamma}{\partial \mathbf{q}} &= \mathcal{C}_{\mathrm{CS}}[f_{e^-}] + \mathcal{C}_{\mathrm{CS}}[f_{e^+}] - \mathcal{C}_{\mathrm{BW}}[f_\gamma]\end{aligned}$$

  avec un système de Maxwell inchangée Eqs. 2.12-2.17, et éventuellement des espèces de particules supplémentaires telles que les ions.

- Le modèle Boltzmann-QED de l'EQD à champ fort a été présenté comme une extension naturelle de la théorie cinétique classique relativiste, fournissant une base théorique pour une conception intuitive de la dynamique générale champ-particules dans l'EQD à champ fort. De manière plus décisive, elle permet également une résolution numérique sans approximation supplémentaire, ou des simulations dites *ab initio*. L'algorithme sous-jacent est connu sous le nom de *Particle-in-Cell* (PIC). Elle est devenu la norme dans la recherche sur les lasers à haute intensité, et admet maintenant des extensions pour inclure les événements EDQ, qui seront désignés sous le nom d'algorithmes «PIC-EDQ». La fonction générale d'un algorithme PIC-QED est de produire des solutions numériques au système fermé d'équations aux dérivées partielles Eqs. 2.12-2.17 et 2.21-2.22. Une vue d'ensemble des variables impliquées et de leurs interactions est présentée dans la Fig. 2.1. Le principe de l'algorithme consiste à résoudre le système par discrétisation temporelle et résolution itérative, ce qui permet de calculer les quantités à des moments ultérieurs à partir de données temporelles initiales.

- Une situation que nous avons étudié en profondeur est l'évolution d'un faisceau MPR dans le vide, et nous souhaitons prédire les effets de son auto-interaction *via* le champ électron-positron. Dans certaines conditions réalistes, il serait possible de dériver une théorie des champs classique effective capturant l'évolution électromagnétique, éventuellement réductible à des corrections non linéaires de l'équation de Maxwell. Nous avons adopté un autre point de vue appelé »émission stimulée du vide»(SVE) [303], basé sur les amplitudes de transition de création de photons, qui est défini de manière simple et cohérente en termes de champs obéissant aux équations classiques de Maxwell. L'estimation précise des quantités d'intérêt, les distributions de photons Eqs. 2.44 et nombre de paires Schwinger Eq. 2.51, peut être réalisée numériquement pour des configurations de champ arbitraires. À cette fin, nous avons développé et optimisé un code capable de fonctionner sur des infrastructures de calcul parallèle à grande échelle.

Partie II – Études théoriques et numériques pour l'électrodynamique quantique dans le vide

Chapitre 3 – Validation de l'algorithme d'émission stimulée du vide sur des configurations de référence

- Pour une meilleure comparaison avec la littérature existante [297, 326] et la compréhension du cas de la lumière MPR, les résultats de notre code SVE ont été validés sur quatre cas de référence. Les résultats attendus pour chacune de nos observables étant connus, nous avons pu les utiliser pour valider notre algorithme, et en particulier étudier l'impact de différentes procédures de propagation et d'initialisation. À cette fin, les valeurs des champs à tout moment ont été calculées par deux méthodes différentes. Soit par des expressions analytiques explicites des champs, dérivées de l'expansion en série paraxiale [330] prise, sauf indication contraire explicite, à l'ordre 5 et complétée par une enveloppe temporelle gaussienne ; soit par propagation exacte (Maxwell) d'une configuration de champ initiale *via* transformées de Fourier rapides 3D. Dans trois cas de référence sur les quatre étudiés, les résultats purement numériques ont été complétés par des calculs semi-analytiques des amplitudes, où il ne reste qu'une intégrale spatiale à une dimension à réaliser numériquement, ce qui constitue une autre validation indépendante du code. Ces travaux concluent à une bonne précision du code sous l'une des variantes d'implémentation possibles que nous avons identifiée.

Chapitre 4 – Estimation analytique de l'auto-diffusion d'un faisceau de lumière MPR

- Le calcul numérique à grande échelle de la diffusion des photons à l'intérieur d'un faisceau focalisé généré par un miroir plasma est très coûteux, alors que l'espace des paramètres décrivant de tels champs MPR est au moins aussi vaste que l'ensemble des spectres réalistes. Par conséquent, une dérivation numérique des lois d'échelle régissant l'autodiffusion de la lumière MPR est pratiquement impossible. D'autre part, une modélisation analytique précise du champ s'avère également difficile, et le calcul des amplitudes de diffusion des photons qui en découle est plutôt dissuasif dans tous les cas. Nous pouvons néanmoins trouver des indications dans des expressions analytiques adoptant des hypothèses simples concernant le champ lumineux MPR, assimilé à un train d'impulsions gaussiennes. Bien que les prédictions quantitatives semblent hors de portée de cette manière, des tendances générales peuvent être dérivées pour les quantités pertinentes en fonction des paramètres du faisceau, y compris une description assez souple du profil spectral de la lumière du MPR. Si nous considérons le spectre généré dans des conditions optimales d'interaction laser-plasma, nous pouvons supposer le spectre de puissance constant au foyer, auquel cas le nombre total de photons diffusés dépend simplmemnt du nombre d'harmoniques n_h dans le champ par la relation,

$$\boxed{N \propto n_h^2}$$

Chapitre 5 – Relation entre l'émission du vide stimulée et des équations de champs effectives

- Le formalisme de l'émission stimulée dans le vide que nous avons utilisé dans ce travail est explicitement fondé sur l'électrodynamique quantique. Néanmoins, il nous a conduit à une expression du nombre de photons observables Eqs. 2.45-2.49 en termes purement classiques d'un spectre de champ rayonné. Nous explicitons ici la possibilité du raisonnement inverse, en partant des équations de mouvement de l'action de Heisenberg-Euler, comprise comme une action effective quantique, afin de calculer les nombres de photons définis à partir des variables de champ classiques, comprises comme des valeurs d'espérance de champ quantique. Cette approche a également été poursuivie dans la littérature, avec l'avantage d'une intégration naturelle dans le cadre de référence de Maxwell-Boltzmann, y compris les implémentations numériques PIC-EDQ permettant de résoudre numériquement les équations de champ autoconsistantes sans autre approximation. Afin de mieux discerner le pouvoir prédictif de ces méthodes, le domaine d'équivalence avec le calcul basé sur l'amplitude est précisé, et une typologie des contributions au-delà de l'ordre principal mise en évidence, délimitant le rôle des solutions exactes aux équations effectives du mouvement.
- Il apparaît que les équations effectives du mouvement pour le champ électromagnétique, associées à une simple hypothèse de champ fort, permettent de retrouver exactement l'expression SVE du champ diffusé. Nous soutenons également que dans les grands volumes d'interaction, la hiérarchie locale des termes d'interaction peut s'effondrer en raison de séquences d'interaction de grande multiplicité ; le rôle des solutions exactes aux équations du mouvement effectives est alors identifié comme garantissant la cohérence des approximations opérées au niveau de l'action quantique effective, à tout moment de l'évolution du système.

Chapitre 6 – Volume de calcul des simulations d'émission du vide stimulée

- Si nous considérons un faisceau comprenant des harmoniques jusqu'à l'ordre $n_h \sim 100$, la fréquence maximale est bien sûr $\nu_{max} \sim 100\nu_0$, tandis que la longueur de décroissance du champ est toujours liée à la durée globale du faisceau $\tau \sim 10\lambda_0$, y compris dans les dimensions transversales encore une fois en raison de la grande divergence d'un faisceau très focalisé, ce qui implique,

$$\begin{aligned}\mathcal{M}_h &\sim 10 \times (2 \times 100\nu_0 \times 20\lambda_0) \times (2 \times 100\nu_0 \times 10\lambda_0)^2 \times 8 \text{ Bytes}\\ &\sim 100 \text{ GB}\end{aligned}$$

Combiné à la contrainte de temps, cela représente un volume de calcul d'environ $2,5 \times 10^4$ heures CPU par exécution, ce qui souligne la nécessité d'une infrastructure de calcul à grande échelle.

Chapitre 7 – Spectres MPR issus de simulations PIC

- Voir Figs. 7.2

Partie III – Processus quantiques dans la lumière de miroirs plasma relativistes

Chapitre 8 – Processus quantiques du vide dans la lumière de miroirs plasma relativistes

- En dessous du seuil de Schwinger $E, B \sim E_S, B_S$, la dynamique porte néanmoins la marque du couplage avec le champ électronique par le biais de paires électron-positron virtuelles, donnant lieu à une auto-interaction électromagnétique effective avec une composante perturbative seulement supprimée par des puissances de $E/E_S, B/B_S$ [327, 347–350]. Étant donné que les champs macroscopiques les plus puissants pouvant être obtenus à ce jour, fournis par des lasers femtosecondes de plusieurs pétawatts focalisés près de la limite de diffraction, atteignent $E_{\mathrm{las}} \sim 10^{-3} \times E_S$, l'observation directe de processus du vide entièrement nonperturbatifs tels que la création de paires semble exclue dans un avenir prévisible, tandis que les efforts de recherche consacrés à la diffusion de la lumière par la lumière ont mis en évidence à la fois la nature encore élusive de ce processus, et la possibilité d'obtenir un signal perceptible dans plusieurs configurations optimisées [176–180, 182–196, 351] (voir aussi [352] et les références qui y figurent). Ces configurations de champ impliquent généralement la collision de plusieurs impulsions optiques intenses ou, dans certains cas, le couplage à un faisceau de photons de haute énergie, ce qui offre aux installations existantes et futures des programmes expérimentaux ambitieux.
- Nous avons montré qu'une focalisation optimale du faisceau produit lors de la réflexion d'un seul laser de classe Petawatt sur un miroir plasma relativiste permet de générer autant de photons dans le vide que deux impulsions infrarouges Petawatt parfaitement contra-propagatives et focalisées à leur limite de diffraction, et de réduire de manière significative les puissances laser nécessaires pour observer la création de paires de Schwinger ($P \sim 200$ PW au lieu des plus de 1 EW requis dans l'infrarouge). La pertinence physique de ce résultat dépend néanmoins de façon cruciale du degré de contrôle des interactions laser-plasma réalisable dans une expérience, et du bruit photonique associé.
- Le couplage à un faisceau auxiliaire bien contrôlé allège considérablement ces contraintes, car il ne nécessite que de faibles émissions de fond dans la direction du faisceau de la «sonde», qui pourraient être réglées à proximité de la contre-propagation avec le faisceau harmonique. En outre, en raison des niveaux élevés de photons de sonde diffusés de manière inélastique dans ce cas, l'évaluation de l'origine quantique du signal pourrait alors être effectuée sur une base spectrale, donc avec une confiance potentiellement beaucoup

plus élevée que sur la seule base d'un critère de discernabilité angulaire. Comme les gains d'énergie associés sont de l'ordre de $+\omega_0$, l'utilisation d'une sonde de fréquence $\omega_p \neq \omega_0$ peut permettre d'obtenir des signatures de vide quantique encore plus claires dans la gamme de fréquences $\omega_p + \omega_0$. En effet, à condition que la probabilité de présence de particules chargées résiduelles dans la région de chevauchement des faisceaux soit suffisamment faible, ces fréquences ne pourraient pas être générées par l'interaction laser-matière.

- Si toutefois la dynamique des électrons du miroir plasma entraîne une création prolifique de paires avant même que le processus de Schwinger ne se produise, la détection des effets de vide quantique à partir des faisceaux générés par les particules nécessiterait probablement des installations plus complexes. Typiquement, ils impliqueraient le désenchevêtrement des étapes de génération et de focalisation du faisceau MPR, de manière à refocaliser le faisceau MPR à l'aide d'une optique visible-UV à large bande, soit dans une partie blindée de la chambre PM, soit peut-être même dans une autre chambre [365]. À ce moment il deviendrait cepednant d'autant plus facile d'étudier l'interaction du faisceau MPR avec la matière directement (comme *e.g.* dans [300]), ouvrant alors la voie à des régimes non encore observés de la dynamique des plasmas dans les champs forts. Cette perspective est au cœur du chapitre 9.

Chapitre 9 – De la lumière des miroirs plasma relativistes aux processus extrêmes dans la matière

- Lorsque des particules de matière chargées sont présentes dans le champ fort, les processus sf-QED se déploient à une échelle beaucoup plus vaste que dans le vide fermionique. Deux facteurs simples concourent directement à ce fait. A l'échelle des processus élémentaires tout d'abord, le paramètre pertinent quantifiant l'interaction d'une particule avec un champ électromagnétique cohérent est proportionnel à la fois à son impulsion et au champ, or l'impulsion est proportionnellle au champ. Par conséquent, de très hauts paramètres microscopique d'interaction peuvent apparaître sous l'effet d'une dynamique classique d'accélération dans le champ. Deuxièmement, à l'échelle macroscopique où de nombreux processus sf-QED non corrélés peuvent se produire, il existe une chaîne d'événements conduisant à la croissance exponentielle du nombre de fermions, amplifiant les effets quantiques dans la dynamique globale. Il apparaît qu'en présence de matière, un champ cohérent suffisamment puissant sur des étendues spatio-temporelles suffisamment grandes se décomposera spontanément et massivement en un système de nombreux photons, électrons et positrons, à travers des séquences connues sous le nom de cascades QED. Nous présentons comment ce scénario général se déroule dans le cas de sources MPR, afin de prédire les propriétés générales des systèmes résultants, d'identifier les signatures observables des régimes décrits et de fournir des orientations pour les applications ultérieures.
- On peut envisager trois origines différentes pour les particules de matière initiales. En continuité directe avec le chapitre précédent sur les interactions dans le vide, la production de paires peut se faire directement à partir du champ cohérent dans le vide fermionique (processus de Schwinger).

Comme les puissances laser requises pour déclencher un tel phénomène restent actuellement hors de portée, les sources exogènes de matière restent d'un intérêt primordial. Dans l'optique de maximiser l'interaction champ-matière tout en conservant la simplicité expérimentale, la focalisation sur une cible solide est présentée en premier lieu. Grâce au grand nombre de particules d'amorçage, cette configuration permet des densités électron-positron extrêmement élevées ($> 10^{28}$ cm^{-3}), pouvant aller jusqu'à la formation d'un plasma relativiste quantique sous la forme de jets e^+e^- quasi-neutres accélérés à des énergie de plusieurs GeV.

- Nous nous intéressons ensuite à la collision du faisceau MPR avec des électrons de haute énergie (10 GeV), produisant des processus microscopiques remarquables grâce à des paramètres χ très élevés (> 1000). Dans des conditions de collision appropriées, on constate que les paramètres d'interaction quantique atteignables dépassent le seuil du régime de Ritus-Narozhny, ce qui présente un intérêt théorique de premier ordre. En effet, le cadre habituel de l'EDQ-cf, reposant sur un développement en série des interactions photons hors champ cohérent avec les électrons-positrons «habillés »par le champ, pourrait alors cesser d'être valide, ouvrant une possible fenêtre empirique vers un approfondissement de notre compréhension de l'électrodynamique.

Conclusions

Les miroirs plasma relativistes pourraient offrir la possibilité d'accéder dans un avenir proche au régime à dominante quantique de l'électrodynamique quantique en champ fort, *via* des champs d'intensités comprises entre 10^{25} W.cm^{-2} et 10^{29} W.cm^{-2}. Dans cette thèse, nous avons prédit les effets produits par cette lumière dans différentes configurations, soit dans le vide, soit en présence de matière pré-existante.

Les processus quantiques du vide ont été étudiés dans le chapitre 8. En adoptant le formalisme de l'émission stimulée du vide [303], nous avons pu calculer le nombre de photons diffusés dans le faisceau MPR, pour deux spectres de faisceau différents, correspondant à différentes conditions de génération sur le miroir plasma. Nous avons montré que la focalisation d'un seul faisceau MPR dans le vide pouvait produire autant de photons diffusés que la collision frontale de deux impulsions infrarouges de 1 PW focalisées à la limite de diffraction, ce qui peut simplifier ce dernier dispositif expérimental. Nous avons également calculé le nombre de photons diffusés dans un faisceau sonde lors de la collision avec une impulsions MPR, ce qui a révélé en particulier que certains photons pouvaient être diffusés avec des énergies absentes des spectres des faisceaux initiaux en collision, ce qui pourrait améliorer de manière significative le rapport signal-bruit, essentiel dans ces expériences. Enfin, un seuil de création de paires de Schwinger a été trouvé, indiquant une puissance laser requise d'environ 200 PW, ce qui est élevé bien que très inférieur aux puissances exawatt typiquement requises dans les configurations infrarouges équivalentes.

Tous ces résultats ont été obtenus grâce à une implémentation numérique du formalisme de l'émission stimulée dans le vide, adaptée à la grande taille des simulations de champ MPR, et donc parallélisée. Cet algorithme a été largement validé sur des configurations de référence connues, et par rapport à différents modes d'implémentation numérique, comme détaillé dans le chapitre 3. Dans le cas plus complexe des impulsions

MPR, il a été possible d'obtenir des estimations analytiques, dont la dérivation détaillée a été présentée au chapitre 4. Nous avons également travaillé à clarifier la théorie en reliant notre approche à la résolution des équations du champ effectif, également étudiée dans la littérature, comme le résume le chapitre 5.

Les interactions de la lumière MPR avec la matière préexistante ont été présentées dans le chapitre 9. Dans le cas de l'interaction avec une cible solide, nous avons pu mettre en évidence que même à des intensités (comparativement) faibles de 10^{25} W.cm^{-2}, les faisceaux de MPR améliorent les signatures sf-QED de plusieurs ordres de grandeur par rapport à l'irradiation directe de la cible avec une impulsion infrarouge d'énergie équivalente. Nous avons également pu étudier la dynamique à une intensité plus élevée et constater que des amas d'électrons et de positons de très haute densité se forment alors et sont accélérés jusqu'à des énergies de l'ordre du GeV. Dans le cas d'une collision de lumière MPR avec un faisceau d'électrons de haute énergie, nous avons pu calculer les paramètres χ obtenus, et établir leur pertinence pour la physique autour du régime de Ritus-Narozhny de l'EDQ-cf, ainsi que les signatures de ces interactions sous la forme de spectres de particules émises.